Computation and Application of Atomic Data for Inertial Confinement Fusion Plasmas

Ping Wang

June 1991

UWFDM-855

Ph.D. thesis.

Computation and Application of Atomic Data for Inertial Confinement Fusion Plasmas

Ping Wang

Fusion Technology Institute
University of Wisconsin
1500 Engineering Drive
Madison, WI 53706

http://fti.neep.wisc.edu

June 1991

UWFDM-855

Ph.D. thesis.

COMPUTATION AND APPLICATION OF ATOMIC DATA FOR INERTIAL CONFINEMENT FUSION PLASMAS

by

PING WANG

A thesis submitted in partial fulfillment of the
requirements for the degree of

DOCTOR OF PHILOSOPHY
(Nuclear Engineering and Engineering Physics)

at the
UNIVERSITY OF WISCONSIN - MADISON
1991

Abstract

With the primary aim of generating large scale, high quality atomic data for ICF/MCF research applications, a basic atomic data calculation package has been created. Atomic structure and radiative data (energy levels, oscillator strengths and photoionization cross sections) are calculated based on the Hartree-Fock method. General accuracy of the data is expected to be better than 15% for the single configuration HF calculation and a few percent for the multiconfiguration HF calculation. Atomic collisional data calculations are based on the distorted wave approximation, the Born approximation and the semiclassical impact parameter method.

The atomic data generated from this package has been applied to analyze the Kα x-ray spectrum produced from an Al plasma heated by an intense proton beam. Such plasmas are currently generated by the PBFA II pulse power accelerator at Sandia National Laboratories. Our calculated wavelengths of Kα transitions agree well with the experimental data. The properties of the emission of Kα satellite line radiation produced by proton-impact ionization and its potential as a temperature diagnostic for light-ion-heated plasmas have also been studied.

A non-LTE collisional-radiative-equilibrium model which self-consistently accounts for pressure ionization effects has been formed. Based on this CRE model and our atomic data, an equation of state and opacity computation code, EOSOPC, has been developed. In EOSOPC, important nonideal effects such as pressure ionization, electron degeneracy effects and Debye-Hükel corrections for charged particle interactions have been included in the calculations of equations of state. In the opacity calculations, the group structure for computing group mean opacities can be setup automatically in a prudent manner. Our calculation results show that the group mean opacities are sensitive to the group structure and the accuracy of the atomic data.

Approved:

Date Professor Gregory A. Moses

Nuclear Engineering and Engineering Physics

Acknowledgment

I would like to express my sincere appreciations to my thesis advisor Professor Gregory A. Moses for his support and encouragement throughout the course of this research. His patience, understanding, guidance as well as the computing environment he has provided were essential in completing this work.

Many thanks go to staff scientists Dr. Joe MacFarlane and Dr. Robert Peterson for their stimulating private discussions that have enriched my education far beyond expectations.

I extend a special thanks to Kim Simmons and Osman Yasar for their friendship and informative discussions

I am also grateful to many teachers I have had in engineering, physics and astrophysics. Special thanks go to Professors Moses, Conrad, Emmert, Maynard, Mathis, Zhou yizun and Zhang zijin, whose lectures constituted in one way or another a milestone for my research and study in general.

Finally, I would like to express my sincere thanks to my wife, Xiaoxia, for the sacrifices she has made and the hardships she has gone through for my graduate study in addition to her own. Her endurance during the past five years represents a debt that I can only try to repay. My mother deserves special thanks for her continued support in the furtherance of my education. She has surely looked forward to this time.

Financial support provided by Sandia National Laboratory, San Diego Supercomputer Center and Kernforschungszentrum - Karlsruhe (GERMANY) is sincerely appreciated.

Contents

List of Figures

List of Tables

Chapter 1

Introduction

1.1 Introductory Remarks

Two distinct approaches have been utilized toward the goal of achieving a fusion reactor — magnetic confinement and inertial confinement. Typical densities and temperatures of fusion plasmas are shown in Figure 1.1. Generally speaking, atomic phenomena in hot dense plasmas found in inertial confinement fusion (ICF) devices are different from those in hot tenuous plasmas found in magnetic confinement fusion (MCF) devices. However, the atomic physics data needed in both ICF and MCF research are basically the same. This basic atomic data includes atomic structure data (energy levels, wavelengths), radiative transition data (oscillator strengths, photoionization cross sections, free-free transition cross sections, damping constants) and collisional data (cross sections for electron-ion impact, ion-ion impact, charge exchange, *etc.*).

In ICF research, atomic physics processes play a significant role in the modeling of target implosions using the indirect drive approach, the modeling of magnetized plasma channels for ion beam transport, the modeling of blast waves in reactor target chamber plasmas, and the diagnostics of the target experiments. Examples are z-pinch plasma channels [1, 2], spherical blast waves generated by ICF target explosions [3, 4] and recent ion beam experiment at Sandia National Laboratories [5].

Z-pinch plasma channels are important to the design of light ion beam (LIB) inertial confinement fusion reactors and near term experiments. In these applications, such as the Laboratory Microfusion Facility (LMF)[8] and Light Ion Beam Reactor (LIBRA), high intensity ion beams are used to ablatively implode a target to achieve extremely high densities and to shock heat deuterium-tritium (D-T) fuel to temperatures sufficiently high to have a thermonuclear burn. A typical schematic diagram of a z-pinch plasma is shown in Figure 1.2. In the modeling of z-pinch plasma channels[2], one must solve a set of time-dependent radiation magnetohydrodynamics (RMHD) equations [6]. The physical properties of the channel plasma, *i.e.*, equations of state and opacities (the resistance of the plasma to the transport of radiative energy, a very important physical parameter that enters any solution of radiation the transfer equation) are very important to the modeling of z-pinch

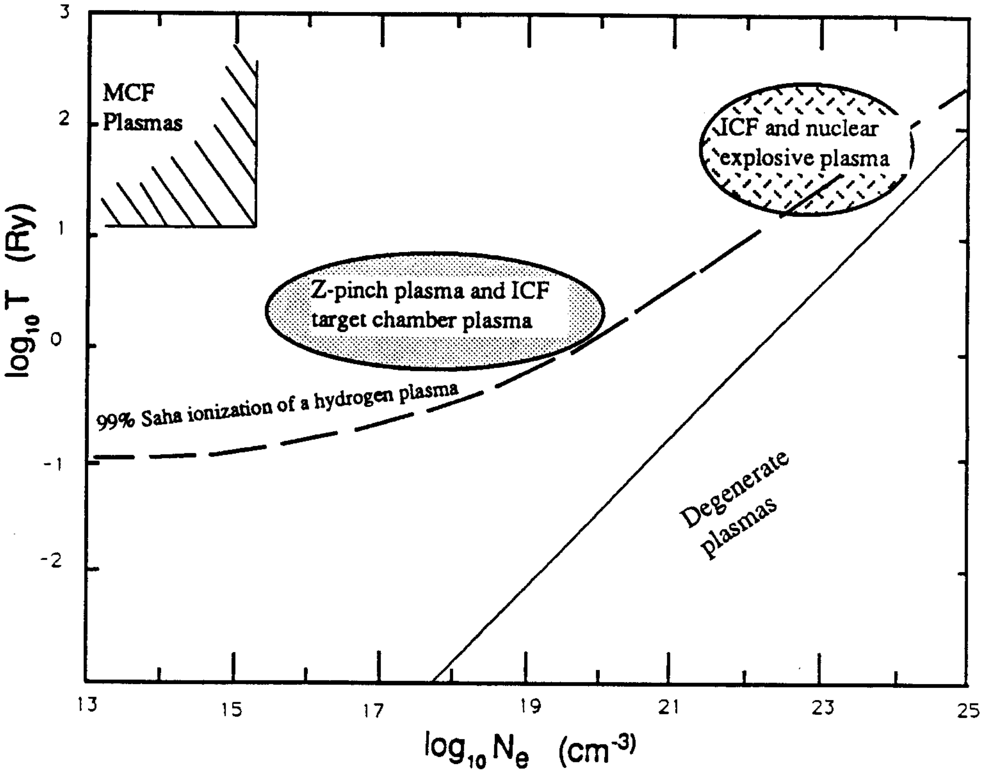

Figure 1.1: Density and temperature conditons of some fusion plasmas.

plasma channels and may directly affect the behavior of plasma channels. Huge amounts of atomic data are required for the computations of equations of state and opacities.

A major concern in designing ICF power reactors, such as LIBRA and SIRIUS-T[7], and near term experiments, such as the Laboratory Microfusion Facility (LMF), is the protection of the target chamber first wall from the target x-rays and debris ions. In order to predict the propagation of the target explosion generated microfireball through the target chamber plasma to the first wall (see Figure 1.5), we need to solve the radiation hydrodynamics equations (RHD) [9]. Two sets of coupled equations are included in RHD. These are moment equations for the radiation field and fluid equations for the radiating fluid. The equations for the radiation field couple to the radiating fluid via emissivity and opacity. Also, we must have the equations of state of the plasma. Target chamber plasmas created after a high-gain ICF target explosion are very far from local thermodynamic equilibrium (LTE). The atomic level populations are not well described by the Saha-Boltzmann distributions. The internal energy and opacity at each point in the plasma depend not only on the local temperature and density, but also the radiation field. Also, the radiation flux escaping the plasma is nothing close to that of a blackbody. Target chamber plasmas can be optically thick at some frequencies (e.g., at line centers), while being optically thin in other parts of the spectrum. Very detailed atomic physics and radiation transfer theory

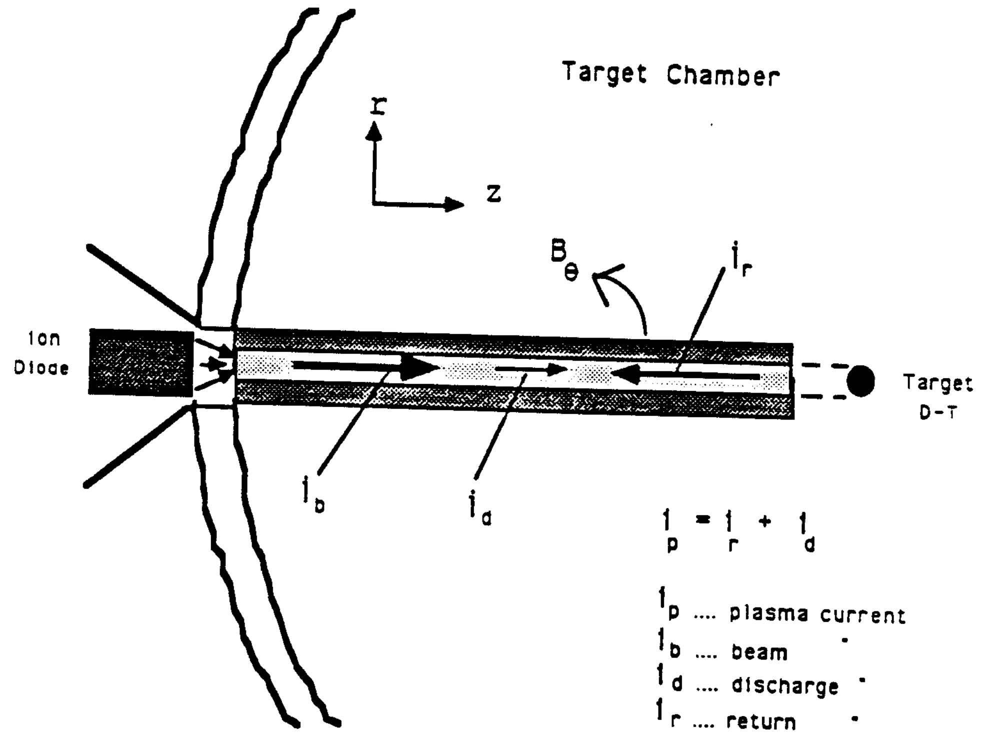

Figure 1.2: Schematic of beam propagating plasma channel in LIB fusion.

are involved to better understand these effects [10, 11].

Kα x-ray satellites from a target heated by an intense ion beam were recently observed in the Particle Beam Fusion Accelerator II (PBFA-II) experiments at Sandia National Laboratories [5]. These spectra contain abundant information of properties of the target plasmas, such as charge state distribution, peak electron temperature and the plasma density. To analyze Kα x-ray satellites, very accurate atomic structure data are required. For example, the identification of the individual term-dependent Kα lines from an aluminum plasma demands that the atomic energy levels be calculated to better than one part in 3000. Our preliminary studies [12, 13] have indicated that these plasmas are not in LTE, and appropriate radiative effects must be considered. This requires reliable atomic collisional data.

It is necessary to indicate that, although the need for accurate atomic data is immense, with applications in such diverse fields as spectroscopy, astronomy, and fusion energy research, few of the ions of interest are attainable in the laboratory. We still depend primarily on theoretical data. In recent years there have been many advances in computational atomic physics and an international collaborative research group led by M.J. Seaton is currently generating a high quality atomic data base [14, 15]. However, from the point of view of local usage, this kind of data base is not yet available. The need for the capability to generate high quality atomic data for the applications of local ICF (and/or MCF) research is obvious. This is one of the goals of this work.

The other motivation for this work comes from the fact that the plasma model and the atomic model for equations of state and opacity in our code, IONMIX [16], need to be improved to give more reliable results. Very simple physical models are currently used in IONMIX. The plasma is treated as an ideal gas and the ions are treated as hydrogenic. For a high density, partially ionized plasma, we can not expect that such simple physical models will provide high quality results. In this thesis work, much better atomic data are employed and non-ideal effects, such as the Debye-Hückel correction [17, 18], partially degenerate electron effect [19] and pressure ionization effect [20] *etc.*, are included in the computations of equations of state and opacities. We expect that these improvements can give us better understanding of z-pinch plasma channels and target chamber plasmas.

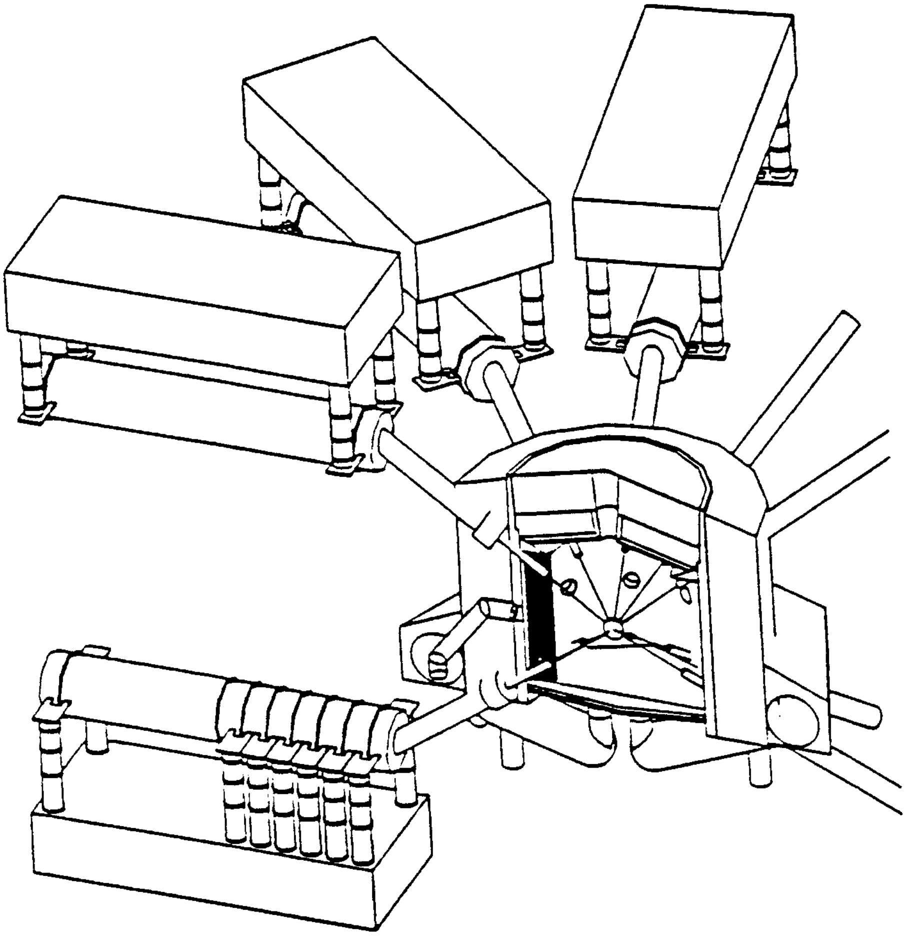

Figure 1.3: LIBRA reactor design

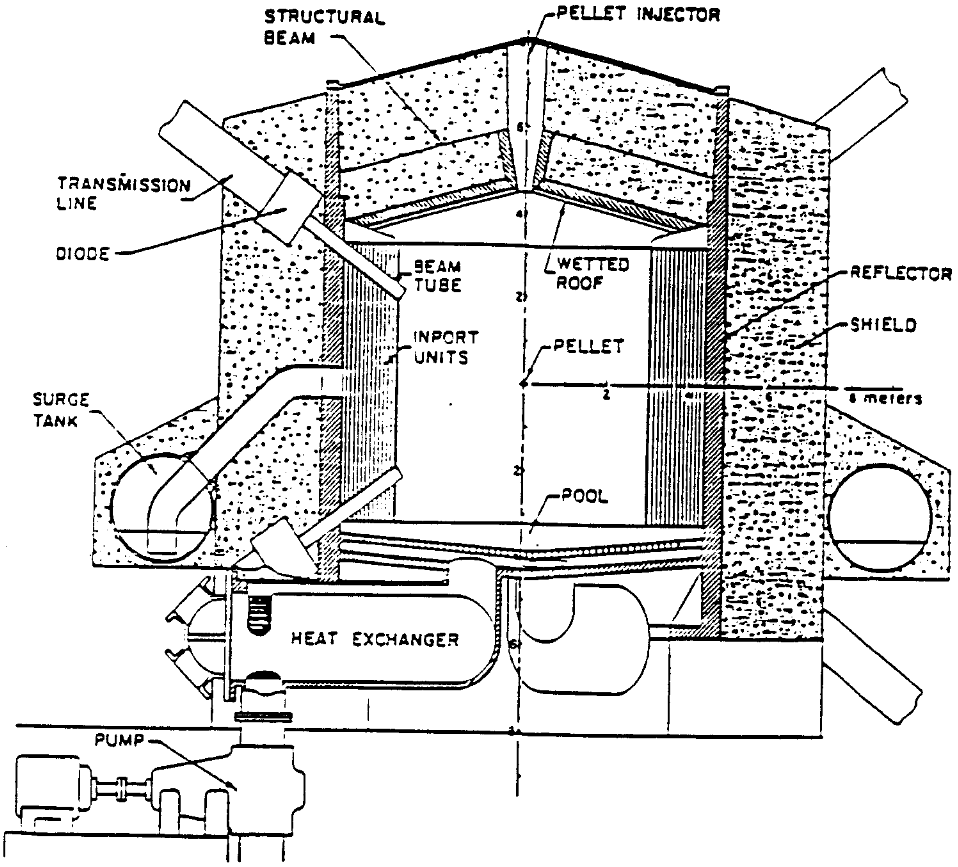

Figure 1.4: Cross section of LIBRA target chamber

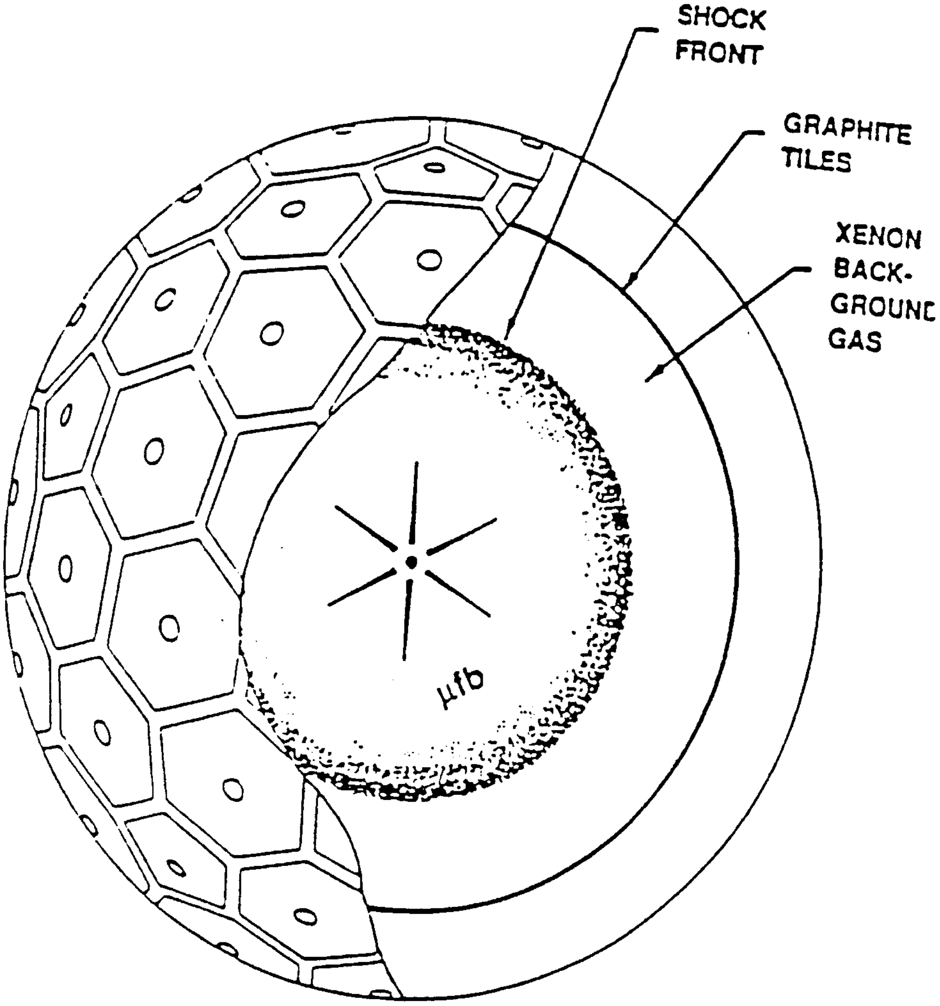

Figure 1.5: Schematic illustration of the SIRIUS-T target chamber.

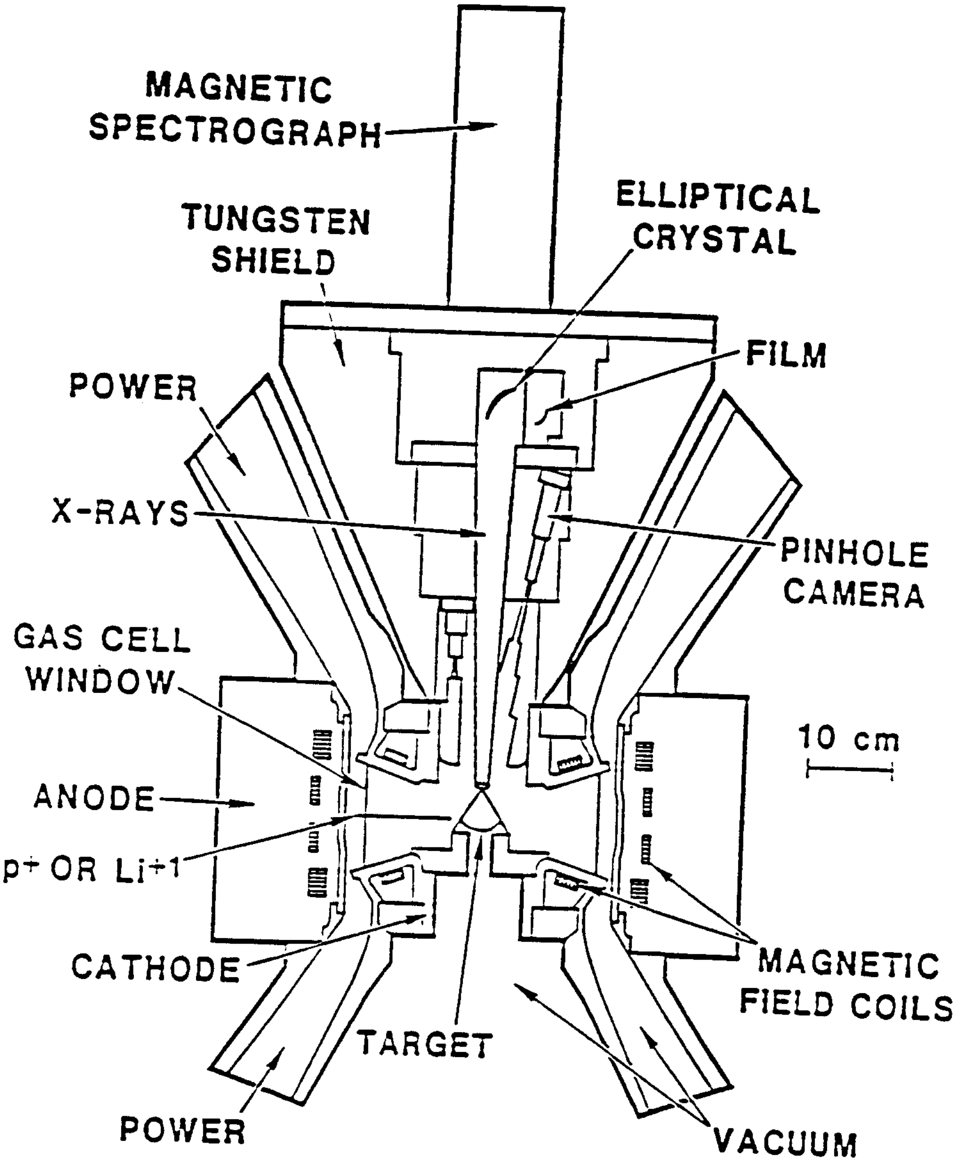

Figure 1.6: Schematic cross sectional diagram of the PBFA-II diode region.

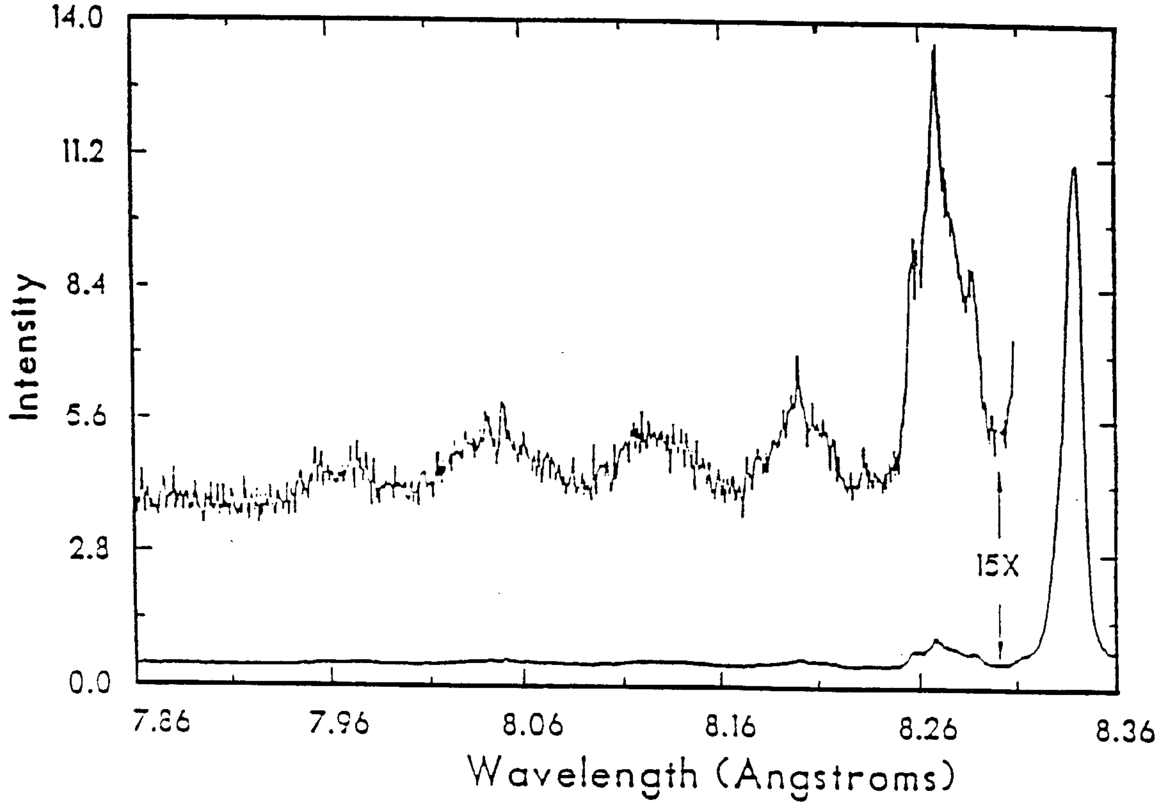

Figure 1.7: Time-integrated spectrum from PBFA-II. experiment.

1.2 Atomic Physics Model Considerations

In this work we consider a hot, partially ionized, collisional plasma and related atomic processes. By this we mean that the plasma is sufficiently hot that all molecules are dissociated, and the components of the plasma are atoms, ions and electrons.

All model plasmas with two or more components can essentially be classified in terms of either the **chemical picture** [21] or the **physical picture** [22]. In the *chemical picture*, bound configurations such as atoms are introduced and treated as independent species. In the *physical picture*, only fundamental particles (electrons and nuclei) enter explicitly. Bound states appear implicitly through the negative energy solutions of the Hamiltonian. In principle the *physical picture* is very attractive. However this formalism is not yet sufficiently well developed for spectroscopy analyses and opacity calculations. The *chemical picture* works well for plasmas with densities bounded by $n \leq 10^{22}\ cm^{-3}$. At very high densities, e.g., in ICF target plasmas, the *chemical picture* breaks down and one must use a cruder atomic model based on a statistical potential, such as the hot Thomas-Fermi model [23]. This approach yields atomic eigenvalues and eigenfunctions that in some rough sense are consistent with the state of the plasma, but it obliterates even the coarsest features (configuration) of the internal structure of the atom and forces one to deal with average orbitals. This method is inferior at low density. Currently, the best way to determine the thermodynamic and optical properties of plasmas in a wide range of temperature and density is a combination of the *chemical picture* and statistic methods: in the low density regime ($n \leq 10^{22}\ cm^{-3}$) using the *chemical picture* along with the best available atomic data, in the very high density regime ($\sim$ ICF target plasma), using statistical models. Between these two limiting regimes lies a " no-man's land" where neither theory works well, and an interpolation scheme [24] is used. In this work we deal only with relatively low density plasmas ($n \leq 10^{22}\ cm^{-3}$), and consider all the plasma physics problems in the framework of the *chemical picture.*

In attacking plasma physics problem under the framework of the *chemical picture*, the first problem faced is the determination of internal structures of the bound configurations (atomic structure) in the plasma. The starting point is Schrödinger's equation for a many-electron system, $\hat{H}\Psi = E\Psi$. In this equation, E is the total energy of the system, Ψ is the total wavefunction, and $\hat{H}$ is the Hamiltonian. The exact form of the Hamiltonian depends on the properties and the environment of the system. It is obvious that the Hamiltonian of an isolated ion is different from that of a plasma ion because of the environmental effects. In principle the atomic calculations for plasma ions should be based on the Hamiltonian with a modified internal potential which takes account of the influence of surrounding particles. However, how to determine this "modified internal potential" correctly is still an open problem. Even for a very simple system such as hydrogenic atoms, there is no satisfactory answer [20]. Fortunately these environmental perturbations are very small in low density plasmas, and accurate atomic data for isolated atoms are still feasible. Now, the basic question is what is the upper bound of the density domain that the atomic data for isolated atoms can be applied? On the basis of previous work [20, 25], we believe that $n \leq 10^{22}\ cm^{-3}$ is a reasonable limit. This is just the region of our interest. Hence in this work we do detailed atomic calculations for isolated atoms, and consider the environmental effects through an "occupation probability formalism" [20] in the computations of the thermodynamic properties and the optical properties of the plasma. This sets a basic limitation on our work.

1.3 Specific Atomic Models

Schrödinger's equation for the steady state of a many-electron system,

$$\hat{H}\Psi = E\Psi \tag{1.1}$$

is a fundamental equation of quantum mechanics and the starting point of all atomic calculations. In this equation E is the total energy, Ψ is the total wavefunction, and $\hat{H}$ is the Hamiltonian of the system. All the interaction information of the system is included in $\hat{H}$. In atomic calculations, it is the different choices of $\hat{H}$ that give different approximate atomic models.

One of the most successful and useful approaches to describing an atom is the Hartree-Fock model [26], which is based on the Schrödinger Hamiltonian of an atom:

$$H = \sum_{i=1}^{N} [\frac{\mathbf{p}_i^2}{2m_e} - \frac{Ze^2}{r_i}] + \sum_{i>j} \frac{e^2}{r_{ij}} \tag{1.2}$$

where the summations are over all bound electrons, $\mathbf{p}_i$ is the momentum of the ith electron, e is the electronic charge, m_e is the electron rest mass, r_i is the distance between the nucleus and the ith electron, and r_{ij} is the distance between the ith and jth electrons.

It should be noted that Eq.(1.1) is unsolvable with the Hamiltonian in Eq.(1.2) because of the existence of $1/r_{ij} = 1/ \mid \mathbf{r}_i - \mathbf{r}_j \mid$. An approximation must be made. From the point of view of perturbation theory, we can introduce a zero order approximation of $\hat{H}$ in Eq.(1.2)

$$\hat{H}_o = \sum_{i=1}^{N} [-\frac{\nabla_i^2}{2} - \frac{Z}{r_i} + V(r_i)] \tag{1.3}$$

where the effect on interactions with other electrons have been replaced by a single-particle potential $V(r)$. Let $\Psi^{(o)}$ be the zero order approximation of Ψ, we have

$$\hat{H}_o \Psi^{(o)} = E^o \Psi^{(o)} \tag{1.4}$$

Eq.(1.4) is separable, let

$$\Psi^{(o)} = \psi(1)\psi(2)\cdots\psi(i)\cdots\psi(N) \tag{1.5}$$

where $\psi(i)$ is a one-electron wavefunction for electron i. Substituting Eq.(1.5) into Eq.(1.4), we have

$$[-\frac{\nabla_i^2}{2} - \frac{Z}{r_i} + V(r_i)]\psi(i) = E_i\psi(i) \tag{1.6}$$

which is the wave equation for a particle in a central field. Like the hydrogenic equations, in spherical coordinates the above equation separates further into a radial, angular, and spin part. In fact one get,

$$\psi(r,\theta,\phi,\sigma) = (\frac{1}{r})P(r)Y_{lm_l}(\theta,\phi)\chi_{m_s} \tag{1.7}$$

where $Y_{lm_l}(\theta,\phi)$ is a spherical harmonic and χ_{m_s} a spin function. The radial function $P(r)$ is now a solution of the radial Schrödinger's equation

$$[\frac{d^2}{dr^2} + \frac{2Z}{r} - 2V(r) - \frac{l(l+1)}{r^2} - \varepsilon]P(r) = 0 \tag{1.8}$$

with boundary conditions $P(0) = P(\infty) = 0$. This is a Sturm-Liouville boundary value problem with possibly an infinite number of eigenvalues and eigenfunctions. Let us denote these by ε_{nl} and $P(nl \mid r)$ respectively, where the integer n now orders the solutions so that $n = l+1$ corresponds to the lowest eigenvalue, $n = l+2$ to the next, and so forth, and the eigenfunction for $n = l+1$ has no node, $n = l+2$ has one node, and so on. The integer then assumes the same role as the principal quantum number for the hydrogen equation. As a result the one electron functions can be specified entirely in terms of four quantum numbers (n, l, m_l, m_s). Such functions are called "spin-orbitals".

In order to satisfy the Pauli exclusion principle, the total wavefunction for a N-electron system must be an antisymmetric function. Hence, a zero order total wavefunction is expressed as a " Slater determinate"

$$\Psi^{(o)} = \frac{1}{\sqrt{N!}} \begin{vmatrix} \psi_1(1) & \psi_1(2) & \cdots & \psi_1(N) \\ \psi_2(1) & \psi_2(2) & \cdots & \psi_2(N) \\ \vdots & \vdots & \vdots & \vdots \\ \psi_N(1) & \psi_N(2) & \cdots & \psi_N(N) \end{vmatrix} \tag{1.9}$$

where $\psi_j(i)$ is a spin-orbital for the jth set of quantum numbers $(n_j, l_j, m_{l_j}, m_{s_j})$ in terms of the space and spin coordinates of the ith electron $(r_i, \theta_i, \phi_i, \sigma_i)$.

For a given electron configuration, there are 'g' corresponding quantum states (*e.g.*, there are 15 quantum states corresponding to the configuration $1s^2 2s^2 2p^2$) . Each quantum state is described by a $\Psi^{(o)}$. By solving Eq.(1.4), we can have 'g' orthonormal zero order atomic wavefunctions

$$\Psi_1^{(o)}, \Psi_2^{(o)}, \cdots, \Psi_i^{(o)}, \cdots, \Psi_g^{(o)}$$

for a specific configuration. The whole eigenfunctions of $\hat{H}_o$ form a complete orthonormal set. Now, the accurate wavefunction Ψ can be expanded in terms of this complete orthonormal set

$$\Psi = \sum_{k=1}^{\infty} C_k \Psi_k^{(o)}. \tag{1.10}$$

However, if $\hat{H} - \hat{H}_o$ is small, to the first order approximation, we can expand Ψ only in a subspace of a specific configuration.

$$\Psi \simeq \Psi^{(1)} = \sum_{k=1}^{g} C_k \Psi_k^{(o)} \tag{1.11}$$

This is called the **single-configuration approximation.** It is obvious that the single-configuration approximation can not be always satisfied because of the incomplete expansion of Ψ. To have better results, we can expand Ψ in a larger subspace of "M" selected configurations

$$\Psi \simeq \sum_{s=1}^{M} \sum_{k=1}^{gs} C_k^s \Psi_k^{(o)s} \tag{1.12}$$

This is called the **multiconfiguration approximation.**

Now, the problem left is how to construct the $\hat{H}_o$? In the Hartree-Fock model, the potential for electron-electron interactions e^2/r_{ij} is approximated by a non-local central potential. The HF potential consists of two parts, the direct Coulomb potential and the exchange potential. The exchange potential comes from the requirement of the Pauli principle. A HF wavefunction represents a specific orbital angular momentum **L** and spin angular momentum **S**. Much of the numerical effort in calculating HF wavefunctions is spent in the exchange part. To reduce numerical effort, several approximate models which are based on the simplified treatments of HF exchange potential have been proposed. These approximated models include:

- Hartree (H) approximation [28] — neglecting the exchange term.
- Hartree-Fock-Slater (HFS) approximation [29] — introducing a self-interaction term and replacing the exchange term by a statistical free-electron expression similar to that used in the Thomas-Fermi-Dirac [30] theory of the atom.
- Hartree-Plus-Statistical-Exchange (HX) approximation [31] — Using exactly the same direct terms as those in the HF equations,making statistical approximation for only the non-self-exchange term.

These approximations allow the radial differential equation to become a homogeneous equation which is free of all the complexities present in the general HF equations. The price of making these simplified approximation is the loss of accuracy. Since dramatic development in computer techniques have been achieved these years, the advantages of these simplified treatments become less and less significant. The Hartree-Fock model has been widely applied in large scale atomic calculations.

In regards to the accuracy, the total atomic energy predicted by a single-configuration HF wavefunction is generally accurate within a percent or two, however the predictions for the transition parameters, i.e., transition energies and oscillator strengths, are somewhat crude (a few to 15%) to be of practical value for detailed spectroscopy analysis. The multiconfiguration HF calculations are required in such cases.

In our current work, we choose the Hartree-Fock method to do atomic calculations. The single-configuration approximation is used to generate large scale atomic data for the computations of equations of state and opacities. Whenever necessary (e.g., in analyzing Kα x-ray spectra) the multiconfiguration approximation is employed.

1.4 Plasma Model

From the point of view of the spectroscopy diagnostics and the computations of equation of state and opacity, a proper plasma model means the best specification of the particle distributions in the plasma. In another word, to specify a partially ionized plasma, we need to indicate the components of it, the energy distribution of the particles, the ionization stage distributions and the atomic level occupation numbers. In this sense, an exact plasma model should include all atomic processes that result in an atom/ion being transferred from one quantum state and charge to another.

The starting point to describe nonequilibrium situations in plasmas is the Boltzmann equation for the set of interacting particle types comprising the plasma. For a particular class of particle, the time rate of change of its distribution function f is given by [32, 33]

$$\frac{df}{dt} = (\frac{\partial f}{\partial t})_{int} \tag{1.13}$$

The right-hand-side of this equation symbolizes the rate of change of f due to interaction with other classes of particles (including photons). The left-hand-side is the rate of change of f in phase space under the influence of external fields. Important classes of particles which must be identified here include free electrons and ions of different species in distinct internal quantum states. In regard to photons, there are two different cases. In optically thin plasmas, the radiation transport effect is not important. In optically thick plasmas, however, the distribution function for photons must also be studied. Since the electron impact processes are the most important processes for the changes in the internal ion state distributions, the first problem we need to solve is the specification of the electron kinetic-energy distribution.

The interaction terms for the electron distribution include electron-electron $(e-e)$ collisions, electron-ion $(e-i)$ collisions and electron-photon $(e-\nu)$ interactions. As is well known, owing to the long range of the Coulomb interaction, distant encounters are most effective in changing the distribution function. For an isotropic distribution of electron kinetic energies, the kinetic energy redistribution time scales τ_{e-e} and τ_{e-i} are significant parameters. It is easy to show that, because of the mass factors,

$$\frac{1}{\tau_{e-e}} \simeq \frac{1846A}{\tau_{e-i}} \tag{1.14}$$

where A is mass number of the ion. Time scales of processes leading to the emission of radiation are much longer. Therefore the interaction term for the electron distribution $f_e(\mathbf{u})$, where $\mathbf{u}$ is the electron velocity, is determined primarily by e-e collisions, and takes the form

$$\begin{aligned}(\frac{\partial f_e(\mathbf{u})}{\partial t})_{int} \simeq & -\int f_e(\mathbf{u})f_e(\mathbf{v})|\mathbf{u}-\mathbf{v}|\sigma(\mathbf{u},\mathbf{v}\rightarrow\mathbf{u}',\mathbf{v}')d\mathbf{u}'d\mathbf{v}'d\mathbf{v} \quad (1.15)\\ & +\int f_e(\mathbf{u}')f_e(\mathbf{v}')|\mathbf{u}'-\mathbf{v}'|\sigma(\mathbf{u}',\mathbf{v}'\rightarrow\mathbf{u},\mathbf{v})d\mathbf{u}'d\mathbf{v}'d\mathbf{v}\end{aligned}$$

with the constraints that total energy and momentum are conserved in each binary collision; σ describes the collisional transition for collisions between pairs of electrons of initial velocities $\mathbf{u}$ and $\mathbf{v}$ and final velocities $\mathbf{u}'$,$\mathbf{v}'$. The invariance of the dynamical equations under time reversal implies that

$$\sigma(\mathbf{u},\mathbf{v}\rightarrow\mathbf{u}',\mathbf{v}')=\sigma(\mathbf{u}',\mathbf{v}'\rightarrow\mathbf{u},\mathbf{v}) \quad (1.16)$$

and so the usual form for the electron collision term is obtained, namely,

$$\begin{aligned}(\frac{\partial f_e(\mathbf{u})}{\partial t})_{int} \simeq & -\int[f_e(\mathbf{u}')f_e(\mathbf{v}')-f_e(\mathbf{u})f_e(\mathbf{v})]|\mathbf{u}-\mathbf{v}|\\ \times & \ \sigma(\mathbf{u},\mathbf{v}\rightarrow\mathbf{u}',\mathbf{v}')d\mathbf{u}'d\mathbf{v}'d\mathbf{v} \quad (1.17)\end{aligned}$$

The isotropic distribution for which the above integral vanishes identically is that for which

$$f_e(\mathbf{u})f_e(\mathbf{v})=f_e(\mathbf{u}')f_e(\mathbf{v}') \quad (1.18)$$

when $\mathbf{u}$, $\mathbf{v}$, $\mathbf{u}'$ and $\mathbf{v}'$ satisfy the conservation constraints. This is the Maxwellian distribution, namely,

$$f_e(\mathbf{u})=n_e(\frac{m_e}{2\pi kT_e})^{3/2}exp(-\frac{m_eu^2}{2kT_e}) \quad (1.19)$$

This distribution is independent of particular form of σ and is usually deduced from general thermodynamic considerations. It is almost a rule to assume a Maxwellian distribution for free electrons in studying the internal ion state distributions. This is because the self-collision time τ_{e-e} for electrons is usually short compared with the time scales for changes in the internal ion state distributions. The main factor in the justification of this assumption is the rate at which energy is imparted to the ions in question.

Now, we come to consider the distributions of the ionization stages and the level occupation numbers. The contributions to the interaction term for the ions in state i are the various encounters of such ions with electrons, other ions and the radiation field. By integrating the interaction term over velocities, we have

$$\begin{aligned}\int\left(\frac{\partial f(Z,z,i,\mathbf{u})}{\partial t}\right)_{int}d\mathbf{u} &= -\sum_{k\neq i} n_e n(Z,z,i)X^e(i\rightarrow k) \\ &\quad +\sum_{k\neq i} n_e n(Z,z,k)X^e(k\rightarrow i)+\cdots\cdots \quad (1.20)\end{aligned}$$

where $f(Z,z,i,\mathbf{u})$ is the distribution function for ions with charge z of element Z in quantum state i,

$$n(Z,z,i)=\int f(Z,z,i,\mathbf{u})d\mathbf{u} \quad (1.21)$$

is the population density, and

$$X^e(i\rightarrow k)=\int_{\Delta E}^{\infty} f_e(\varepsilon)v\sigma_{i\rightarrow k}(\varepsilon)d\varepsilon \quad (1.22)$$

is the electron collisional transition rate coefficient. The Boltzmann equation for the distribution function of ions in a particular state is then simplified to a statistical balance rate equation

$$\frac{dN_i}{dt} = \sum_{k \neq i} [C_{ki} N_k - C_{ik} N_i] \tag{1.23}$$

where C_{ki} are the rate coefficients for the processes which populate i; and C_{ik} the corresponding rate coefficients for depopulation. In principle any atomic process that results in an ion being transferred from one quantum state to another should be included. In practice, however, a selection must be made of those processes considered to be sufficiently significant for the level of approximation in mind. For a partially ionized plasma, the most common collisional and radiative processes considered are:

- $A(z,i) + e \rightleftharpoons A(z,k) + e$ (excitation and deexcitation by e^-)
- $A(z,i) + e \rightleftharpoons A(z+1,k) + 2e$ (ionization and recombination by e^-)
- $A(z+1,i) + e \rightarrow A(z,k) + h\nu$ (radiative recombination)
- $A(z+1,i) + e \rightarrow A(z,j)^* \rightarrow A(z,k) + h\nu$ (dielectronic recom.)
- $A(z,i) + h\nu \rightarrow A(z+1,k) + e$ (photoionization)
- $A(z,i) \rightarrow A(z,k) + h\nu$ (spontaneous decay)
- $A(z,i) + h\nu \rightarrow A(z,k)$ (photoexcitation and stimulated decay)

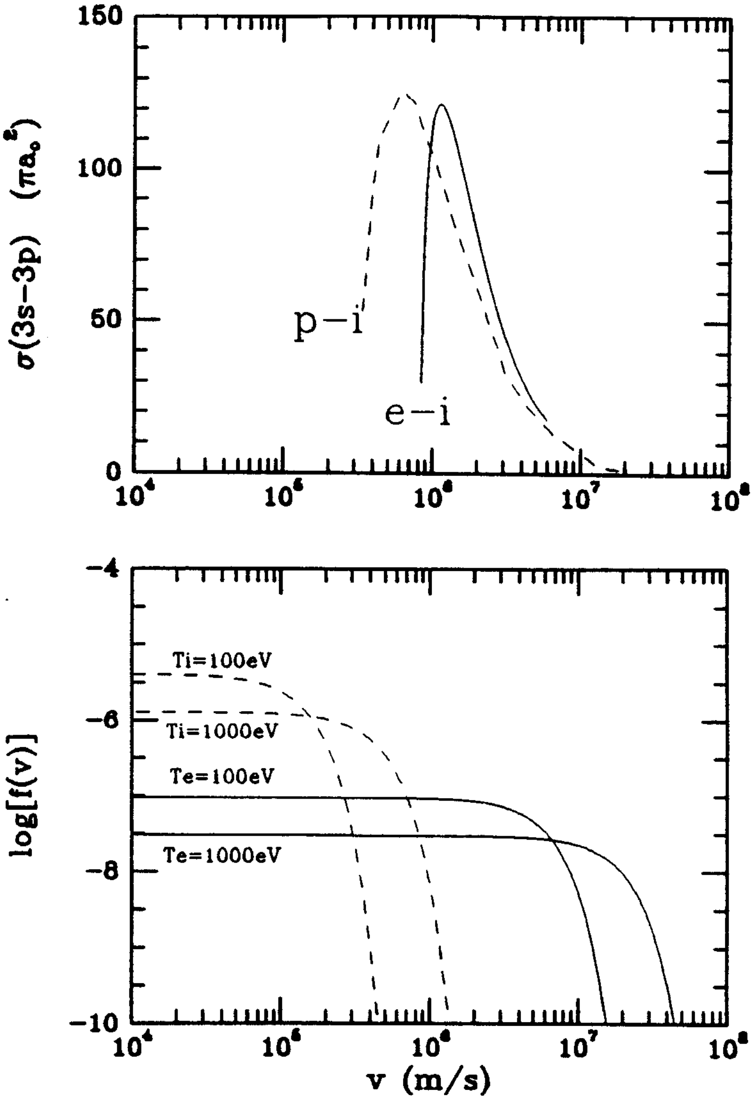

Figure 1.8: Comparison of impact excitation cross sections by electron and proton.

Here, the collisional processes between ions are neglected. This approximation is based on the following arguments. In the condition of approximate equipartition of kinetic energy between electrons and ions, the electrons have much greater velocities and since the rate coefficients are the product of cross section with velocity, electrons are usually much more effective than ions in causing collisional transitions among the states of the ions. In Figure 1.8 we compare a typical electron collisional excitation cross section and proton collisional cross section, along with the corresponding particle velocity distribution functions. It is obvious that the rate coefficient of ion impact is negligible compared with that of electron impact in such a case. There are, however, special circumstances where the ion impact cross sections are sufficiently large to overcome the disadvantage of low velocity and make this process important. Of particular importance in this connection are collisions which redistribute populations between fine-structure levels and high excited Rydberg levels. Fortunately, in such a circumstance the total collisional rate is sufficiently large to dominate that of the radiative processes, and a Boltzmann distribution is achieved among these levels.

Eq.(1.23) is a very general form of statistical balance equation. To obtain a solution of Eq.(1.23), a detailed description of any charge state is needed, and a very large number of transitions and energy levels have to be taken into account. This makes the calculations quite complicated. In two extreme limits (high density limit and low density limit), however, Eq.(1.23) can be reduced to very simple formulas.

In the high density limit, the collisional processes dominate the radiative processes. In such a case, the plasma is in local-thermodynamic-equilibrium (LTE), and we have

$$\frac{N_i^z}{N_o^z} = \frac{g_i^{(z)}}{g_o^{(z)}} exp(-\frac{\varepsilon_i - \varepsilon_o}{kT}) \tag{1.24}$$

and

$$\frac{N^{z+1}}{N^z} = 2(\frac{m_e kT}{2\pi\hbar^2})^{3/2} N_e^{-1} \frac{G^{z+1}}{G^z} exp(-\frac{I_z}{kT}) \tag{1.25}$$

where

$$G^z = \sum_k g_k^{(z)} exp(-\frac{\varepsilon_k - \varepsilon_o}{kT}) \tag{1.26}$$

is the partition function for ion X^z. The generally used criteria for LTE validity is deduced by requiring that the energy-dissipating radiative decay of the ionic levels will be at least 10 times less frequent than that of energy-conserving electron impact deexcitation [34, 35]. Generally speaking, higher excitation states are expected to be in LTE at lower densities.

In another limit, the plasma density is so low that the collisional ionization is balanced by only the radiative recombination. In such a case, the plasma is in Coronal equilibrium (CE), and we have

$$N^z = (\frac{S_o}{\alpha_1})(\frac{S_2}{\alpha_2}) \cdots (\frac{S_{z-1}}{\alpha_z}) N^o \tag{1.27}$$

$$N^o = [1 + \sum_{z=1}^{Z} (\frac{S_o}{\alpha_1})(\frac{S_1}{\alpha_2}) \cdots (\frac{S_{z-1}}{\alpha_z})]^{-1} N_{total} \tag{1.28}$$

and

$$\frac{N_k^z}{N_j^z} = N_e \frac{X_{jk}^e}{A_{kj}} \tag{1.29}$$

where S_z denotes ionization rate coefficient of the zth ion, α_z the recombination rate coefficient, X_{jk}^e the electron collision excitation rate coefficient, and A_{kj} the spontaneous decay rate. A commonly used criterion for the validity of CE is [36, 37]

$$n_e(cm^{-3}) \leq 10^{16}(T_e(eV))^{7/2} \tag{1.30}$$

For a specific problem, more strict criteria may be deduced by requiring that the radiative decay rates of the ionic levels are at least 10 times greater than those of electron collision deexcitation [34, 35].

In our work, a Collisional-Radiative-Equilibrium (CRE) model for the plasma is employed. By combining the CRE model with "occupation probability formalism" [20], the pressure ionization effect can be taken into account self-consistently. Detailed discussion on this model is given in Chapter 4.

1.5 Thesis Guide

In this section we give a synopsis of the problems considered and particular points of interest in each of the chapters of the thesis.

In this first chapter we have given an introduction to the thesis problem. In this regard we have discussed the goals of our work and the general aspects of the atomic and plasma models which are related to this work. In the next chapter the atomic processes in ICF plasmas and related data calculations are considered in detail. In doing so, first the atomic energy-level structure is specified. Next, important radiative transition parameters (oscillator strengths, photoionization cross sections, etc.) are studied and computed. Finally, atomic collisional processes are studied and several approximations for computing related cross sections are discussed and compared. Detailed calculation results are also given.

In chapter 3, we first discuss some general aspects of Kα spectroscopy as a plasma temperature diagnostic. Then we make a detail analysis of the Kα x-ray spectra which are produced from an aluminum target heated by an intense proton beam. Particular attention is given to the line identifications. The effects of radiation transport are also discussed.

In chapter 4, a CRE model which takes account of the pressure ionization effect self-consistently is formed. The equations of state and opacities of non-LTE plasmas are studied and computed. Detailed computational methods and data management procedures are discussed.

In chapter 5, we give a general summary of the work and further considerations.

Chapter 2

Atomic Data Calculations

With the primary aim of generating large scale high quality atomic data for our ICF/MCF research applications, we have setup a basic atomic data calculation package. In this chapter, we discuss the important atomic processes and the related theoretical computation methods which are included in our atomic data calculation package. Generally speaking, the atomic processes may be classified into two groups, radiative processes and collisional processes. In the following, we first determine the atomic structure, then we consider the atomic radiative processes. Finally, we discuss the atomic collisional processes.

Throughout the rest of this chapter, Z is the nuclear charge, z is the ion charge (*e.g.*, $z = 0$ for neutral atom, $z = 1$ for a single ionized atom, *etc.*), and z^* is the charge of the atomic core, i.e., the charge of the atom or ion without the optical electron. For a neutral atom $z^* = 1$, for a single ionized atom $z^* = 2$, and so on. Everywhere below, unless otherwise stated, we use a system of atomic units base on the *hartree* as the unit for energy. In this unit system, the first Bohr radius a_o is the unit for length; the basic electric charge e is the unit for electric charge; the reduced electron mass μ_e is the unit for mass; the Planck constant $\hbar$ is the unit for angular momentum. For convenient, some of the important energy conversion relations are listed below:

$$1\ hartree = 2\ Ry = 27.2116529\ (eV)$$

$$1\ hartree = 4.3598282 \times 10^{-11}\ (erg)$$

$$1\ hartree = 6.5796846 \times 10^{15} \nu\ (Hz)$$

$$1\ hartree = \frac{455.635}{\lambda\,(\AA)}$$

2.1 Atomic Structure Calculations

2.1.1 General Features of Atomic Structure

Theoretical treatment of an atom containing N electrons requires first of all knowledge of a suitable Hamiltonian operator $\hat{H}$. After $\hat{H}$ is specified, we can solve the Schrödinger equation

$$\hat{H}\Psi_k = E_k\Psi_k \tag{2.1}$$

to obtain the wavefunction Ψ_k and energy E_k of the atom for every stationary quantum state k of interest. Atomic structure is then determined. It is easy to understand that for different approximate Hamiltonian operators, we may have different atomic structure. An appropriate Hamiltonian operator for describing the development of approximate atomic structure can be take as

$$\begin{aligned} \hat{H} &= \hat{H}_{kin} + \hat{H}_{elec-nucl} + \hat{H}_{elec-elec} + \hat{H}_{s-o} \\ &= -\sum_i \frac{\nabla_i^2}{2} - \sum_i \frac{Z}{r_i} + \sum_{i<j} \frac{1}{r_{ij}} + \frac{1}{2}\sum_i \zeta_i(r_i)(\mathbf{l}_i \cdot \mathbf{s}_i) \end{aligned} \tag{2.2}$$

Here $r_i = |\mathbf{r}_i|$ is the distance of the ith electron from the nucleus, $r_{ij} = |\mathbf{r}_i - \mathbf{r}_j|$ is the distance between the ith and jth electrons, and the summation for $i < j$ is over all pairs of electrons. To discuss the development of the atomic energy, we first omit the spin-orbit interaction term $\hat{H}_{s-o}$, and begin with the central field model of the atom: we make the approximation that any given electron i moves independently of the others in the electrostatic field of the nucleus (assumed stationary) and the other $N-1$ electrons; this field is assumed to be time-averaged over the motion of the $N-1$ electron, and therefore (neglecting correlation with the position of the ith electron) to be spherically symmetric. In this central field, each orbital is a product of a radial function, a spherical harmonic and a spin function:

$$\psi_j(r_i, \theta_i, \phi_i, \sigma_i) = (\frac{1}{r_i})P(n_j l_j | r_i) Y_{l_j m_{l_j}}(\theta_i, \phi_i) \chi_{m_{s_j}}, \tag{2.3}$$

the total wavefunction of the N-electron system is a “Slater determinate”[38]:

$$\Psi^{(o)} = \frac{1}{\sqrt{N!}} \begin{vmatrix} \psi_1(1) & \psi_1(2) & \cdots & \psi_1(N) \\ \psi_2(1) & \psi_2(2) & \cdots & \psi_2(N) \\ \vdots & \vdots & \vdots & \vdots \\ \psi_N(1) & \psi_N(2) & \cdots & \psi_N(N) \end{vmatrix}, \tag{2.4}$$

and each atomic energy level is described by an “electron configuration average energy ” [27] — all the states belong to an electron configuration are degenerate. Now, how we account for the omitted effects, i.e., the non-spherically symmetric part of the electrostatic interaction between electrons and the spin-orbit interaction effect, can lead to different coupling schemes [27] and level structures. Two limiting coupling schemes are the LS-coupling and jj-coupling.

LS-Coupling

If the electrostatic interaction has a much greater value than that of spin-orbit interaction, we first consider to add the non-spherically symmetric electrostatic contribution. The non-spherically symmetric electrostatic contribution leads to a splitting of the level corresponding to a given configuration into quite a number of levels, characterized by different values of the total orbital angular momentum of the electrons $\mathbf{L}$ and the total spin $\mathbf{S}$. From the viewpoint of angular momentum coupling, after we add the non-spherically symmetric contribution, one-electron orbital angular momentum $\mathbf{l}$ is not a constant of motion any more and hence the uncoupling representation can not be used to describe the atomic states. We need to work under a coupling representation. It is easy to prove that the total orbital angular momentum **L** and the total spin angular momentum **S** are constants of motion, and hence the atomic states are the eigenfunctions of $\hat{\mathbf{L}}^2$ and $\hat{\mathbf{S}}^2$. This is the LS-coupling. We now add the omitted spin-orbit interaction. This effect splits the atomic levels into "fine-structure", and makes the atomic states become the eigenfunctions of $\hat{\mathbf{L}}^2$, $\hat{\mathbf{S}}^2$ and $\hat{\mathbf{J}}^2$. Here, $\mathbf{J} = \mathbf{L} + \mathbf{S}$ is the total angular momentum of the atomic system. *LS* coupling is a good approximation for low Z ($Z << 137$) elements. A schematic drawing of the developing of the energy-level structure of a '*pd*' configuration under LS-coupling conditions is shown in Figure 2.1.

jj-coupling

In the limit in which the spin-orbit interactions are much stronger than the Coulomb terms (*e.g.*, for high Z elements) we should first consider the spin-orbit interaction effect. The spin-orbit interactions couple **L** and **S** together and hence both **L** and **S** are not the constants of motion. In such a case, the spin of each electron first couples to its own orbital angular momentum, and then coupling together the various resultant $\mathbf{j}_i$ in some arbitrary order to obtain the total angular momentum **J**. This is the *jj*-coupling scheme. In the *jj*-coupling scheme, the state of each electron is described by four quan-

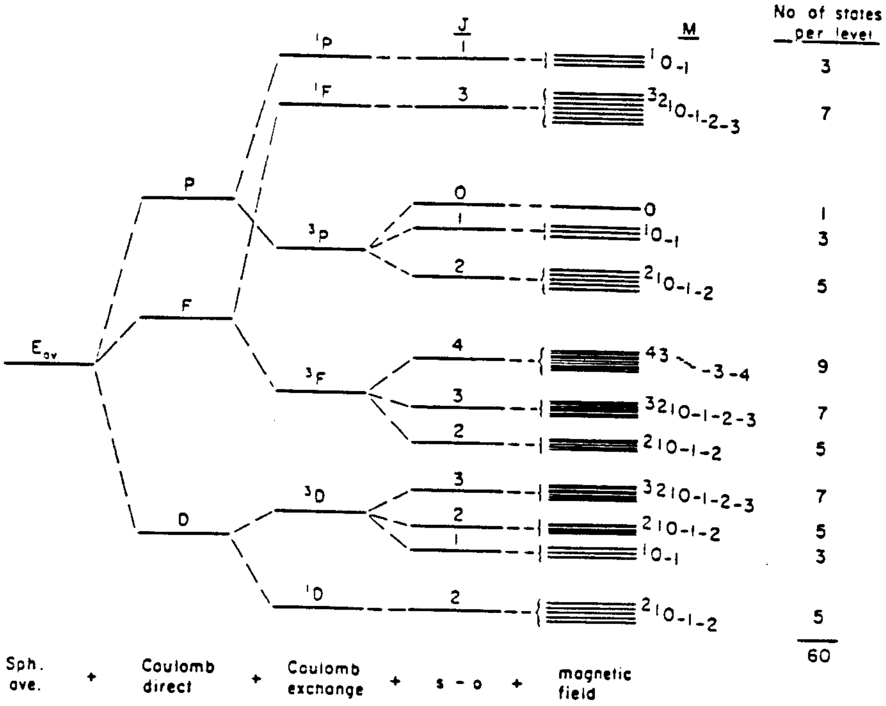

Figure 2.1: Schematic illustration of the development of the energy-level structure of a pd configuration under LS-coupling conditions[27]

tum numbers $(nljm_j)$, and each atomic state is described by a determinate constructed from one-electron wavefunctions $\psi_{nljm_j}(\mathrm{x})$. A schematic illustration of the development of the energy-level structure of a '*pd*' configuration under jj-coupling conditions is shown in Figure 2.2.

A number of other types of coupling [27, 40], such as intermediate coupling, jK-coupling, LK-coupling, *etc.*, are possible besides LS and jj couplings. However, we are only interested in relative low Z ($Z << 137$) elements where the LS-coupling is a good approximation. Everywhere below, we consider problems under the LS-coupling scheme.

It is necessary to indicate that although different coupling schemes may lead to different atomic structures, in most situations (but not always), there is a unique correspondence between the levels of one coupling approximation, *e.g.*, intermediate coupling, and the levels of the LS coupling approximation. This enables us to use the LS coupling terminology in the cases when the LS coupling approximation itself losses its meaning. In such cases, however, the wavefunction of a "$LSJM$" state is not the corresponding eigenfunction of $\mathbf{L}^2$, $\mathbf{S}^2$ and $\mathbf{J}^2$, but some sort of mixing of these eigenfunctions [40].

2.1.2 Atomic Energy Expressions

Atomic energy E is the expectation value of the Hamiltonian $\hat{H}$, i.e.,

$$E =< \Psi|\hat{H}|\Psi > \tag{2.5}$$

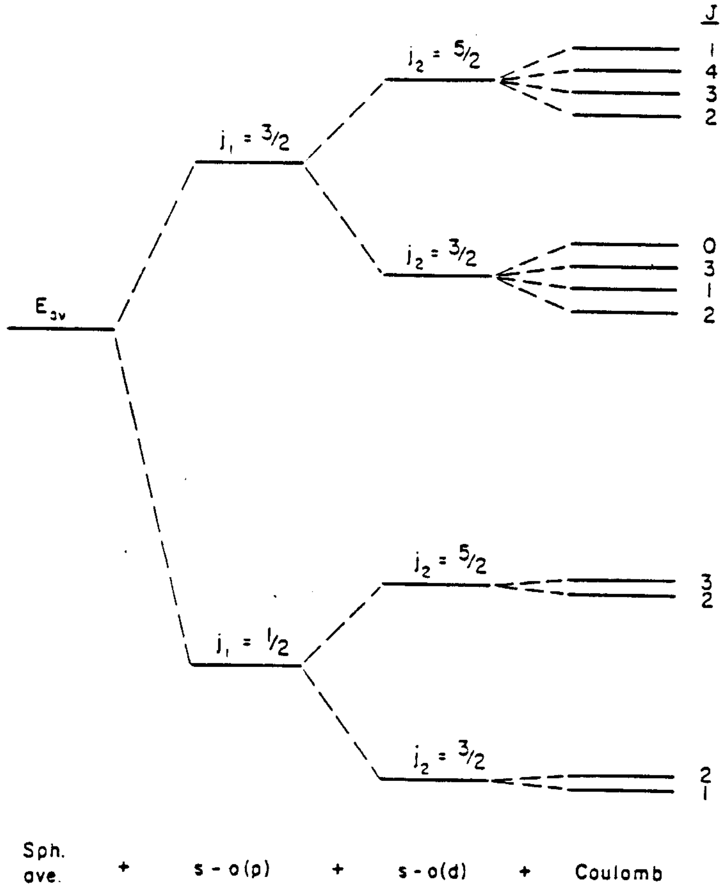

Figure 2.2: Schematic illustration of the development of the energy-level structure of a pd configuration under jj-coupling conditions[27]

where Ψ is the total wavefunction of the atomic system, and is constructed from one-electron wavefunctions of the N-electrons in the system. A one-electron wavefunction can be separated into radial, angular and spin parts. From the angular momentum theory [27, 41, 42], we can evaluate the angular and spin parts of the atomic energy matrix elements and leave the atomic energy E as some sort of linear combinations of the radial integrals. This expression for E is called the *atomic energy expression.* By applying the variational principle to the atomic energy expressions, we can obtain the radial equations for the radial functions and hence determine the atomic structure. A flow chart of the atomic structure calculation is shown in Figure 2.3.

For a non-relativistic Hamiltonian operator

$$\hat{H} = \sum_i (-\frac{\nabla_i^2}{2} - \frac{Z}{r_i}) + \sum_{i<j} \frac{1}{r_{ij}} \tag{2.6}$$

The corresponding energy matrix elements are

$$< \Psi | \sum_i (-\frac{\nabla_i^2}{2} - \frac{Z}{r_i}) | \Psi' >= \sum_{\sigma,\sigma'} x(\sigma,\sigma') I(n_\sigma l_\sigma, n_{\sigma'} l_{\sigma'}) \delta_{l_\sigma l_{\sigma'}} \tag{2.7}$$

$$< \Psi | \sum_{i<j} \frac{1}{r_{ij}} | \Psi' >= \sum_{\sigma\rho,\sigma'\rho'} \sum_k y(\sigma,\rho,\sigma',\rho') R^k(n_\sigma l_\sigma n_\rho l_\rho; n_{\sigma'} l_{\sigma'} n_{\rho'} l_{\rho'}) \tag{2.8}$$

where x and y are the coefficients determined by the angular momentum coupling of the system, and can be calculated by using the Racah algebra techniques[27, 41, 42]. The evaluation of these coefficients has been well

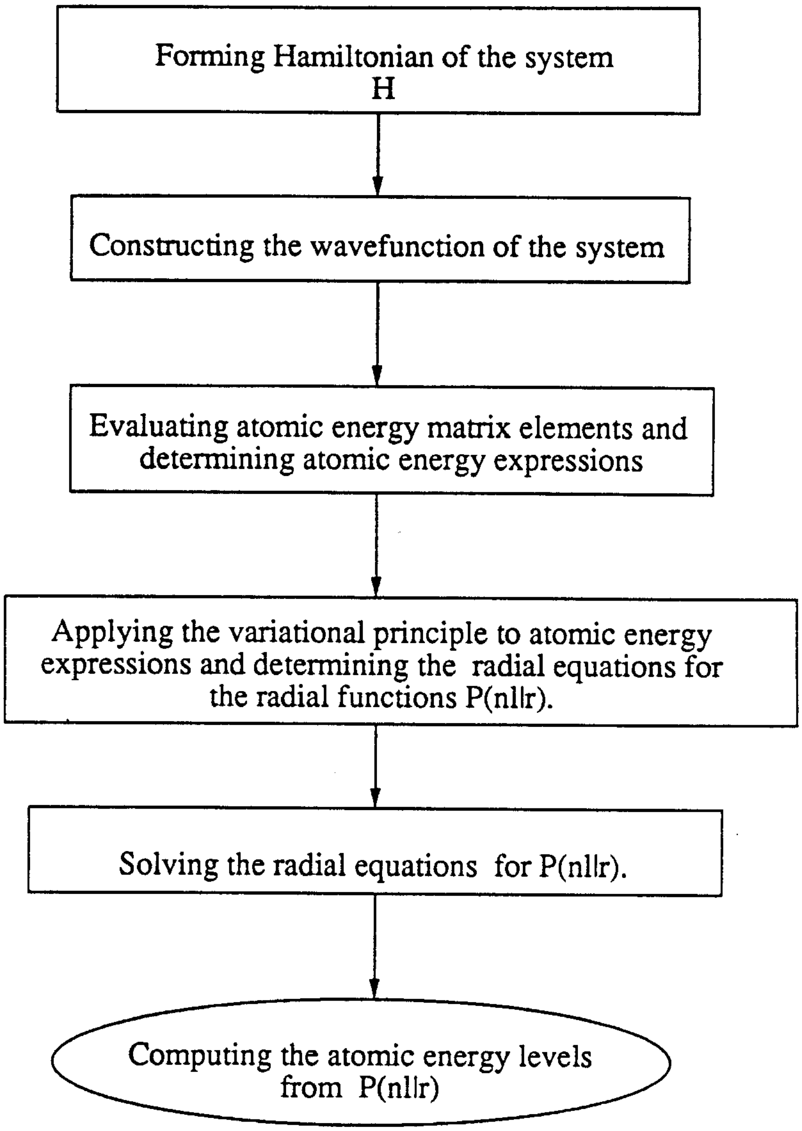

Figure 2.3 : Flow chart of atomic structure calculation

described and programmed by Hibbert *et al.*[43, 44];

$$I(n_\sigma l_\sigma, n_{\sigma'} l_{\sigma'}) = \frac{1}{2}\int_0^\infty P(n_\sigma l_\sigma|r)[-\frac{d^2}{dr^2} + \frac{l_\sigma(l_\sigma+1)}{r^2} - \frac{2Z}{r}]P(n_{\sigma'} l_{\sigma'}|r)dr \tag{2.9}$$

is the one-electron radial integral; and

$$\begin{aligned} & R^k(n_\sigma l_\sigma n_\rho l_\rho; n_{\sigma'} l_{\sigma'} n_{\rho'} l_{\rho'}) \qquad (2.10) \\ = & \int_0^\infty \int_0^\infty \frac{r_<^k}{r_>^{k+1}} P(n_\sigma l_\sigma|r_1)P(n_\rho l_\rho|r_2)P(n_{\sigma'} l_{\sigma'}|r_1)P(n_{\rho'} l_{\rho'}|r_2)dr_1 dr_2 \end{aligned}$$

is the two-electron radial integral.

In the single-configuration approximation, a general expression for atomic energy, under the assumption that orbitals are orthonormal, has the form

$$\begin{aligned} & E(\gamma LS) = \sum_\sigma w_\sigma I(n_\sigma l_\sigma) \qquad (2.11) \\ + & \sum_{\sigma\leq\rho}\sum_k f_k'(l_\sigma l_\rho)F^k(n_\sigma l_\sigma, n_\rho l_\rho) + \sum_{\sigma<\rho}\sum_k g_k'(l_\sigma l_\rho)G^k(n_\sigma l_\sigma, n_\rho l_\rho) \end{aligned}$$

here w_σ is the electron number in σth subshell, $f_k'(l_\sigma l_\rho)$ and $g_k'(l_\sigma l_\rho)$ are the angular-spin coefficients,

$$I(n_\sigma l_\sigma) = \frac{1}{2}\int_0^\infty P(n_\sigma l_\sigma|r)[-\frac{d^2}{dr^2} + \frac{l_\sigma(l_\sigma+1)}{r^2} - \frac{2Z}{r}]P(n_\sigma l_\sigma|r)dr \tag{2.12}$$

$$F^k(n_\sigma l_\sigma n_\rho l_\rho) = \int_0^\infty \int_0^\infty \frac{r_<^k}{r_>^{k+1}}|P(n_\sigma l_\sigma|r_1)|^2|P(n_\rho l_\rho|r_2)|^2 dr_1 dr_2 \tag{2.13}$$

and

$$\begin{aligned} & G^k(n_\sigma l_\sigma n_\rho l_\rho) \qquad (2.14) \\ = & \int_0^\infty \int_0^\infty \frac{r_<^k}{r_>^{k+1}} P(n_\sigma l_\sigma|r_1)P(n_\rho l_\rho|r_1)P(n_\sigma l_\sigma|r_2)P(n_\rho l_\rho|r_2)dr_1 dr_2 \end{aligned}$$

are the radial integrals.

For the multiconfiguration approximation, the atomic wavefunctions have the form

$$\Psi(\Gamma LS) = \sum_i c_i \Psi(\gamma_i LS) \tag{2.15}$$

and the atomic energy expression becomes

$$E(\Gamma LS) = \sum_{i \leq j} (2 - \delta_{ij}) c_i c_j E(I(ij)) + \sum_{i \leq j} (2 - \delta_{ij}) c_i c_j E(R(ij)) \tag{2.16}$$

where

$$E(I(ij)) = \sum_{\sigma_i \sigma_j} x(\sigma_i, \sigma_j) I(n_{\sigma_i} l_{\sigma_i}, n_{\sigma_j} l_{\sigma_j}) \tag{2.17}$$

and

$$E(R(ij)) = \sum_{\sigma_i \rho_i, \sigma_j \rho_j} \sum_k y(\sigma_i, \rho_i, \sigma_j, \rho_j) R^k(n_{\sigma_i} l_{\sigma_i} n_{\rho_i} l_{\rho_i}; n_{\sigma_j} l_{\sigma_j} n_{\rho_j} l_{\rho_j}) \tag{2.18}$$

The general Hartree-Fock equations are obtained by applying the variational principle to the atomic energy expressions as in Eq.(2.11), and the equations for multiconfiguration Hartree-Fock approximation are determined from the atomic energy expression in Eq.(2.16). In the Hartree-Fock SCF approach, relativistic effects are usually not entered into the variation energy expression directly. This is because the relativistic corrections to the radial functions $P(nl|r)$ are usually small for low Z and intermediate-Z atoms. In many cases, it is sufficient to calculate the relativistic energy corrections by the perturbation method. In fact, we can write

$$E = E_{NR} + \Delta E_{RE} \tag{2.19}$$

where E_{NR} is the nonrelativistic atomic energy and ΔE_{RE} is the relativistic correction. Like the nonrelativistic atomic energy expressions, the expressions for ΔE_{RE} are also a linear combination of radial integrals. These radial integrals are evaluated by using nonrelativistic radial functions $P(nl|r)$ as bases [45, 46].

The most commonly used approximation for describing the relativistic interactions between electrons is the Breit-Pauli Hamiltonian [47, 48, 49]:

$$\hat{H}_{BP} = \hat{H}_{NR} + \hat{H}_{RE} \tag{2.20}$$

where

$$\hat{H}_{NR} = \sum_i -\frac{\nabla_i^2}{2} - \sum_i \frac{Z}{r_i} + \sum_{i<j} \frac{1}{r_{ij}} \tag{2.21}$$

is the nonrelativitic Hamiltonian, and

$$\hat{H}_{RE} = \hat{H}_{so} + \hat{H}_{mass} + \hat{H}_{D1} + \hat{H}_{soo} + \hat{H}_{ss} + \hat{H}_{oo} + \hat{H}_{D2} + \hat{H}_{ssc} \tag{2.22}$$

is the relativistic correction.

$$H_{so} = \frac{\alpha^2 Z}{2} \sum_i \frac{1}{r_i^3} (\mathrm{l}_i \cdot \mathrm{s}_i) \tag{2.23}$$

represents the one-body spin-orbit interaction of each electron's magnetic moment with the magnetic field arising from the electron's own motion in the Coulomb field of the nucleus;

$$H_{mass} = -\frac{\alpha^2}{8}\sum_i \nabla_i^4 \tag{2.24}$$

is the relativistic mass correction;

$$H_{D1} = -\frac{\alpha^2 Z}{8}\sum_i \nabla_i^2(\frac{1}{r_i}) \tag{2.25}$$

is the one-body Darwin term, i.e., the relativistic correction to the potential energy;

$$H_{soo} = -\frac{\alpha^2}{2}\sum_{i\neq j}(\frac{\mathbf{r}_{ij}}{r_{ij}^3} \times \mathbf{p}_{ij}) \cdot (\mathbf{s}_i + 2\mathbf{s}_j) \tag{2.26}$$

represents the spin-other-orbit interaction and is made up of two parts. The first one containing the factor $\mathbf{s}_i$ is the spin orbit coupling of electron i in the Coulomb field of electron j. The second, with the factor $2\mathbf{s}_j$ comes from the interaction of the spin magnetic moment of electron j with the orbital current of electron i;

$$H_{ss} = \alpha^2 \sum_{i<j} \frac{1}{r_{ij}^3}[(\mathbf{s}_i \cdot \mathbf{s}_j) - 3\frac{(\mathbf{s}_i \cdot \mathbf{r}_{ij})(\mathbf{s}_j \cdot \mathbf{r}_{ij})}{r_{ij}^2}] \tag{2.27}$$

is the ordinary dipole interaction of the spin magnetic moments of two electrons;

$$H_{oo} = -\frac{\alpha^2}{2}\sum_{i<j}[\frac{\mathbf{p}_i \cdot \mathbf{p}_j}{r_{ij}} + \frac{\mathbf{r}_{ij}(\mathbf{r}_{ij} \cdot \mathbf{p}_i) \cdot \mathbf{p}_j}{r_{ij}^3}] \tag{2.28}$$

is the orbit-orbit interaction;

$$H_{D2} = \frac{\alpha^2}{4}\sum_{i<j} \nabla_i^2(\frac{1}{r_{ij}}) \tag{2.29}$$

is the two-body Darwin term, i.e., the relativistic correction to the potential energy;

$$H_{ssc} = -\frac{8\pi\alpha^2}{3}\sum_{i<j}(\mathbf{s}_i \cdot \mathbf{s}_j)\nabla_i^2(\frac{1}{r_{ij}}) \qquad (2.30)$$

is the electron-contact term. The operators in Eq.(2.23) — (2.30) have been transformed to tensor forms and the corresponding matrix elements have been evaluated by Hibbert *et.al.*[50, 51]

Terms being responsible for the fine structure splitting are H_{so}, H_{soo} and H_{ss}. In most cases, however, the fine structure splitting is usually calculated taking into account only the single-electron spin-orbit interaction H_{so}. This is connected with the fact that for most elements except for those with very low Z (*e.g.*, He), the interaction H_{so} plays the principle role in determining the fine structure splitting.

2.1.3 The Hartree-Fock Equations

From the previous discussions we can see that all the atomic structure calculation problems sum up to the determination of the quantitative form of the radial function $P(nl|r)$. For a multiplet term

$$\{[(n_1l_1)^{w_1}L_1S_1\mathcal{L}_1\mathcal{S}_1,(n_2l_2)^{w_2}L_2S_2]\mathcal{L}_2\mathcal{S}_2,\cdots(n_ql_q)^{w_q}L_qS_q\}\mathcal{L}\mathcal{S} \qquad (2.31)$$

there are q different radial functions, one for each subshell of equivalent electrons $(n_il_i)^{w_1}$. These radial functions are determined by the criterion that they should be such as to minimize the calculated energy of the atom, $E(\gamma LS)$, within the limitations set by the orthonormalization condition:

$$\int_0^\infty P(n_il_i|r)P(n_jl_i|r)dr = \delta_{n_in_j} \tag{2.32}$$

According to the variational principle, the condition for minimum $E(\gamma LS)$ may be written as

$$\begin{aligned}\delta\{E(\gamma LS) \quad &- \quad \sum_{i=1}^{q} \varepsilon_{ii} w_i \int_0^\infty P(n_il_i|r)P(n_il_i|r)dr \\ &- \quad \sum_{i=1}^{q}\sum_{j\neq i}^{q} \delta_{l_il_j}\varepsilon_{ij}w_i \int_0^\infty P(n_il_i|r)P(n_jl_j|r)dr\} = 0\end{aligned} \tag{2.33}$$

where $-\varepsilon_{ij}w_i$ is the Lagrangian multiplier for the orthogonality restriction between $P(n_il_i|r)$ and $P(n_jl_j|r)$, and $-\varepsilon_{ii}w_i$ the normalization restriction on $P(n_il_i|r)$. The variations $\delta P(nl|r)$ employed in Eq.(2.33) may now be completely arbitrary (except that boundary conditions on $P(nl|r)$ require $\delta P(nl|r) = 0$ at $r = 0$ and $r = \infty$); it is necessary only that the values of ε_{ii} and ε_{ij} be so chosen that the functions $P(nl|r)$ deduced from Eq.(2.33) indeed satisfy the corresponding normalization and orthogonality conditions.

We already knew that the expressions for $E(\gamma LS)$ are linear combinations of radial integrals, i.e.,

$$\begin{aligned}E(\gamma LS) &= \sum_i w_i I(n_il_i) \\ &+ \sum_{i\leq j}\sum_k f_k^l(l_il_j)F^k(n_il_i,n_jl_j) + \sum_{i<j}\sum_k g_k^l(l_il_j)G^k(n_il_i,n_jl_j)\end{aligned} \tag{2.34}$$

The variations for the corresponding radial integrals are the following:

$$\delta_i \int_0^\infty P(n_il_i|r)P(n_il_i|r)dr = 2\int_0^\infty [\delta P(n_il_i|r)]P(n_il_i|r)dr \tag{2.35}$$

$$\delta_i \int_0^\infty P(n_il_i|r)P(n_jl_j|r)dr = \int_0^\infty [\delta P(n_il_i|r)]P(n_jl_j|r)dr \tag{2.36}$$

$$\delta_i I(n_il_i) = \int_0^\infty [\delta P(n_il_i|r)][-\frac{d^2}{dr^2} - \frac{2Z}{r} + \frac{l_i(l_i+1)}{r^2}]P(n_il_i|r)dr \tag{2.37}$$

$$\begin{aligned} &\delta_i F^k(n_il_i, n_jl_j) \\ = \; & 2\int_0^\infty \int_0^\infty \frac{r_<^k}{r_>^{k+1}}[\delta P(n_il_i|r_1)]P(n_il_i|r_1)P^2(n_jl_j|r_2)dr_1dr_2 \end{aligned} \tag{2.38}$$

$$\begin{aligned} &\delta_i F^k(n_il_i, n_il_i) \\ = \; & 4\int_0^\infty \int_0^\infty \frac{r_<^k}{r_>^{k+1}}[\delta P(n_il_i|r_1)]P(n_il_i|r_1)P^2(n_il_i|r_2)dr_1dr_2 \end{aligned} \tag{2.39}$$

$$\begin{aligned} &\delta_i G^k(n_il_i, n_jl_j) \\ = \; & \int_0^\infty \int_0^\infty \frac{r_<^k}{r_>^{k+1}}[\delta P(n_il_i|r_1)]P(n_il_i|r_2)P(n_jl_j|r_1)P(n_jl_j|r_2) \\ + \; & \int_0^\infty \int_0^\infty \frac{r_<^k}{r_>^{k+1}}[\delta P(n_il_i|r_2)]P(n_il_i|r_1)P(n_jl_j|r_1)P(n_jl_j|r_2) \\ = \; & 2\int_0^\infty \int_0^\infty \frac{r_<^k}{r_>^{k+1}}[\delta P(n_il_i|r_1)]P(n_jl_j|r_1)P(n_il_i|r_2)P(n_jl_j|r_2) \end{aligned} \tag{2.40}$$

Since the form of the variation $\delta P(n_il_i|r_1)$ is completely arbitrary (except for the requirement that it be zero at $r_1 = 0$ and $r_1 = \infty$), we may take it to zero everywhere except in the immediate vicinity of some point $r_1 = r$. Then we have

$$\int_0^\infty [\delta P(n_i l_i|r_1)]P(n_i l_i|r_1) = P(n_i l_i|r) \int_0^\infty \delta P(n_i l_i|r_1) dr_1 \tag{2.41}$$

and all other integrals in Eq.(2.36) — (2.40) simplify similarly. Substituting all these into Eq.(2.33) and dividing out a factor

$$2 \int_0^\infty \delta P(n_i l_i|r_1) dr_1 \tag{2.42}$$

we have the general Hartree-Fock equations[26]:

$$\begin{aligned} & [\frac{d^2}{dr^2} - \frac{l_i(l_i+1)}{r^2} + \frac{2Z}{r} - 2D_i(r)]P(n_i l_i|r) \\ = & -2\varepsilon_{ii} P(n_i l_i|r) - \sum_{j\neq i} 2\delta_{l_i l_j} \varepsilon_{ij} P(n_j l_j|r) + 2X_i(r) \end{aligned} \tag{2.43}$$

where

$$D_i(r) = \sum_j \sum_k (1+\delta_{ij}) \frac{f'_k(l_i l_j)}{w_i} \int_0^\infty \frac{r_<^k}{r_>^{k+1}} P^2(n_j l_j|r_1) dr_1 \tag{2.44}$$

$$X_i(r) = \sum_{j\neq i} \sum_k \frac{g'_k(l_i l_j)}{w_i} P(n_j l_j|r) \int_0^\infty \frac{r_<^k}{r_>^{k+1}} P(n_i l_i|r_1) P(n_j l_j|r_1) dr_1 \tag{2.45}$$

and

$$\begin{aligned} \varepsilon_{ii} = & -\frac{1}{w_i}[w_i I(n_i l_i) \\ + & \sum_{j\neq i} \sum_k f'_k(l_i l_j) F^k(n_i l_i, n_j l_j) + \sum_{j\neq i} \sum_k g'_k(l_i l_j) F^k(n_i l_i, n_j l_j)] \end{aligned} \tag{2.46}$$

$$\begin{aligned} \varepsilon_{ij} &= -\int_0^\infty P(n_il_i|r)[\frac{d^2}{dr^2} + \frac{2Z}{r} - \frac{l_i(l_i+1)}{r^2}]P(n_jl_i|r)dr \\ &+ \int_0^\infty P(n_il_i|r)[D_i(r)P(n_il_i|r) + X_i(r) + \frac{I(n_il_i)}{r}]dr \qquad (2.47) \end{aligned}$$

The Hartree-Fock equations are the "q" coupled equations — one for each subshell n_il_i — in the forms of Eq.(2.43) — (2.47). Because the radial function $P(nl|r)$ oscillates more rapidly near the origin, it is convenient from the point of view of numerical procedures, to introduce a logarithmic variable as independent variable, namely

$$\rho = ln(Zr)$$

Let,

$$\bar{P}(nl|r) = \frac{P(nl|r)}{r}$$

Then Eq.(2.43) becomes

$$\begin{aligned} &[\frac{d^2}{d\rho^2} + 2rZ - (l_i + \frac{1}{2})^2 - 2r^2D_i(r)]\bar{P}(n_il_i|r) \\ = \quad &-2r^2\varepsilon_{ii}\bar{P}(n_il_i|r) - 2r^2\sum_j \delta_{l_il_j}\varepsilon_{ij}\bar{P}(n_jl_j|r) + 2r^2\bar{X}_i(r) \qquad (2.48) \end{aligned}$$

Here

$$\bar{X} = \frac{X}{r^{1/2}}$$

The radial mesh may be chosen as equal step size in ρ variable starting from a finite value of $\rho_1 = ln(Zr_1)$. Numerous tests on the hydrogen equations suggest that for computers with a word length of at least 48 bits, appropriate value of ρ_1 and step size h are $\rho_1 = -4$ and $h = 1/16$.

We now study the physical significance of terms in the HF equations. The first two terms in the left-hand-side of Eq.(2.43) are the electron kinetic energy operators. The third term is the potential energy operator of the electron due to the nucleus. The fourth term, $D_i(r)$, comes from the direct portion F^k of the electron-electron electrostatistic interactions. The second term in the right-hand-side of Eq.(2.43), $X_i(r)$, is the exchange potential energy operator. The parameter ε_{ii} can be interpreted as the binding energy of the electron in the ith subshell. Under the "*frozen frame*" approximation, we have

$$I_i = -\varepsilon_{ii} \tag{2.49}$$

i.e., the negative of the eigenvalue ε_{ii} of the HF equation is equal to the ionization energy for an electron in the ith subshell. This is called Koopman's theorem [52].

The equations for the multiconfiguration Hartree-Fock (MCHF) approximation can be obtained by using basically the same procedures as we have shown above. The only difference is that we need to add a new Lagrange multiplier associated with the normalization of the configuration mixing coefficients.

Since the variational principle is applied to the energy expression of a specific LS term, the HF equations are "*term*" dependent.

The numerical method for the solutions of the HF equations has been well documented by C.F.Fischer [26, 53]. The basic idea is the following:

1. assuming a set of trial functions $P(n_jl_j|r)$ (*e.g.*,hydrogenic functions with a Z_{eff}) , $(1 \leq j \leq q)$;
2. for each i, computing $D_i(r)$, $X_i(r)$ and estimating the ε_{ij};
3. solving the ith HF equation for a new $P(n_il_i|r)$, each i;
4. repeating (2) (3) until the output functions are identical with the input functions, and all functions with the same l are mutually orthogonal, within the desired tolerances.

This procedure is called a self-consistent-field (SCF) method. A Flow chart of a SCF procedure for the numerical solution of a MCHF problem is shown in Figure 2.4. The single-configuration HF approximation may be seen as a special case of the MCHF.

For the MCHF calculations, because of practical limitation, the basis set employed for the expansion

$$\Psi(\Gamma LS) = \sum_i c_i \Psi(\gamma_i LS) \tag{2.50}$$

must be kept manageable small, and the set of configurations to be included in the calculations must therefore be chosen judiciously. Some of the important selection rules are listed below[26, 27]:

- Specify a principal configuration.

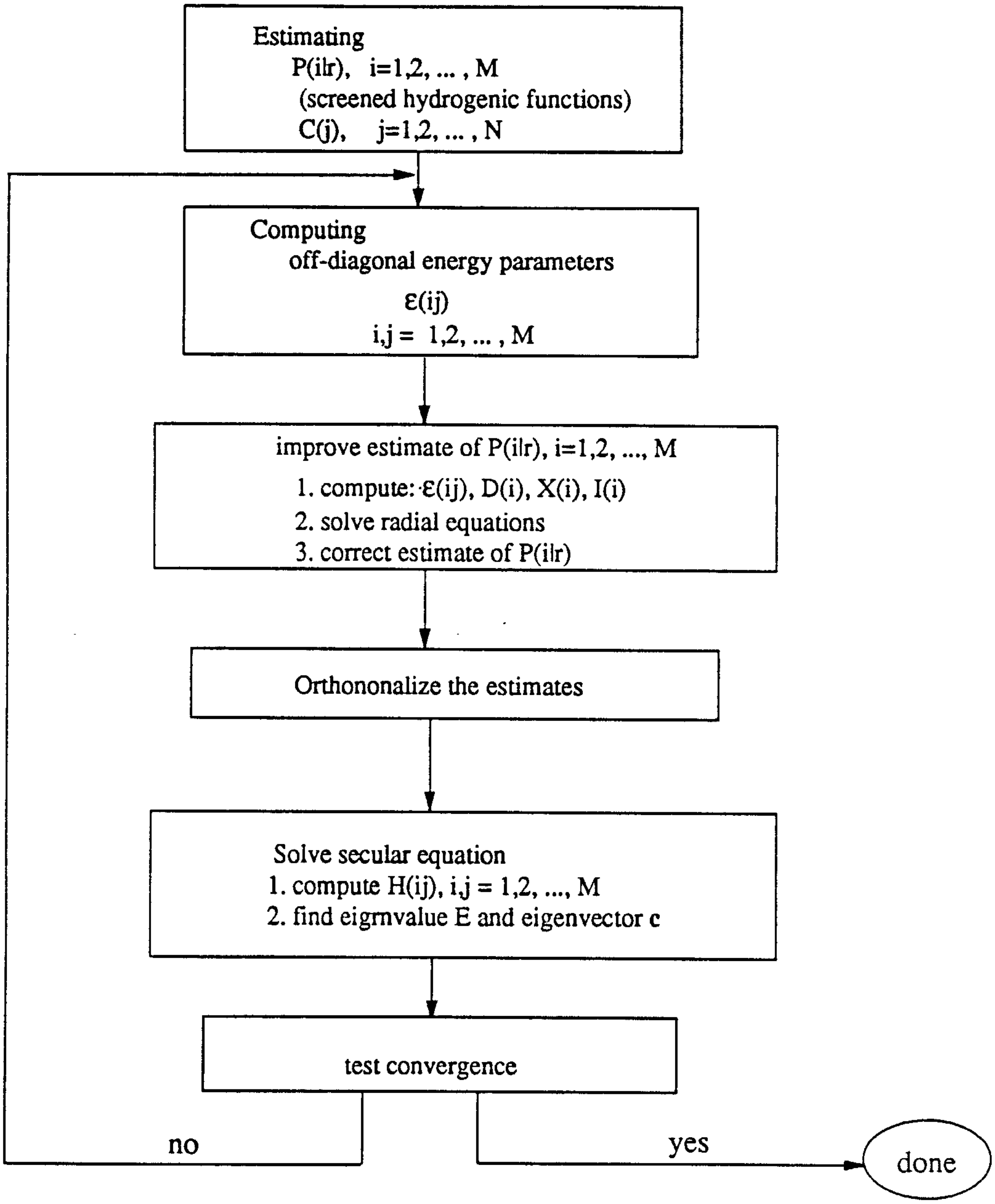

Figure 2.4: Flow chart of a SCF procedure for the numerical solution of a MCHF problem.

- All the selected configurations should have the same parity as the principal configuration. This selection rule comes from the fact that the Hamiltonian operator has even parity, and so the configuration-interaction (CI) matrix elements are zero unless the bra and ket functions have the common parity.

- All the selected configurations differ in at most two orbitals. This is because the Hamiltonian involves only one- and two- electron operators.

- All those configurations differ only in principle quantum number n of one electron from the principal configuration may usually be omitted. This is because in most cases Brillouin's theorem [54] holds for single-configuration HF wavefunctions. However, in general CI calculations, this is not necessary true if the basis set is not the HF wavefunctions.

- The largest configuration-interaction effects come from the configurations within the same *complex*.

2.1.4 The Atomic Continuum Wavefunctions

There are two distinct states for an atomic system — discrete energy states and continuum energy states. A discrete energy state corresponds to a configuration in which all electrons of the atom are more or less tightly bound. In a continuum energy state, however, there is at least one *free electron* in the atomic system. Atomic continuum wavefunctions are very important to the studies of atomic continuous processes (*e.g.*, photoionization, f–f and electron-ion collision processes).

For an atomic continuum state

$$\{(n_1 l_1)^{w1}(n_2 l_2)^{w2}\cdots(n_c l_c)^{w_c}\}[\gamma_c L_c S_c]\varepsilon l; LSM_L M_S \tag{2.51}$$

the corresponding wavefunction can be constructed from one-electron spin-orbitals, with

$$\psi(nlm_l m_s|\mathbf{x}) = \frac{1}{r}P(nl|r)Y_{lm_l}(\theta,\phi)\chi_{m_s} \tag{2.52}$$

for bound electrons, and

$$\psi(\varepsilon lm_l m_s|\mathbf{x}) = \frac{1}{r}P(\varepsilon l|r)Y_{lm_l}(\theta,\phi)\chi_{m_s} \tag{2.53}$$

for free electron. $P(\varepsilon l|r)$ in Eq.(2.53) is a one-electron continuum radial function.

The Hartree-Fock equation for the continuum radial function $P(\varepsilon l|r)$ can be obtained in the same way as that for the bound radial function by treating εl as a *subshell*, i.e.,

$$\begin{aligned}[\frac{d^2}{dr^2} - \frac{l(l+1)}{r^2} &+ \frac{2Z}{r} - 2D_\varepsilon(r)]P(\varepsilon l|r) \qquad (2.54)\\ &= -2\varepsilon P(\varepsilon l|r) - 2\sum_j \delta_{ll_j}\varepsilon_{n_j\varepsilon}P(n_j l_j|r) + 2X_\varepsilon(r)\end{aligned}$$

where

$$D_\varepsilon(r) = \sum_j^c \sum_k f_k^l(ll_j)\int_0^\infty \frac{r_<^k}{r_>^{k+1}}P^2(n_j l_j|r_1)dr_1 \tag{2.55}$$

$$X_\varepsilon(r) = \sum_j^c \sum_k g'_k(ll_j) P(n_j l_j|r) \int_0^\infty \frac{r_<^k}{r_>^{k+1}} P(\varepsilon l|r_1) P(n_j l_j|r_1) dr_1 \qquad (2.56)$$

with the boundary conditions

$$P(\varepsilon l|0) = 0 \qquad (2.57)$$

and

$$P(\varepsilon l|r) \overset{r\to\infty}{\longrightarrow} (\frac{2}{\pi\sqrt{2\varepsilon}})^{1/2} sin[\sqrt{2\varepsilon}\cdot r + \frac{z}{\sqrt{2\varepsilon}} ln(2\sqrt{2\varepsilon}\cdot r) - \frac{l\pi}{2} + \delta_l + \eta] \qquad (2.58)$$

$$P(\varepsilon = 0l|r) \overset{r\to\infty}{\longrightarrow} (\frac{2r}{\pi z})^{1/4} sin[\sqrt{8zr} - \frac{\pi}{4} - l\pi + \eta] \qquad (2.59)$$

The asymptotic behaviour of $P(\varepsilon l|r)$ in Eq.(2.58) and Eq.(2.59) correspond to the normalization condition

$$\int_0^\infty P(\varepsilon l|r) P(\varepsilon' l|r) dr = \delta(\varepsilon - \varepsilon') \qquad (2.60)$$

It is important to note that the nonlocal potential in Eq.(2.54) caused by the exchange interaction adds considerable complication to the calculation of $P(\varepsilon l|r)$. A general way to deal with this problem is to use the *frozen frame* approximation[58]: keeping the bound electron wavefunctions unchanged, do self-consistent calculations only for the continuum wavefunction. A further approximation is to replace the exchange potential by a local potential[57], and the equation for $P(\varepsilon l|r)$ become

$$[\frac{d^2}{dr^2} - \frac{l(l+1)}{r^2} + \frac{2Z}{r} - V_{\varepsilon l}(r)] P(\varepsilon l|r) = 2\varepsilon P(\varepsilon l|r) \qquad (2.61)$$

One of the good approximations for $V_{\varepsilon l}(r)$ is the HX potential [31]. For a HX potential, the problem of solving Eq.(2.61) is very simple. We first solve the HF equations for bound radial functions $P(nl|r)$, a HX potential can then be constructed from these bound radial functions.The HX potential is independent of ε, hence for each desired value of ε, $P(\varepsilon l|r)$ can be obtained simply by integrating the differential equation Eq.(2.61) once; there is no iteration on ε and no self-consistent iteration on the core wavefunctions.

We now consider some numerical detail for the solutions of the continuum radial function $P(\varepsilon l|r)$. First, we deal with the problem of normalization for $P(\varepsilon l|r)$. Let

$$\phi_l(r) = \begin{cases} \sqrt{2\varepsilon}\cdot r + \frac{z}{\sqrt{2\varepsilon}} ln(2\sqrt{2\varepsilon}\cdot r) - \frac{l\pi}{2} + \delta_l & \varepsilon > 0 \\ \sqrt{8zr} - \frac{\pi}{4} - l\pi & \varepsilon = 0 \end{cases} \tag{2.62}$$

Then

$$\frac{d\phi_l(r)}{dr} = \begin{cases} \sqrt{2\varepsilon} + \frac{z}{r\sqrt{2\varepsilon}} \xrightarrow{r\to\infty} \sqrt{2\varepsilon} & \varepsilon > 0 \\ \sqrt{\frac{8z}{r}} & \varepsilon = 0 \end{cases} \tag{2.63}$$

The asymptotic $P(\varepsilon l|r)$ can then be expressed as

$$P(\varepsilon l|r) \xrightarrow{r\to\infty} \sqrt{\frac{2}{\pi}}\left(\frac{d\phi_l(r)}{dr}\right)^{-1/2} sin(\phi_l(r) + \eta) \tag{2.64}$$

In practical calculations, an unnormalized $\tilde{P}(\varepsilon l|r)$ from Eq.(2.61) can only be evaluated to some large but finite radius $r = r_{max}$. In order to properly normalize $\tilde{P}(\varepsilon l|r)$, it is necessary to extrapolate to find its amplitude on infinity. For sufficiently large r ($r > r_o$) where the potential is essentially the Coulomb potential, i.e.,

$$-\frac{2Z}{r}+V_{\varepsilon l}(r)\simeq-\frac{2z}{r} \tag{2.65}$$

Then we have

$$[\frac{d^2}{dr^2}+A(r)]P(\varepsilon l|r)=0 \quad r>r_o \tag{2.66}$$

where

$$A(r)\simeq\frac{2z}{r}+2\varepsilon-\frac{l(l+1)}{r^2} \tag{2.67}$$

By comparing with Eq.(2.64), we can express the unnormalized radial function $\tilde{P}(\varepsilon l|r)$ as

$$\tilde{P}(\varepsilon l|r)=C\sqrt{\frac{2}{\pi}}(\frac{d\theta(r)}{dr})^{-1/2}sin\theta(r) \tag{2.68}$$

where C is the normalization constant, i.e.,

$$P(\varepsilon l|r)=\frac{1}{C}\tilde{P}(\varepsilon l|r) \tag{2.69}$$

Let

$$X(r)=\frac{d\theta(r)}{dr} \tag{2.70}$$

From Eq.(2.66) and Eq.(2.68), we have

$$X^2(r)=A(r)+X^{1/2}(r)\frac{d^2}{dr^2}[X^{-1/2}(r)] \tag{2.71}$$

$X(r)$ can then be obtained by solving Eq.(2.71) iteratively. Assuming

$$X_o^2(r)=A(r) \tag{2.72}$$

then

$$X^2(r) \simeq X_1^2(r) = A - 0.25A^{-1}\frac{d^2A}{dr^2} + 0.3125A^{-2}(\frac{dA}{dr})^2 \tag{2.73}$$

This one step iteration approximation is accurate to terms in r^{-2}. Now, we pick any two points of $\tilde{P}(\varepsilon l|r)$ in the asymptotic region: $\tilde{P}(\varepsilon l|r_1)$ and $\tilde{P}(\varepsilon l|r_2)$, then

$$\begin{aligned} a_1 &= X^{1/2}(r_1)\tilde{P}(\varepsilon l|r_1) = C\sqrt{\frac{2}{\pi}}sin\theta(r_1) \\ a_2 &= X^{1/2}(r_2)\tilde{P}(\varepsilon l|r_2) = C\sqrt{\frac{2}{\pi}}sin\theta(r_2) \\ \alpha &= \int_{r_1}^{r_2} X(r)dr = \theta(r_2) - \theta(r_1) \end{aligned} \tag{2.74}$$

And hence

$$C = [\frac{\pi}{2}(\frac{a_1^2 + a_2^2 - 2a_1a_2cos\alpha}{sin\alpha})]^{1/2} \tag{2.75}$$

This normalization procedure is referred as the Cooper[59] method.

Another numerical problem in calculating the continuum radial function is radial mesh selection. Normal HF logarithmic radial mesh for bound radial functions is no longer suitable for continuum functions because of the oscillation asymptotic behavior of $P(\varepsilon l|r)$. Acceptable accuracy of the numerical integration of Eq.(2.60) requires that there be at least a half dozen mesh points per half-cycle of $P(\varepsilon l|r)$, and therefore from Eq.(2.57) that the mesh size Δr satisfy

$$\Delta r < \frac{\pi}{6\sqrt{2\varepsilon}} \tag{2.76}$$

over the entire integration mesh. Two common ways to deal with this problem are:

- Applying the Herman-Skillman[60] linear mesh, doubling the step size every 40 steps until $\Delta r = \pi/(6\sqrt{2\varepsilon})$ and keeping Δr constant afterward.
- Introducing variable [61]

  $$\rho = \alpha r + \beta ln r \tag{2.77}$$

  where α and β are certain constants determined by the cut-off value r_{max} and the mesh size requirement in Eq.(2.76).

2.1.5 Numerical Computations And Discussions

Our atomic structure calculation code "HFBASE" is a semirelativistic multiconfiguration HF code which is based on the modifications of MCHF77 [55] and WEIGHT[56]. The main features of this code are the following:

- multiconfiguration HF wavefunctions (single-configuration as a special case);
- relativistic correction for energy levels;
- allow any electron configuration with no more than two equivalent electrons in any shell with $l \geq 3$ (this limitation may be extended by inclusion of further fractional parentage coefficient packages);

- suitable for large scale computations, may compute up to 1000 levels in one run (this limitation may be extended by enlarging the corresponding array parameters within the limit of computer memory).

A simplified flow diagram of HFBASE is shown in Figure 2.5.

Our atomic calculations are carried out in two ways. We use the single-configuration HF method to do large scale calculations to generate atomic data tables for the computations of equation of state and opacity. We use the multiconfiguration HF method to do accurate calculations for those levels of particular interest for plasma diagnostics. In the following, we present some of the calculation results. By comparing with the available experimental and other theoretical calculation results, we can have a general judgment on the accuracy of our calculations.

In Table 2.1, we present the calculation energies for the ground level and several low excited levels of OIII. All effective quantum numbers ν are calculated relative to the ground state of the next higher ionization stage (OIV $1s^2 2s^2 2p^1\ {}^2P$), i.e.,

$$\frac{z^{*2}}{2\nu^2} = E_o(\mathrm{OIV}) - E(\mathrm{OIII}\cdots) \tag{2.78}$$

A sensitive indicator of the accuracy is the agreement between the experimental and the calculated quantum defects ($\mu = n - \nu$): it is generally of the order of ten percent for the single-configuration HF calculations and one percent for the multiconfiguration HF calculations. In the multiconfiguration

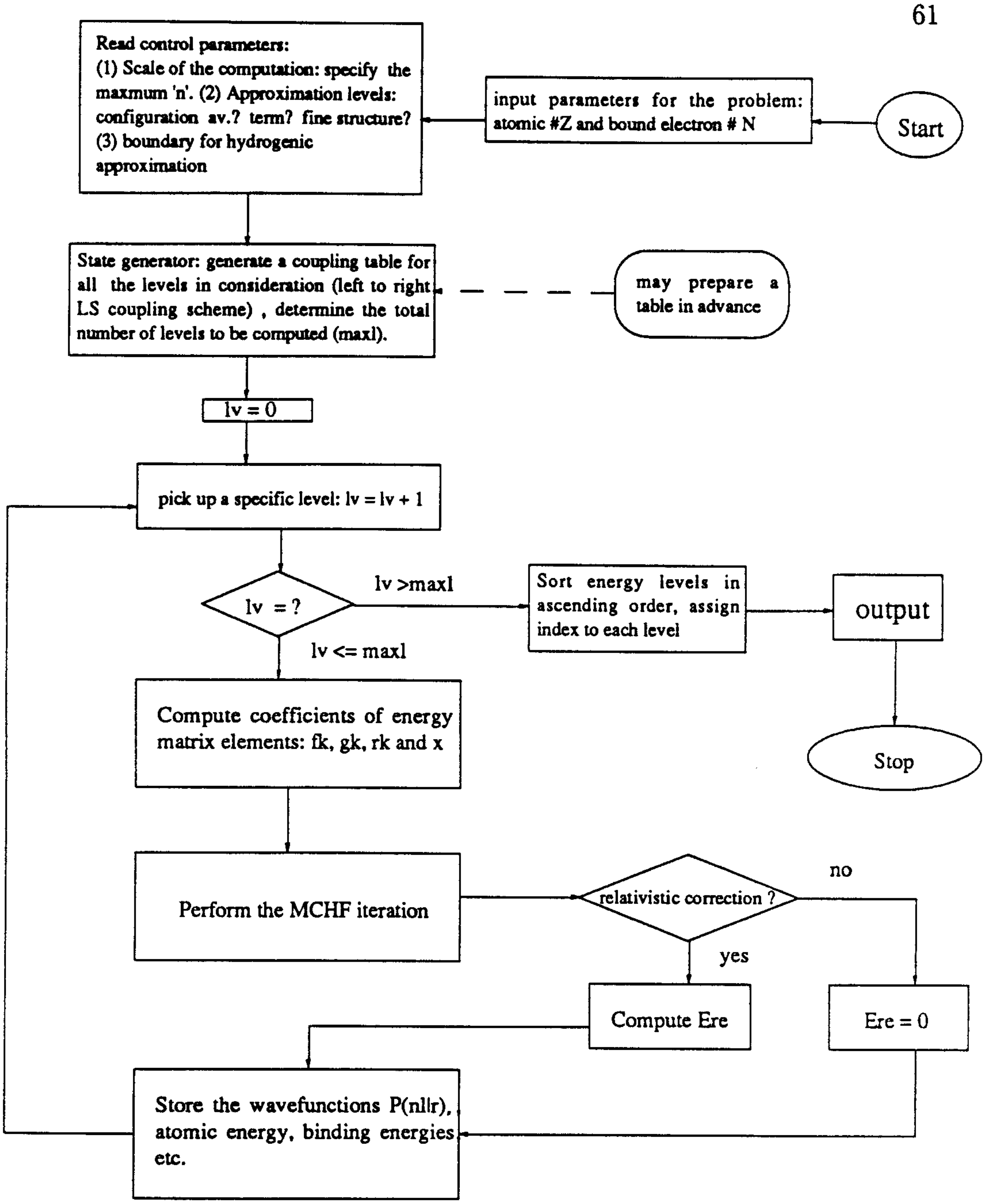

Figure 2.5: A simplified flow diagram of HFBASE

Table 2.1: Energy levels of OIII

level	ν^{expt}	ν^{mchf}	ν^{hf}	μ^{expt}	μ^{mchf}	μ^{hf}	$\Delta\mu^{mchf}$ (%)	$\Delta\mu^{hf}$ (%)
$2s^2 2p^2 [^3P]$	1.4929	1.4960	1.4979	0.5071	0.5040	0.5021	0.61	0.98
$2p^4 [^3P]$	2.4886	2.5001	2.5315	0.5114	0.4999	0.4685	2.2	8.3
$2p^1 3p^1 [^3P]$	2.6283	2.6302	2.5852	0.3717	0.3698	0.4147	0.51	11.0
$2p^1 4p^1 [^3P]$	3.6814	3.6821	3.6217	0.3186	0.3179	0.3783	0.21	15.0
$2p^1 3p^1 [^3S]$	2.6028	2.6023	2.6288	0.3972	0.3977	0.3711	0.13	6.5
$2p^1 4p^1 [^3S]$	3.6195	3.6201	3.6464	0.3805	0.3799	0.3535	0.16	7.0
$2p^1 3p^1 [^3D]$	2.5723	2.5788	2.5971	0.4277	0.4212	0.4028	1.5	5.8
$2p^1 4p^1 [^3D]$	3.5891	3.5899	3.6182	0.4109	0.4101	0.3817	0.2	7.1
$2s^1 2p^3 [^1P]$	2.0606	2.0624	2.1104	0.9394	0.9376	0.8896	0.2	5.0
$2p^1 3d^1 [^1P]$	2.9925	3.0058	3.0147	0.0075	-0.0055	-0.0147	0.45	0.74
$2p^1 4s^1 [^1P]$	3.4208	3.4211	3.4379	0.5792	0.5789	0.5621	0.06	2.9
$2p^1 4d^1 [^1P]$	3.9913	4.0018	4.0069	0.0087	-0.0018	-0.0069	0.26	0.39
$2p^1 5s^1 [^1P]$	4.4326	4.4350	4.4426	0.5684	0.5650	0.5574	0.60	1.9
$2p^1 5d^1 [^1P]$	4.9977	4.9983	5.0033	0.0023	0.0017	-0.0033	0.0022	0.012

Table 2.2: Interacting configurations for $1s^2 2s^2 2p^2\ {}^3P$

State	mixing coefficient
$1s^2 2s^2 2p^2$ $[{}^3P]$	0.9900334
$1s^2 2p^4$ $[{}^3P]$	0.1340580
$1s^2 2s^2 3p^2$ $[{}^3P]$	-0.0245318
$1s^2 3s^2 3p^2$ $[{}^3P]$	-0.0190684
$1s^2 2s^2 2p^1\ 3p^1$ $[{}^3P]$	-0.0022525
$1s^2 2s^2 2p^1\ 4p^1$ $[{}^3P]$	0.0101796
$1s^2 3s^2 3d^2$ $[{}^3P]$	-0.0280736

HF calculations, we include at least 5 important configurations to account for the electronic correlation effect. As an example, the included interacting configurations and the corresponding mixing coefficients for $1s^2 2s^2 2p^2\ {}^3P$ are listed in Table 2.2.

In regard to the relativistic effect, we can consider it in two aspects: first, as Z increases, the relativistic effect becomes more important; second, the tighter bound the electrons are, the more significant the relativistic effect will be. In our current work, we are interest in the low- and intermediate-Z atoms.

It is important for us to determine whether the relativistic correction needs to be considered for these atoms. In Figure 2.6, we plot the percent of the relativistic corrections for the ground level of neutral atoms versus the atomic number Z. In Figure 2.7, we show the percent of the relativistic correction for the ground level of nitrogen isoelectronic sequence. In Figure 2.8, we show the percent of the relativistic correction for the levels with different subshell electrons involved. It is easy to see that the relativistic correction is generally less than a few percent for low- and intermediate-Z atoms. This small percent correction may not be important to the computations of equation of state and opacity, but it may have significant effect on the detailed plasma diagnostics.

So far, we have only talked about the atomic energy levels and their corrections. In spectroscopy analysis, however, we are actually interested in the difference of two levels, i.e., the transition energy. In Table 2.3, we present the wavelengths of four different sets of calculations for the transition $1s^2 2s^2 2p^6 3s^1\ {}^2S \rightarrow 3p^1\ {}^2P$ in Na isoelectronic sequence. The results of the nonrelativistic single-configuration HF calculation are labeled HF; the results of the single-configuration HF calculation with relativistic correction are labeled $HF+re$; the results of the nonrelativistic multiconfiguration HF calculation are labeled $HF+cr$ (i.e., HF plus electronic correlation); the results of the multiconfiguration HF calculation with relativistic correction are labeled $HF+cr+re$. Also shown in the table are the experimental data[62] and the corresponding differences of the calculations. It can be

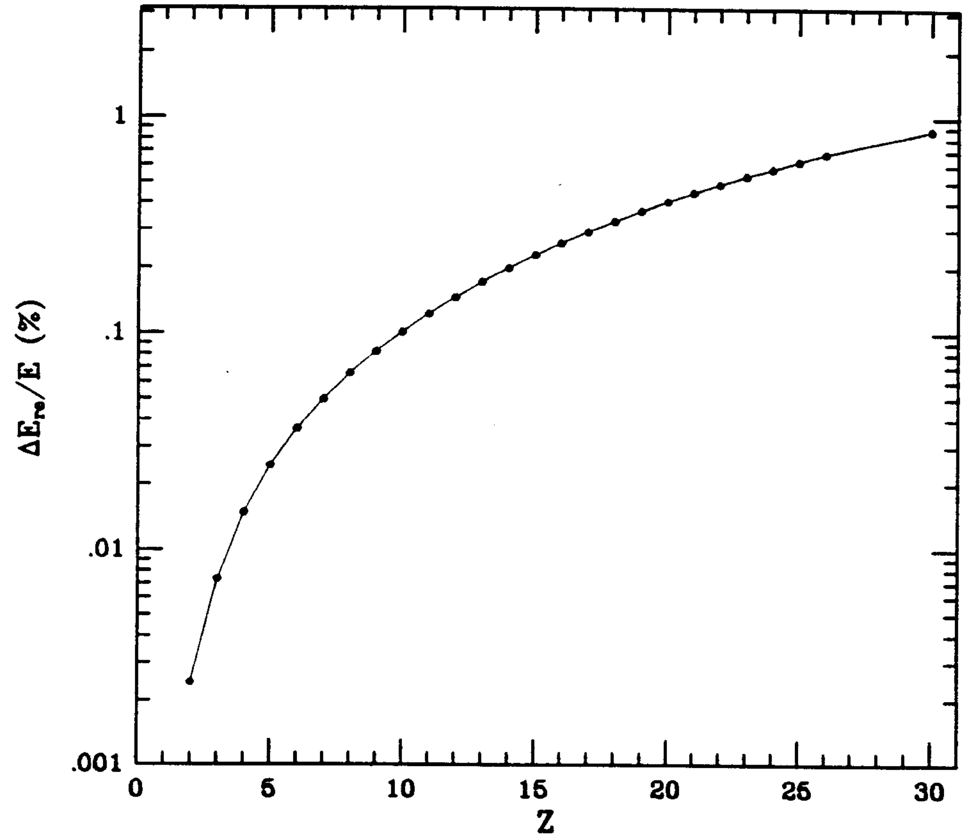

Figure 2.6: Relativistic correction for the ground level of neutral atoms

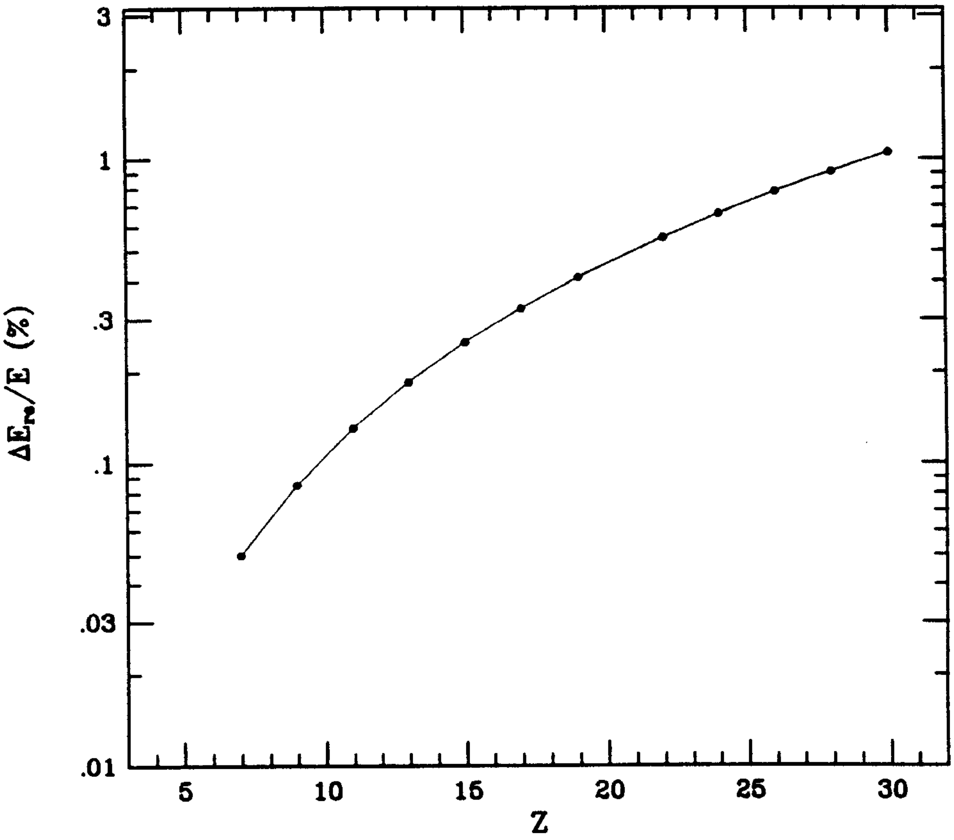

Figure 2.7: Relativistic correction for the ground level of N isoelectronic sequence

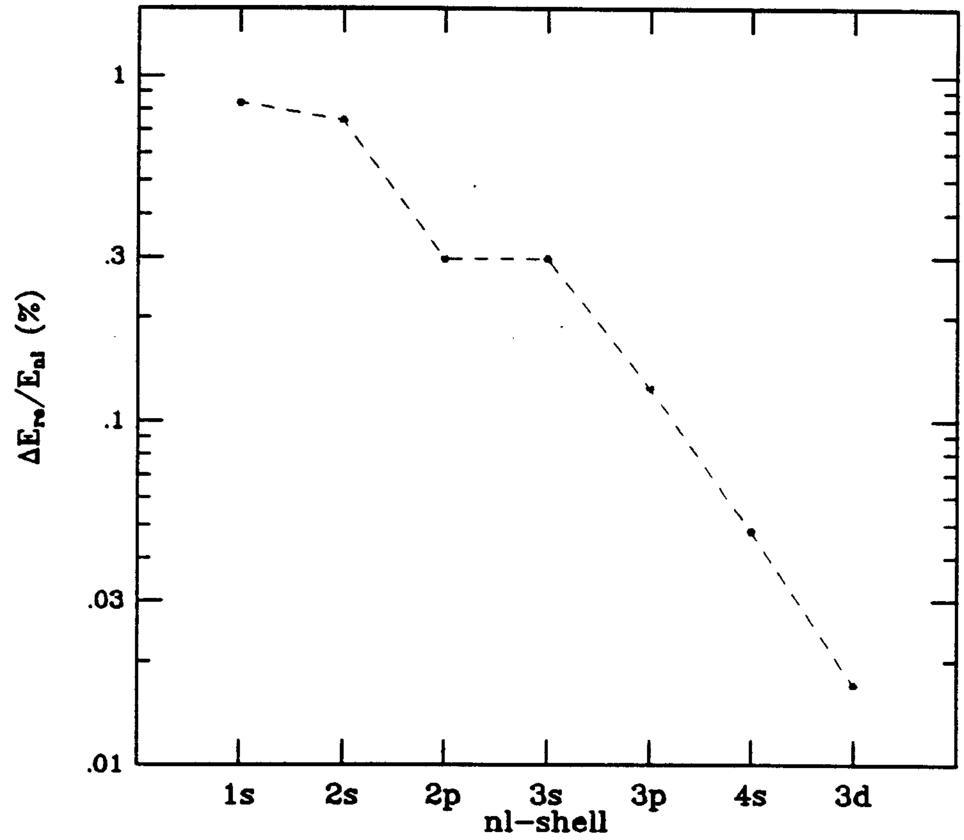

Figure 2.8: Relativistic correction for the levels of Fe with different subshell electrons are involved

seen that the electronic correlation effect dominates the relativistic effect in neutral and low ionized ions, while the relativistic effect becomes dominate for highly ionized ions. If the transition involves the inner shell electrons, the situation may be more complicated. For Kα transitions, the electronic correlation effect causes a red shift, while the relativistic effect causes a blue shift to the wavelength. Hence in doing detailed spectroscopy analysis, both effects should be considered very carefully.

It is well known that the hydrogenic approximation is appropriate for electronic states with high principal quantum number n and orbital quantum number l. In order to determine a general " *boundary*" for the validity of the hydrogenic approximation, we compute the effective quantum number ν as functions of n and l for NI and ArI. The results are presented in Figure 2.8 and Figure 2.9. It is obvious that for low- and moderate-Z atoms, $n > 10$ and $l > 3$ is a reasonnable "*boundary*" for the validity of the hydrogenic approximation.

Table 2.3: Wavelengths for $1s^22s^22p^63s^1\ {}^2S$ -- $3p^1\ {}^2P$ transition in Na isoelectronic sequence

Element	Experiment data	HF		HF+*re*		HF+*cr*		HF+*re*+*cr*	
	λ(A)	λ	%	λ	%	λ	%	λ	%
Na	5891.8	6282.6	6.6	6264.3	6.3	5907.5	0.27	5891.25	0.01
Mg^{+1}	2797.9	2898.5	3.6	2885.2	3.1	2802.5	0.16	2789.9	0.28
Al^{+2}	1857.4	1901.1	2.3	1888.9	1.7	1861.2	0.20	1850.1	0.39
Si^{+3}	1396.7	1422.2	1.8	1410.2	0.96	1401.8	0.37	1389.8	0.47
S^{+5}	937.07	952.96	1.7	939.8	0.29	945.2	0.87	935.05	0.21
Ar^{+7}	704.87	719.6	2.0	704.83	0.005	715.8	1.55	702.85	0.28
Ca^{+9}	563.6	579.27	2.7	562.5	0.19	577.1	2.4	561.07	0.44
Fe^{+15}	343.2	366.9	6.9	343.1	0.03	366.2	6.7	342.87	0.1

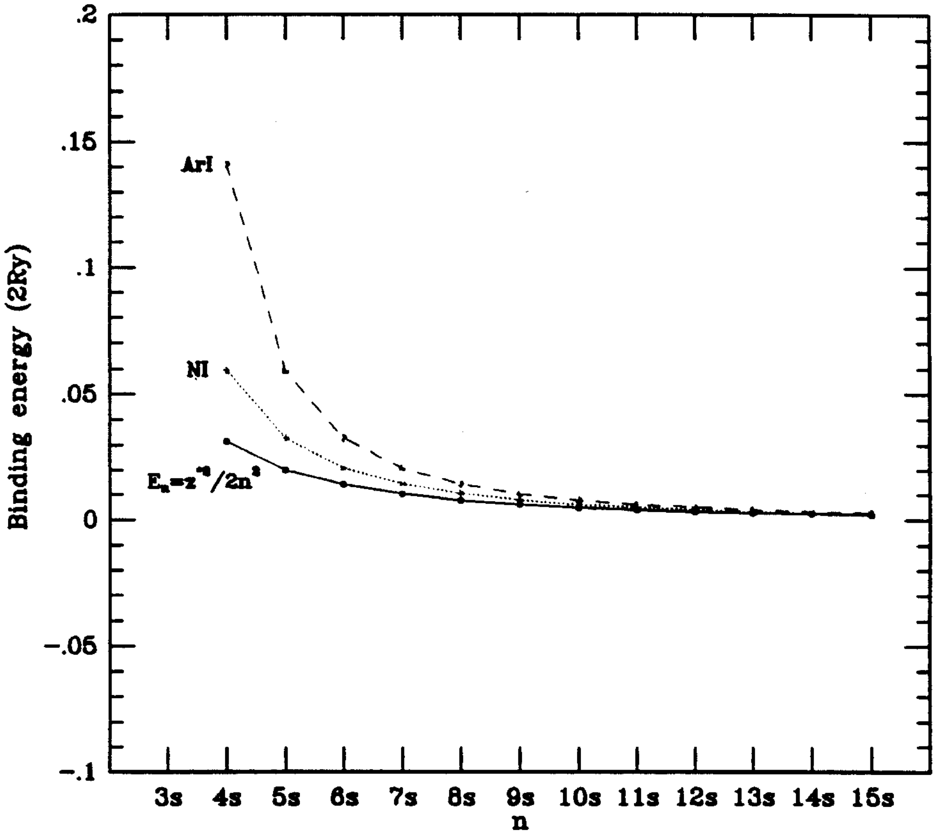

Figure 2.9: Binding energy as a function of n

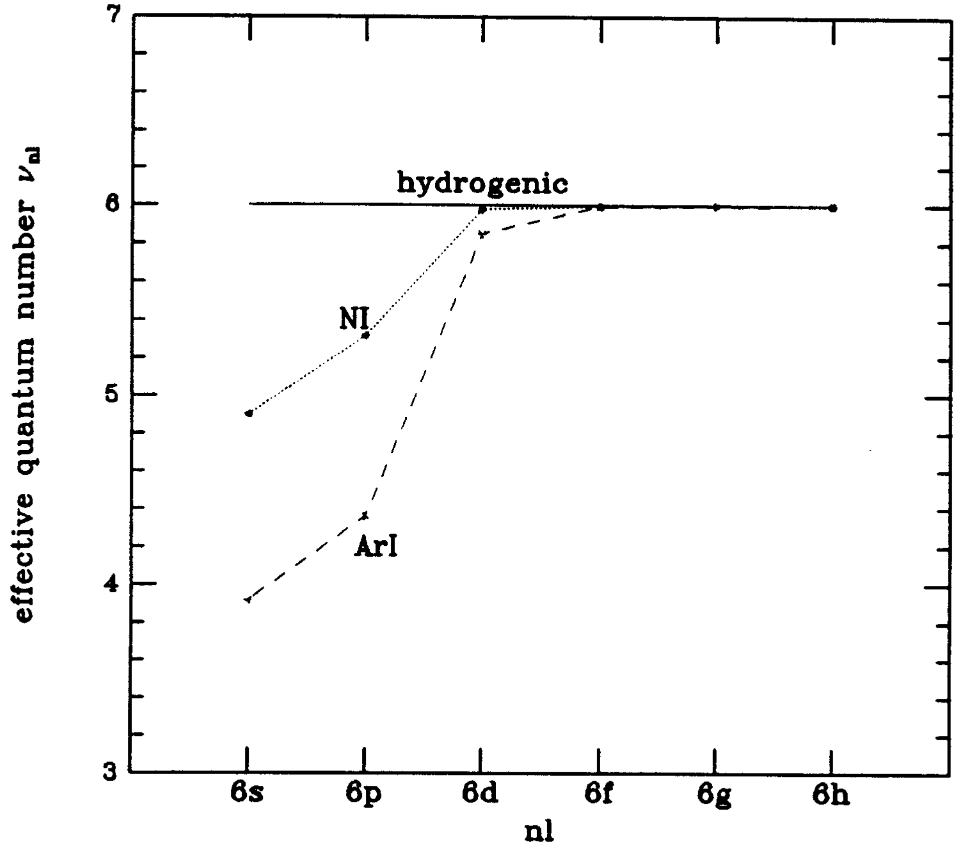

Figure 2.10: Effective quantum number as a function of l

2.2 Atomic Radiative Processes

When an atom is placed in a radiation field, because the atom interacts with electromagnetic radiation, it may make a transition from a state i of energy E_i to another state j of energy E_j by absorbing or emitting a photon of energy

$$\varepsilon_p = |E_i - E_j| \tag{2.79}$$

Depending on the propertities of the initial and the final state, the radiative transition processes may be classified into

- bound - bound transition;
- bound - free transition;
- free - free transition.

These are what we are going to discuss in this section.

2.2.1 Bound-Bound Transitions

The probability per unit time that an atom makes a transition from bound state i to bound state j by absorbing a photon of energy ε_p is given by [40]:

$$\begin{aligned} W_{ab} &= \frac{4\alpha^3\varepsilon_p^3 n_p}{3} |<j|\mathbf{D}|i>|^2 \\ &+ \frac{4\alpha^3\varepsilon_p^3 n_p}{3} |<j|\mathbf{M}|i>|^2 \\ &+ \frac{\alpha^5\varepsilon_p^5 n_p}{10} |<j|\vec{\mathbf{Q}}|i>|^2 + \cdots \end{aligned} \tag{2.80}$$

and the corresponding expression for emission is

$$\begin{aligned} W_{em} &= \frac{4\alpha^3\varepsilon_p^3(n_p+1)}{3}|<j|\mathbf{D}|i>|^2 \\ &+ \frac{4\alpha^3\varepsilon_p^3(n_p+1)}{3}|<j|\mathbf{M}|i>|^2 \\ &+ \frac{\alpha^5\varepsilon_p^5(n_p+1)}{10}|<j|\vec{\mathbf{Q}}|i>|^2 + \cdots \end{aligned} \tag{2.81}$$

here, n_p is the number of photons with energy ε_p; α is the fine structure constant;

$$\mathbf{D} = \sum_i r_i \mathbf{C}^{(1)}(i) \tag{2.82}$$

is the electric dipole moment operator;

$$\mathbf{M} = -\frac{\alpha}{2}\sum_i(\mathbf{l}_i^{(1)} + 2\mathbf{s}_i^{(1)}) = -\frac{\alpha}{2}(\mathbf{L}^{(1)} + \mathbf{S}^{(1)}) \tag{2.83}$$

is the magnetic dipole moment operator; and

$$\vec{\mathbf{Q}} = \sum_i r_i^2 \mathbf{C}^{(2)}(i) \tag{2.84}$$

is the electric quadrupole operator.

If there is no radiation field, i.e., $n_p = 0$, we have the spontaneous emission probability,

$$\begin{aligned} W_{sp} &= \frac{4\alpha^3\varepsilon_p^3}{3}|<j|\mathbf{D}|i>|^2 \\ &+ \frac{4\alpha^3\varepsilon_p^3}{3}|<j|\mathbf{M}|i>|^2 \\ &+ \frac{\alpha^5\varepsilon_p^5}{10}|<j|\vec{\mathbf{Q}}|i>|^2 + \cdots \end{aligned} \tag{2.85}$$

The transition probability can be related to the oscillator strength by the relation

$$W_{sp}(a-b) = 2\varepsilon^2\alpha^3|f(a-b)| \tag{2.86}$$

In the following, we discuss the numerical calculations of oscillator strengths for the electric dipole, magnetic dipole, electric quadrupole and intercombination transitions.

Electric Dipole (E_1) Oscillator Strength

In the electric dipole approximation, the oscillator strength for a transition from an initial state, $|\gamma LSJ>$, to a final state, $|\gamma' L' S' J' >$ can be expressed in three forms:

(1) the length form

$$f_L = \frac{2\Delta E}{3(2J+1)}| < \gamma LSJ || \sum_i \mathbf{r}_i || \gamma' L' S' J' > |^2 \tag{2.87}$$

(2) the velocity form

$$f_V = \frac{2}{3\Delta E(2J+1)}| < \gamma LSJ || \sum_i \nabla_i || \gamma' L' S' J' > |^2 \tag{2.88}$$

(3) the acceleration form

$$f_A = \frac{2Z^2}{3\Delta E^3(2J+1)}| < \gamma LSJ || \sum_i \frac{\mathbf{r}_i}{r_i^3} || \gamma' L' S' J' > |^2 \tag{2.89}$$

In each case, the operation is a spin-independent tensor of rank 1. For exact total wavefunctions, the three forms are identical, but for approximate total wavefunctions the value may differ appreciably, indicating a luck of accuracy. It has been customary to use this as an indicator of the accuracy of the calculation.

Since the operation is a spin-independent tensor, the J dependence of the oscillator strength can be found in explicit form:

$$f(\gamma LSJ - \gamma' L'S'J') = (2J+1)(2J'+1) \begin{Bmatrix} L & J & S \\ J' & L' & 1 \end{Bmatrix}^2 f(\gamma LS - \gamma' L'S')\delta_{SS'} \tag{2.90}$$

Here $f(\gamma LS - \gamma' L'S')$ is the multiplet oscillator strength for a transition from an initial state $|\gamma LS>$ to a final state $|\gamma' L'S>$

$$f_L(\gamma LS - \gamma' L'S) = \frac{2\Delta E}{3(2L+1)} | < \gamma LS || \sum_i \mathbf{r}_i || \gamma' L'S > |^2 \tag{2.91}$$

$$f_V(\gamma LS - \gamma' L'S) = \frac{2}{3\Delta E(2L+1)} | < \gamma LS || \sum_i \nabla_i || \gamma' L'S > |^2 \tag{2.92}$$

In the multiconfiguration calculations, the total wavefunction for a state, $\Psi(\Gamma LS)$ may be represented by a linear combination of the configuration state functions, $\Phi(\gamma_i LS)$. Let the wavefunction for the initial state be

$$\Psi(\Gamma LS) = \sum_{i=1}^{M} c_i \Phi(\gamma_i LS) \tag{2.93}$$

and that for the final state be

$$\Psi(\Gamma' L'S) = \sum_{i=1}^{M'} c_i' \Phi(\gamma_i' L'S) \tag{2.94}$$

where the sum is over configuration γ_i and γ'_i respectively (in the single configuration case, $M = M' = 1$). Then the matrix elements which appear in the formulae for the oscillator strength can be expressed in terms of matrix elements involving only the configuration state functions, i.e.,

$$< \Gamma LS||\tilde{T}^{(1)}||\Gamma' L'S >= \sum_{i=1}^{M} \sum_{j=1}^{M'} c_i c'_j < \gamma_i LS||\tilde{T}^{(1)}||\gamma'_j L'S > \qquad (2.95)$$

where $\tilde{T}^{(1)}$ denotes the tensor of rank 1 appearing in the formulas for the oscillator strength. Since $\tilde{T}^{(1)}$ is a one-electron operator, Eq.(2.95) may be reduced further to a one-electron integral,

$$< \Gamma LS||\tilde{T}^{(1)}||\Gamma' L'S >= \sum_{k} c_{i_k} c'_{j_k} \bar{S}^{1/2}(\gamma_{i_k} LS - \gamma'_{j_k} L'S) < n_k l_k||\tilde{T}^{(1)}||n'_k l'_k > \qquad (2.96)$$

where $\bar{S}$ is the reduced multiplet strength, $< nl||\tilde{T}^{(1)}||n'l' >$ is the one-electron integral. In the length form,

$$< nl||\tilde{T}^{(1)}||n'l' >= (-1)^{l_> - l}\sqrt{l_>} \int_0^\infty P(nl|r) r P(n'l'|r) dr \qquad (2.97)$$

and in the velocity form,

$$< nl||\tilde{T}^{(1)}||n'l' >= (-1)^{l_> - l + 1}\sqrt{l_>} \int_0^\infty P(nl|r)[\frac{d}{dr} + \frac{(l,l')}{2r}] P(n'l'|r) dr \qquad (2.98)$$

In Eq.(2.97) and Eq.(2.98), $l_> = max(l, l')$ and $(l, l') = l(l+1) - l'(l'+1)$.

The reduced multiplet strength is a factor related to the types of transition. The evaluation of $\bar{S}$ involves the basic principles of Racah algebra, i.e., cfp expansions, recouplings and uncouplings[27]. A general formula for evaluating $\bar{S}$ under the LS-coupling representation has been given by Cowan *et al.*[27, 40].

In the single-configuration approximation, it is possible to define an array oscillator strength (for transition between configurations). This is usually of interest only when ΔE is approximately the same for all lines of the transition array. For a general transition array

$$(n_1 l_1)^{w1} \ \cdots \ (n_i l_i)^{w_i} \cdots (n_j l_j)^{w_j - 1} \cdots (n_q l_q)^{wq} \rightarrow$$
$$(n_1 l_1)^{w1} \cdots (n_i l_i)^{w_i - 1} \cdots (n_j l_j)^{w_j} \cdots (n_q l_q)^{wq} \quad (2.99)$$

By summing the multiplet oscillator strength over all states of the final configuration and averaging over all states of the initial configuration, we have

$$f(\gamma - \gamma') = \frac{w_i(4l_j + 3 - w_j)}{(4l_j + 2)} \cdot \frac{2\Delta E_{av}}{3(2l_i + 1)} | < n_i l_i || \mathbf{r} || n_j l_j > |^2 \qquad (2.100)$$

In one-electron ions or highly excited levels of multi-electron atoms, energies depend only slightly on the quantum numbers l_i and l_j of the excited electron, and ΔE therefore depends strongly on only n_i and n_j. In such a case, we may define a complex oscillator strength, $f(n_i - n_f)$,

$$\begin{aligned} f(n_i - n_j) &= \frac{\sum_{l_i}(4l_i + 2)\sum_{l_j} f(n_i l_i - n_j l_j)}{\sum_{l_i}(4l_i + 2)} \\ &\simeq \frac{1.96}{n_i^5 n_j^3}\left(\frac{1}{n_i^2} - \frac{1}{n_j^2}\right)^{-3} \end{aligned} \qquad (2.101)$$

The selection rules for electric dipole transitions can be summarized as following

$$\begin{aligned} \Delta l &= \pm 1 \\ \Delta L &= 0, \pm 1, L + L' \geq 1 \\ \Delta S &= 0 \\ \Delta J &= 0 \pm 1, J + J' \geq 1 \end{aligned} \tag{2.102}$$

Magnetic Dipole (M_1) Oscillator Strength

In the magnetic dipole approximation, the oscillator strength for a transition from an initial state, $|\gamma LSJ>$, to a final state, $|\gamma' L' S' J'>$, is expressed in the form

$$f(J - J') = \frac{2\Delta E}{3(2J+1)} | < \gamma LSJ || \mathbf{M}^1 || \gamma' L' S' J' > |^2. \tag{2.103}$$

where

$$\mathbf{M}^1 = -\frac{\alpha}{2}(\sum_i \mathbf{l}_i + 2\sum_i \mathbf{s}_i) = -\frac{\alpha}{2}(\mathbf{J} + \mathbf{S}) \tag{2.104}$$

is the operator of magnetic moment.

Because the operator of magnetic moment does not involved radii, the magnetic dipole matrix is diagonal in the configuration. By using the Racah algebra techniques [27], we have

$$f(J-J') = \frac{\alpha^2 \Delta E}{6(2J+1)} \delta_{\gamma LS, \gamma' L' S'} (2J+1)(2J'+1) \left\{ \begin{array}{ccc} L & S & J \\ 1 & J' & S \end{array} \right\} [S(S+1)(2S+1)] \tag{2.105}$$

The selection rules are then expressed as

$$\Delta L = 0$$
$$\Delta S = 0 \tag{2.106}$$
$$\Delta J = \pm 1$$

In the single configuration approximation, the magnetic dipole transition is impossible between two levels belonging to two different configurations. However, in the multiconfiguration approximation, this transition become possible as a consequence of configuration mixing [27].

Electric Quadrupole (E_2) Oscillator Strength

The oscillator strength for the electric quadrupole transition can be expressed as

$$f(\gamma LSJ - \gamma' L'S'J') = \frac{2\Delta E}{3(2J+1)} | < \gamma' L'S'J' || \vec{\mathbf{Q}}^2 || \gamma LSJ > |^2 \tag{2.107}$$

where

$$\vec{\mathbf{Q}}^2 = \sum_i r_i \mathbf{C}^2(i) \tag{2.108}$$

is the electric quadrupole operator.

Since $\vec{\mathbf{Q}}^2$ is an even parity operator, the initial state and the final state of an electric quadrupole transition must have the same parity. This means that the electric quadrupole transition is possible for both inter-configuration and intra-configuration transitions.

The calculation for the inter-configuration transitions is basically the same as that for the electric dipole case. The basic formulae are the following

$$f(\gamma LSJ-\gamma' L'S'J') = \delta_{SS'}(2J+1)(2J'+1)\left\{\begin{array}{ccc} L & J & S \\ J' & L' & 2 \end{array}\right\}^2 f(\gamma LS-\gamma' L'S') \tag{2.109}$$

$$f(\gamma LS-\gamma' L'S') = \frac{2\Delta E}{3(2L+1)}[\sum_k c_{i_k} c'_{j_k} \bar{S}_2^{1/2}(\gamma_{i_k} LS-\gamma'_{j_k} L'S')s(n_k l_k, n'_k l'_k)]^2 \tag{2.110}$$

$$s(n_k l_k, n'_k l'_k) = (-1)^l \sqrt{(2l+1)(2l'+1)} \left(\begin{array}{ccc} l & 2 & l' \\ 0 & 0 & 0 \end{array}\right) \int_0^\infty P(nl|r) r^2 P(n'l'|r) dr \tag{2.111}$$

where $\bar{S}_2$ is an angular coefficient similar to the reduced multiplet strength for electric dipole oscillator strength. The general formula for evaluating $\bar{S}_2$ has been given by Cowan *et al.* [27, 40]

For the intra-configuration transitions, we have

$$< \gamma' L'S'J'||\vec{\mathbf{Q}}^2||\gamma LSJ >= \delta_{spins}(-1)^{L+S+J'}\sqrt{(2J+1)(2J'+1)}$$
$$\times \sum_j \bar{S}_j'^{1/2}(\gamma L-\gamma' L')\left\{\begin{array}{ccc} L & S & J \\ J' & 2 & L' \end{array}\right\} s(n_j l_j, n_j l_j) \tag{2.112}$$

Here the summation is over all the subshells, $\bar{S}'$ is an angular coefficient[27].

The selection rules for the electric quadrupole transition are

$$\Delta l = 0, \pm 2, l + l' \geq 2$$

$$\begin{aligned} &\Delta L = 0, \pm 2, L + L' \geq 2 \\ &\Delta S = 0 \qquad (2.113) \\ &\Delta J = 0, \pm 1, \pm 2, J + J' \geq 2 \end{aligned}$$

Higher multipole transitions are a lot slower than electric dipole transitions. These "forbidden" transitions are often observable only when the decaying state cannot emit E1 radiation. Such a state is termed *metastable.* As Z goes up, one should note that there are many exceptions to this rule.

A characteristic feature is

$$\frac{I(E2)}{I(E1)} = (\frac{\pi a_o}{\lambda})^2$$

where a_o is the Bohr radius and λ the wavelength. For visible light, this ratio is about 10^{-7}. The ratio of transition probabilities for a given frequency is

$$A(E1) : A(M1) : A(E2) = 1 : (Z\alpha)^2 : (Z\alpha)^2$$

.

Intercombination Transitions

The selection rule $\Delta S = 0$ which prohibits any change in the spin multiplicity S in single-photon electric dipole transitions is rigorously obeyed only in the limit of pure LS coupling. In reality the spin-orbit interaction causes a mixing of different spin multiplicity states of the same total angular momentum $\mathbf{J} =$

$\mathbf{L}+\mathbf{S}$, and the electric dipole intercombination transitions become allowed. The intensities of intercombination lines increase rapidly with increasing Z.

In the calculation of intercombination oscillator strengths, we first need to determine the "mixing" wavefunctions. This is a representation transformation procedure, i.e., a transformation from LS representation to intermediate representation. Assuming that there are m states corresponding to specific values JM for a configuration in LS representation, these states may mix together in the intermediate representation for an intermediate state, namely,

$$\Phi(\gamma LSJM)=\sum_{i}^{m}c_i\Phi(\gamma L_iS_iJM) \tag{2.114}$$

The mixing coefficients, c_i, can be determined by the system of equations

$$\begin{aligned}\sum_{j}^{m}(H_{ij}-\varepsilon\delta_{ij})\quad c_j &= 0 \\ i &= 1,2,3,\cdots m\end{aligned} \tag{2.115}$$

Here $H=H_o+H_{so}$ is the Hamiltonian including spin-orbit interaction, and ε, the correction to the energy, can be obtained by solving the scalar equation

$$|H_{ij}-\varepsilon\delta_{ij}|=0 \tag{2.116}$$

Once the mixing coefficients for the initial state, $|\gamma LSJM>$, and the final state, $|\gamma' L'S'J'M'>$, are determined, the calculation of the intercombination oscillator strength becomes straightward:

$$f(\gamma LSJ-\gamma' L'S'J')=\frac{2\Delta E}{3(2J+1)}|<\gamma LSJ||\sum_i r_i\mathbf{c}^1||\gamma' L'S'J'>|^2$$

$$= \frac{2\Delta E}{3(2J+1)} \left| \sum_{j,k} c_j c'_k < \gamma L_j S_j J || \sum_i r_i \mathbf{c}^1 || \gamma' L'_k S'_k J' > \right|^2 \quad (2.117)$$

As a descriptive example, we discuss the calculation of oscillator strength for the intercombination transition

$$1s^2[^1S_0] \longrightarrow 1s2p[^3P_1]. \quad (2.118)$$

For the initial level, there is only one basis function with $J = 0$, we have

$$|^1S_0 >_{true} = |^1S_0 > . \quad (2.119)$$

For the final level, assuming

$$|1s2p^3P_1 >_{true} = c_1|1s2p^3P_1 > + c_2|1s2p^1P_1 > \quad (2.120)$$

and

$$(H_o + H_{so})|1s2p^3P_1 >_{true} = \varepsilon|1s2p^3P_1 >_{true}, \quad (2.121)$$

we have

$$\begin{cases} < {}^3P_1|H_o + H_{so}|{}^3P_1 > c_1 + < {}^3P_1|H_{so}|{}^1P_1 > c_2 = & \varepsilon \\ < {}^1P_1|H_{so}|{}^3P_1 > c_2 + < {}^1P_1|H_o + H_{so}|{}^1P_1 > c_1 = & \varepsilon \end{cases} \quad (2.122)$$

where ε is determined by the scalar equation

$$\begin{vmatrix} < {}^3P_1|H_o + H_{so}|{}^3P_1 > -\varepsilon & < {}^3P_1|H_{so}|{}^1P_1 > \\ < {}^1P_1|H_{so}|{}^3P_1 > & < {}^1P_1|H_o + H_{so}|{}^1P_1 > -\varepsilon \end{vmatrix} = 0 \quad (2.123)$$

We may have two roots, ε_1 and ε_2 for Eq (2.123). They are the eigenenergies for $|1s2p\,^1P_1>_{true}$ and $|1s2p\,^3P_1>_{true}$ respectively. Once the coefficient c_2 are determined from Eq.(2.122), we have the oscillator strength

$$f(\,^1S_0 - \,^3P_1) = \frac{2\Delta E}{3}\,[\,c_2\,|<\,^1S_0||\mathbf{r}||\,^1P_1>|\,]^2 \qquad (2.124)$$

Numerical Results And Discussions

We have developed a code, HFOS, for calculating the oscillator strengths. This code can be easily adapted to HFBASE and hence suitable for generating large scale oscillator strength data. A simplified flow diagram of HFOS is shown in Figure 2.11.

There are two ways to check the accuracy of the oscillator strength calculation. A direct way is to compare the calculation values to the experimental data, while an indirect way is to compare the oscillator strengths calculated from different formulations. We have checked our calculations both ways. Figure 2.12 shows the results from a plot of a large number of oscillator strengths of our calculation for ArI, ArII and ArIII, plotted to show the level of agreement between the length and the velocity formulations. Of more than one thousand points in the plot, it is seen that the vast majority lie on or close to the straight line that signifies the equality of the values in the length and the velocity formulations. Thus the internal consistency and the numerical accuracy of the computed data appears to be quite good.

In Table 2.4 a comparison is presented between the oscillator strengths obtained from HFOS by using the single configuration Hartree-Fock wavefunctions and the empirical data compiled by Smith and Weise [98] and the theoretical data of Opacity Project calculations[14, 113]. For most transitions, the discrepancies are within the twenty percent range. This is the typical accuracy of oscillator strengths for the single configuration Hartree-Fock calculations. Generally speaking, for transitions where only the outer valence electron is involved, the single configuration Hartree-Fock calculations can give very good results; however for the transitions with inner shell electrons involved, because of the strong electronic correlation effect, the single configuration Hartree-Fock calculations are generally less accurate. For this kind of transition, the multiconfiguration Hartree-Fock calculations are necessary to obtain accurate results. In Table 2.5 we show a typical comparison of oscillator strengths for this kind of transition calculated using the single configuration Hartree-Fock and the multiconfiguration Hartree-Fock method. In this comparison, we only include the three important configurations for the multiconfiguration calculations, significant improvement is achieved.

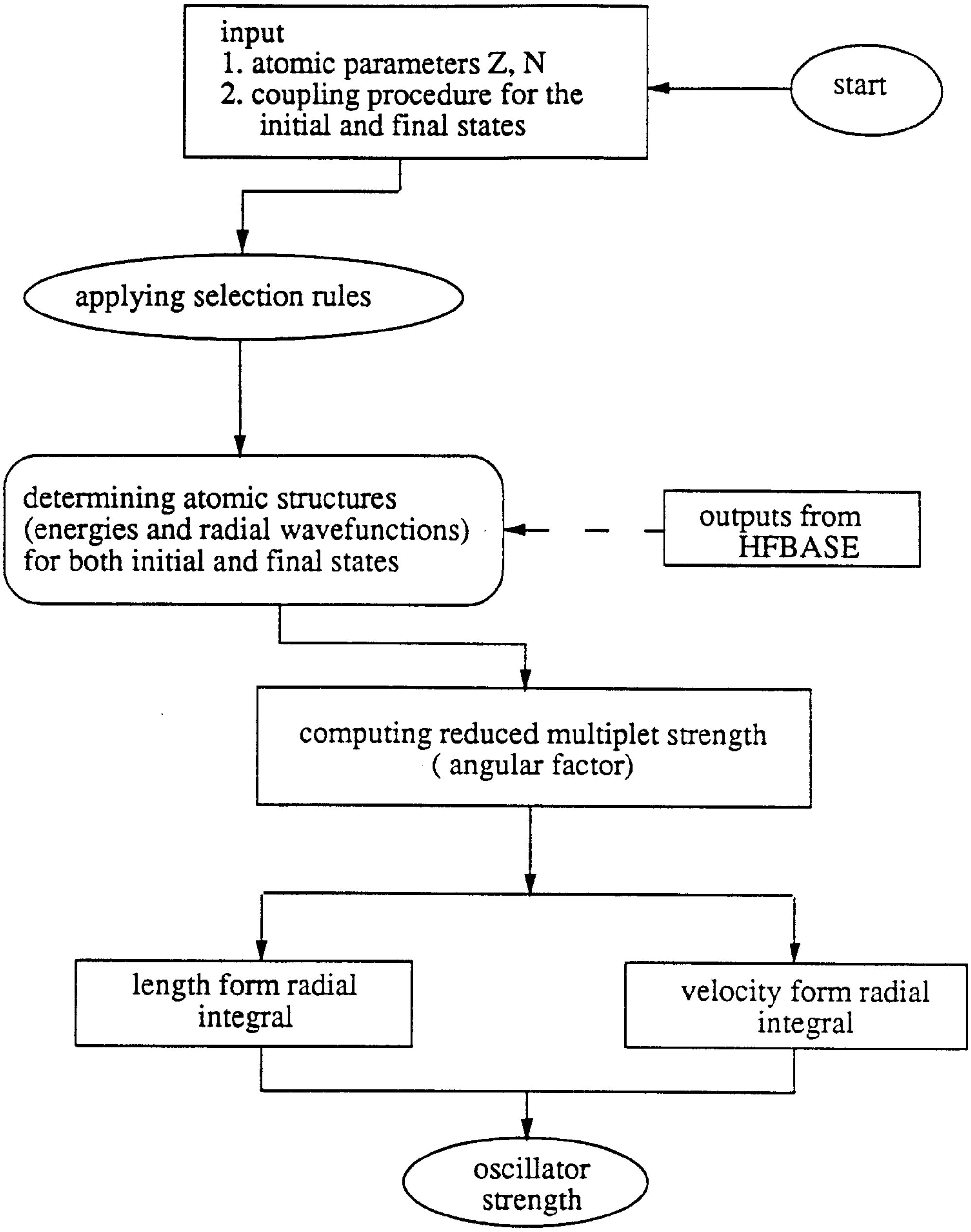

Figure 2.11: A simplified flow diagram of HFOS

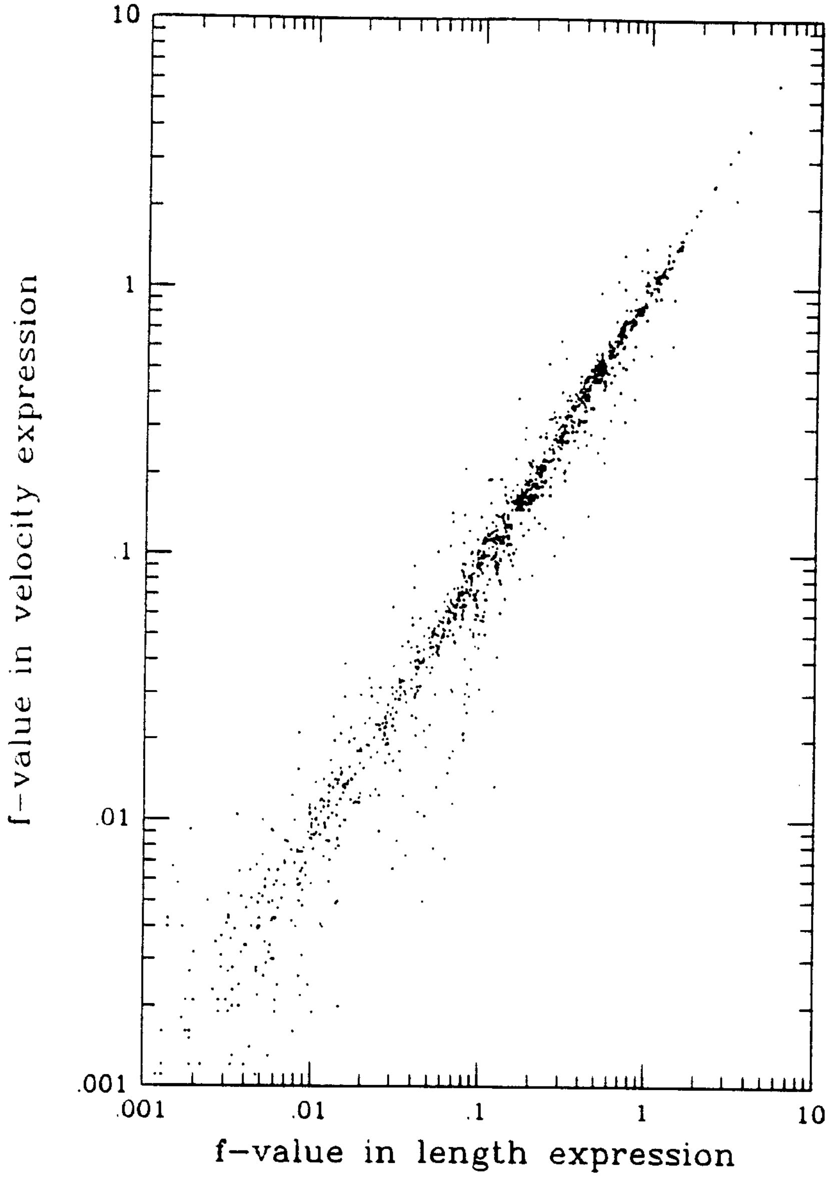

Figure 2.12: f-values for ArI,ArII and ArIII from dipole-length and dipole-velocity calculations

Table 2.4: Oscillator strengths for CI and OIII

Atom	Transition	f_L^{HF}	f_L^{OP}	f_{ws}^{exp}
CI	$2s^22p^2$ [^3P] - $2s^22p3s$ [^3P]	0.0886	0.1476	0.12
	[^3P] - $2s^22p3d$[^3D]	0.0673	0.1094	
	[^1D] - $2s^22p3s$[^1P]	0.0923	0.1202	0.096
	[^1S] - $2s^22p3s$[^1P]	0.0880	0.0853	
	$2s^22p3s$ [^3P] - $2s^22p3p$[^3D]	0.5445	0.4933	0.53
	[^3P] - $2s^22p3p$[^3S]	0.1224	0.1062	0.11
	[^3P] - $2s^22p3p$[^3P]	0.3101		0.37
	[^1P] - $2s^22p3p$[^1D]	0.5377		0.56
	[^1P] - $2s^22p3p$[^1S]	0.1247		0.13
	$2s^22p3p$[^1P] - $2s^22p3d$[^1D]	0.7217	0.6937	0.70
	[^1P] - $2s^22p3d$[^1P]	0.2535		0.31
	[^1D] - $2s^22p3d$[^1F]	0.8203		0.74
	[^3D] - $2s^22p3d$[^3D]	0.1428		0.15
	[^3P] - $2s^22p3d$[^3P]	0.2488		0.26
	[^3P] - $2s^22p3d$[^3D]	0.7191		0.63
OIII	$2s^22p^2$ [^3P] - $2s^22p^3$ [^3D]	0.1994	0.107	0.108
	[^3P] - $2s^22p^3$ [^3P]	0.1434	0.137	0.14
	[^3P] - $2s^22p3s$[^3P]	0.0817	0.0835	0.0896
	$2s^22p3s$[^3P] - $2s^22p3p$[^3D]	0.3935	0.346	0.348
	[^3P] - $2s^22p3p$[^3P]	0.2213	0.276	0.289
	$2s^22p3p$[^3P] - $2s^22p3d$[^3D]	0.0957	0.0890	0.0899
	[^3P] - $2s^22p3d$[^3P]	0.1819	0.104	0.105

Table 2.5: Comparison of oscillator strengths of SCHF and MCHF calculations

Atom	Transitions	f^{HF}	f^{MCHF}	f^{exp}
CI	$2s^22p^2$ $[^3P]$ - $2s2p^3$ $[^3D]$	0.2084	0.0837	0.094
	$[^3P]$ - $2s2p^3$ $[^3P]$	0.1681	0.0694	0.072
	$[^3P]$ - $2s2p^3$ $[^3S]$	0.3057	0.1601	
OII	$2s^22p^2$ $[^3P]$ - $2s2p^3$ $[^3D]$	0.1994	0.1144	0.11
	$[^3P]$ - $2s2p^3$ $[^3P]$	0.1434	0.1396	0.14
	$[^3P]$ - $2s2p^3$ $[^3S]$	0.2734	0.2010	0.18
	$2s^22p^2$ $[^1D]$ - $2s2p^3$ $[^1D]$	0.2766	0.3097	0.30
	$[^1D]$ - $2s2p^3$ $[^1P]$	0.2025	0.2303	0.23
	$[^1S]$ - $2s2p^3$ $[^1P]$	0.4077	0.2658	0.27

2.2.2 Line Profile

The spectral lines are not strictly sharp, but have a finite width. The cross section for bound–bound transitions should be given by

$$\sigma(i-j) = \frac{2\pi^2 e^2}{mc} f(i-j)\phi(\omega) \tag{2.125}$$

where $\phi(\omega)$ is a normalized line profile factor. The three main causes of spectral line broadening are:

1. The natural broadening of atomic energy levels, which arises from their finite lifetime and consequent uncertainty in the energy values;
2. Doppler broadening, which arises from the Doppler effect that modifies the apparent frequency of the radiation from atoms moving with random thermal velocities;
3. Stark broadening, which is determined by two main processes: ion micro-fields in the plasma that split the energy levels by Stark effects; and line broadening by electron impact.

Natural Broadening

The phenomenon of natural broadening can be understood both from the classical viewpoint and quantum mechanical viewpoint. Classically, the natural broadening can be understood in terms of the radiation damping of an electron oscillator. Quantum mechanically, it is argued that if the lifetime of the excited state of the atom is τ, the energy of the state can not be defined to better than $\Delta E \sim \hbar/\tau$. Thus the width of the spectral line is $\Delta\omega \sim \Delta E/\hbar \sim 1/\tau$.

The line profile for the natural broadening is described by the Lorentz distribution function, namely

$$\phi_n(\omega) = \frac{\Gamma_n/2\pi}{(\omega - \omega_o)^2 + (\Gamma_n/2)^2} \tag{2.126}$$

where ω is the angular frequency of the radiation; Γ_n is the full width of half-maximum (FWHM) of the natural broadening, i.e., $\Gamma_n = 2\Delta\omega$ with $\phi_n(\omega_o \pm \Delta\omega) = \phi_n(\omega_o)/2$.

Classically, Γ_n is the damping constant

$$\begin{aligned} \Gamma_n(rad/sec) &= \frac{2e^2\omega_o^2}{3mc^3} \\ &\simeq 6.27 \times 10^{-24}\omega_o^2 = 1.07 \times 10^{10}(\Delta E)^2 \qquad (2.127) \end{aligned}$$

where ΔE is the transition energy in hartree.

Quantum mechanically, Γ_n is the sum of the reciprocal of the mean lifetime of both upper and lower levels

$$\begin{aligned} \Gamma_n(rad/sec) &= \sum_{i<l} A_{li} + \sum_{j<u} A_{uj} \qquad (2.128) \\ &= 3.213 \times 10^{10}[\sum_{i<l}(\Delta E_{li})^2|f_{li}| + \sum_{j<u}(\Delta E_{uj})^2|f_{uj}|] \end{aligned}$$

Doppler Broadening

The frequency of the radiation from a radiating atom whose velocity in the direction of observation is v is displaced in accordance to the Doppler principle by an amount

$$\Delta\omega = \omega_o \frac{v}{c} \tag{2.129}$$

Let the distribution of the radiating atoms with respect to v be defined by function $F(v)$, then the spectral line profile for the Doppler broadening is

$$\phi_D(\omega) = F(c \cdot \frac{\omega - \omega_o}{\omega_o}) \cdot \frac{c}{\omega_o} \tag{2.130}$$

Assuming the plasma is characterized by a kinetic temperature T(K), the velocity distribution is Maxwellian, namely

$$F_M(v)dv = \frac{1}{\sqrt{\pi}} exp[-(v/v_o)^2] \frac{dv}{v_o} \tag{2.131}$$

where $v_o = \sqrt{2kT/m}$ is the average thermal velocity. Then we have [15]

$$\begin{aligned} \phi_D(\omega) &= \frac{1}{\Delta\omega_D \sqrt{\pi}} exp[-(\omega/\Delta\omega_D)^2] \\ \Delta\omega_D &= \omega_o \frac{v_o}{c} \end{aligned} \tag{2.132}$$

$\phi_D(\omega)$ is a normalized Gaussian distribution function with a full half-intensity width given by

$$\Gamma_D(rad/sec) = 2\sqrt{ln2}\Delta\omega_D = 3.184 \times 10^{12} \Delta E \sqrt{\frac{T}{A}}. \tag{2.133}$$

Where T is the plasma temperature in eV, A is the atom's atomic weight, and ΔE is the transition energy in hartree.

Stark Broadening

There are two main approximations for dealing with the problems of Stark broadening: (1)*Quasi-static approximation*[65, 66],(2)*impact approximation*[65, 66]. If particles are moving sufficiently slowly so that the frequencies characterizing the actual time-dependence of the perturbing electric field $F(t)$ produced in the vicinity of the radiator during the interaction are much smaller than the resulting Stark shifts $\Delta\omega_{if}(F) = \omega_{if}(F) - \omega_{if}(0)$, i.e.,

$$|\frac{dF(t)/dt}{F(t)}| \ll |\Delta\omega_{if}(F)| \tag{2.134}$$

the line profile then consists of an average over perturber configurations of profiles calculated for fixed perturber configurations. This is called the *quasi-static approximation.* If the duration of collision is small as compared with the mean time between collisions, then we can neglect radiation during collision and consider the collisions to be instantaneous. This is called the *impact approximation.* Generally speaking, the quasi-static approximation is applicable for the far wing of the line and the broadening by ions, the impact approximation is usually applicable to the broadening by electrons.

Although both electrons and ions have contributions to the Stark broadening of lines of atomic spectra in a plasma, electrons play the principal role in the broadening of a line of atomic spectra. The interaction with ions only slightly increases the impact width and shift of a line of atomic spectra, by approximately $15 - 20\%$[65]. In our calculations, we only consider the

Stark broadening by electrons. There are several theoretical methods used for computing the widths of Stark-broadening of spectrum lines. However, as pointed out by Griem[67], many of the more complicated semi-classical and quantum mechanical calculations are in several cases less reliable than a simpler semi-empirical procedureS[67, 68, 69]. This method, which is based on the use of effective Gaunt factors for the electron-radiator collisions, has been tested for a number of ions in the past[68, 69]. Agreement between theory and experiment was typically within a factor of 1.5, and in many cases much better. Hence we choose this method for our calculations. The main features of this method are discussed in the following.

Starting with the expression, due to Baranger[70], for the width (FWHM) of an isolated ion line, in the unit of angular frequency:

$$\Gamma_s = N_e < v[\sum_{i'} \sigma_{i'i} + \sum_{f'} \sigma_{f'f} + \int |\phi_i - \phi_f|^2 d\Omega] >_{av} \tag{2.135}$$

Here N_e is the electron (perturber) density, v is the electron speed and the average is to be performed over the Maxwellian electron velocity distribution. The symbol $\sigma_{i'i}$ and $\sigma_{f'f}$ represent the inelastic cross sections for collisional transitions to levels i',f' from the initial (i) and the final (f) levels, respectively, of the optical transition. The ϕ_i and ϕ_f are elastic scattering amplitudes for the two states of the perturbed system, the integral being performed over the scattering angles (Ω). The collisional excitation cross section $\sigma_{i'i}$ may be calculated using the formula[69]:

$$\sigma_{i'i} = \frac{2\pi^2}{\sqrt{3}} \cdot \frac{f_{i'i} a_o^2}{\varepsilon_e (E_{i'} - E_i)} \bar{g}\, (cm^2) \tag{2.136}$$

Where $f_{i'i}$ is the absorption oscillator strength, $E_{i'}$ and E_i the level energies, $\bar{g}$ the effective Gaunt factor, and the kinetic energy $\varepsilon_e \geq E_{i'} - E_i$ is that of the incident electron. In the absence of more reliable estimates for the elastic terms, a reasonable way to deal with them is to omit them in Eq. (2.130) but to allow for the effects of such collisions by extrapolating the effective Gaunt factor in Eq. (2.131) below threshold[67, 69]. Then we have

$$< v\sigma_{i'i} >= \frac{4\sqrt{2}}{\sqrt{3}} \frac{\pi^{3/2}}{T^{1/2}} \frac{f_{i'i}}{\Delta E_{i'i}} < \bar{g}_{i'i} > \frac{a_o^3}{\tau}\, (cm^3.sec^{-1}) \tag{2.137}$$

where $< \bar{g} >$ represents the Maxwellian average of the effective Gaunt factor,

$$< \bar{g} >= \int_0^{\infty} \bar{g} exp(-\varepsilon_k/T) d(\varepsilon_k/T) \tag{2.138}$$

Hence, the Stark width can be expressed as

$$\Gamma_s = \frac{4\sqrt{2}}{\sqrt{3}} \frac{\pi^{3/2}}{T^{1/2}} N_e \Big(\sum_{i'} \frac{f_{i'i}}{\Delta E_{i'i}} < \bar{g}_{i'i} > + \sum_{f'} \frac{f_{f'f}}{\Delta E_{f'f}} < \bar{g}_{f'f} > \Big) \frac{a_o^3}{\tau} \tag{2.139}$$

where, N_e is electron density in cm^{-3}, and Γ_s is in the unit of rad/s.

Now provided that the relevant levels $i'(f')$ which combine with the initial(final) state of the line according to the electric dipole selection rules are sufficiently separated from $i(f)$ for the $\bar{g}$-values to remain near threshold for all terms, the summation may be carried out directly over the $i'(f')$, using[70]

$$\sum_{i'} \frac{f_{i'i}}{\Delta E_{i'i}} < \bar{g}_{i'i} >= \frac{2}{3} < i|r^2|i >< \bar{g}_{i'i} > \tag{2.140}$$

where the Gaunt factor on the right hand side has the value appropriate for the nearest perturbing level, and r is the distance of the radiating electron from the nucleus in Bohr radius a_o. Finally we have

$$\begin{aligned} \Gamma_s &= \frac{8\sqrt{2}}{\sqrt{T}}(\frac{\pi}{3})^{3/2}N_e(\bar{R}_i^2 < \bar{g}_{i'i} > + \bar{R}_f^2 < \bar{g}_{f'f} >)\frac{a_o^3}{\tau}\,(rad/s) \\ &= \frac{0.74 \times 10^{-7}}{\sqrt{T}}N_e(\bar{R}_i^2 < \bar{g}_{i'i} > + \bar{R}_f^2 < \bar{g}_{f'f} >)\,(rad/s) \quad (2.141) \\ &= \frac{0.3943 \times 10^{-10}}{\sqrt{T}}N_e\lambda^2(\bar{R}_i^2 < \bar{g}_{i'i} > + \bar{R}_f^2 < \bar{g}_{f'f} >)\,(\mathring{A}) \end{aligned}$$

Where T is plasma temperature in $2Ry$, λ is the wavelength of the transition in cm. In the Coloumb approximation, $\bar{R}^2$ can be calculated from[71]

$$\bar{R}_i^2 = \frac{1}{2}(\frac{\nu_i}{z*})^2[5\nu_i^2 + 1 - 3l_i(l_i + 1)] \quad (2.142)$$

in terms of the effective principal (ν) and orbital (l) quantum numbers and the core charge.

Detailed discussions on the systematic errors which could be incurred through the use of the above semi-empirical procedure have been given by Hey et al.[68, 69]. Generally speaking, within twenty percent accuracy is expected.

Convolution of The Doppler and Lorentzian Distribution

If the plasma density is not very high, the mean free path L of the radiating atom is much larger than the wavelength of the observed line λ. Then the Doppler and the Stark broadening may be treated as statistically independent. The combined treatment of the natural, Doppler and the Stark broadenings leads to the convolution of Doppler and Lorentzian distributions. The Lorentzian profile with width $\Gamma_L = \Gamma_n + \Gamma_s$, corresponding to the atom with velocity v in the direction of observation, is given by

$$\phi_v(\omega) = \frac{\Gamma_L}{2\pi} \frac{1}{(\omega - \omega_o v/c - \omega_o)^2 + (\Gamma_L/2)^2} \tag{2.143}$$

Average Eq.(2.143) over the velocity distribution $F(v)$, we have

$$\phi(\omega) = \int F(v) \phi_v(\omega) dv \tag{2.144}$$

For a Maxwellian distribution $F_M(v)$, we have

$$\begin{aligned} \phi(\omega) &= \frac{\Gamma_L}{2\pi} \frac{1}{\sqrt{\pi} v_o} \int \frac{exp[-(v/v_o)^2] dv}{(\omega - \omega_o v/c - \omega_o)^2 + (\Gamma_L/2)^2} \\ &= \frac{1}{2\pi\sqrt{\pi}} \frac{\Gamma_L}{\Delta\omega_D^2} \int \frac{exp[-(v/v_o)^2] d(v/v_o)}{(\frac{\omega-\omega_o}{\Delta\omega} - \frac{v}{v_o})^2 + (\frac{\Gamma_L}{2\Delta\omega})^2} \end{aligned} \tag{2.145}$$

Defining

$$\begin{aligned} t &= \frac{v}{v_o} \\ x &= \frac{\omega - \omega_o}{\Delta\omega_D} = \frac{\omega - \omega_o}{\Delta\Gamma_D} 2\sqrt{ln2} \\ y &= \frac{\Gamma_L}{2\Delta\omega_D} = \frac{\Gamma_L}{\Gamma_D}\sqrt{ln2} \end{aligned} \tag{2.146}$$

we have

$$\phi(\omega) = \frac{1}{\pi} \frac{1}{\sqrt{\pi}\Delta\omega_D} y \int \frac{exp(-t^2)}{y^2 + (x-t)^2} dt$$

$$= \frac{2}{\Gamma_D}(\frac{ln2}{\pi})^{1/2}\frac{y}{\pi}\int\frac{exp(-t^2)}{y^2+(x-t)^2}dt \tag{2.147}$$

This is called the Voight profile.

When $\Delta\omega_D \ll \Gamma_L/2$ the term $\omega_o v/c$ can be neglected in the denominator in Eq.(2.145), after which the integration over v gives a Lorentzian profile with width Γ_L. Consequently, when $\Delta\omega \ll \Gamma_L/2$ Doppler broadening can be neglected.

2.2.3 Bound-Free Transitions

Photoionization

We consider ionization of a N-electron atom by a photon of energy ω. A general formula for the photoionization cross section is

$$\sigma_\omega = \frac{4\pi\alpha a_o^2}{3g_o}\omega\sum| < a|\mathbf{D}|b,\varepsilon > |^2 \tag{2.148}$$

The initial atomic state is $|a>$, the final state for the system of ion plus ejected electron is $|b,\varepsilon>$. ε is the ejected electron kinetic energy. The energy conservation condition is $\omega = I+\varepsilon$ where I is the threshold ionization energy. The initial wavefunction is normalized to unity and the final wavefunction to

$$< b,\varepsilon|b,\varepsilon' >= \delta(\varepsilon-\varepsilon') \tag{2.149}$$

The summation in Eq.(2.148) is over all initial and final states of fixed energy and g_o is the degeneracy of the initial energy level of the atom.

In the LS-coupling scheme, we have

$$\begin{aligned}
&\sigma_\omega(\gamma LS - \gamma_1 L_1 S_1) \qquad (2.150)\\
= &\frac{4\pi^2\alpha a_o^2}{3(2L+1)(2S+1)}(I+\varepsilon)\sum_{l'=l\pm1,L'} | <\gamma LS||\mathbf{D}||(\gamma_1 L_1 S_1)\varepsilon l'; SL'> |^2\\
= &\frac{4\pi^2\alpha a_o^2}{3(2L+1)(2S+1)}(I+\varepsilon)\sum_{l'=l\pm1,L'} \bar{S}[\gamma LS - (\gamma_1 L_1 S_1)\varepsilon l'; SL']s(nl-\varepsilon l')
\end{aligned}$$

Where $\bar{S}$ is the reduce multiplet strength which can be calculated by using the same method for that of bound-bound transitions. Here, we list $\bar{S}$ for two cases of greatest practical importance:

1. $\{\cdots l_o^N(L_1S_1)nl\}LS \rightarrow \{\cdots l_o^N(L_1S_1)\varepsilon l'\}L'S$

$$\bar{S} = \frac{(2L+1)(2S+1)(2L'+1)}{2}\begin{Bmatrix} l' & l & 1\\ L & L' & L_1\end{Bmatrix}^2 \qquad (2.151)$$

$$\sum_{L'}\bar{S} = \frac{(2L+1)(2S+1)}{2(2l+1)}$$

2. $\{\cdots(nl)^N(LS\}LS \rightarrow \{\cdots l^{N-1}(L_1S_1)\varepsilon l'\}L'S$

$$\bar{S} = N|G^{LS}_{L_1S_1}|^2\frac{(2L+1)(2S+1)(2L'+1)}{2}\begin{Bmatrix} l' & l & 1\\ L & L' & L_1\end{Bmatrix}^2 \qquad (2.152)$$

$$\sum_{L'}\bar{S} = N|G^{LS}_{L_1S_1}|^2\frac{(2L+1)(2S+1)}{2(2l+1)}$$

$s(nl-\varepsilon l')$ is the one electron electric dipole line strength. In the length form

$$s(nl-\varepsilon l') = 2l_>|\int_o^\infty P(nl|r)rP(\varepsilon l'|r)dr|^2 \qquad (2.153)$$

and in the velocity form

$$s(nl-\varepsilon l') = \frac{2l_>}{(I+\varepsilon)^2} | \int_0^\infty P(nl|r)[\frac{d}{dr} \pm l_> \frac{1}{r}] P(\varepsilon, l\pm 1|r) dr|^2 \tag{2.154}$$

In the calculation of photoionization cross sections, we need the discrete orbital, $P(nl|r)$, in the initial state, and the continuum orbital, $P(\varepsilon l|r)$, which is obtained by solving the radial Schrödinger equation with a potential determined by the residual ion. In principle, the discrete orbitals for the electrons of the residual ion are different from those for the electrons of the initial ion because of the relaxation effect, and the Hartree-Fock calculations should be done separately. Such a scheme, however, adds computational complexity due to the overlap integrals, and yields initial and final states in different basis sets which would render further improvement based on the HF orbitals. Thus, for our purposes, we use a " frozen frame" scheme, i.e., we use the same HF discrete orbitals in both initial and final state. For the continuum orbital,$P(\varepsilon l|r)$, we use the HX method[27], namely, we solve the radial equation

$$[-\frac{d^2}{dr^2} + \frac{l(l+1)}{r^2} + 2V_{HX}(r) - 2\varepsilon]P(\varepsilon l|r) = 0 \tag{2.155}$$

where $V_{HX}(r)$ is the HX potential determined by the residual ion. A general HX potential for the ith subshell electron is expressed as

$$V^i(r) = -\frac{Z}{r} + \sum_{j=1}^{q}(w_j - \delta_{ij})[\int_0^r \frac{1}{r} P^2(n_j l_j|t)dt + \int_r^\infty \frac{1}{t} P^2(n_j l_j|t)dt] - k_x(\frac{24\rho'}{\pi})^{1/3} \tag{2.156}$$

where $\rho'(r)$ is the modified electron number density

$$\rho'(r) = \frac{1}{4\pi r^2} \sum_{j=1}^{q} w_j P^2(n_j l_j|r) - [min(2, w_i)] P^2(n_i l_i|r), \tag{2.157}$$

and k_x is a correction factor and may be taken as 0.5. It is easy to find that, under the frozen core approximation, the HX potential for the continuum orbital is exactly the same as that for the discrete orbital of the ionized subshell in the initial ion. This may be a good approximation for the ionization of the outer shell electron, but it definitely is inadequate for the ionization of the inner shell electrons. It may be more reasonable to take the HX potential for the outer shell electron in the initial ion as the potential for the continuum orbital in all cases. Our sample calculations confirm this analysis. In Figure 2.13 we show the $3s$-subshell photoionization cross section of ArI. Where circles represent the measurement of Marr *et al.*[72].; curve 1 is our calculational result with the HX potential for the outer shell electrons; curve 2 is our calculational result with the HX potential for the ionized subshell electrons; curve 3 is the HS results of Cooper and Manson[73]. The important feature here is the minimum in the cross section which is absent in curve 2 and curve 3. Curve 1 reproduces the experimental data nicely. The detailed physical mechanism for the formation of this minimum is complicated[74, 75], although our calculation of curve 1 didn't include those complicated effects directly, it at least indicates that the HX potential for the outer shell electrons is a better potential for the continuum orbital.

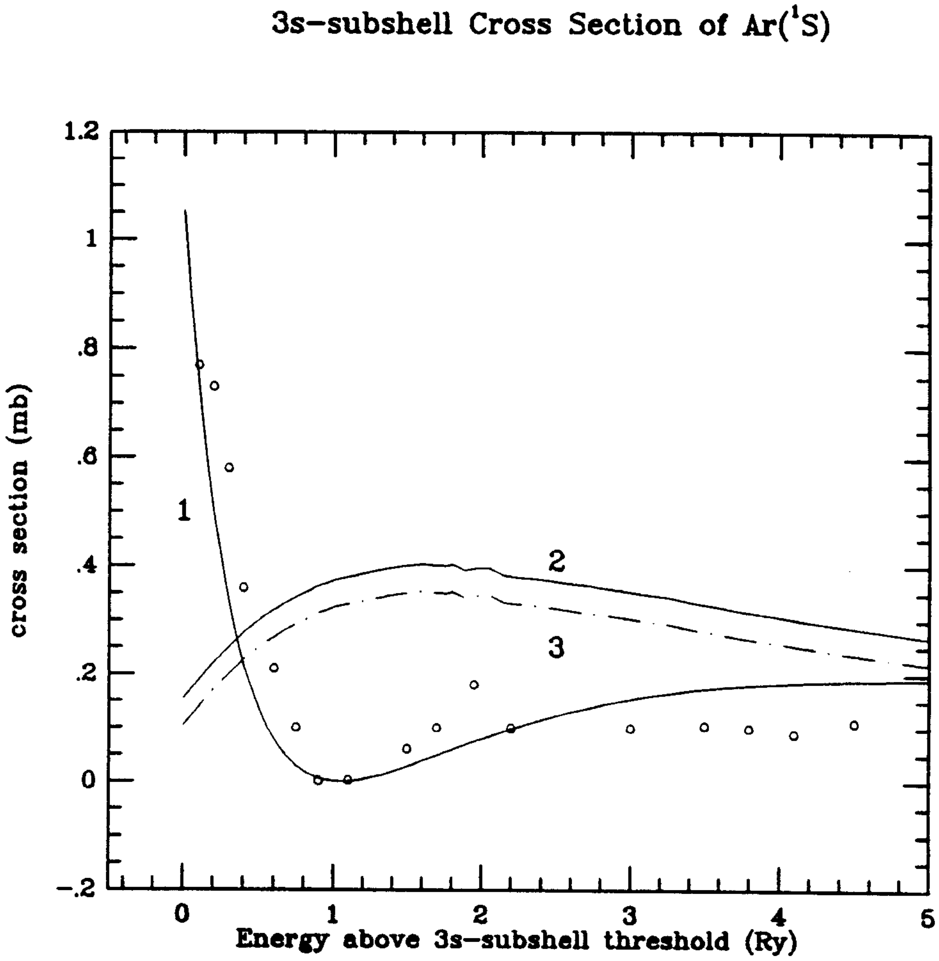

Figure 2.13: 3s-subshell photoionization cross section of ArI

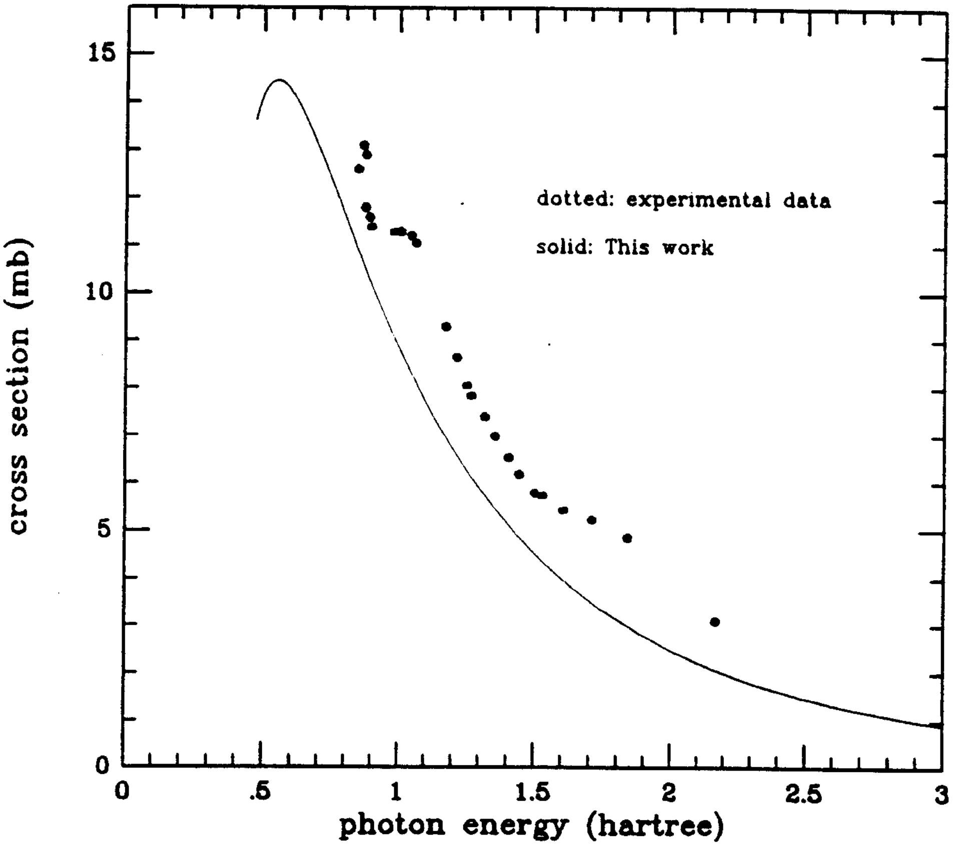

Figure 2.14: Total photoionization cross section of NI($2p^3\ ^4S$)

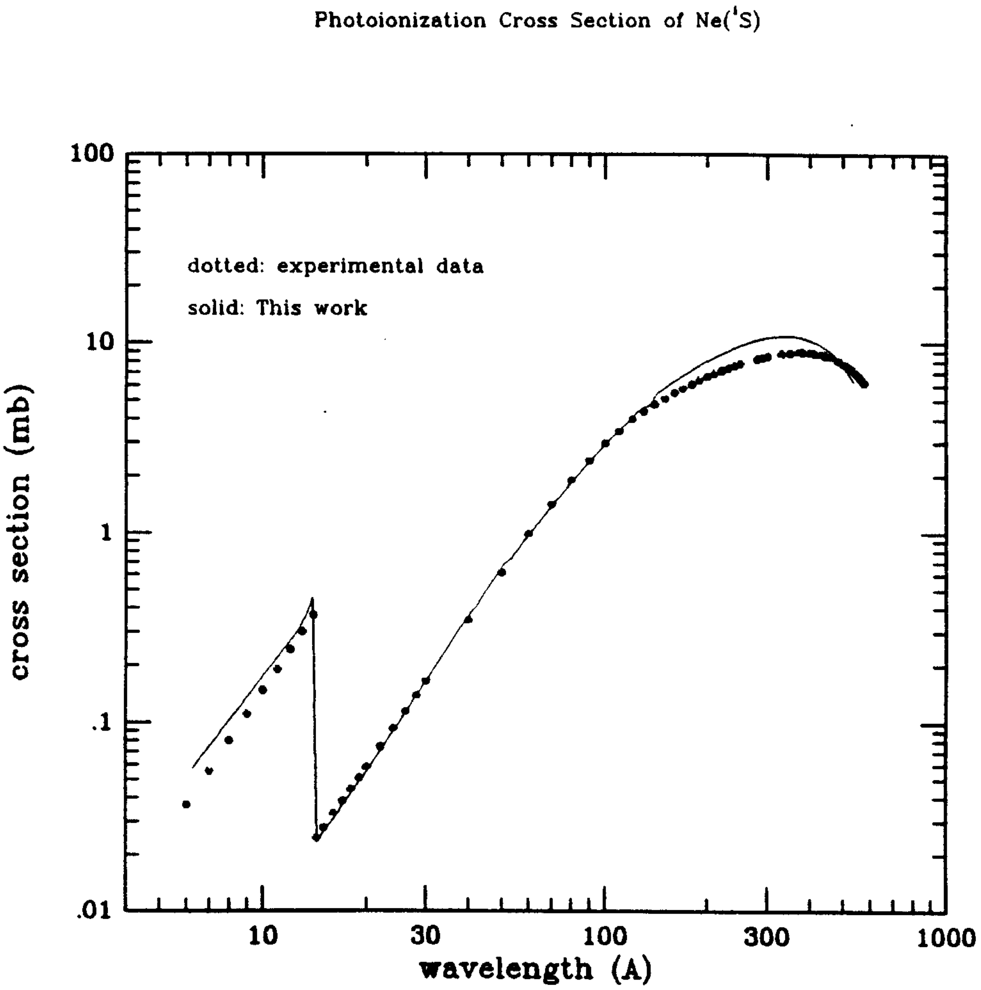

Figure 2.15: Total photoionization cross section of NeI($2p^{6\,1}S$)

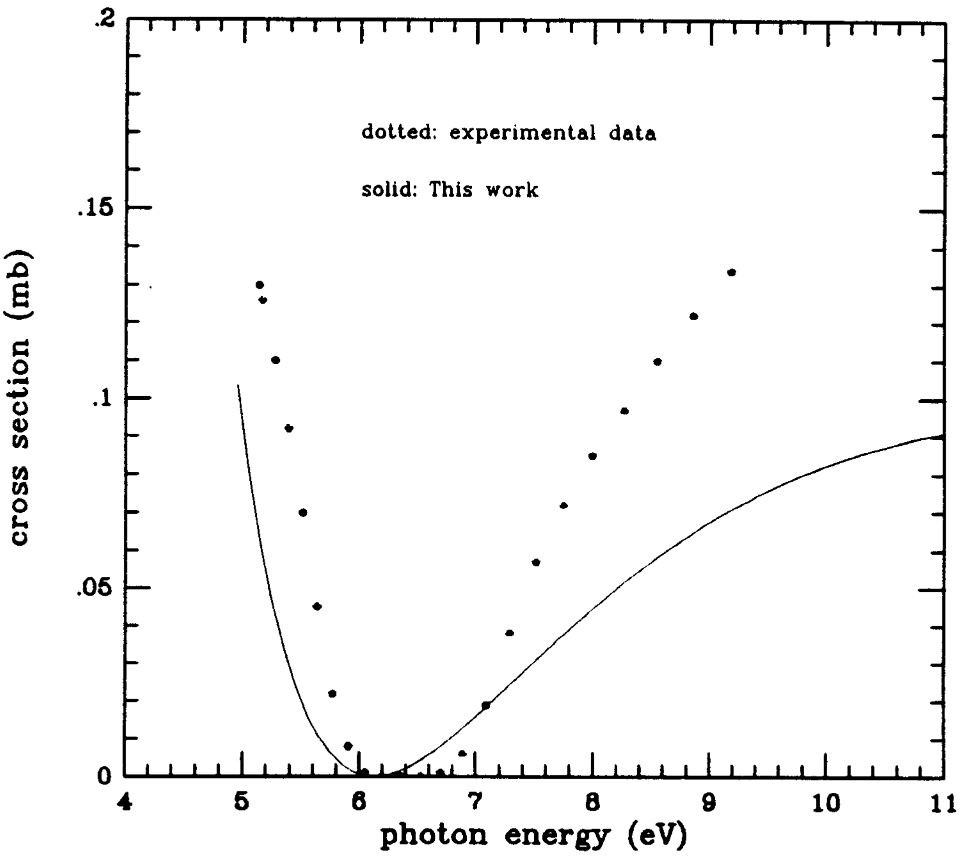

Figure 2.16: Total photoionization cross section of NaI($3s^2S$)

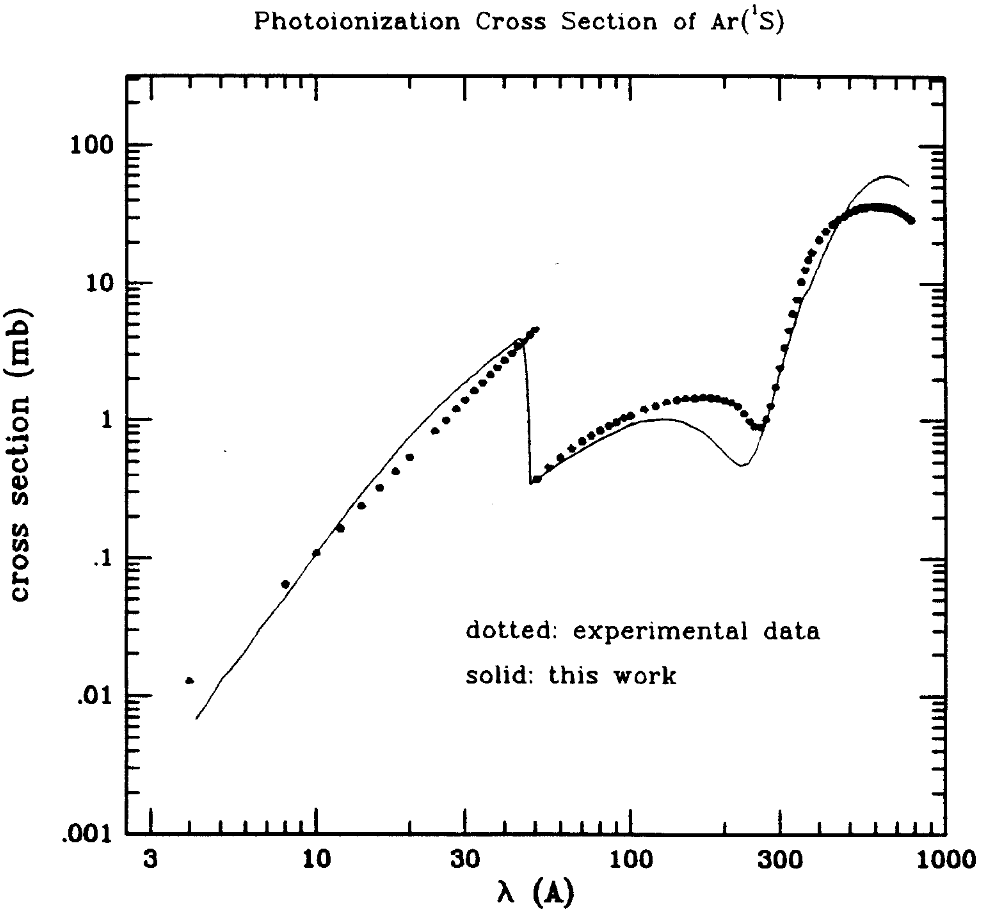

Figure 2.17: Photoionization cross section of ArI($3p^{6}\,{}^1S$)

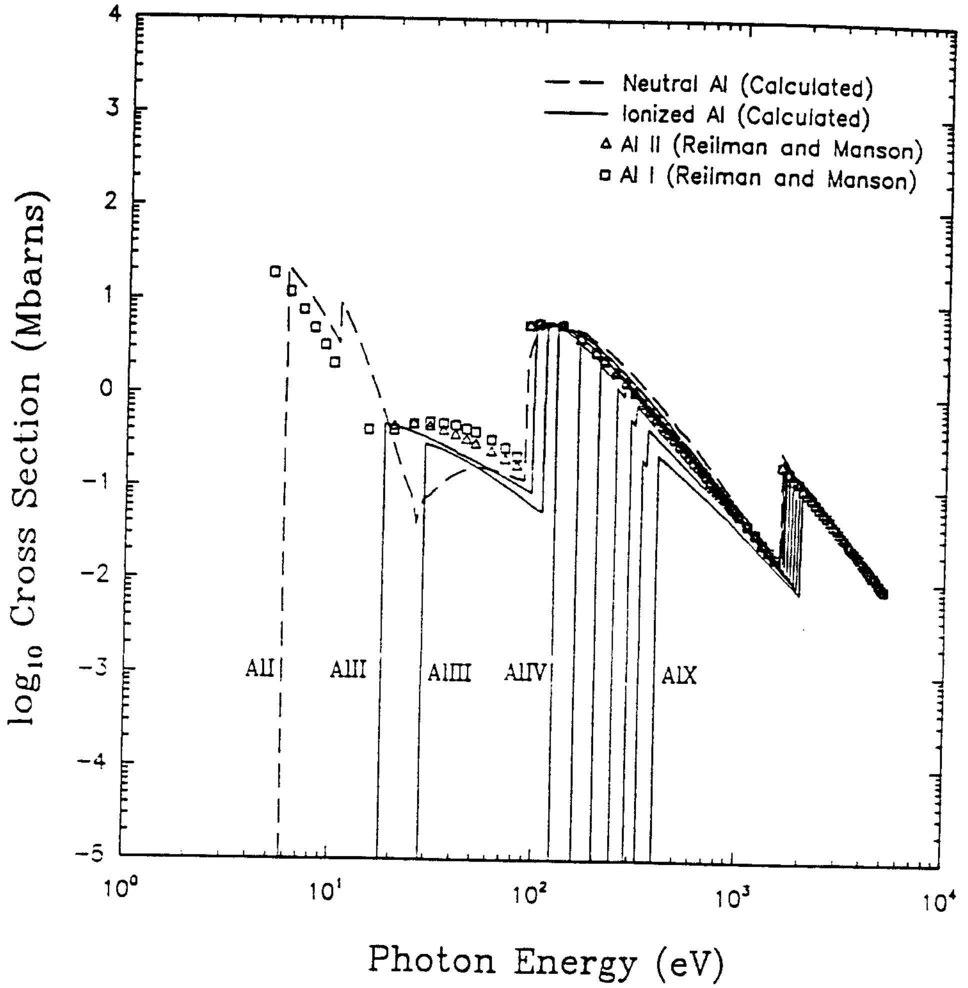

Figure 2.18: Photoionization cross section of Al

In Figure 2.14 – Figure 2.18 we show some of our calculational results and compare them with the available experimental data[108, 109, 110] and the other theoretical results[111]. It can be seen that in most cases our calculations give good estimates for the photoionization cross sections.

For the hydrogenlike ions and the high excited states of complex ions, the hydrogenic model can be used. In the hydrogenic approximation, the cross section for photoionization from level n is

$$\sigma(n \rightarrow \varepsilon) = \frac{2^6 \alpha \pi a_o^2}{3\sqrt{3}} \frac{n}{z^*} (1 + 2n^2 z^* \varepsilon)^{-3} g_{bf}(n, \varepsilon) \tag{2.158}$$

where g_{bf} is bound-free Gaunt factor. The detailed expression of g_{bf} has been given by Karzas and Latter[76]. The asymptotic expansion for g_{bf} is[76]

$$\begin{aligned} g_{bf}(n, \varepsilon) &= 1 + \frac{0.1728}{[n(u+1)]^{2/3}}(u-1) \\ &- \frac{0.0496}{[n(u+1)]^{4/3}}(u^2 + \frac{4}{3}u + 1) + \cdots \end{aligned} \tag{2.159}$$

where $u = n^2 \varepsilon z^*$.

Radiative Recombination

The radiative recombination cross section is related to the corresponding photoionization cross section by the Milne formula

$$\sigma^r(\varepsilon \rightarrow nl) = \frac{\alpha^2 (I_{nl} + \varepsilon)}{2\varepsilon} \frac{g_k}{g_{k'}^+} \sigma^i(nl, \omega) \tag{2.160}$$

where $\sigma^r(\varepsilon \rightarrow nl)$ is the cross section for an ion in k' state recombining with an electron with kinetic energy ε to the nl subshell and $\sigma^i(nl, \omega)$ is the cross section for a nl electron ionized from an atom in the k state by absorbing a photon with energy ω.

The radiative recombination rate coefficient can be obtained by averaging the cross section over the electron velocity distribution, i.e,

$$\begin{aligned} Q_k^r(T) &= \int_0^\infty vF(v)\sigma_k^r(v)dv \\ &= \int_0^\infty \sqrt{2\varepsilon}F(\varepsilon)\sigma_k^r(\varepsilon)d\varepsilon \end{aligned} \tag{2.161}$$

where σ_k^r is the total recombination cross section

$$\sigma_k^r(\varepsilon) = \sum_{nl} \sigma^r(\varepsilon \to nl) \tag{2.162}$$

Assuming a Maxwellian distribution for electrons, then

$$Q_k^r(T) = \int_0^\infty \frac{1}{\sqrt{\pi}}(\frac{2}{T})^{3/2}\varepsilon \cdot exp(-\varepsilon/T)\sigma_k^r(\varepsilon)d\varepsilon \tag{2.163}$$

substituting Eq.(2.157) into Eq.(2.160) we have

$$Q_k^r(T) = \frac{0.93 \times 10^{-14}}{T^{3/2}} \frac{g_k}{g_{k'}^+} \sum_{nl} \int_0^\infty (I_{nl} + \varepsilon)^2 exp(-\varepsilon/T)\sigma^i(nl,\omega)d\varepsilon \tag{2.164}$$

where $\sigma^i(nl,\omega)$ is in the unit of 10^{-18} cm^2 and Q is in $cm^3 sec^{-1}$.

In the hydrogenic approximation, the coefficient for recombination on to levels n is[77]

$$Q_n^r(z^*,T) = 5.197 \times 10^{-14} \frac{z^*}{g^+} \frac{\sqrt{y}}{n} x_n S_n(y) \tag{2.165}$$

where Q is in the unit of cm^3sec^{-1} and

$$\begin{aligned} y &= \frac{13.6055z^*}{T(eV)} \\ x_n &= \frac{y}{n^2} \\ S_n(y) &= \int_0^\infty \frac{g_{bf}(n,\varepsilon)e^{-x_n u}}{1+u}du \end{aligned} \tag{2.166}$$

By using the asymptotic expansion of g_{bf} in Eq.(2.159), we have

$$S_n(y) = S^{(0)}(x_n) + y^{-1/3}S^{(1)}(x_n) + y^{-2/3}S^{(2)}(x_n) + \cdots \tag{2.167}$$

where

$$\begin{aligned} S^{(0)}(x) &= e^x E_i(x) \\ S^{(1)}(x) &= 0.1728x^{1/3}X_1(x) \\ S^{(2)}(x) &= -0.0496x^{2/3}X_2(x) \end{aligned} \tag{2.168}$$

and

$$\begin{aligned} E_i(x) &= \int_x^\infty \frac{e^{-v}}{v}dv \\ X_1(x) &= \int_0^\infty (u+1)^{-5/3}(u-1)e^{-xu}du \\ X_2(x) &= \int_0^\infty (u+1)^{-7/3}(u^2+\frac{4}{3}u+1)e^{-xu}du \end{aligned} \tag{2.169}$$

2.2.4 Free-Free Transitions in a Coulomb Field

Free-Free Absorption

The continuous radiation absorption process is generally termed "free-free absorption". The classical calculation of the radiation absorbed by an electron being scattered in a Coloumb field was first carried out by Kramers, with the resulting so-called Kramers cross section given by [78]

$$\sigma_K^{ff}(\varepsilon_i, \omega) = \frac{16\pi^3}{3\sqrt{3}} \frac{\alpha z^2}{\omega^3 \sqrt{2\varepsilon_i}} a_o^5 \tag{2.170}$$

Here ω is the energy of the emitted photon, ε_i is the energy of the incident electron.

The quantum theory calculation was studied very early by Gaunt, and it has since been customary to write the result in terms of the Kramers cross section

$$\sigma^{ff}(\varepsilon_i, \omega) = \sigma_K^{ff}(\varepsilon_i, \omega) g_{ff}(\varepsilon_i, \varepsilon_f) \tag{2.171}$$

where $g_{ff}(\varepsilon_i, \varepsilon_f)$ is called the free-free Gaunt factor, and can be expressed as[76]

$$g_{ff} = \frac{2\sqrt{3}}{\pi \eta_i \eta_f} [(\eta_i^2 + \eta_f^2 + 2\eta_i^2 \eta_f^2) I_o - 2\eta_i \eta_f (1 + \eta_i^2)^{1/2} (1 + \eta_f^2)^{1/2} I_1] I_o \tag{2.172}$$

where

$$I_l = \frac{1}{4} [\frac{4k_i k_f}{(k_i - k_f)^2}]^{l+1} e^{\pi|\eta_i - \eta_f|/2} \frac{|\Gamma(l+1+i\eta_i)\Gamma(l+1+i\eta_f)}{\Gamma(2l+2)} G_l \tag{2.173}$$

with

$$G_l = |\frac{k_f - k_i}{k_f + k_i}|_2^{i(\eta_i + \eta_f)} F_1(l+1-i\eta_f; l+1-i\eta_i; 2l+2; -\frac{4k_i k_f}{(k_i - k_f)^2}) \tag{2.174}$$

and

$$\begin{gathered} \eta_i^2 = \frac{z^2}{2\varepsilon_i} \quad \eta_f^2 = \frac{z^2}{2\varepsilon_f} \\ k_i^2 = 2\varepsilon_i \quad k_f^2 = 2\varepsilon_f \end{gathered} \tag{2.175}$$

Assuming a Maxwellian distribution for electrons, then

$$\begin{aligned}\sigma^{ff}(\omega) &= \int_0^\infty F_M(\varepsilon)\sigma^{ff}(\varepsilon_i,\omega)d\varepsilon_i \\ &= \frac{16\sqrt{2}\pi^{5/2}}{3\sqrt{3}}\frac{\alpha z^2 a_o^5}{\omega^3 T^{3/2}}\int_0^\infty e^{-\varepsilon_i/T} g_{ff} d\varepsilon_i \\ &= \frac{16\sqrt{2}\pi^{5/2}}{3\sqrt{3}}\frac{\alpha z^2 a_o^5}{\omega^3 T^{3/2}} < g_{ff} > \qquad (2.176)\end{aligned}$$

where the temperature averaged free-free Gaunt factor is defined as

$$< g_{ff} >= \int_0^\infty dx e^{-x} g_{ff}(\eta_i = \gamma x^{-1/2}, \omega = \frac{uz^2}{\gamma^2}) \qquad (2.177)$$

with

$$\begin{aligned} u &= \frac{\omega}{T} \\ \gamma^2 &= \frac{z^2}{2T} \qquad (2.178)\end{aligned}$$

This temperature-averaged Gaunt factor is plotted in Figure 2.19 as a function of γ^2 and u.

Free-Free Emission

The cross section for an electron of energy ε_o, normalized to unit density at infinity, to emit a photon in the energy range ω - $\omega + d\omega$, when passing an ion with charge z, is given by[26, 76]

$$\frac{d\sigma^{em}}{d\omega} = \frac{8\pi}{3\sqrt{3}}\frac{\alpha^3 z^2 a_o^2}{\varepsilon_o \omega} g_{ff}(\varepsilon_o - \omega, \varepsilon_o) \qquad (2.179)$$

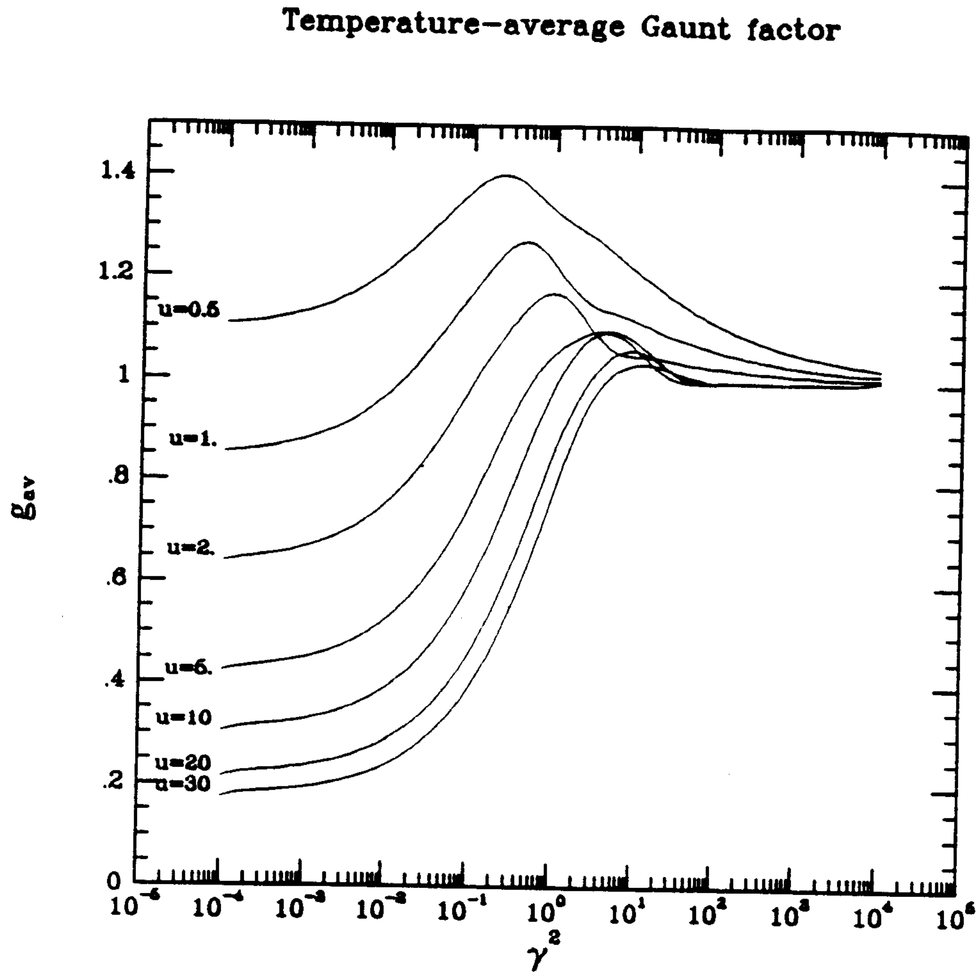
Temperature-average Gaunt factor

Figure 2.19: Temperature-average free-free Gaunt factor

The energy emitted per unit time can be found by multiplying by ω and by the electron flux, $N_e\sqrt{2\varepsilon_o}$:

$$W(\omega)d\omega = \frac{8\sqrt{2}\pi}{3\sqrt{3}}\frac{\alpha^3 z^2 a_o^2}{\sqrt{\varepsilon_o}} N_e g_{ff} d\omega \tag{2.180}$$

Assuming a Maxwellian distribution for electron energies, we have[76]

$$\begin{aligned} < W(\omega) > d\omega &= \frac{2^5\sqrt{2}\pi^{3/2}\alpha^3}{3\sqrt{3}} z^2 N_e a_o^3 T^{1/2} e^{-u} < g_{ff}(u,\gamma^2) > du \\ &= 1.53 \times 10^{-25} z^2 N_e \sqrt{T} e^{-u} < g_{ff} > du \end{aligned} \tag{2.181}$$

where T is in eV in the second expression, N_e is in cm^{-3} and W is in $ergs.sec^{-1}$.

Finally, the energy emitted per unit volume per unit time is found by multiplying by the density of positive ions which serve as targets for the bremsstrahlung production and integrating over the photon spectrum

$$\epsilon(\frac{ergs}{cm^3 sec}) = 1.53 \times 10^{-25} z^2 N_e N_i T^{1/2} \int_0^\infty due^{-u} < g_{ff} > \tag{2.182}$$

2.2.5 Dielectronic Recombination Process

Dielectronic recombination is not a radiative process but relates to radiative processes very closely. In the dielectronic recombination process, there are two stages: first, the nonradiative attachment of an electron and excitation of the ion takes place. Then there are two possibilities, nonradiative decay (autoionization), or radiative transition into a '*stable*' state below the ionization limit. This latter process provides the net recombination. The basic processes of dielectronic recombination are shown in Figure 2.20.

Since dielectronic recombination is a two stage process, the corresponding rate coefficient can be calculated in two steps:

1. rate coefficient for the nonradiative capture;
2. rate coefficient for the radiative stabilization.

For a LTE plasma, the rate coefficient for the nonradiative capture can be expressed as[87]

$$\alpha_d^{mj}(T) = 4a_o^3\left(\frac{\pi}{2T}\right)^{3/2}\frac{g_j A_a^{jm}}{g_m} exp(-\Delta E_{jm}/T)\,(cm^3.sec^{-1}) \tag{2.183}$$

where A_a^{jm} is the possibility per unit time that an ion (Z,N) in the level j will autoionize, leave an ion (Z,N-1) in the level m.

Once the ion (Z,N) has been formed in the state j, there is a possibility that it may be reionized at a rate A_a^{jm}. Considering this effect, the probability that decay will be via a radiative transition to a specific lower level k is given by the branching ratio (or the fluorescence yield in x-ray emission case):

$$B^{jk} = \frac{A_r^{jk}}{\sum_{m'} A_a^{jm'} + \sum_{k'} A_r^{jk'}} \tag{2.184}$$

Where the summation over m' extends over all possible levels of the ion (Z,N-1) that lie below j, and the summation over k' extends over all levels of ion

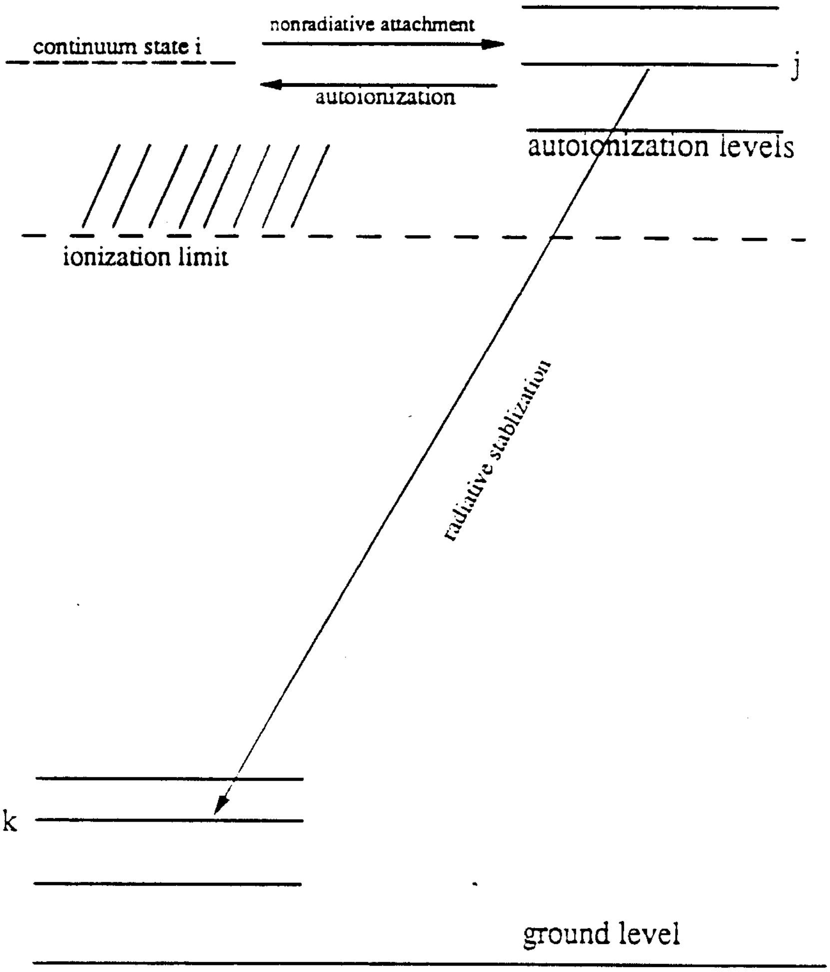

Figure 2.20: Schematic diagram of basic processes involved in the dielectronic recombination

(Z,N) that lie below j. The summation over m' represents reautoionization transition, or (in another vocabulary) single-electron Auger transition.

The rate of dielectronic recombination to level k of ion (Z,N) is [87]

$$R_d(T,k) = \sum_j [\sum_m n_{N-1}^m \alpha_d^{mj}(T)] B^{jk} \tag{2.185}$$

Where the summation is over the states of the ion (Z,N-1). Finally, the total net dielectronic recombination rate is

$$\begin{aligned} R_d(T,k) &= \sum_k R_d(T,k) \\ &= \sum_j [\sum_m n_{N-1}^m \alpha_d^{mj}(T)] \sum_k B^{jk} \end{aligned} \tag{2.186}$$

Calculation of Autoionization Rate A_a

As shown by Fano[88], autoionization transition probabilities may be calculated from the first-order perturbation theory expression

$$\begin{aligned} A_a^{ji} &= \frac{2\pi}{\hbar} | < j|H|i > |^2 = 2.5976 \times 10^{17} [\sum_{\sigma_i \sigma_j} x(\sigma_i, \sigma_j) I(\bar{n}_{\sigma_i} l_{\sigma_i}, n_{\sigma_j} l_{\sigma_j}) \\ &+ \sum_{\sigma_i \rho_i \sigma_j \rho_j} \sum_k y(\sigma_i \rho_i; \sigma_j \rho_j) R^k (\bar{n}_{\sigma_i} l_{\sigma_i} n_{\rho_i} l_{\rho_i}; n_{\sigma_j} l_{\sigma_j} n_{\rho_j} l_{\rho_j})]^2 \end{aligned} \tag{2.187}$$

where one of the "$\bar{n}l$" orbitals is a continuum function $P(\varepsilon l|r)$ for a free electron of kinetic energy $\varepsilon = E(Z, N-1, m) - E(Z, N, j)$, and m is the state of the residual ion after autoionization.

The calculation for the angular coefficients x and y is the same as that for atomic energy expressions. In the calculation of radial integrals I and R^k, the continuum function $P(\varepsilon l|r)$ is normalized in the energy scale.

Burgess-Merts Semiempirical Formula

We present here a semiempirical formula for the total rate coefficient of dielectronic recombination proposed by Burgess[89] and modified by Merts *et al.*[87]. This formula is written as

$$\alpha_d = 1.69 \times 10^{-11} T^{-3/2} B(z) \sum_{m=i+1} f_{im} A(x) e^{-\Delta E_{mi}/T} \tag{2.188}$$

The quantities appearing in this expression are:

T_e = electron temperature in the unit of $2Ry$;

z = the charge number of the recombining ion;

i = the initial state of the recombining ion;

m = a state of the excited core configuration j_o of the recombined ion (before radiative stabilization);

f_{im} = oscillator strength of the transition $i \rightarrow m$ of the recombining ion;

ΔE_{mi} is the energy of transition and may be calculated from

$$\frac{\Delta E_{mi}}{T} = 5.0 \times 10^{-7} (z+1)^2 \frac{(\nu_i^{-2} - \nu_m^{-2})}{Ta}$$

where ν_i and ν_m are the effective principal quantum numbers;

$$a = 1.0 + 0.015 \frac{z^3}{(z+1)^2}$$

$$B(z) = \frac{z^{1/2}(z+1)^{5/2}}{(z^2+13.4)^{1/2}}$$

$$A(x, \Delta n = 0) = \frac{x^{1/2}}{(1 + 0.105x + 0.015x^2)}$$

$$A(x, \Delta n \neq 0) = \frac{0.5x^{1/2}}{(1 + 0.21x + 0.03x^2)}$$

where $x = (z+1)(\nu_i^{-2} - \nu_m^{-2})$.

In regard to the accuracy of this semiempirical formula, Mert *et al.*[87] has made a very detailed discussion. It is expected that the accuracy is within a factor of two or three.

2.3 Atomic Collisional Processes

In this section we consider the problems of atomic collisional data calculations. As we already mentioned in the last chapter, usually electrons play the main role in collisional excitation and ionization processes in a plasma. Interaction with heavy particles (protons,ions) is important only for transitions between levels with very small energy splitting (*e.g.*, within fine structure). However, in ICF research, especially in the ion beam - plasma interaction experiments, because the ion beam couples with the plasma directly, the collisional effect of the beam ion may become important for the plasma diagnostics. Hence, the atomic collisional processes of our interest include:

- electron collisional excitation and deexcitation

$$A(z,i) + e \rightleftharpoons A(z,k) + e$$

- electron collisional ionization and recombination

$$A(z,i) + e \rightleftharpoons A(z+1,k) + 2e$$

- proton collisional excitation and deexcitation

$$A(z,i) + p \rightleftharpoons A(z,k) + p$$

- proton collisional ionization

$$A(z,i) + p \rightarrow A(z+1,k) + p$$

2.3.1 Electron Collisional Excitation And Deexcitation

The Schrödinger equation for the electron-ion collisional problem may be expressed in terms of the scattering electron moving in the potential of the target ion. The radial part of the wavefunction of the scattering electron is written as[79]:

$$[\frac{d^2}{dr^2} - \frac{l(l+1)}{r^2} - k^2]P(\Gamma|r) = 2\sum_{\Gamma'}[U_{\Gamma\Gamma'} \pm V_{\Gamma\Gamma'}]P(\Gamma'|r) \qquad (2.189)$$

where P is the radial function in a given channel (represented by Γ and Γ'). The summation on the right-hand-side of Eq. (2.189) is over all discrete and continuum states. $U_{\Gamma\Gamma'}$ and $V_{\Gamma\Gamma'}$ are direct and exchange potential operators, respectively. $V_{\Gamma\Gamma'}$ are integral operators and therefore Eq.(2.189) represents an infinite set of coupled integro-differential equations. Truncating the sum on the rhs of Eq.(2.189) to a finite number of excited states of the target ion and solving the remaining coupled equations exactly yield the N-close-coupling approximation, where N is the number of states included. The close-coupling approximation is the most accurate method for solving the electron-ion collision problem as it allows for full coupling between channels which is often strong at low energies. However the computations of this kind are very complicated. In our calculations, we only consider the first-order approximation, i.e., we omit the coupling between scattering channels and therefore the relevant matrix elements include only the initial and the final channels.

In the first-order approximation, the general expression for the electron impact excitation cross section is[79]

$$\begin{aligned} \sigma_{\Gamma_o\Gamma} &= \sigma'_{\Gamma_o\Gamma} + \sigma''_{\Gamma_o\Gamma} \\ &= \sum_{\kappa}[Q'_{\kappa}(\Gamma_o\Gamma)\sigma'_{\kappa}(l_o,l) + Q''_{\kappa}(\Gamma_o\Gamma)\sigma''_{\kappa}(l_o,l)] \qquad (2.190) \end{aligned}$$

where $\sigma'_{\kappa}(l_o,l)$ and $\sigma''_{\kappa}(l_o,l)$ are one-electron cross sections, depending on quantum number n_ol_o,nl only:

$$\sigma'_{\kappa}(l_o,l) = \frac{4}{(2l_o+1)k_i^2}\sum_{l_il_f} R^d_{\kappa}(R^d_{\kappa} - \sum_{\kappa'} R^e_{\kappa'\kappa})\pi a_o^2 \qquad (2.191)$$

$$\sigma''_{\kappa}(l_o,l) = \frac{4}{(2l_o+1)k_i^2}\sum_{l_il_f}(\sum_{\kappa'} R^e_{\kappa'\kappa})^2\pi a_o^2 \qquad (2.192)$$

where R^d and R^e are direct and exchange radial integrals, given by

$$\begin{aligned} R^d_{\kappa} &= \frac{\Pi(l_oll_il_f)}{\Pi(\kappa)}\begin{pmatrix} \kappa & l_o & l \\ 0 & 0 & 0 \end{pmatrix}\begin{pmatrix} \kappa & l_i & l_f \\ 0 & 0 & 0 \end{pmatrix} \qquad (2.193) \\ &\times\ 2\int\int P(nl|r')P(k_fl_f|r'')\frac{r_<^{\kappa}}{r_>^{\kappa+1}}P(n_ol_o|r')P(k_il_i|r'')dr'dr'' \end{aligned}$$

$$\begin{aligned} & R^e_{\kappa'\kappa} = (-1)^{\kappa'+\kappa}\Pi(\kappa l_ol_il_f) \\ &\times\ 2\begin{pmatrix} \kappa' & l_o & l_f \\ 0 & 0 & 0 \end{pmatrix}\begin{pmatrix} \kappa' & l_i & l \\ 0 & 0 & 0 \end{pmatrix}\begin{Bmatrix} \kappa' & l_o & l_f \\ \kappa & l_i & l \end{Bmatrix} \qquad (2.194) \\ &\times\ \int\int P(nl|r')P(k_fl_f|r'')\frac{r_<^{\kappa'}}{r_>^{\kappa'+1}}(1 - Cr_>\delta_{\kappa'0})P(n_ol_o|r'')P(k_il_i|r')dr'dr'' \end{aligned}$$

with

$$C = \frac{1}{2}(-2\varepsilon_a + k_i^2) = \frac{1}{2}(2\varepsilon_{a_o} + k_f^2) \tag{2.195}$$

$$\Pi(j_1 j_2 \cdots) = (2j_1+1)^{1/2}(2j_2+1)^{1/2}\ldots \tag{2.196}$$

In accordance with the properties of $3nj$ symbols, the values of κ and κ' in Eq.(2.193) - (2.194) lie between the limits κ_{min}, κ_{max} and κ'_{min}, κ'_{max} respectively, where

$$\begin{aligned} \kappa_{min} &= max(|l-l_o|, |l_i - l_f|); \quad \kappa_{max} = min(l+l_o, l_i+l_f) \\ \kappa'_{min} &= max(|l_f-l_o|, |l_i - l|); \quad \kappa'_{max} = min(l+l_i, l_o+l_f) \end{aligned} \tag{2.197}$$

Q'_κ and Q''_κ in Eq.(2.101) are the angular factors which depend only on the angular momentum quantum numbers of the initial and final states (a_o,a). For transitions of type

$$l_o^m L_o S_o \rightarrow l_o^{m-1}[L_p S_p] l L S$$

we have

$$Q'_\kappa(L_oS_o, LS) = \Pi^2(l_oL)\left\{\begin{array}{ccc} \kappa & L_o & L \\ L_p & l & l_o \end{array}\right\} m|G^{LS}_{L_pS_p}|^2 \delta_{SS_o} \tag{2.198}$$

$$Q''_\kappa(L_oS_o, LS) = \frac{2S+1}{2(2S_p+1)}\Pi^2(l_oL)\left\{\begin{array}{ccc} \kappa & L_o & L \\ L_p & l & l_o \end{array}\right\} m|G^{LS}_{L_pS_p}|^2 \tag{2.199}$$

For transitions between configurations $l_o^m \rightarrow l_o^{m-1}l$:

$$Q'_\kappa(l_o^m, l_o^{m-1}l) = Q''_\kappa(l_o^m, l_o^{m-1}l) = 1 \tag{2.200}$$

Distorted Wave Calculations

In our distorted wave calculations, the radial wavefunctions for bound electrons are the Hartree-Fock wavefunctions, the continuum wavefunctions, $P(kl|r)$, are obtained by solving the equation

$$[\frac{d^2}{dr^2} - \frac{l(l+1)}{r^2} - 2V(r) + k^2]P(kl|r) = 0 \tag{2.201}$$

$$P(kl|r) \overset{r\to 0}{\longrightarrow} 0$$

$$P(kl|r) \overset{r\to\infty}{\longrightarrow} \frac{1}{\sqrt{k}} sin[kr - \frac{l\pi}{2} + \frac{z-1}{k} ln(kr) - \eta]$$

The asymptotic behaviour of $P(kl|r)$ here corresponds to the normalization condition

$$\int_0^\infty P(\varepsilon l|r)P(\varepsilon' l|r)dr = \frac{\pi}{2}\delta(\varepsilon - \varepsilon') \tag{2.202}$$

The potential function in Eq.(2.201) is taken as the modified HX potential which includes the screen and exchange effect of the bound electrons in target:

$$\begin{aligned} V(r) &= -\frac{Z}{r} + \sum_{j=1}^{q} w_j [\int_0^r \frac{1}{r} P^2(n_j l_j|t)dt \\ &+ \int_r^\infty \frac{1}{t} P^2(n_j l_j|t)dt] - k_x[\frac{24}{\pi}\rho(r)]^{1/3} \end{aligned} \tag{2.203}$$

with

$$\rho(r) = \frac{1}{4\pi r}\sum_{j=1} q w_j P^2(n_j l_j|r)$$

For the exchange radial integral, we can write

$$\begin{aligned} &\int_0^\infty \int_0^\infty P(nl|r_1)P(k_f l_f|r_2)\frac{r_<^\kappa}{r_>^{\kappa+1}}(1 - Cr_>\delta_{\kappa,0})P(n_o l_o|r_2)P(k_i l_i|r_1)dr_1 dr_2 \\ = &\int_0^{rmax} f_{e1}(r_2)dr_2 + \int_0^{rmax} f_{e2}(r_2)dr_2 \end{aligned} \tag{2.204}$$

where $f_{e1}(r)$ and $f_{e2}(r)$ are defined as

$$f_{e1}(r) = P(k_f l_f|r)P(n_o l_o|r)\frac{(1 - Cr\delta_{\kappa 0})}{r^{\kappa+1}} \int_0^r P(nl|t)P(k_i l_i|t)t^{\kappa} dt \tag{2.205}$$

$$f_{e2}(r) = P(k_f l_f|r)P(n_o l_o|r)r^{\kappa} \int_r^{r_{max}} P(nl|t)P(k_i l_i|t)\frac{(1 - Ct\delta_{\kappa 0})}{t^{\kappa+1}} dt \tag{2.206}$$

and r_{max} is determined by the condition

$$P(nl|r > r_{max}) = 0 \tag{2.207}$$

The direct radial integral is a slowly converging integral,so we write

$$\begin{aligned} &\int_0^{\infty}\int_0^{\infty} P(nl|r_1)P(k_f l_f|r_2)\frac{r_<^{\kappa}}{r_>^{\kappa+1}}P(n_o l_o|r_1)P(k_i l_i|r_2)dr_1 dr_2 \\ = &\int_0^{\infty} f_{d1}(r_2)dr_2 + \int_0^{\infty} f_{d2}(r_2)dr_2 \end{aligned} \tag{2.208}$$

where $f_{d1}(r)$ and $f_{d2}(r)$ are defined as

$$f_{d1}(r) = P(k_f l_f|r)P(k_i l_i|r)\frac{1}{r^{\kappa+1}} \int_0^r P(nl|t)P(n_o l_o|t)t^{\kappa} dt \tag{2.209}$$

$$f_{d2}(r) = P(k_f l_f|r)P(k_i l_i|r)r^{\kappa} \int_r^{\infty} P(nl|t)P(n_o l_o|t)\frac{1}{t^{\kappa+1}} dt \tag{2.210}$$

When $r \geq r_{max}$, we have

$$\begin{aligned} \int_0^r P(nl|t)P(n_o l_o|t)t^{\kappa} dt &= \int_0^{r_{max}} P(nl|t)P(n_o l_o|t)t^{\kappa} dt \\ \int_r^{\infty} P(nl|t)P(n_o l_o|t)\frac{1}{t^{\kappa+1}} dt &= 0 \end{aligned} \tag{2.211}$$

Hence 'f' functions can be divided into two parts: For $r < r_{max}$,

$$f_{d1}(r) = P(k_f l_f|r)P(k_i l_i|r)\frac{1}{r^{\kappa+1}} \int_0^r P(nl|t)P(n_o l_o|t)t^{\kappa} dt$$

$$f_{d2}(r) = P(k_f l_f|r)P(k_i l_i|r)r^{\kappa} \int_r^{r_{max}} P(nl|t)P(n_o l_o|t)\frac{1}{t^{\kappa+1}}dt \qquad (2.212)$$

For $r \geq r_{max}$,

$$f_{d1}(r) = P(k_f l_f|r)P(k_i l_i|r)\frac{1}{r^{\kappa+1}} \int_0^{r_{max}} P(nl|t)P(n_o l_o|t)t^{\kappa}dt$$

$$f_{d2}(r) = 0 \qquad (2.213)$$

In order to obtain accurate results for $\int_0^{\infty} f_{d1}(r)dr$, the cut point for r must be very large in the direct numerical integration. An asymptotic expansion method for the fast, accurate evaluation of such integrals has been developed by J.A. Belling[80].

A flow diagram of our distorted wave calculation code, EACOLL, is shown in Figure 2.21.

Generally speaking, the DW calculation can provide excitation cross sections with accuracy sufficient for most applications. Typical accuracy is within a factor of 1.5 - 2. For high charge of the ion, the DW method is even comparable to the CC approximation. In Figure 2.22 we show a sample result of our DW calculational result and compare with the available CC calculational result[114, 115]. Curve 1 is our DW calculational result, curve 2 is Cristensen *et al.* multiconfiguration CC calculational result and curve 3 is Van Wyngaarden *et al.* multiconfiguration CC calculational result. The agreement is better than a factor of two.

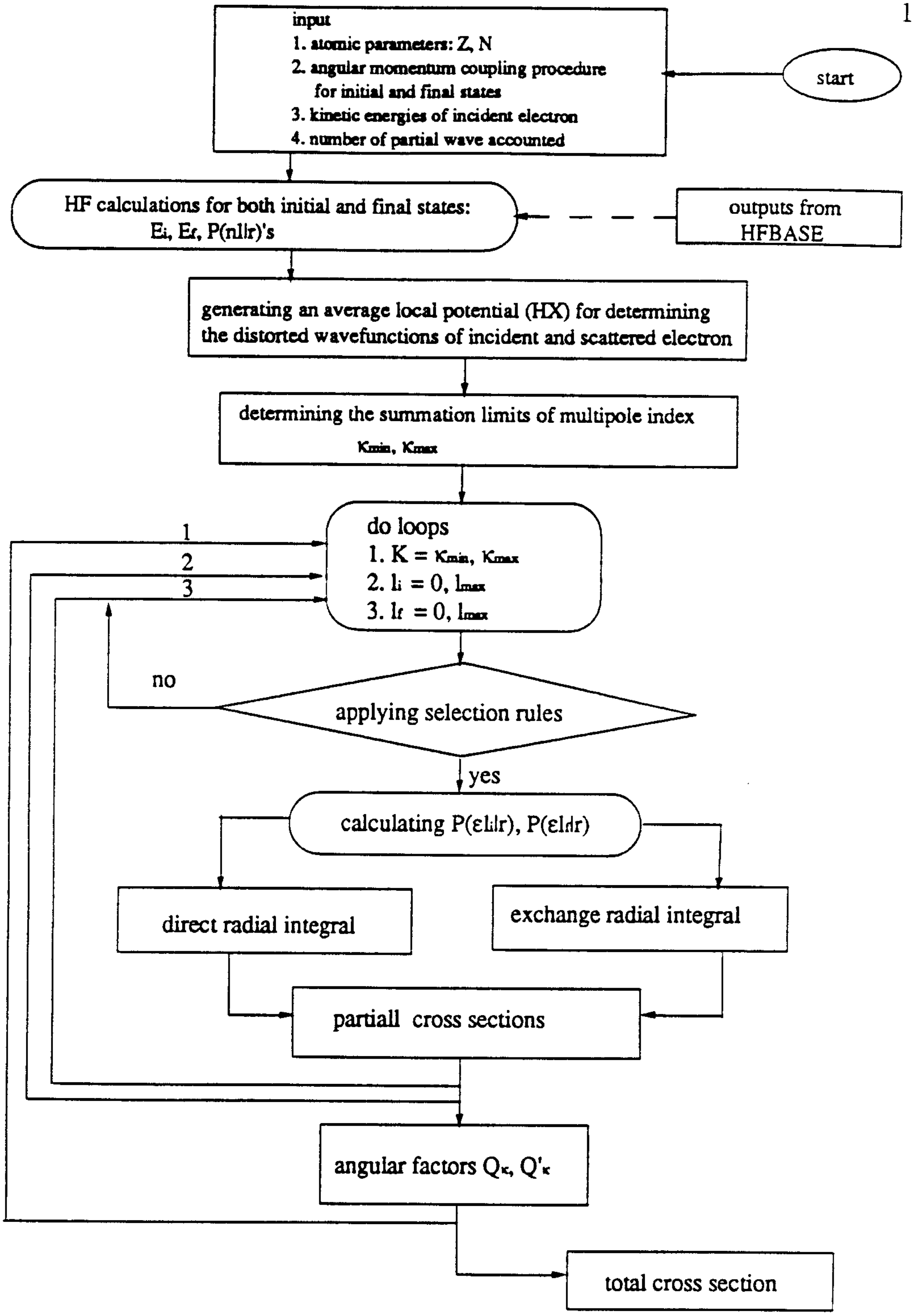

Figure 2.21: Flow diagram of DW calculation code -- EACOLL

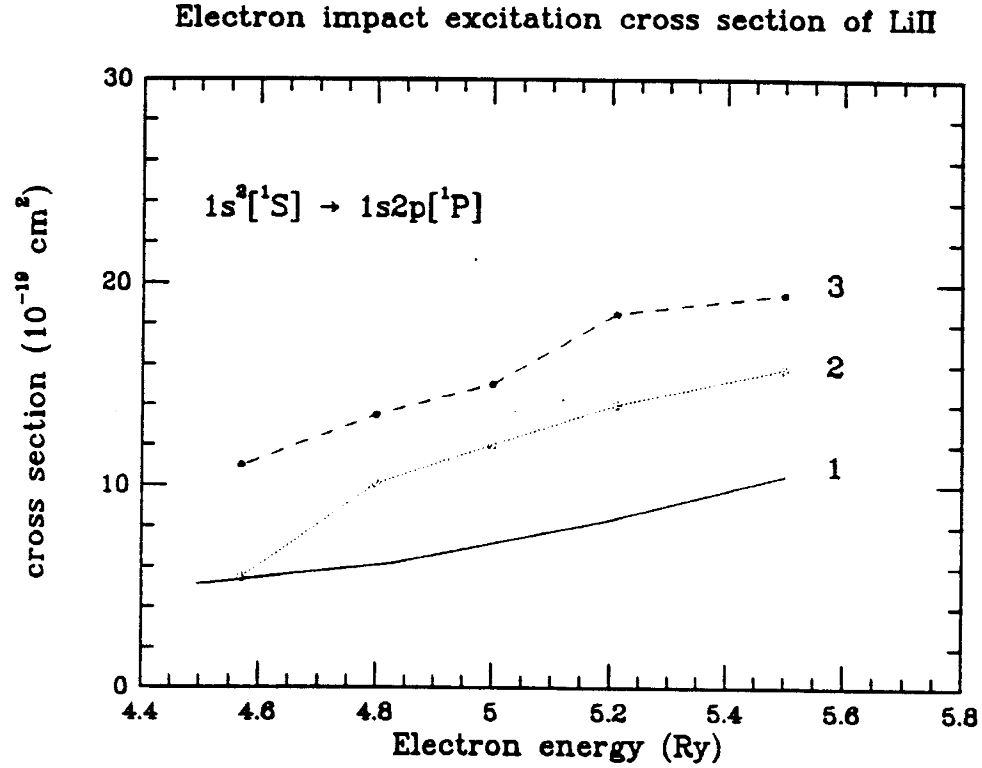

Figure 2.22: Electron impact excitation cross section of LiII. Curve 1: this work; Curve 2: Cristensen *et al.*; Curve 3: Wyngaarden *et al.*.

Born Approximation

For very high electron energies, the scattering potential may be treated as a small perturbation. The scattered electron then has a plane-wave form in both the incident and the outgoing channels. Assuming

$$P(kl|r) = 2krj_l(kr) \tag{2.214}$$

then the first Born cross section can be expressed as [79]

$$\sigma^B_{a_o a} = \frac{8}{(2l_o+1)k_i^2} \sum_\kappa Q_\kappa(a_o,a) \int_{k_i-k_f}^{k_i+k_f} [R_\kappa(q)]^2 \frac{dq}{q^3} \pi a_o^2 \tag{2.215}$$

where

$$R_\kappa(q) = \Pi(\kappa l_o l) \begin{pmatrix} \kappa & l_o & l \\ 0 & 0 & 0 \end{pmatrix} \int_0^\infty P(nl|r)P(n_o l_o|r)[j_\kappa(qr) - \delta_{\kappa 0}]dr$$

$$q^2 = k_i^2 + k_f^2 - 2k_i k_f cos\theta \tag{2.216}$$

and

$$j_l(x) = \sqrt{\frac{\pi}{2x}} J_{l+1/2}(x) \tag{2.217}$$

is a spherical Bessel function of the first kind,

$$\begin{aligned} j_o(x) &= \frac{sinx}{x} \\ j_1(x) &= \frac{sinx}{x^2} - \frac{cosx}{x} \\ j_{l+1}(x) &= (2l+1)\frac{j_l(x)}{x} - j_{l-1}(x) \end{aligned} \tag{2.218}$$

The general Born approximation is totally inadequate for the intercombination transitions ($\Delta S = 1$) because of the omission of the exchange interaction. The corresponding generalization of the Born approximation, taking account of exchange interaction, is the Born-Oppenheimer approximation:[81] for $\Delta S = 1$,

$$\sigma_{a_o a} = \sum_{\kappa} Q''(a_o, a)\sigma''_{\kappa}(l_o, l) \tag{2.219}$$

$$\sigma''_{\kappa}(l_o l) = \frac{4}{(2l_o+1)k_i^2}\pi a_0^2 \sum_{l_i l_f}(\sum_{\kappa'} R^e_{\kappa'\kappa})^2 \tag{2.220}$$

$$\begin{aligned} R^e_{\kappa'\kappa} &= (-1)^{\kappa+\kappa}\Pi(\kappa l_o l l_i l_f) \\ & \begin{pmatrix} \kappa' & l_o & l_f \\ 0 & 0 & 0 \end{pmatrix} \begin{pmatrix} \kappa' & l_i & l \\ 0 & 0 & 0 \end{pmatrix} \begin{Bmatrix} \kappa' & l_o & l_f \\ \kappa & l_i & l \end{Bmatrix} \\ &\times\ 2\int\int P(n_o l_o|r_2)\tilde{P}(k_i l_i|r_1)\frac{r_<^{\kappa'}}{r_>^{\kappa'+1}}\tilde{P}(k_f l_f|r_2)P(nl|r_1)dr_1 dr_2 \end{aligned} \tag{2.221}$$

where $\tilde{P}(kl|r)$ is a modified radial function of $P(kl|r)$ to ensure the orthogonality,

$$\tilde{P}(k_i l_i|r) = P(k_i l_i|r) - < P(k_i l_i|r)|P(nl|r) > \cdot P(nl|r)\delta_{ll_i}$$

$$\tilde{P}(k_f l_f|r) = P(k_f l_f|r) - < P(k_f l_f|r)|P(n_o l_o|r) > \cdot P(n_o l_o|r)\delta_{l_o l_f} \tag{2.222}$$

The Born method provides a sufficiently accurate qualitative description of electron collisional excitation cross sections, and usually does not lead to large quantative disagreements with experimental data. For many types of transitions from the ground state, an over estimate of the maximum cross section by a factor of 2 is typical. A comparison of Born approximation results and the CC calculation[79] for the transition $3s-3p$ and $3s-4p$ of Na atom is shown in Figure 2.23.

Semiclassical Impact Parameter Method (SCI)

The semiclassical impact parameter method for the calculation of electron collisional excitation cross section was developed by Burgess *et al.* [82]. This method expresses the excitation cross section for optically allowed transitions as

$$\sigma_{ij} = \frac{4\pi}{\sqrt{3}} \frac{f_{ij}}{k_i^2 \Delta E_{ij}} \bar{g} (\pi a_o^2) \tag{2.223}$$

where f_{ij} is the electric dipole oscillator strength, and $\bar{g}$ is the effective Gaunt factor. A general expression for $\bar{g}$ is[82]

$$\begin{aligned} \bar{g}(\xi, \delta_o) &= \frac{\sqrt{3}}{\pi} Y(\xi, \delta_o) \\ &= \frac{\sqrt{3}}{\pi} e^{\pi\xi} |K_{i\xi}(\delta+\xi) K'_{i\xi}(\delta+\xi)| (\delta+\xi) \end{aligned} \tag{2.224}$$

where

$$\xi = z \left| \frac{1}{k_i} - \frac{1}{k_f} \right| = z \left| \frac{1}{\sqrt{2\varepsilon_i}} - \frac{1}{\sqrt{2(\varepsilon_i - \Delta E_{ij})}} \right|$$

$$\delta_o = |\sqrt{2\varepsilon_i} - \sqrt{2(\varepsilon_i - \Delta E_{ij})}| \bar{R}_o \tag{2.225}$$

The quantity $\bar{R}_o$, the lowest allowed value for the impact parameter, can be estimated from

$$\bar{R}_o = \frac{[3\nu_{nl} - l(l+1)]}{2z^*} \tag{2.226}$$

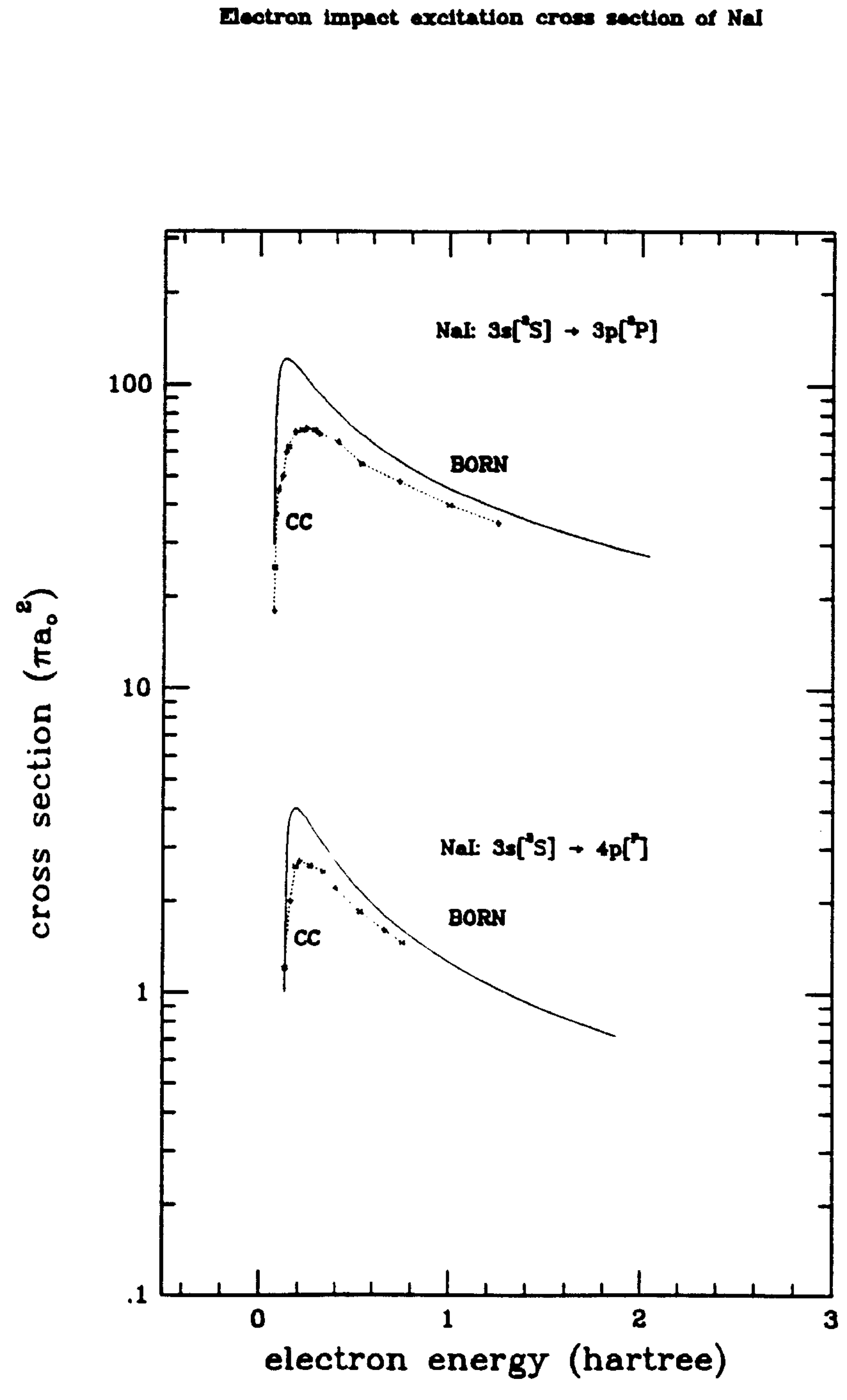

Figure 2.23: Electron impact excitation cross sections for NaI

and

$$K_{i\xi}(\xi+\delta_o)=\int_0^{\infty} exp[-(\xi+\delta_o)cosh(t)]cos(\xi t)dt \qquad (2.227)$$

$$K'_{i\xi}(\xi+\delta_o)=-\int_0^{\infty} cosh(t)cos(\xi t)exp[-(\xi+\delta_o)cosh(t)]dt$$

are the modified Bessel function and its derivative.

The expression in Eq.(2.223) for excitation cross section is restricted to dipole allowed excitations and could usually be accurate to about a factor of two. A comparison of the calculation results of DW, Born and SCI methods is shown in Figure 2.24. It can be seen that except in the threshold the results of all three calculations are within a factor of two.

Of the three approximations discussed above, the distorted wave method has the best accuracy. However it is very time consuming compared to the Born and SCI methods. In practical applications for the collisional-radiative equilibrium calculations, the enormous amount of relevant transitions needed to determine the level populations does not enable a direct application of the commonly used DW method due to computer time limitations. A general way to cope with this problem is that we compute the excitation cross sections with DW method only for the important resonant transitions from the ground state to the higher levels, while the cross sections for the less important transitions are approximated by the SCI model or the Born calculation.

The cross section σ is related to the collision strength as

$$\sigma_{ij}=\frac{\Omega_{ij}}{g_i k_i^2}(\pi a_o^2), \qquad (2.228)$$

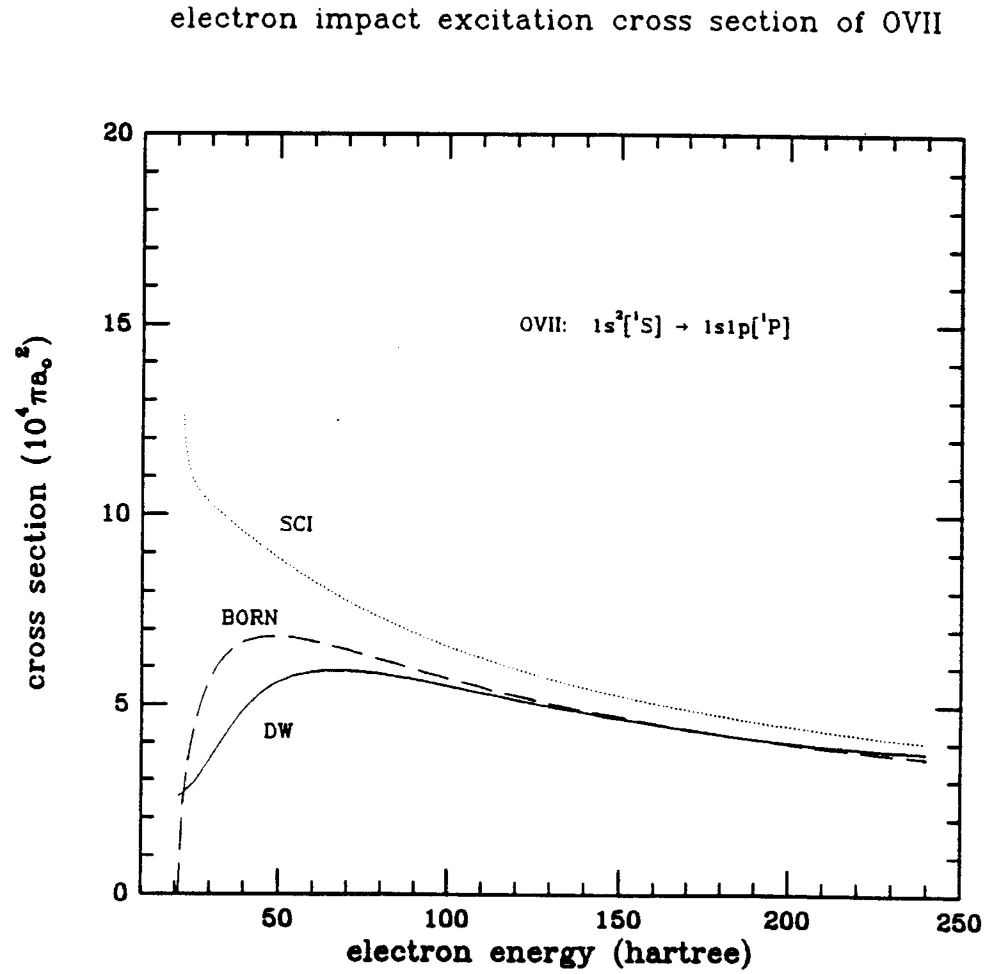

Figure 2.24: A comparison of DW, Born and SCI calculations

For practical applications the quantity of interest is the Maxwellian average collision strength, given by

$$\Gamma(T) = \int_{\Delta E_{ij}}^{\infty} \Omega_{ij}(\varepsilon_i) e^{-\varepsilon_i/T} d(\varepsilon_i/T) \tag{2.229}$$

Finally, the excitation rate coefficient is given by

$$Q_{ij}(T) = \frac{2.733 \times 10^{-11}}{g_i\sqrt{T}} \Gamma(T)\, (cm^3.sec^{-1}) \tag{2.230}$$

with T in hartree.

From detailed balance it follows that the deexcitation rate coefficient is given as

$$Q_{ji}(T) = Q_{ij}(T) \frac{g_i}{g_j} e^{\Delta E_{ij}/T} \tag{2.231}$$

2.3.2 Electron Collisional Ionization And Recombination

It is not difficult to generalize the calculation formulae for the collisional excitation cross section discussed in the last section to transitions for which the initial or the final state of the target ion belongs to the continuum, i.e., electron collisional ionization and recombination. Here, we discuss the two most commonly used methods: Born approximation and an empirical procedure suggested by Burgess *et al.*[83]

Born Approximation

In this case the final state a belongs to the continuum: $a = a_i \varepsilon l LSJ$, where a_i is the state of the ion, and ε is the energy of ejected electron. If the continuum radial function $P(\varepsilon l|r)$ is normalized to $\delta(\varepsilon - \varepsilon')$, the differential ionization cross section is[79]

$$\frac{d\sigma^i(a_o, a_i\varepsilon l)}{d\varepsilon} = \frac{8}{(2l_o+1)k_i^2}\sum_{\kappa} Q_\kappa \int_{k_i-k_f}^{k_i+k_f} [R_\kappa(q)]^2 \frac{dq}{q^3}(\pi a_o^2) \qquad (2.232)$$

The radial integral R_κ can be calculated according to Eq.(2.216) with the function $P(\varepsilon l|r)$ in place of $P(nl|r)$. For applications, the total ionization cross section is required:

$$\begin{aligned} \sigma^i(a_o, a_i) &= \sum_{LSJl\kappa} \int_0^{\varepsilon_i - I_z} \frac{d\sigma^i(a_o, a_i\varepsilon l)}{d\varepsilon} d\varepsilon \\ &= \frac{8Q_i}{(2l_o+1)k_i^2}\sum_{l\kappa} \int_0^{\varepsilon_i - I_z} d\varepsilon \int_{k_i-k_f}^{k_i+k_f} [R_\kappa(q)]^2 \frac{dq}{q^3}(\pi a_o^2) \end{aligned} \qquad (2.233)$$

where

$$Q_i = \sum_{LSJ} Q_\kappa(a_o, a)$$

does not depend on κ, and I_z is the ionization energy of the target ion.

The Empirical Procedure

In collisional-radiative equilibrium calculations, for plasma near to ionization balance, ionization cross sections mainly near to threshold are required and the formula due to Seaton[84] has been widely used. However, for rapidly evolving non-equilibrium plasma, cross sections well above threshold may be required and formulations such as that of Lotz[85] may then be more appropriate. Based on more newly available cross-beam experimental data, Burgess *et al.*[83] suggested a new empirical formula which takes account of inner-shell excitation and autoionization. This empirical formula of simple functional form similar to that of Lotz has been shown to be capable of representing a wide range of cross-beam experimental data to a good accuracy.

For incident electron energy ε_i, the Burgess formula for the ionization cross section is

$$\sigma^i(\varepsilon_i) = C \sum_j \xi_j (\frac{1}{2I_j})^2 (\frac{I_j}{\varepsilon_i}) ln(\frac{\varepsilon_i}{I_j}) W(\frac{\varepsilon_i}{I_j})\, (\pi a_o^2) \qquad (2.234)$$

where the summation is over subshells j of the target ion, ξ_j is the effective number of electrons in j, I_j is the effective ionization energy of j (this may differ from the real ionization energy because of autoionization effects), C is a fitting parameter and may be taken as 2.3 in general. The function $W(\varepsilon/I)$ represents approximately the deviation from linear behavior in the threshold neighborhood, and is given by

$$W(\varepsilon_i/I_j) = \begin{cases} 0 & \text{if } \varepsilon_i \le I_j \\ ln(\varepsilon_i/I_j)^{\beta I_j/\varepsilon_i} & \text{if } \varepsilon_i > I_j \end{cases} \qquad (2.235)$$

with

$$\beta = \frac{1}{4}\{[\frac{(100z+91)}{(4z+3)}]^{1/2} - 5\}$$

W has a significant effect only for small z and ε_i very near threshold.

To take into account the autoionization contributions, we need to follow the following procedure for the assignment of ξ_j and I_j:

(1) for the outer-shells, ξ_j is the actual number of electrons of the shell, and I_j is the real ionization energy;

(2) for the inner-shells, if the lowest configuration obtainable by excitation of an electron of the subshell lies above the outer-shell ionization threshold, ξ_j is the actual number of electrons in the shell and I_j is set equal to the excitation energy of the lowest autoionization state reachable.

(3) if the lowest configuration obtainable by excitation of an electron of the jth subshell lies below the outer shell ionization threshold, I_j is set equal to the outer shell ionization energy.

A comparison of the total ionization cross sections from Burgess's formula and the experimental data is shown in Figure 2.25.

For the Maxwellian velocity distribution, to a good approximation, the corresponding ionization rate coefficient can be written as

$$Q^I(T) = 2.1715 \times 10^{-8} C \sum_j \xi_j (\frac{1}{2I_j})^{3/2} (\frac{I_j}{T})^{1/2} E_1(I_j/T) w \, (cm^3.sec^{-1}) \tag{2.236}$$

where $E_1(x)$ is the first exponential integral, and

$$w = [ln(1 + \frac{T}{I_j})]^{\beta/(1+T/I_j)}$$

From detail balance, it follows that the 3-body recombination rate coef-

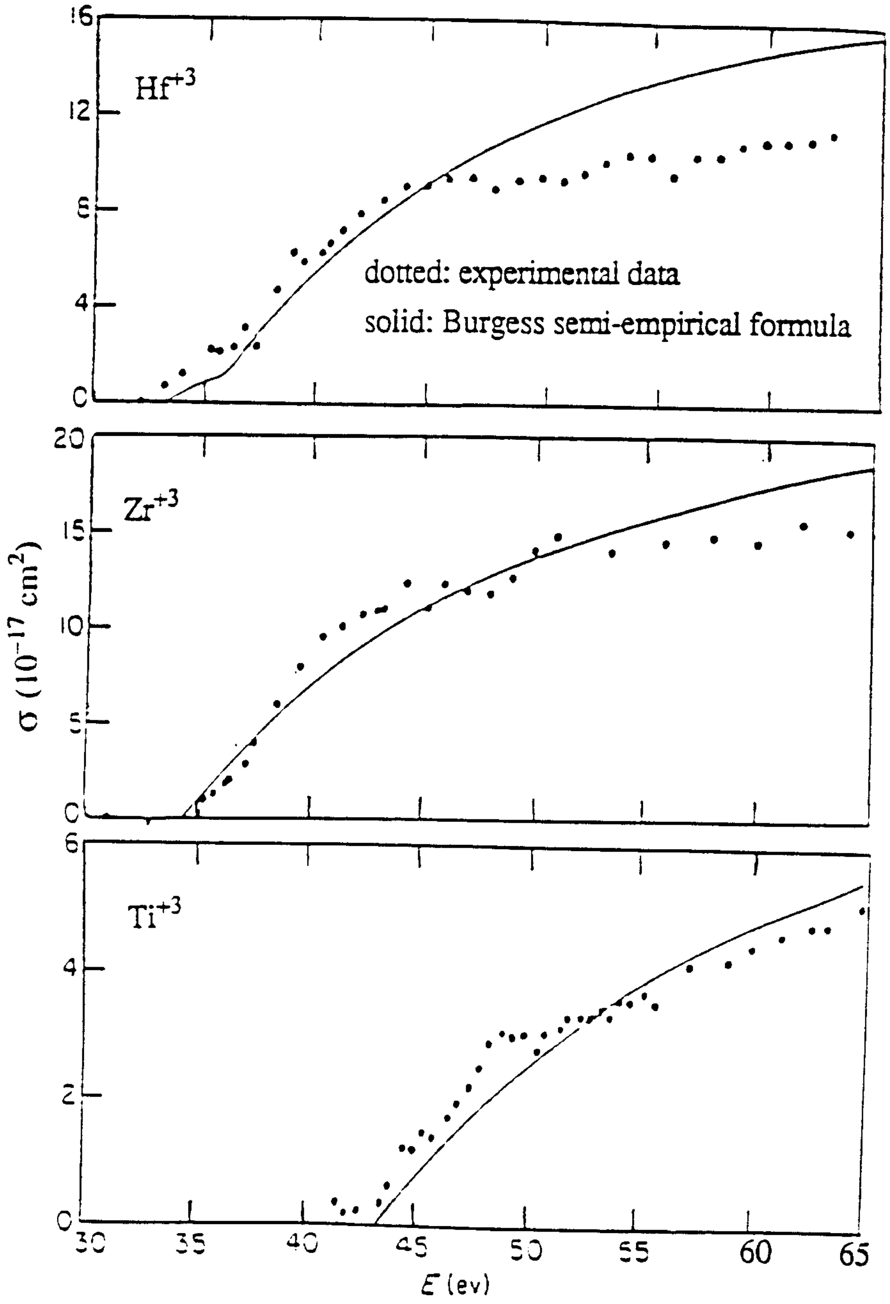

Figure 2.25: Electron impact ionization cross sections for Ti^{+3}, Zr^{+3}, Hf^{+3}

ficient is given by

$$Q^{3R}(T) = Q^{I}(T)\frac{g_k}{g_o^{+}}e^{I_k/T} \tag{2.237}$$

2.3.3 Proton Collisional Excitation And Ionization

The most commonly used method of calculation for the total cross section of excitation and ionization of ions by high energy heavy projectiles (P, He, *etc.*) is based upon the plane-wave Born approximation (PWBA). In the limit of high impact energies the Born collision cross sections are the same for protons and electrons with the same incident velocity[86].

For excitation, we have

$$\sigma^{B}_{a_o a} = \frac{8}{(2l_o + 1)k_i^2}\sum_{\kappa} Q_{\kappa}(a_o, a)\int_{k_i - k_f}^{k_i + k_f}[R_{\kappa}(q)]^2\frac{dq}{q^3}\pi a_o^2 \tag{2.238}$$

where

$$R_{\kappa}(q) = \Pi(\kappa l_o l)\begin{pmatrix} \kappa & l_o & l \\ 0 & 0 & 0 \end{pmatrix}\int_0^{\infty} P(nl|r)P(n_o l_o|r)[j_{\kappa}(qr) - \delta_{\kappa 0}]dr$$

$$q^2 = k_i^2 + k_f^2 - 2k_i k_f cos\theta \tag{2.239}$$

k_i and k_f here are the momenta of the incident and outgoing proton, respectively:

$$\begin{aligned} k_i^2 &= \frac{2\varepsilon_i}{1836} \\ k_f^2 &= k_i^2 - \frac{2\Delta E_{aa_o}}{1836} \end{aligned} \tag{2.240}$$

For ionization, we have exactly the same formulae as those for electron impact:

$$\begin{aligned}\sigma^i(a_o, a_i) &= \sum_{LSJl\kappa} \int_0^{\varepsilon_i - I_z} \frac{d\sigma^i(a_o, a_i\varepsilon l)}{d\varepsilon} d\varepsilon \qquad (2.241)\\ &= \frac{8Q_i}{(2l_o+1)k_i^2} \sum_{l\kappa} \int_0^{\varepsilon_i - I_z} d\varepsilon \int_{k_i - k_f}^{k_i + k_f} [R_\kappa(q)]^2 \frac{dq}{q^3} (\pi a_o^2)\end{aligned}$$

but with k_i and k_f defined by Eq.(1.240).

In our calculations, the Hartree-Fock wavefunctions are used for all the initial and final bound states, together with a distorted continuum wavefunction for the ejected electron in the ionization case. In Figure 2.26 - 2.27, we show some of our calculational results and compare them with the available experimental data[112]. From a systematic viewpoint, the PWBA calculation can be accurate to a factor of 1.5 - 2 or better at high projectile velocities.

Finally, we conclude this chapter with a summary of our atomic data calculation package in Figure 2.28.

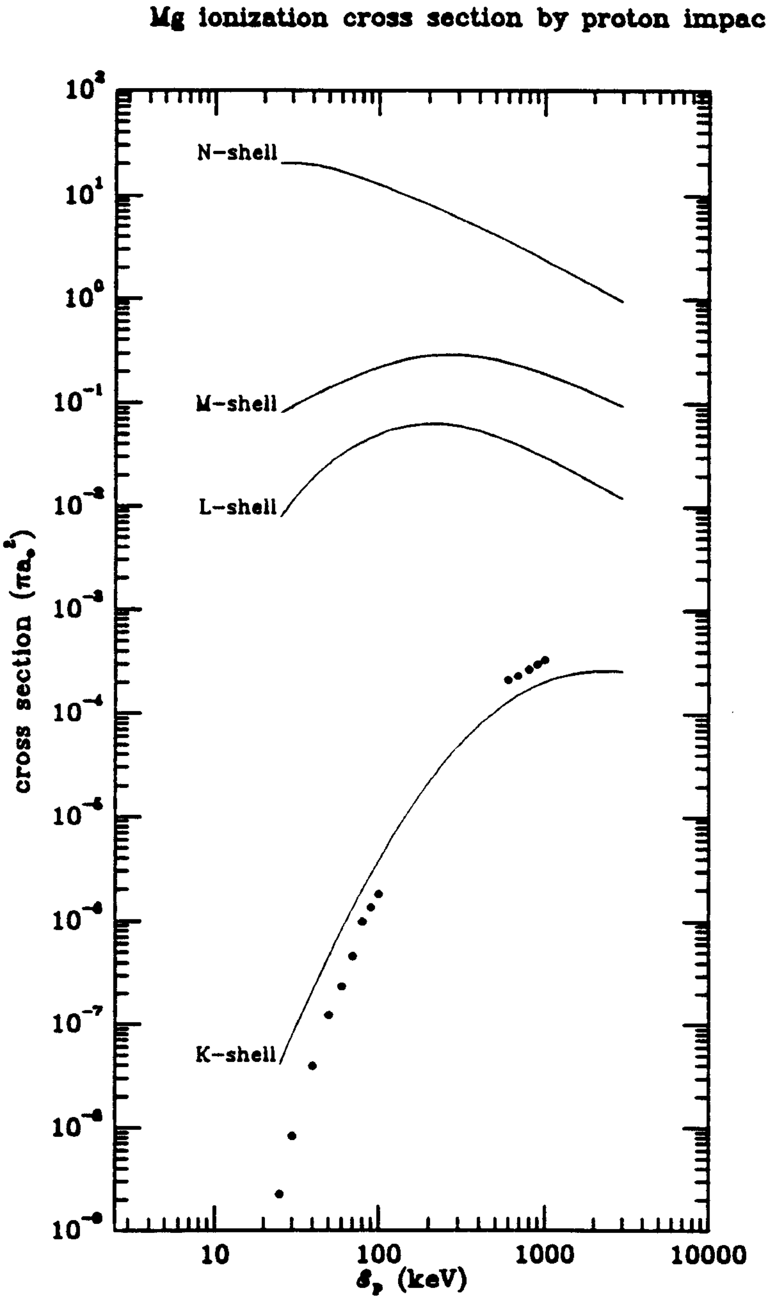

Figure 2.26: Subshell ionization cross section of MgI by proton impact

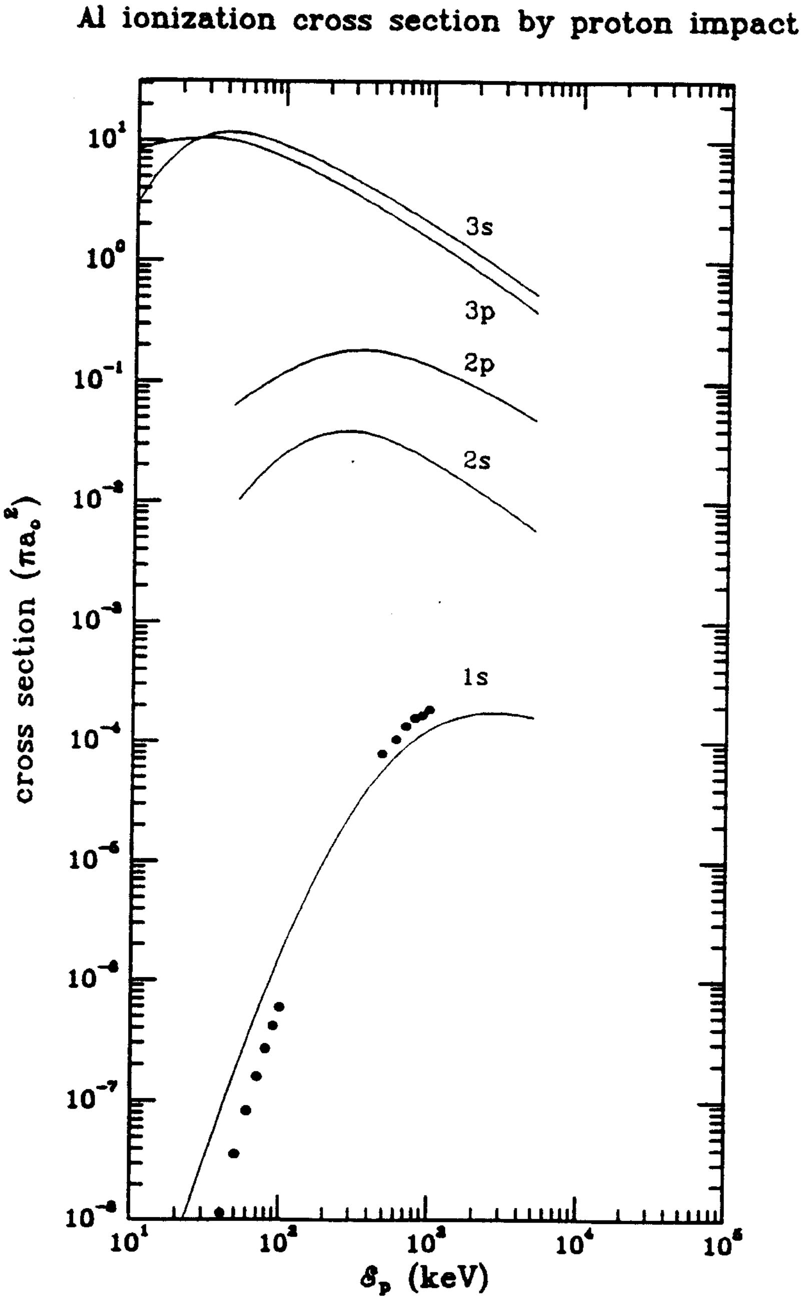

Figure 2.27: Subshell ionization cross section of AlI by proton impact

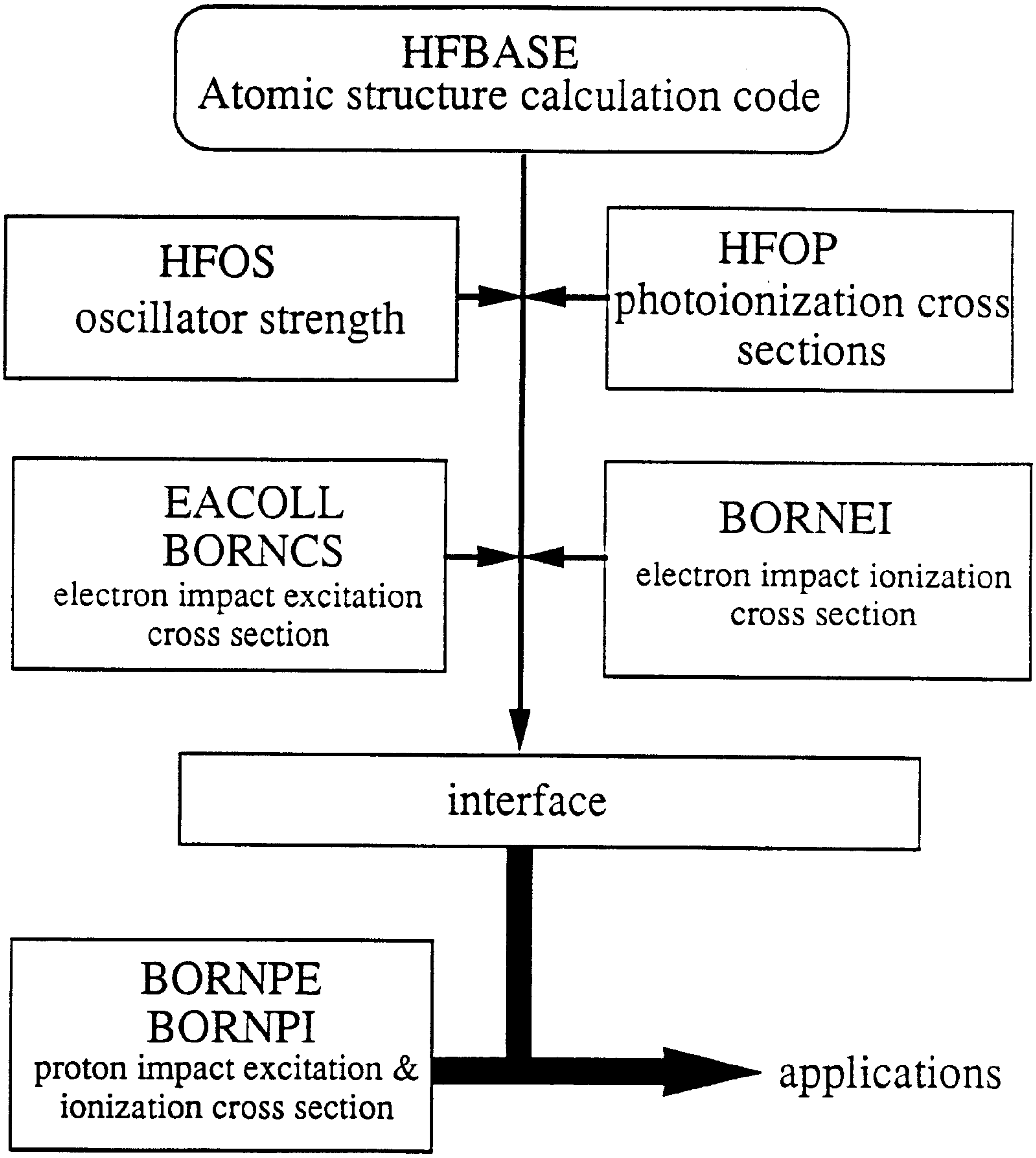

Figure 2.28: A summary of the atomic data calculation package

Chapter 3

Aluminum Plasma Kα Satellite Spectra Analysis

3.1 Introduction

The process of intense particle beam-target interaction, which is essential in inertial confinement fusion systems, has been studied by using an extensive variety of diagnostics[90, 91, 92, 93]. With present-day beam-power densities [5, 93], target temperature of about 30 eV can be reached. At such temperatures thermal ionization of the L(n=2) shell of intermediate-Z elements such as aluminum takes place. It has been suggested[95] that the spectrum of Kα satellite lines which are emitted under such conditions can be used as a temperature diagnostic.

A basic property of the interaction of charged particles with matter is the production of K-shell ionization, which is accompanied by the emission of Kα x-radiation. The transition energy for the Kα transition (1s-2p) is sensitive to the number of electrons populating the L shell, because of the differences in shielding by different L-shell populations. In Table 3.1 we present the Kα transition energies for carbon and aluminum, which are calculated by using the single-configuration Hartree-Fock method. It has been shown by the experiments[5, 95] these Kα satellite lines can be straightforwardly resolved by plane-crystal spectrometry. Since Kα satellite lines are blue-shifted with respect to the normal Kα 1s-2p transition with increasing L-shell vacancies(or reducing the shielding effect), the Kα satellite spectra can give information on the distribution of ionization state in the plasma, and thus on the plasma temperature. In such cases, a temperature measurement is possible through the detailed analysis of the Kα satellite spectra.

Recently, a Kα satellite spectrum from an aluminum target heated by an intense proton beam was observed in the PBFAII(Particle Beam Fusion Accelerator II) at Sandia National Laboratories[5]. The typical experimental conditions are presented in Figure 3.1, and the corresponding physical processes involved are shown in Figure 3.2. The experimental spectrum is given in Figure 3.3. In this chapter, we give detailed analysis for the Kα satellite spectrum. First, we perform the multi-configuration Hartree-Fock calculations with relativistic corrections to identify the term-dependent satel-

Table 3.1: Kα Transition Energies For Carbon and Aluminum

Ions	Transitions	Transition energy (eV)	Wavelength (A)
AlII	$1s^{1}2s^{2}2p^{6}3s^{2}3p^{1} - 1s^{2}2s^{2}2p^{5}3s^{2}3p^{1}$	1484.995	8.347
AlIII	$1s^{1}2s^{2}2p^{6}3s^{2} - 1s^{2}2s^{2}2p^{5}3s^{2}$	1485.351	8.345
AlIV	$1s^{1}2s^{2}2p^{6}3s^{1} - 1s^{2}2s^{2}2p^{5}3s^{1}$	1485.885	8.342
AlV	$1s^{1}2s^{2}2p^{6} - 1s^{2}2s^{2}2p^{5}$	1486.955	8.336
AlVI	$1s^{1}2s^{2}2p^{5} - 1s^{2}2s^{2}2p^{4}$	1497.373	8.278
AlVII	$1s^{1}2s^{2}2p^{4} - 1s^{2}2s^{2}2p^{3}$	1509.408	8.212
AlVIII	$1s^{1}2s^{2}2p^{3} - 1s^{2}2s^{2}2p^{2}$	1523.133	8.138
AlIX	$1s^{1}2s^{2}2p^{2} - 1s^{2}2s^{2}2p^{1}$	1538.254	8.058
AlX	$1s^{1}2s^{2}2p^{1} - 1s^{2}2s^{2}$	1554.619	7.973
CII	$1s^{1}2s^{2}2p^{2} - 1s^{2}2s^{2}2p^{1}$	286.9272	43.20
CIII	$1s^{1}2s^{2}2p^{1} - 1s^{2}2s^{2}$	291.6531	42.50
CIV	$1s^{1}2s^{1}2p^{1} - 1s^{2}2s^{1}$	296.2537	41.84
CV	$1s^{1}2p^{1} - 1s^{2}$	304.1780	40.75

lite lines accurately. Then a thin plasma collisional-radiative equilibrium (CRE) model is used to generate a theoretical Kα satellite spectrum. This calculated spectrum is compared with the experimental result and that of non-LTE radiation transport model[96]. Finally, we discuss the importance of line opacity in the interpretation of Kα spectra of light-ion beam heated plasma.

Typical Experimental Conditions

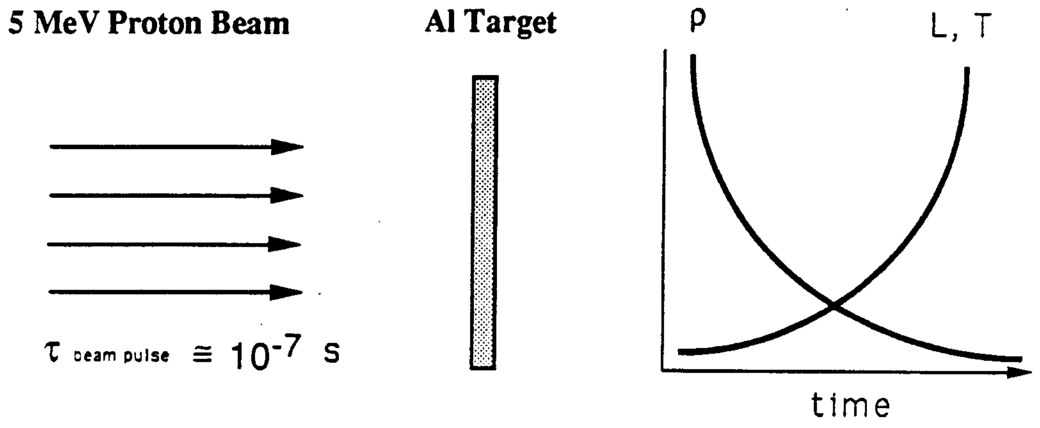

1. Plasma expand ≅ 100 times by the end of the beam pulse.
2. Target is primarily heated by proton collisions with outer shell electrons
3. Proton impact ionization of K-shell electrons results in Kα satellite lines

Figure 3.1: Typical experimental conditions in PBFA II

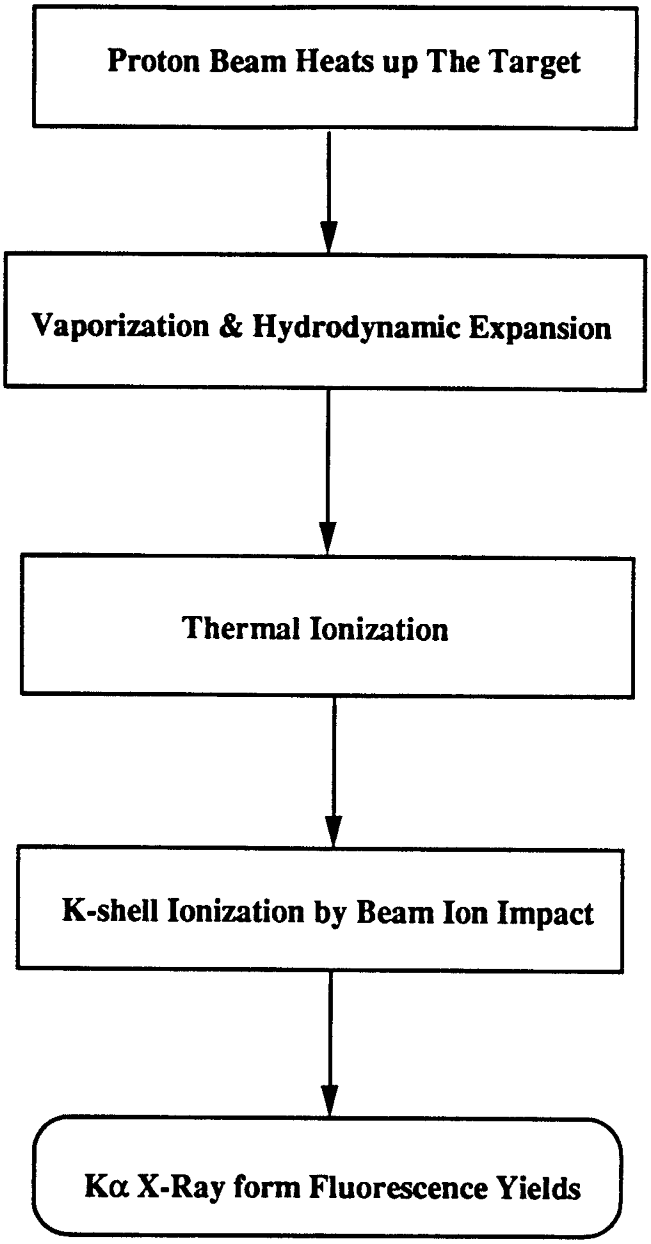

Figure 3.2: Physical processes of Kα x-ray satellites produced from a target heated by an intense proton beam.

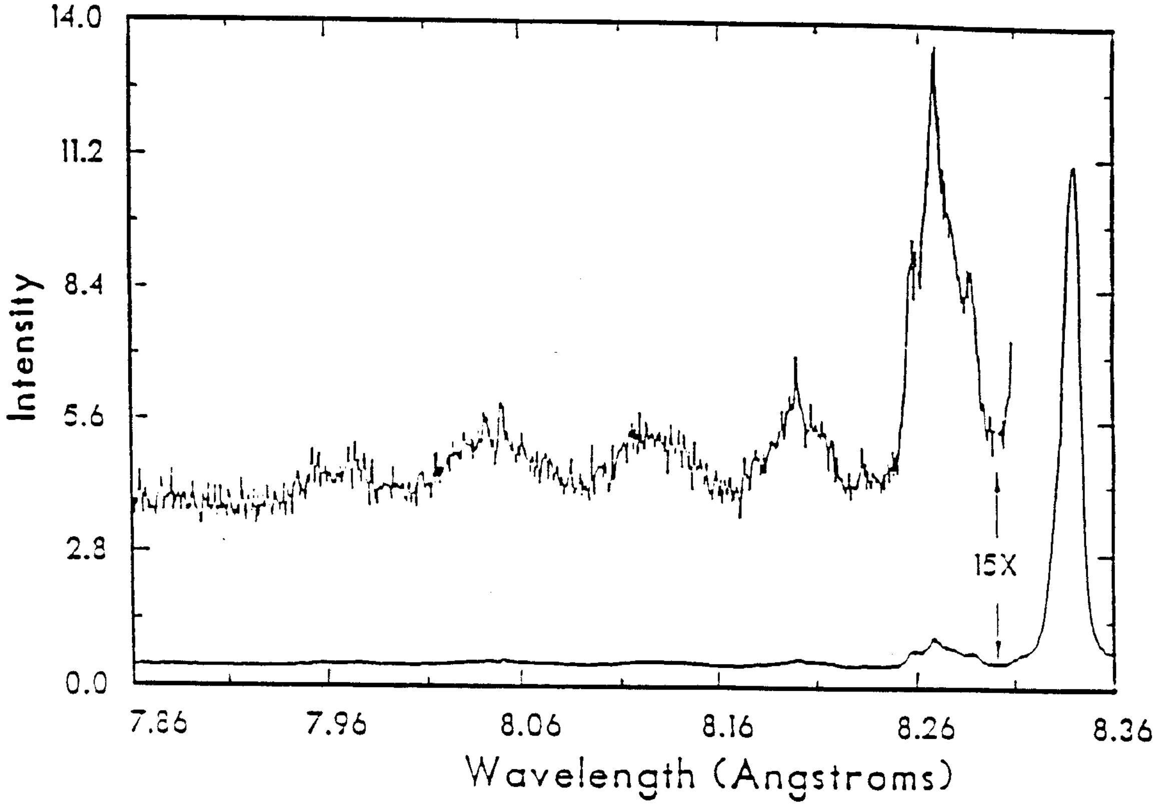

Figure 3.3: The experimental Kα spectrum

3.2 Satellite Line Identification

To be able to identify the individual lines in the Kα spectrum, the related atomic energy levels must be calculated to high accuracy.

In Figure 3.4 we present the single-configuration Hartree-Fock calculation Kα satellite line wavelengths and compare with the experimental spectrum. It is easy to see that the single-configuration Hartree-Fock calculation is sufficiently accurate to determine the main peaks of Kα transitions of ions with different ionization degree. Our calculation shows that the Kα satellite lines appearing in the experimental spectrum are from AlI to AlIX (ion stages before the beam induced inner-shell ionization). The Kα lines of AlI to AlIV are mixing together because of overlaps, while the Kα lines of AlV to AlIX are well resolved.

The experimental spectrum also shows a high degree of structure. Especially for F-like Al (AlV), three emission peaks are clearly seen. These structures come from the term-dependent transitions caused by the electrostatic splitting within the configurations. The calculation of the wavelengths of the individual term-dependent lines is difficult because this demands that the energy levels be calculated to better than one part in 3000. The accuracy of the single-configuration Hartree-Fock calculation is not sufficient to allow reliable term-dependent Kα line identifications. Since the transitions with K-shell electrons are involved and both relativistic and electronic corre-

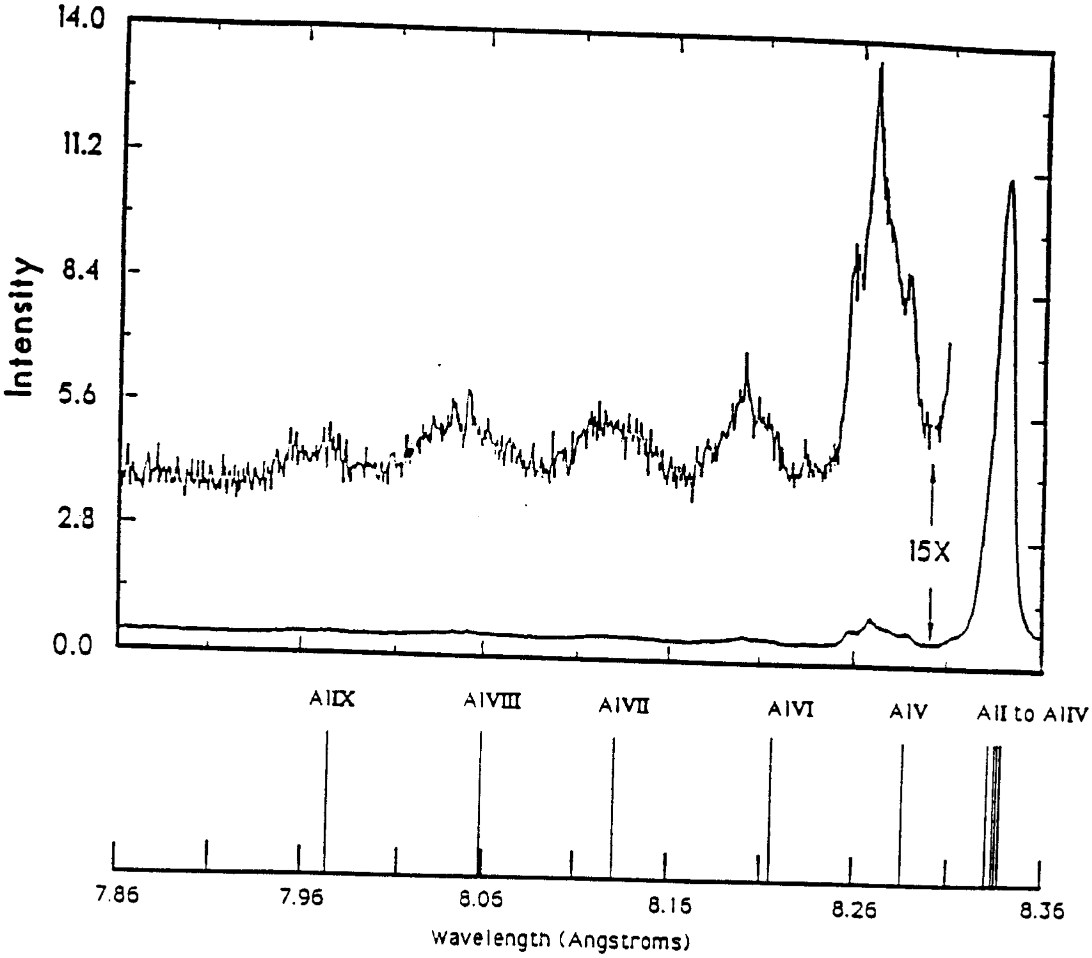

Figure 3.4: Kα line Identification with Hartree-Fock calculation

lation corrections are important, we have performed the multiconfiguration Hartree-Fock calculations with relativistic correction to determine the accurate atomic energy levels which are associated with the Kα transitions. We included at least 7 configurations for each level. The calculation results are presented in Table 3.2 and Table 3.3. Table 3.2 shows the energies of the atomic levels, while Table 3.3 shows the calculated wavelengths and compares with the peaks in Sandia experimental data[94]. Good agreement is achieved. Figure 3.5 is detail from the aluminum Kα satellite spectrum showing the AlV satellite. Our calculation shows that there are two lines contributing to the center peak of AlV Kα emission.

Our calculational results represent a significant improvement in accuracy over previous results presented in Bailey *et al.*[94], where wavelengths were determined from Herman-Skillman calculations (based on the Hartree-Fock-Slater model). The good agreement between our calculations and experimental data gives us confidence that we can determine which transitions are responsible for the peaks in the experimental emission spectra. This in turn means that plasma temperature in ion beam-heated targets can be determined more reliably.

Table 3.2: Energies of Kα atomic levels for Al

Ion	Configuration	Term	E_{mchf}	ΔE_{re}	$E_{tot}(2Ry)$
AlII	1s(1)2s(2)2p(6)3s(2)	^{2}S	-183.80137	-0.15891	-183.96028
	1s(2)2s(2)2p(5)3s(2)	^{2}P	-238.38741	-0.20861	-238.59602
AlIII	1s(1)2s(2)2p(6)3s(1)	^{1}S	-182.66834	-0.15789	-182.82623
		^{3}S	-182.67897	-0.15800	-182.83697
	1s(2)2s(2)2p(5)3s(1)	^{1}P	-237.23792	-0.20932	-237.44724
		^{3}P	-237.25841	-0.20937	-237.46778
AlIV	1s(1)2s(2)2p(6)	^{2}S	-181.03049	-0.15648	-181.18697
	1s(2)2s(2)2p(5)	^{2}P	-235.64703	-0.20806	-235.85509
AlV	1s(1)2s(2)2p(5)	^{1}P	-174.76074	-0.15601	-174.91675
		^{3}P	-175.02640	-0.15622	-175.18261
	1s(2)2s(2)2p(4)	^{1}S	-229.67681	-0.20769	-229.88450
		^{1}D	-229.86675	-0.20790	-230.07475
		^{3}P	-230.05752	-0.20780	-230.26531
	1s(1)2s(1)2p(6)	^{1}S	-173.42654	-0.14560	-173.57217
		^{3}S	-173.52542	-0.14610	-173.67151
	1s(2)2s(1)2p(5)	^{1}P	-227.92166	-0.19759	-228.11926
		^{3}P	-228.56012	-0.19835	-228.75847
AlVI	1s(1)2s(2)2p(4)	^{2}S	-167.03434	-0.15481	-167.18914
		^{2}D	-167.24941	-0.15505	-167.40445
		^{4}P	-167.60196	-0.15535	-167.75731
	1s(2)2s(2)2p(3)	^{2}P	-222.61890	-0.20704	-222.82594
		^{2}D	-222.81809	-0.20717	-223.02525
		^{4}S	-223.12157	-0.20738	-223.32894
AlVII	1s(1)2s(2)2p(3)	^{1}P	-157.72217	-0.152813	-157.87497
		^{1}D	-157.94252	-0.15300	-158.09552
		^{3}P	-158.01708	-0.15312	-158.17020
		^{3}D	-158.24069	-0.15330	-158.39399
		^{3}S	-158.12499	-0.15313	-158.27812
	1s(2)2s(2)2p(2)	^{1}S	-213.76244	-0.20538	-213.96781
		^{1}D	-214.01984	-0.20568	-214.22545
		^{3}P	-214.23553	-0.20577	-214.44130
AlVIII	1s(1)2s(2)2p(2)	^{2}S	-146.79065	-0.14983	-146.94048
		^{2}D	-147.14976	-0.15014	-147.3002
	1s(2)2s(2)2p(1)	^{2}P	-203.77520	-0.20327	-203.97850
AlIX	1s(1)2s(2)2p(1)	^{1}P	-134.35842	-0.14571	-134.50411
		^{3}P	-134.71062	-0.14612	-134.85674
	1s(2)2s(2)	^{1}S	-191.80689	-0.19975	-192.00664

Table 3.3: Calculated wavelengths of Ka transitions for Al

Ion	Initial State	Final State	Wavelength	Exp. data
AlII	1s(1)2s(2)2p(6)3s(2)	1s(2)2s(2)2p(5)3s(2)		
	2S	2P	8.3373	
AlIII	1s(1)2s(2)2p(6)3s(1)	1s(2)2s(2)2p(5)3s(1)		
	1S	1P	8.3395	≅8.340
	3S	3P	8.3380	
AlIV	1s(1)2s(2)2p(6)	1s(2)2s(2)2p(5)		
	2S	2P	8.3324	
AlV	1s(1)2s(2)2p(5)	1s(2)2s(2)2p(4)		
	1P	1S	8.2869	≅8.288
	1P	1D	8.2583	≅8.258
	3P	3P	8.2696	≅8.270
	1s(1)2s(1)2p(6)	1s(2)2s(1)2p(5)		
	1S	1P	8.3508	
	3S	3P	8.2690	
AlVI	1s(1)2s(2)2p(4)	1s(2)2s(2)2p(3)		
	2S	2P	8.1873	
	2D	2P	8.2191	
	2D	2D	8.1896	
	4P	4S	8.1970	≅8.202
AlVII	1s(1)2s(2)2p(3)	1s(2)2s(2)2p(2)		
	1P	1S	8.1207	
	1P	1D	8.0836	
	1D	1D	8.1153	
	3P	3P	8.0949	
	3S	3P	8.1105	
	3D	3P	8.1273	≅8.126
AlVIII	1s(1)2s(2)2p(2)	1s(2)2s(2)2p(1)		
	2S	2P	7.9861	
	2D	2P	8.0370	≅8.044
AlIX	1s(1)2s(2)2p(1)	1s(2)2s(2)		
	1P	1S	7.9216	
	(intercombination line) 3P	1S	7.9705	≅7.969

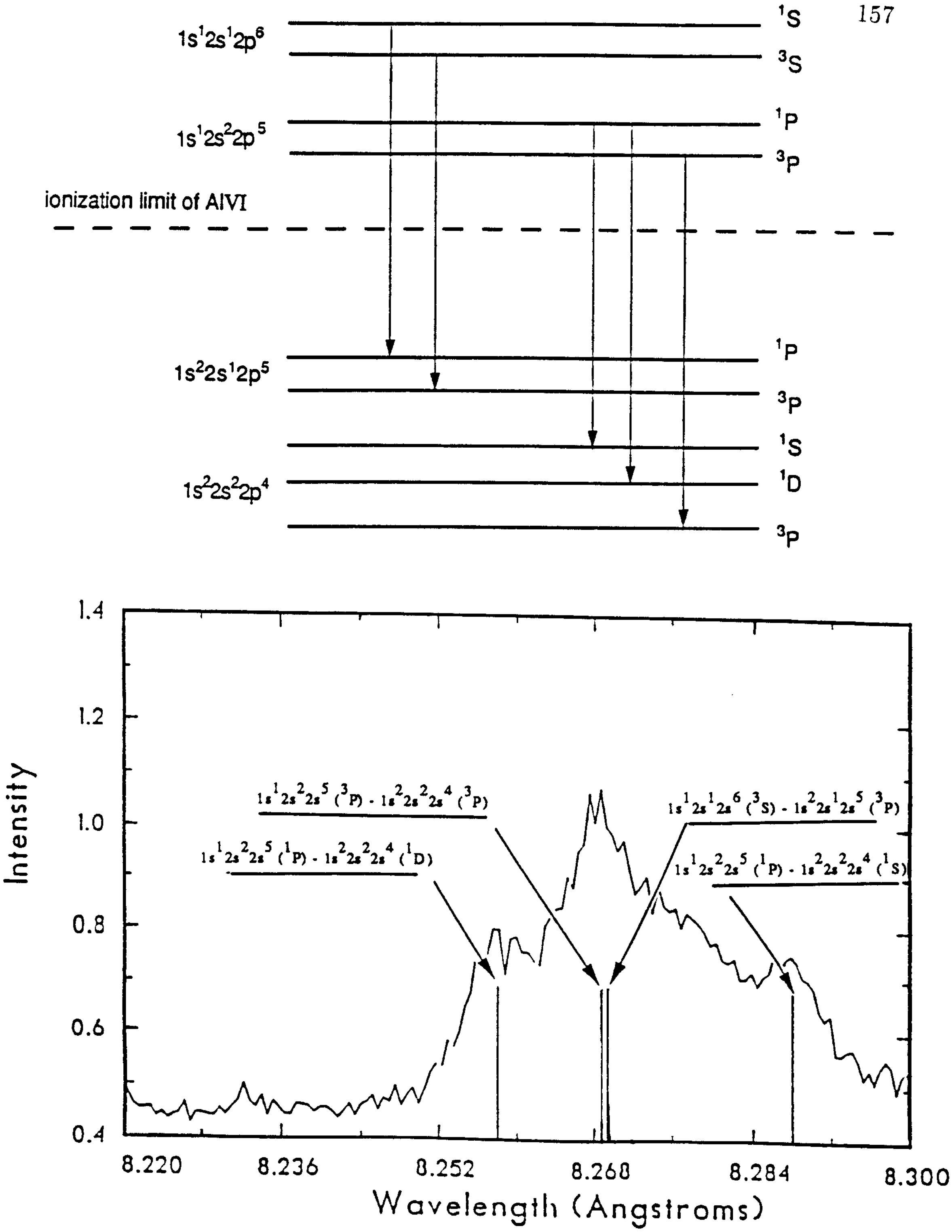

Figure 3.5: Detail Kα satellite of AlV

3.3 The Theoretical Kα Spectra

The calculation of a theoretical Kα spectrum consists of two steps:

1. determining the ionization distribution of the plasma and atomic level occupation numbers;
2. computing the individual Kα line intensity from fluorescence yield and the continuum background.

3.3.1 Ionization Distribution And Level Occupation Numbers

We have assumed a simple physical model for this preliminary study. The plasma is taken as a uniform isothermal slab. For the optically thin plasma calculations, the geometry of the plasma is not important because the radiation flux is proportional to the radiation intensity. A completely self-consistent collisional-radiative equilibrium model is used for determining the ionization distribution and level populations.

Consider a level i in an ion z, and let the number density (level population) be $N_{z,i}$. The rate of change of $N_{z,i}$ is determined by the rates of all the processes which populate and depopulate the level i:

$$\frac{dN_{z,i}}{dt} = \sum_{j\neq i} C_{ji} N_{z,j} - \sum_{j\neq i} C_{ij} N_{z,i} + \sum_{k} R_{ki}^{z+1} N_{z+1,k}$$

$$- \sum_k R_{ik}^z N_{z,i} + \sum_k I_{ki}^{z-1} N_{z-1,k} - \sum_k I_{ik}^z N_{z,i} \qquad (3.1)$$

where C_{ij} are the rate coefficients for the processes which populate level i from level j of the ion, R_{ik}^z are the recombination coefficients for ion z in level i to recombine an electron to the level k of ion z-1, and I_{ik}^z are the ionization rate coefficients for ion z in level i with the residual ion in level k.

For a complete calculation, all the atomic processes contributing to the population and depopulation of the levels should be included. These processes are: *(1) beam proton impact ionization; (2) beam proton impact excitation and deexcitation; (3) electron impact ionization and recombination; (4) electron impact excitation and deexcitation; (5) photoionization and radiative recombination; (6) photon stimulated excitation and radiation; (7) spontaneous decay; (8) dielectronic recombination and autoionization.* In our calculation, for an optically thin plasma, photoionization, photon stimulated excitation and deexcitation are omitted. Also, since the incident beam power is as high as 5 TW/cm^2, we expect that the plasma temperature should be high enough that electron impact processes dominate the proton impact processes except for the K-shell ionization. Hence, we include the following processes in our CRE calculation: (1) beam proton impact ionization; (2) electron impact ionization and recombination; (3) electron impact excitation and deexcitation; (4) radiative recombination; (5) dielectronic recombination; (6) spontaneous decay; (7) autoionization effect.

The calculations of the related rate coefficients have been discussed in the last chapter. The calculated proton impact ionization cross sections for each subshell of neutral Al are given in Figure 2.28. Note that the outer shell cross sections are substantially larger than the inner shell values. This tells us that the primary heating (*i.e.*, ion stopping) mechanism is the interaction of the proton beam with the outer shell electrons. Although K-shell ionization is not important to the heating of the plasma, it is the *only* mechanism of creating a K-shell hole for the plasma condition we are discussing. Hence the accuracy of the K-shell ionization cross section directly affects the accuracy of the calculated Kα spectrum. In Figure 3.6 we present the K-shell ionization cross sections by 5 MeV proton impact for aluminum ions. It can be seen that as the ionization stage of Al increases the cross sections decrease in an almost linear fashion. Our calculation indicates that the proton impact ionization cross section for K-shell electrons of AlII is about a factor of 2 higher than that of AlXIII.

With regard to the atomic level structure, all the ground states are included in addition to several low excitation states. Also included are those levels related to the Kα transitions. Totally there are 105 levels and 21 autoionization levels. Figure 3.7 shows the level structure for AlVI which is typical in our CRE calculation.

The ionization distribution from our CRE calculation for plasma with density $N_{ion} = 10^{20}\ cm^{-3}$ is shown in Figure 3.8. For such a plasma, the ionization stage +8 appears in the temperature range 40 eV — 60 eV.

3.3.2 Calculation of the Theoretical Kα Satellite Spectra

The Kα x-ray emissivity can be expressed as

$$\eta(\nu) = \sum_{z}\sum_{l}\sum_{k>l} N_{z,k} A_z(k;l) \phi_{z,kl}(\nu) \omega_z \tag{3.2}$$

where η is the emissivity in the units of $photon.cm^{-3}.sec^{-1}.Hz^{-1}$, l and k are the index of the levels related to the Kα transitions, $N_{z,k}$ is the number density of level k, $A_z(k;l)$ is the spontaneous decay rate from level k to level l of ion z, $\phi_{z,kl}(\nu)$ is the emission profile, and ω_z is the fluorescence yields of ion z. The oscillator strengths for all Kα transitions we are considering are given in Table 3.4. Also given are the corresponding fluorescence yields[96]. Using Eq.(3.2) and the values given in Table 3.4, we have calculated the emissivities for aluminum plasma at three different densities and temperatures. Figure 3.9 shows the Kα spectrum for an Al plasma at $T = 5\ eV$, $N_{ion} = 10^{20} cm^{-3}$. In this case, the plasma temperature is so low that only those Kα lines from low ionized ions (AlI–AlIV) are presented. For a plasma at $T = 20\ eV$, $N_{ion} = 10^{20} cm^{-3}$, the most abundent ion is AlV, the Kα peaks of AlV in the spectrum become the highest. In Figure 3.11 we show the Kα spectrum of an Al plasma at $T = 30\ eV$, $N_{ion} = 10^{20} cm^{-3}$. In this case, the thermal

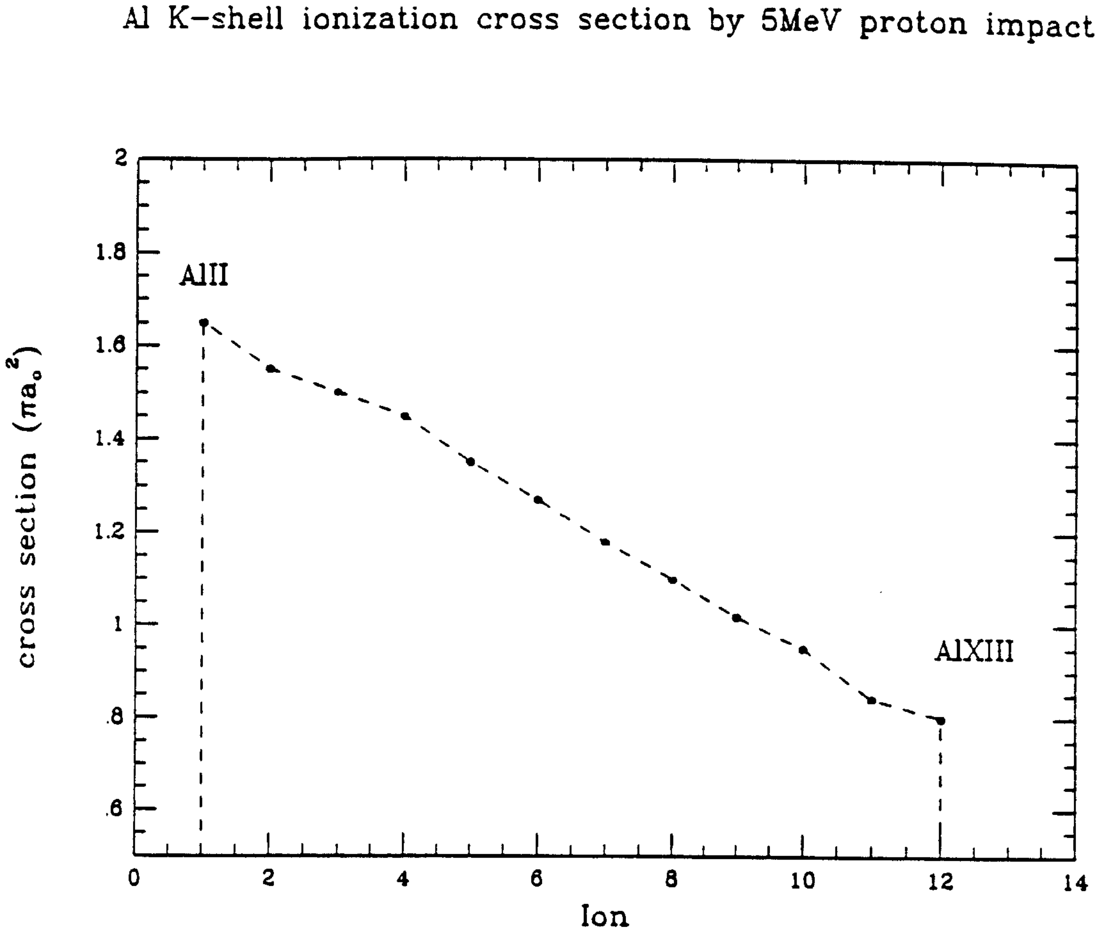

Al K-shell ionization cross section by 5MeV proton impact

Figure 3.6: 5MeV proton impact ionization cross section for K-shell electrons of Al

All the ground states are included in addition to several low excitation states. Also included in the model are all those levels related to the Kα transitions. Totally , there are 105 levels and 21 autoionization levels

Schematic of the level structure of AlVI

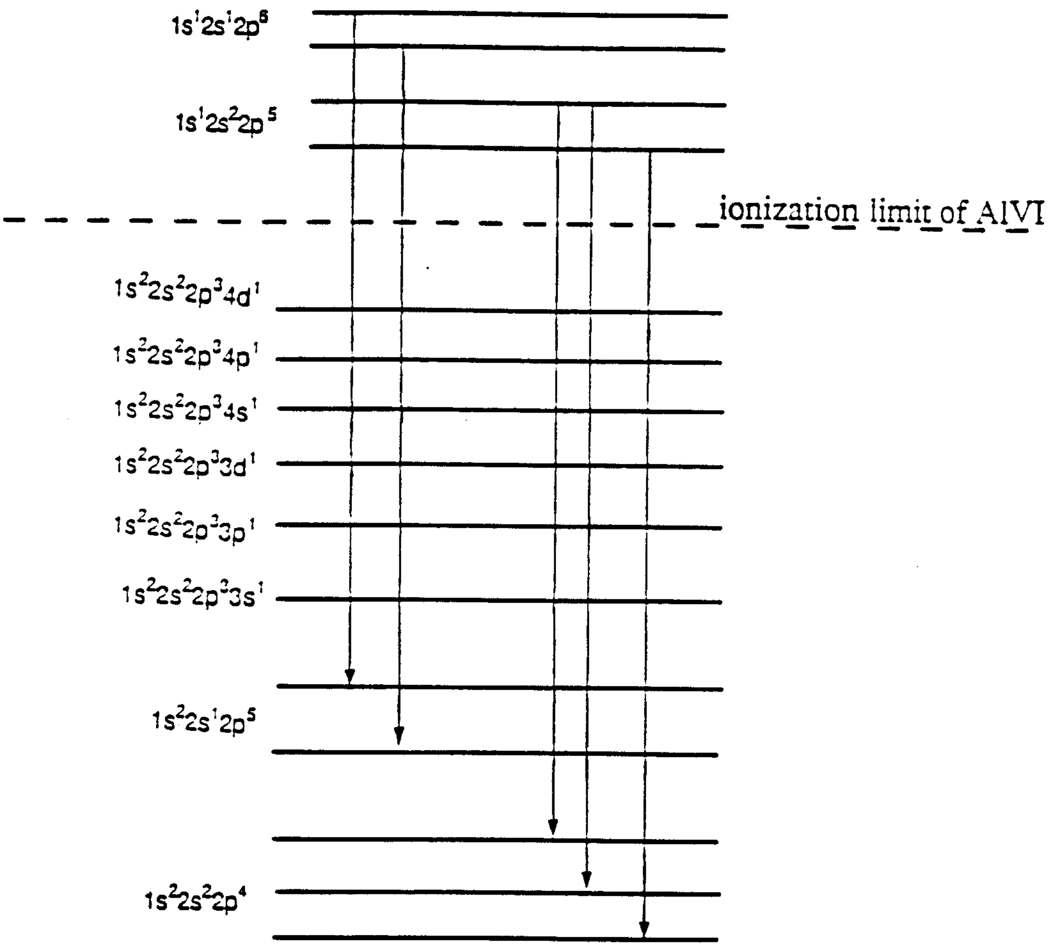

Figure 3.7: Atomic level structure of AlVI in CRE calculations

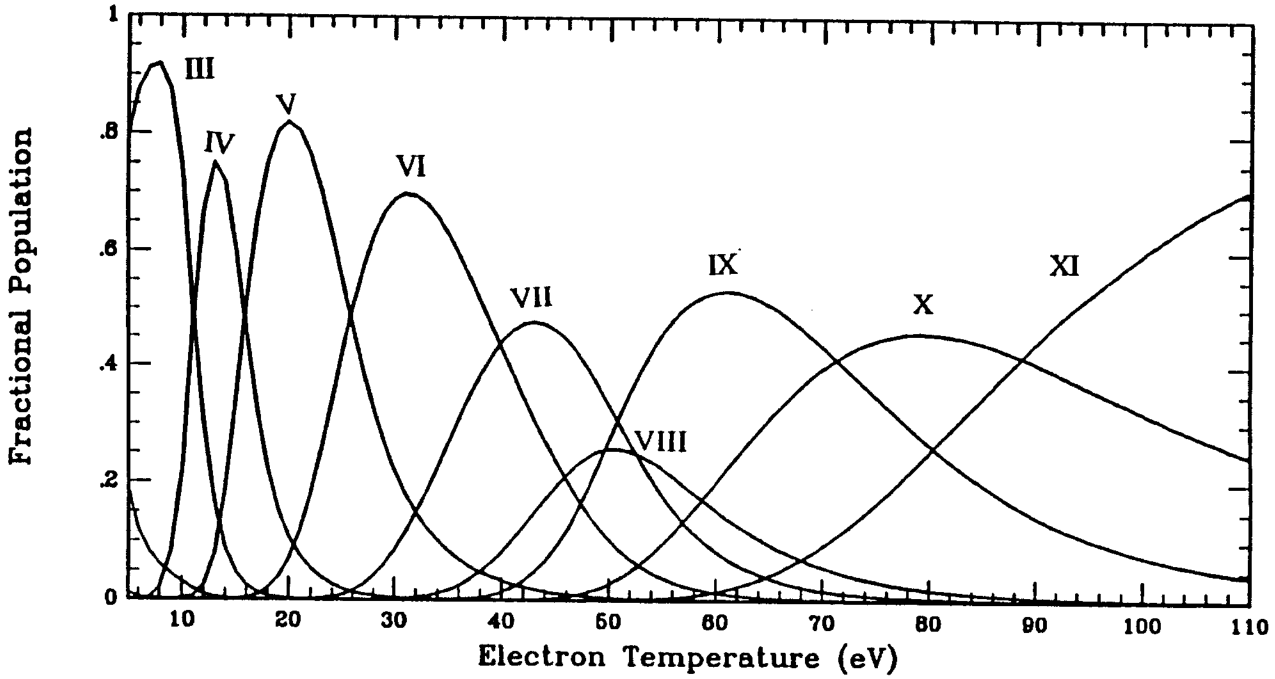

Figure 3.8: Ionization distribution of an Al plasma with $N_{ion} = 10^{20}\ cm^{-3}$

Table 3.4: Oscillator strengths and fluorescence yields for Al Kα transitions

Ion	Transition	Oscillator strength	Fluorescence yield
AlII	$1s^22s^22p^53s^23p^1(^3S)-1s^12s^22p^63s^23p^1(^3P)$	0.0884	0.046
	^3D - ^3P	0.0884	0.046
	^1D - ^1P	0.0885	0.046
	^1P - ^1P	0.0885	0.046
	^3P - ^3P	0.0884	0.046
	^1S - ^1P	0.0884	0.046
AlIII	$1s^22s^22p^53s^2$ $(^2P)-1s^12s^22p^63s^2$ (^2S)	0.0885	0.045
AlIV	$1s^22s^22p^53s^1$ $(^3P)-1s^12s^22p^63s^1$ (^3S)	0.0889	0.0434
	^1P - ^1S	0.0887	0.0434
AlV	$1s^22s^22p^5$ $(^2P)-1s^12s^22p^6$ (^2S)	0.0894	0.0479
AlVI	$1s^22s^22p^4$ $(^3P)-1s^12s^22p^5$ (^3P)	0.1911	0.0522
	^1D - ^1P	0.1890	0.0522
	^1S - ^1P	0.1897	0.0522
AlVII	$1s^22s^22p^3$ $(^4S)-1s^12s^22p^4$ (^4P)	0.3062	0.0619
	^2D - ^2D	0.1515	0.0619
	^2P - ^2D	0.0838	0.0619
	^2P - ^2S	0.0670	0.0619
AlVIII	$1s^22s^22p^2$ $(^3P)-1s^12s^22p^3$ (^3D)	0.1789	0.0700
AlIX	$1s^22s^22p^1$ $(^2P)-1s^12s^22p^2$ (^2D)	0.1871	0.0623
AlX	$1s^22s^2$ $(^1S)-1s^12s^22p^1$ (^1P)	0.6830	0.0650

ionization of the L-shell takes place, and Kα emissions for AlIV – AlX have almost the same intensity.

By comparing our results of thin calculations with the experimental data, we can see that the calculated spectra of the thin plasma model qualitatively explain the experimental data (line positions, temperature dependence, *etc.*). Quantitatively, however, there is a significant discrepancy. This is due to the fact that Kα radiation is optical thick in most cases, and the role of line self-absorption for Kα lines is very important. Hence, the thin plasma assumption made in our calculation is not correct.

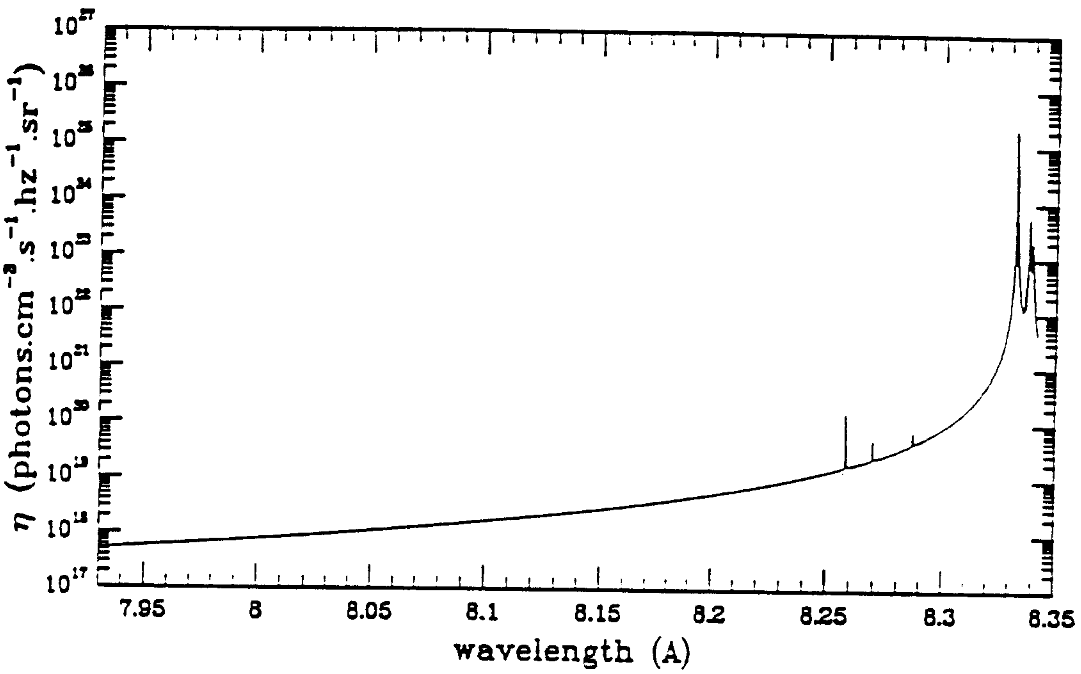

Figure 3.9: Theoretical Kα spectrum for Al plasma at T=5eV, $N_{ion} = 10^{20} cm^{-3}$

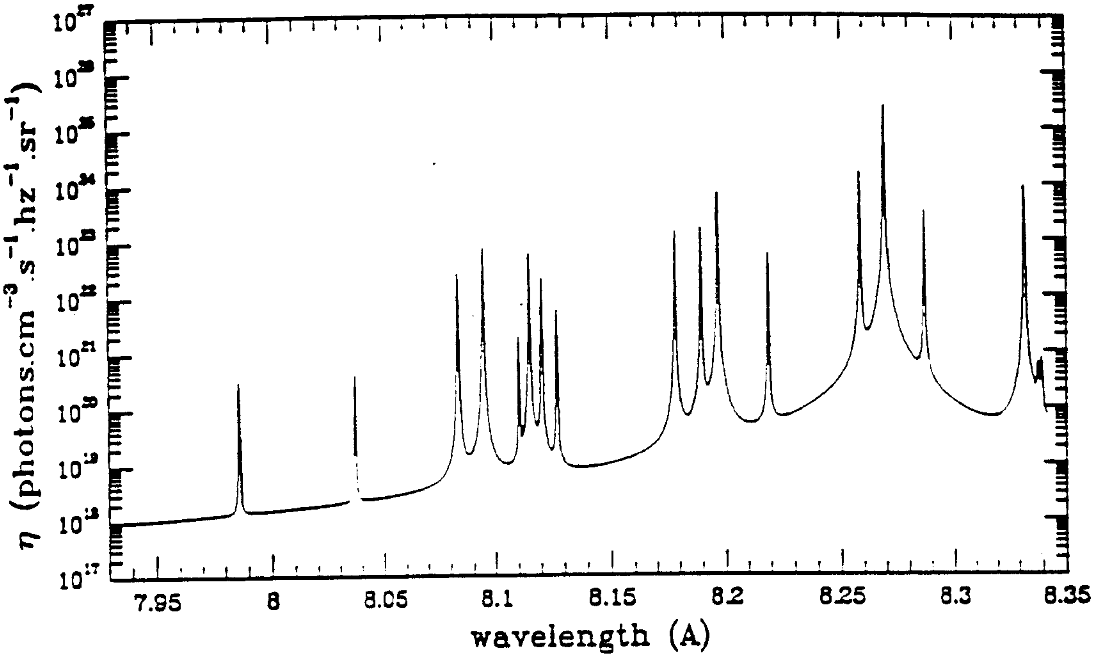

Figure 3.10: Theoretical Kα spectrum for Al plasma at T=20eV, $N_{ion} = 10^{20} cm^{-3}$

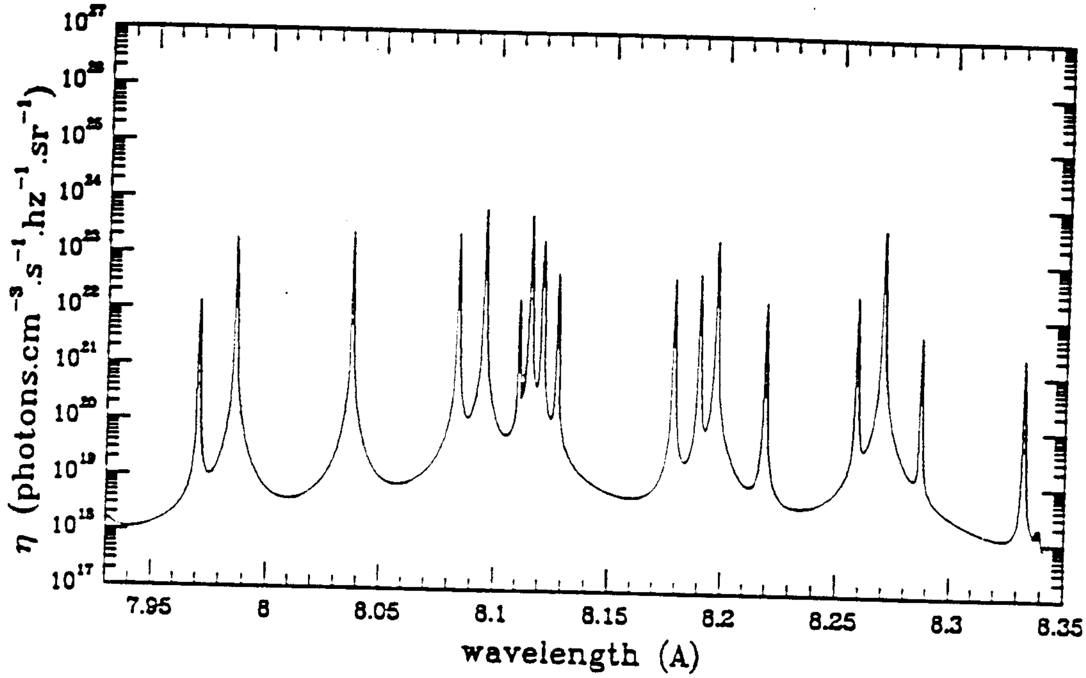

Figure 3.11: Theoretical Kα spectrum for Al plasma at T=30eV, $N_{ion} = 10^{20} cm^{-3}$

3.4 Line Opacity Effect of Kα X-Ray Radiation

In this section, we study the physical process of line self-absorption for the Kα x-ray radiation in a proton beam heated plasma.

A K-shell vacancy is created by proton impact ionization, which is accompanied by the emission of a Kα photon. This photon may have three fates: *(1) being absorbed in a bound-bound transition of an ion with L-shell holes; (2) being absorbed in a photoionization process; (3) escaping from the plasma.* For AlI – AlIV, the only vacancies in L shell are due to the short-lived multiple ionization events produced in the proton-ion collisions, and the concentration of such multiply ionized ions is very small. Hence, for the Kα photon from AlI – AlIV, the main self-absorption mechanism is the photoionization effect. This may be described as in Figure 3.12(a), where we take AlIII and AlV as examples. When the plasma temperature is sufficiently high that L-shell vacancies can be produced by thermal ionization, the abundance of ions with L-shell holes in the plasma can be quite high. In such a case, the bound-bound resonant self-absorption for Kα line of these ions (AlV – AlIX) becomes the most important.

The Kα line opacity effect can be clearly seen in Figure 3.13, where the Kα line fluxes from a $T = 50eV$, $N_{ion} = 10^{-2}N_{solid}$, $L = 1mm$ Al plasma are plotted for two cases. The dotted curve is from a calculation in which the

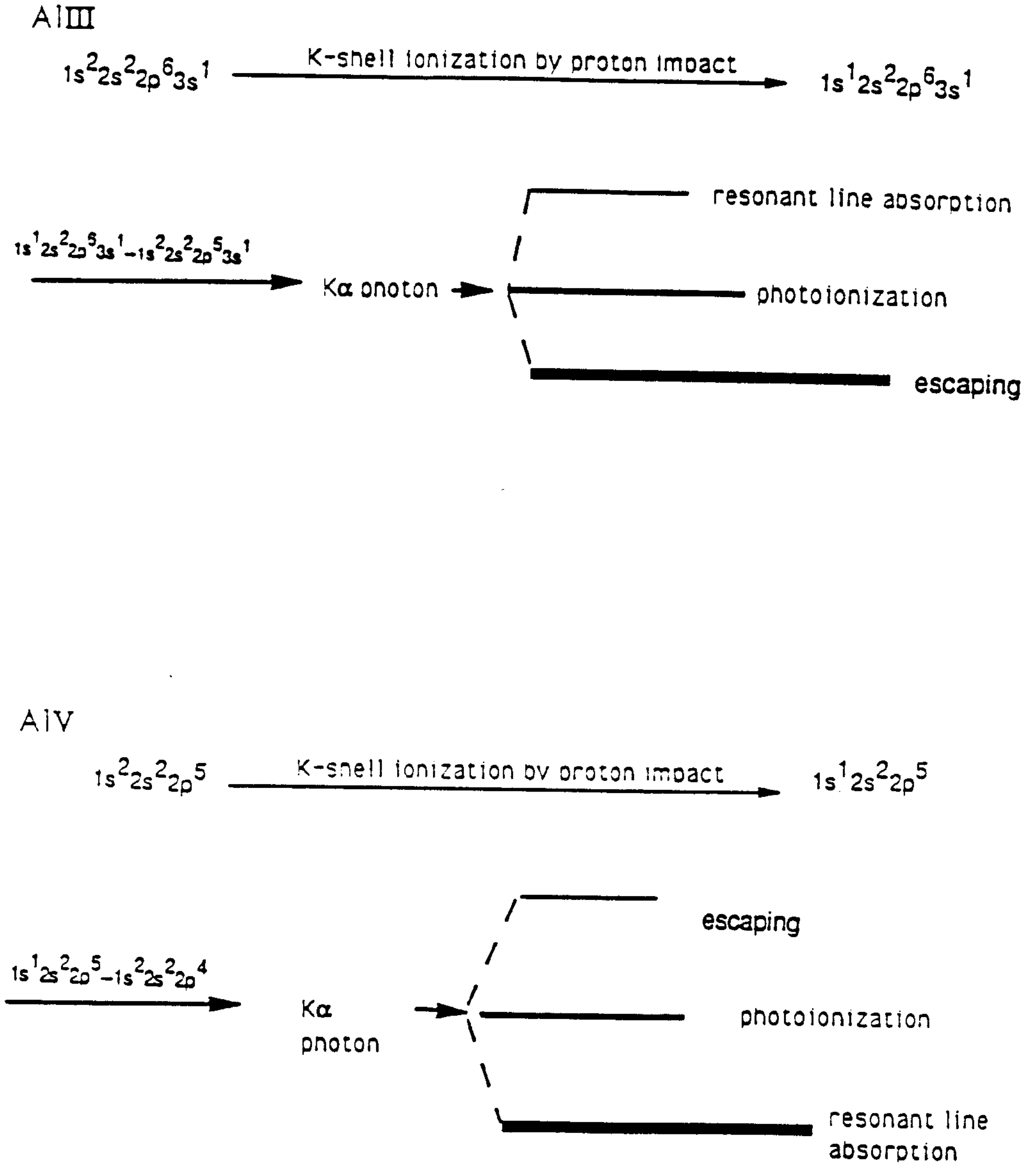

Figure 3.12: Fates of Kα photon in a plasma

plasma was assumed to be optically thin. The solid curve was obtained from a calculation for which opacity effects were fully accounted [97]. For such a plasma, the Al ions with L-vacancies are quite abundant and the line opacity effect is expected to be important. Note that the fluxes in the optically thin case are typically 3 orders of magnitude higher than in the optically thick case. Because of the line opacity effect, Kα photons with line center frequencies can actually *travel* such a short distance within the plasma that only those photons produced in the edge of the plasma are contributed to the *emerge fluxes* (*i.e.*, detected by the detector), while the Kα photons with line wing frequencies can *travel* much longer within the plasma than those with line center frequencies and hence the emerge fluxes of these photons come from both edge and interior of the plasma. Optically thin model calculations neglect this effect and hence over estimate the contributions of line center photons. It is also seen that the relative fluxes of two lines can be significantly influenced by the opacity effects. For instance, the AlVIII line at 8.04 $\AA$ is about a factor of 5 higher than the AlIX line at 7.98 $\AA$ in the optically thin case. However, when opacity effects are included, these two lines have peak fluxes that are nearly equal. This clearly demonstrates the importance of line opacity effects in this spectral region.

The importance of line opacity effect to the Kα spectrum analysis is obvious. In order to predicate the observability of Kα satellite lines under certain experimental conditions and deduce plasma conditions from observed spectra, we must do detailed radiative transfer calculations for fully considering the line opacity effects.

Ion beam - induced transitions offer many possibilities for deducing plasma conditions in ICF target experiments. Experimental Kα spectra in conjunction with a judicious mix of hydrodynamics simulations and non-LTE radiative transfer calculations can lead to an improved understanding of beam-plasma interaction physics. This is what we are going to do in the near future.

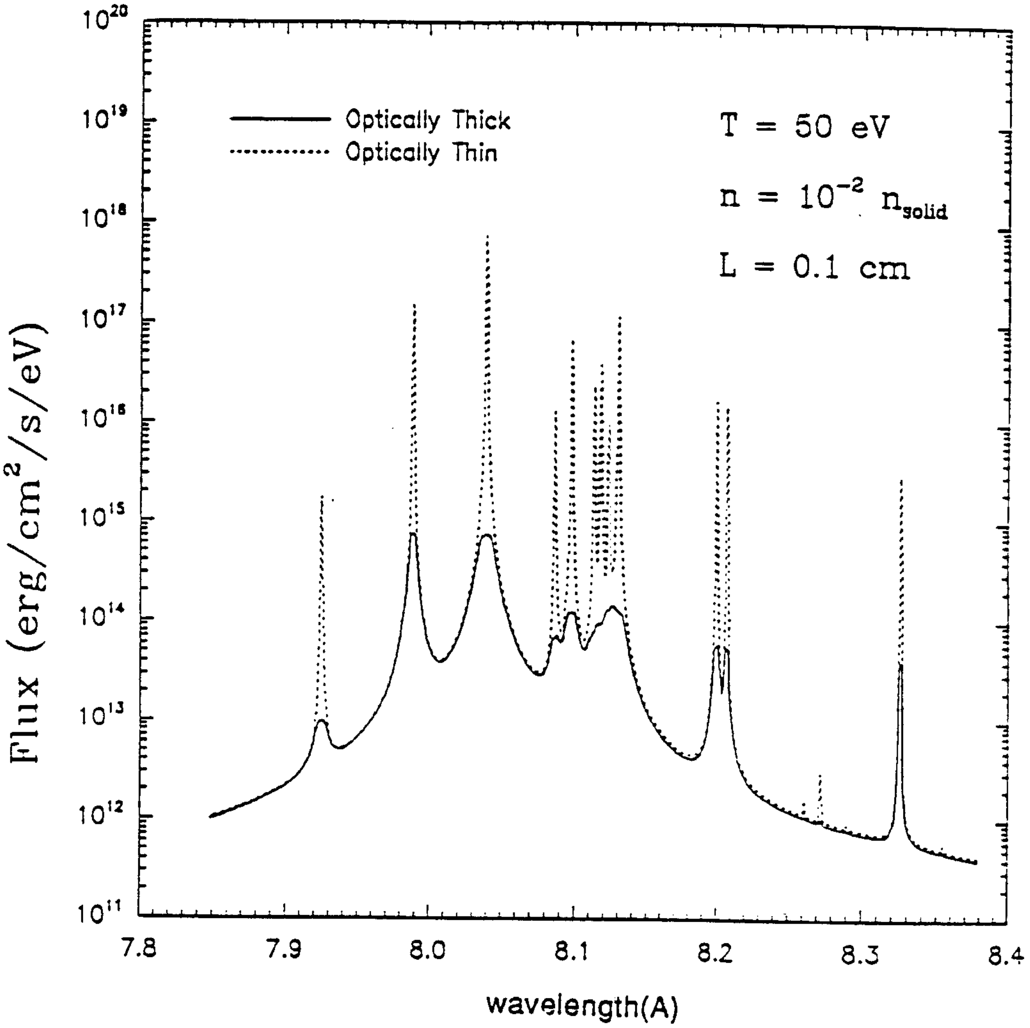

Figure 3.13: Comparison of two sets of calculated Kα spectral fluxes for an Al plasma at $T = 50eV$, $N_{ion} = 10^{-2}N_{solid}$, $L = 1mm$

Chapter 4

Equations of State And Opacities for ICF Plasmas

4.1 Introduction; A Summary of Statistical Mechanics of Partially Ionized Plasmas

The equations of state and opacities of partially ionized plasmas are often required to study the physical properties of ICF plasmas. For a thermodynamic equilibrium ideal gas, the Saha-Boltzmann equations can be used to describe the ionization balance and the level occupation numbers, and the equations of state and opacities are readily obtained. However, for the physical conditions encountered in most laboratory plasmas, especially ICF plasmas, where plasma densities can vary from $\sim 10^{14}$ to $\sim 10^{22}$ $ions/cm^3$ and temperatures from $\sim$ 1 eV to 1 keV, the calculations of equations of state and opacities become quite difficult because the electrons and different ionic and atomic species cannot be always regarded as simple ideal gases. A number of physical effects, including electron degeneracy, coulomb interactions among free charges, bound-state level perturbation (destroy or/and shifts), and neutral atomic interactions, *etc.*, must be taken into account. On the other hand, the approximation of thermodynamic equilibrium (or even local thermodynamic equilibrium) may not be adequate for such plasmas. Detailed solutions of rate equations are required in determining the ionization balance and level occupation numbers in such cases.

For a thermodynamic equilibrium nonideal plasma, the free-energy minimization method pioneered by G. Harris and her associates[100, 101, 102] has proven to be a powerful and flexible tool for producing equations of state for plasma conditions of $N_{ion} \leq 10^{22}$ cm^{-3}. The method is both simple and elegant: given a mathematical model for the Helmholtz free energy $F(T, V, \{N\})$, where $\{N\}$ is a set of particle numbers, one minimizes F subject to the stoichiometric relations governing possible reactions among the particle species in the plasma. This process determines F and the equilibrium values of the particle number $\{N\}$ for a specified T and V. A good feature of the free-energy minimization method is that because of the assumed factorizability of the translational, configurational, and internal components of the total partition function Z, the free energy $F = kTlnZ$ is modular, and the nonideal terms can be directly introduced.

Consider a nonideal plasma composed of several chemical elements k, each in several ionization stages j. Then the free energy is

$$\begin{aligned} F = & - kT\sum_s N_s[\frac{3}{2}lnT + ln(\frac{V}{N_s}) + lnG_s + 1] \\ & - kT\sum_{j,k} N_{kj}lnZ^I_{kj} + F_{nonideal} \end{aligned} \tag{4.1}$$

where the internal partition function is

$$Z^I_{kj} = \sum_i exp(-\varepsilon_{kji}/kT) \tag{4.2}$$

and

$$G_s = (\frac{2\pi km_s}{h^2})^{3/2} \tag{4.3}$$

In Eq.(4.1), the sum on s runs over all particle species but electrons, whereas the sum on j runs only over species having bound states. The nonideal term includes the partially degenerate electrons and other nonideal effects. The equilibrium among molecule/atom/ion species can be determined from stoichiometric relations of the form

$$\frac{\partial F}{\partial N_j} - \frac{\partial F}{\partial N_{j+1}} - \frac{\partial F}{\partial N_e} = 0 \tag{4.4}$$

for an ionization process $j \longleftrightarrow (j+1) + e$, and

$$\frac{\partial F}{\partial N_{AB}} - \frac{\partial F}{\partial N_B} - \frac{\partial F}{\partial N_B} = 0 \tag{4.5}$$

for a molecular dissociation $AB \longleftrightarrow A+B$, along with constraints of number and charge conservation. Once F and the $\{N\}$ are determined, the equations of state (pressure, entropy, and internal energy) can be computed from the following thermodynamics relations

$$P = -\frac{\partial F}{\partial V}|_{T,\{N\}} \tag{4.6}$$

$$S = -\frac{\partial F}{\partial T}|_{V,\{N\}} \tag{4.7}$$

$$E = -T^2\frac{\partial}{\partial T}(\frac{F}{T})|_{V,\{N\}} \tag{4.8}$$

In a partially ionized plasma, the major nonideal effect is known to be the coulombic interactions between the charged components. The coulomb perturbation enters the equations of state in two ways: through the interparticle interaction potential it modifies the configuration integral[99], and through the internal potential it perturbs the bound states (destroy or/and shifts). The latter effect partially contributes to the effects of '*pressure ionization*' which will be discussed in detail in the next section. A modified Debye-Hückel model[102] may be used for describing the configurational coulomb interaction. In this modified DH model, the electrons are treated as fermions, but the ions are treated as classical particles, and the Helmholtz free energy is given by

$$F_{DH} = -(\frac{2\sqrt{\pi}e^3}{3\sqrt{k}})\frac{1}{\sqrt{VT}}(\sum_s N_s z_s^2\theta_s)^{3/2}\tau(x) \tag{4.9}$$

where the sum on s runs over all charged species with $z_s = 0$ for neutral, and $z_s = -1$ for electron;

$$\theta_e = \frac{F_{-1/2}(\eta)}{2F_{1/2}(\eta)} \tag{4.10}$$

$$\theta_s = 1 \tag{4.11}$$

$$\tau(x) = 3x^{-3}[ln(1+x) - x + 0.5x^2] \tag{4.12}$$

$$x = (\frac{2\sqrt{\pi}e^3}{k^{3/2}}\frac{1}{V^{1/2}T^{3/2}})\frac{F_{1/2}(\eta)}{F_{3/2}(\eta)}(\frac{\sum_{s\neq e} N_s z_s}{\sum_{s\neq e} N_s})(\sum_s N_s z_s^2 \theta_s)^{1/2} \tag{4.13}$$

It is important to note that, when F_{DH} is included in the total free energy for an isolated-atom model, a modified Saha equation describing the system can be derived in which the only modification is that the ionization potential I_o is replaced by $I_o - \Delta I(T, N)$. This feature of the configurational coulomb contribution is generally referred to as a lowering of the ionization potential, and refers to the decrease of the interaction potential between electron and nucleus due to shielding by the surrounding charged particles. However, it is necessary to indicate that the effects of '*pressure ionization*' do not physically relate to a '*lowing of ionization potential*', though they may formally imply this concept if the stoichiometric equations are rewritten in the form of Saha equations. Rather, the '*pressure ionization*' effects should either follow from, or imply, an interaction term in the free energy, which partially substitutes for effects contained in a realistic, but currently unobtainable, solution of the full N-body problem for the plasma.

The free energy minimization method is feasible only for the thermodynamic equilibrium plasmas. For non-LTE plasmas, the ionization balance and the level populations need to be determined by solving the rate equations. In the free energy minimization method, the free energy is modular and hence all the first-order thermodynamic quantities are modular, *i.e.,* a sum of physically different contributions: translational contribution, configurational contribution and internal contribution. Are these expressions for the thermodynamic quantities still the same in the non-LTE calculations? From the view point of statistical mechanics, each thermodynamic quantity has a corresponding microscopic quantity, the macroscopic thermodynamic quantity is the statistical average of its corresponding microscopic term, *i.e.,*

$$E = \int \varepsilon \psi(\varepsilon) d\varepsilon \tag{4.14}$$

where $\psi(\varepsilon)$ is the distribution function. In our applications, what is different between LTE and non-LTE is just the occupation number. Hence, in a non-LTE calculation, we can use the same expressions of the first-order thermodynamic quantities as in LTE with the replacement of a new set of occupation numbers. However, this is not necessarily true for the thermodynamic relations and higher order thermodynamic quantities.

4.2 Pressure Ionization Effect And Level Survival Probability

The great difference between atomic structure for isolated atoms and those in the plasma is the finite number of bound states in the latter case. As the plasma density rises and the number and intensity of interparticle interactions increase, less tightly bound states are strongly perturbed, broadened into distributions resembling conduction bands, and ultimately destroyed and shifted into the continuum. These phenomena imply a '*pressure ionization*' which leads at very high densities to a fully ionized plasma comprising, in the first approximation, an ideal gas of degenerate electrons that can move freely with respect to a "Lattice" of bare ions. *Pressure ionization* is dominately a volume effect: When particles are jammed closely together, bound electron orbitals filling too large a volume fail to survive and the electrons migrate from atom to atom.

The two most widely adopted models for describing *pressure ionization* effects are (1) the confined atom (CA) model[99, 102, 103], and (2) the static screened coulomb potential (SSCP) model[24, 104]. The CA model imposes an infinite potential barrier at the mean interparticle separation and thus stimulates an extremely stiff interaction. This model seems appropriate for neutral-neutral interactions, but is clearly problematical for the long-range coulomb potential operative in ionized media. The SSCP model attempts to stimulate the intra-atomic effects of the Debye-shielded coulomb interaction among free charged particles. This model seems appropriate when the medium is strongly ionized. Although the SSCP model has become increasingly popular, it is more fragile than the CA model because it fails when the gas becomes completely neutral. In contrast, the CA model is obviously rough, but works at all temperatures and densities of interest.

It has been argued that one cannot rely upon the very predictions of the CA and SSCP models that are essential to produce pressure ionization. In a partially ionized plasma one must be able to account for the effects of both neutrals and ions simultaneously. But because no potential function can describe all of the possible interactions, most published calculations have employed one extreme model or the other. Unfortunately the two models predict rather different perturbed energy-level spectra (both positions and numbers of levels) at a given (N_i, T). The point is that even though each model partially describes the inter-atomic potential between neighboring particles, neither provides an accurate description of actual forces produced inside atoms by their surrounding, and neither leads to a fully consistent theory. Also, the existing experimental evidence has shown that the energy-level shifts predicted by both CA and SSCP models are not reliable[20].

Another procedure for dealing with the pressure ionization effect has been suggested by Hummer and Mihalas[20], *i.e.,* the " occupation probability formalism ". In this procedure, a factor, w_{ijk} $(0 \leq w_{ijk} \leq 1)$, is introduced for each atomic level. The physical significant of w_{ijk} is the probability of finding the ion in question in state i relative to that of finding it in a similar ensemble of non-interacting ions. Alternatively, w_{ijk} can be considered as a factor expressing the *survival probability* of the level due to the perturbation of surrounding particles, neutral and charged. The *survival probability* has to be calculated directly from a physical description of interparticle interactions. It is here that one makes contact with atomic physics and can attempt to introduce some level of realism into the model.

In the models suggested by Hummer *et al.*[20], perturbations by neutral particles are based on an excluded volume treatment and perturbations by charges are calculated from a fit to a quantum mechanical Stark ionization theory. The level *survival probability* can then be expressed as

$$\begin{aligned} ln\, w_{ijk} &= -(\frac{4\pi}{3})\{\sum_{\nu' k'}[(r_{ijk}+r_{1\nu' k'})^3+\beta(r_{1jk}+r_{1\nu' k'})^\gamma] \\ &+ 16[\frac{\sqrt{z_{jk}+1}e^2}{\sqrt{K_{ijk}I_{ijk}}}]^3\sum_{s\neq e} n_s z_s^{3/2}\} \end{aligned} \tag{4.15}$$

Here the index ν' runs over neutral particles, the index s runs over charged ions, r_{ijk} is the radius assigned to a particle in state i of ion j of species k, I_{ijk} is the ionization potential of such a particle, z_{jk} is the net charge of a particle of ion j of species k, β and γ are two empirical parameters, and

$$K_{ijk} = \begin{cases} 1 & p_i \leq 3 \\ \frac{16}{3}(\frac{p_i}{p_i+1}^2 \frac{p_i+7/6}{p_i^2+p_i+1/2} & p_i > 3 \end{cases} \tag{4.16}$$

is a quantum mechanical correction and p_i is the effective quantum number of the state i.

The *occupation probability formalism* has several advantages. (1) The w_{ijk} decrease continuously and monotonically as the strength of the relevant interaction increases relative to the binding energy of a level. (2) The continuous state-by-state fadeout with decreasing w_{ijk} allows one to assure continuity of all material properties (pressure, internal energy, opacity, *etc.*). (3) The probabilistic interpretation of w_{ijk} allows us to combine survival probabilities from statistically independent interactions. It is thus straightforward to allow for the simultaneous action of different mechanisms, as well as of several different species of perturbers by any one mechanism. Hence the method provides a scheme for treating partially ionized plasmas, and it goes smoothly to the limits of completely neutral or completely ionized gas.

In our work, we adopt the Hummer-Mihalas occupation probability formalism to take account of *pressure ionization* effects.

4.3 A Collisional-Radiative Equilibrium Model for Plasmas

In this section we develop a collisional-radiative equilibrium model for calculating ionic charged-state abundance and the level occupation number in plasmas. The nonideal effects on the population distribution are considered by introducing a survival probability factor for each level included in the calculation.

A general rate equation for the population density in level j of ion z, $n_{z,j}$ can be written as

$$\begin{aligned}
\frac{dn_{z,j}}{dt} = & - \sum_k I(z,j;z+1,k)n_e n_{z,j} + \sum_k I(z-1,k;z,j)n_e n_{z-1,k} \\
& - \sum_k R(z,j;z-1,k)n_e n_{z,j} + \sum_k R(z+1,k;z,j)n_e n_{z+1,k} \\
& - \sum_{u>j} E(z,j;z,u)n_e n_{z,j} - \sum_{l<j} D(z,j;z,l)n_e n_{z,j} \\
& + \sum_{l<j} E(z,l;z,j)n_e n_{z,l} - \sum_{u>j} D(z,u;z,j)n_e n_{z,u} \qquad (4.17)
\end{aligned}$$

where n_e is the density of electrons, $I(z,j;z+1,k)$ is the ionization rate coefficient for the ionization of ion z in level j to ion $z+1$ in level k, $R(z,j;z-1,k)$ is the recombination rate coefficient (radiative+collisional+dielectronic), $E(z,j;z,u)$ is electron collisional excitation rate coefficient, and $D(z,j;z,l)$ is the deexcitation rate coefficient (spontaneous decay + collisional).

In plasmas with $n_e \leq 10^{22}\ cm^{-3}$, the coupling between excited levels of neighboring ionization stages through ionization and recombination is, in general, negligible. Assuming that the residual ions (for ionization) and the target ions (for recombination) are in the ground state only, we have

$$\begin{aligned}\frac{dn_{z,j}}{dt} = & - I(z,j;z+1,1)n_e n_{z,j} + [\sum_k I(z-1,k;z,j)n_e n_{z-1,k}]\delta_{j1} \\ & + R(z+1,1;z,j)n_e n_{z+1,1} - [\sum_k R(z,j;z-1,k)n_e n_{z,j}]\delta_{j1} \\ & - \sum_{u>j} E(z,j;z,u)n_e n_{z,j} - \sum_{l<j} D(z,j;z,l)n_e n_{z,j} \\ & + \sum_{l<j} E(z,l;z,j)n_e n_{z,l} - \sum_{u>j} D(z,u;z,j)n_e n_{z,u} \qquad (4.18)\end{aligned}$$

The ideal gas model, which assumes that interparticle interaction is negligible, leads to an infinite coupled set of the rate equations because of the infinite number of existing levels. In reality, however, the pressure ionization determines that there are only a finite number of levels for each ion and hence truncates the coupling rate equations to a finite set.

There are two factors affecting the atomic level occupation numbers : (1) *does this level survive ?* (2) *how is it occupied ?* If we assume the level survival probability is $w_{z,j}$ and the occupation probability is $p_{z,j}$, then the level occupation number density can be expressed as

$$n_{z,j} = w_{z,j} p_{z,j} A_z \qquad (4.19)$$

with

$$\sum_j n_{z,j} = \sum_j w_{z,j} p_{z,j} A_z = N_z \qquad (4.20)$$

where N_z is the ion abundance of ion z. Now, the rate equation becomes

$$\begin{aligned}
\frac{d(w_{z,j}p_{z,j})A_z}{dt} &= -I(z,j;z+1,1)n_e(w_{z,j}p_{z,j})A_z \\
&+ [\sum_k I(z-1,k;z,j)n_e(w_{z-1,j}p_{z-1,j})A_{z-1}]\delta_{j1} \\
&+ R(z+1,1;z,j)n_e w_{z,j}(w_{z+1,j}p_{z+1,j})A_{z+1} \\
&- [\sum_k R(z,j;z-1,k)n_e w_{z-1,k}(w_{z,j}p_{z,j})A_z]\delta_{j1} \\
&- \sum_{u>j} E(z,j;z,u)n_e(w_{z,j}p_{z,j})A_z \\
&- \sum_{l<j} D(z,j;z,l)n_e(w_{z,j}p_{z,j})A_z \\
&+ \sum_{l<j} E(z,l;z,j)n_e(w_{z,l}p_{z,l})A_z \\
&+ \sum_{u>j} D(z,u;z,j)n_e(w_{z,u}p_{z,u})A_z \qquad (4.21)
\end{aligned}$$

Note that for the recombination processes we need to account for the survival probability of the final level. By summing over all levels of the ion, we have

$$\begin{aligned}
\frac{d}{dt}\sum_j (w_{z,j}p_{z,j})A_z &= -\sum_j I(z,j;z+1,1)n_e(w_{z,j}p_{z,j})A_z \qquad (4.22) \\
&+ [\sum_{j,k} I(z-1,k'z,j)n_e(w_{z-1,j}p_{z-1,j})A_{z-1}]\delta_{j1} \\
&+ \sum_j R(z+1,1;z,j)n_e w_{z,j}(w_{z+1,j}p_{z+1,j})A_{z+1} \\
&- [\sum_{j,k} R(z,j;z-1,k)n_e w_{z-1,k}(w_{z,j}p_{z,j})A_z]\delta_{j1}
\end{aligned}$$

Defining the effective ionization rate coefficient for the ionization of ion $z-1$ to ion z as

$$\alpha_{z-1} = \sum_{j,k} I(z-1,k;z,j)w_{z-1,k}p_{z-1,k} \qquad (4.23)$$

and the effective recombination rate coefficient for the recombination of ion z to ion $z-1$ as

$$\beta_z = \sum_{j,k} R(z,j;z-1,k)w_{z-1,k}w_{z,j}p_{z,j} \tag{4.24}$$

Then the equation for the proportional factor A_z become

$$\frac{dN_z}{dt} = -n_e(\alpha_z A_z + \beta_{z+1}A_{z+1} + \alpha_{z-1}A_{z-1} - \beta_z A_z) \tag{4.25}$$

Assuming the plasma is in steady state, namely,

$$\begin{aligned} \frac{dN_z}{dt} &= 0 \qquad (4.26) \\ z &= 0,1,2,3,\cdots,Z. \end{aligned}$$

We have a recursive equation

$$\begin{aligned} \frac{A_z}{A_{z-1}} &= \frac{\alpha_{z-1}}{\beta_z} \qquad (4.27) \\ z &= 1,2,3,\cdots,Z. \qquad (4.28) \end{aligned}$$

This recursive equation can be solved in the following way, set

$$\frac{\beta_z}{\alpha_{z-1}} = c_z. \tag{4.29}$$

Then

$$\begin{aligned} A_z &= c_{z+1}A_{z+1} \\ &= c_{z+1}\cdot c_{z+2}\cdot c_{z+3}\cdots c_Z\cdot A_Z \qquad (4.30) \\ z &= 0,1,2,\cdots,Z-1. \qquad (4.31) \end{aligned}$$

By using the particle conservation condition

$$\sum_z N_z = \sum_z (\sum_j w_{z,j} p_{z,j}) A_z = N_{total}, \tag{4.32}$$

we have

$$A_Z = \frac{N_{total}}{\sum_j w_{Z,j} p_{Z,j} + \sum_{z=0}^{Z-1} [(\sum_j w_{z,j} p_{z,j} \cdot c_{z+1} \cdot c_{z+2} \cdots c_Z]} \tag{4.33}$$

Finally, the ion abundances and the level number densities are given by

$$n_{z,j} = w_{z,j} p_{z,j} A_z$$

$$N_z = \sum_j w_{z,j} p_{z,j} A_z \tag{4.34}$$

This model has two advantages: (1) by combining the general CRE model and the level survival probability formalism, the pressure ionization effects can be directly introduced in the calculations of ion abundances and level occupation numbers for a non-LTE plasma; (2) this model reduces to the Coronal equilibrium result at low densities and Saha-Boltzmann equilibrium at high densities. At intermediate densities, the average charge state of the plasma estimated from this model lays between those estimated from Coronal and Saha models. In Figure 4.1 we plot the average charge state of a C plasma as a function of plasma density at $T_e = 10$ eV. It can be seen that the result from our model converges to the Coronal equilibrium, at the density of about 10^{18} cm^{-3}, our result merges smoothly to the LTE curve. The average charge state as a function of plasma temperature is plotted in Figure 4.2, and our result is between the estimations of the LTE model and Coronal model. The pressure ionization effect can be clearly seen in Figure 4.3, where the dashed line represents the result of no pressure ionization included (by setting $w_{z,j} = 1$ for all levels), and the solid curve was obtained by introducing the Hummer-Mihalas level survival probability into the calculation. At low temperatures, where the pressure ionization effects are expected to be small, the two curves match. As densities increase, the curve without accounting for pressure ionization drops down very fast and eventually reaches a completely neutral state (a non-physical result!), while the solid curve drops down slower and has a increased trend when $N_{ion} \geq 10^{22}\ cm^{-3}$.

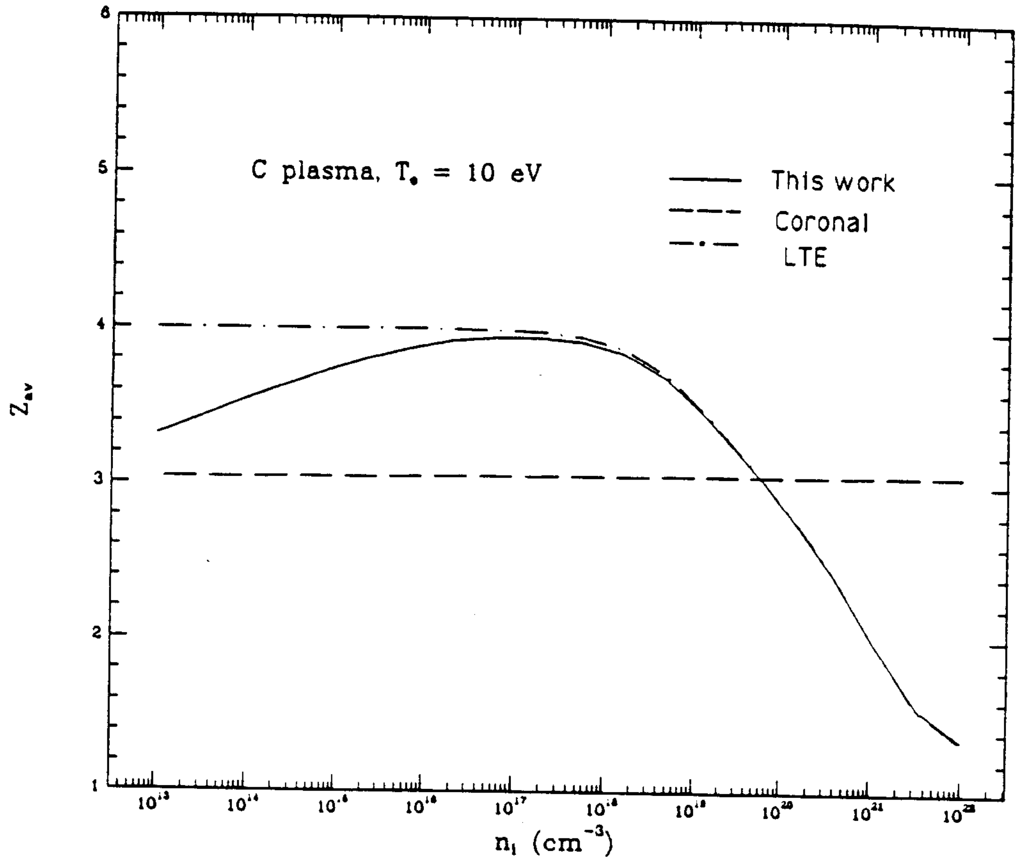

Figure 4.1: Z_{av} as a function of plasma density for C plasma at T=10 eV

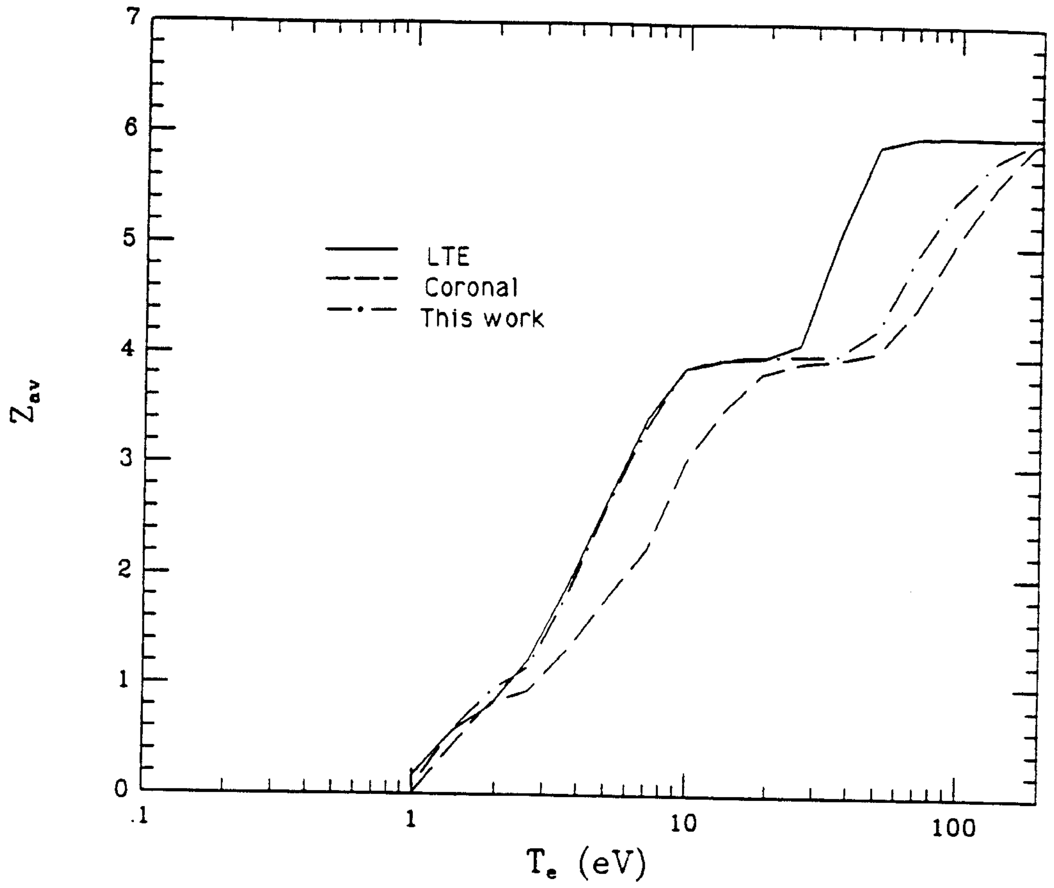

Figure 4.2: Z_{av} as a function of plasma temperature for C plasma at $N_i = 10^{18}\ cm^{-3}$

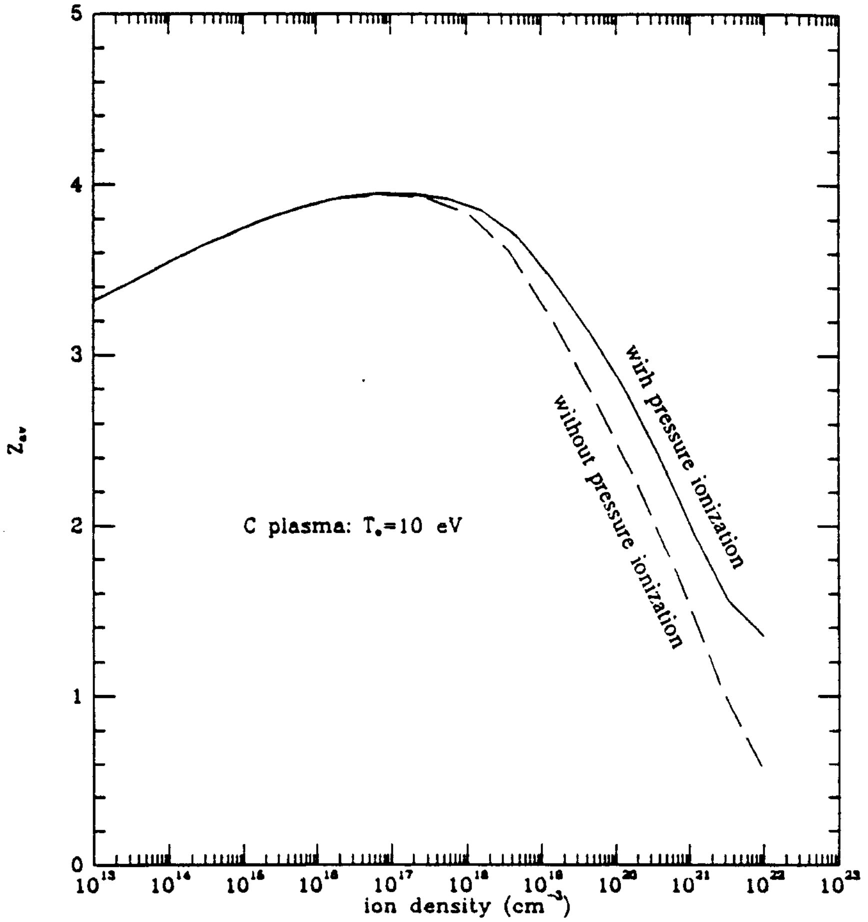

Figure 4.3: Effect of pressure ionization on Z_{av}

4.4 Equations of State of Non-LTE Plasmas

As we already mentioned before, for the physical conditions encountered in most laboratory plasmas, especially ICF plasmas, where plasma densities can vary from 10^{14} to 10^{22} $ions/cm^3$ and temperatures from 1 eV to 1 keV, the ideal gas model is not appropriate. Non-ideal effects need to be taken into account in the computations of equations of state for these plasmas. In our calculations, the equations of state of plasmas come from four different contributions: *(1) the translation of ions and atoms, (2) the partially degenerate electrons, (3) configuration effects from coulomb interaction (Debye-Hükel correction), (4) atomic internal contributions.*

4.4.1 Analytical Expressions for Equations of State of Plasmas

In this section we summarize the analytical expressions for the equations of state of plasma for a given set of occupation numbers $\{N_z\}$ and $\{n_{z,j}\}$.

I. Translational Contribution of The Ions And Atoms

$$E_1 = \frac{3}{2}kT \sum_{s \neq e} N_s = 2.403 \times 10^{-12} T(eV) \sum_{s \neq e} N_s (erg/cm^3) \tag{4.35}$$

$$P_1 = kT \sum_{s \neq e} N_s = 1.602 \times 10^{-12} T(eV) \sum_{s \neq e} N_s (dyn/cm^2) \tag{4.36}$$

II. Contribution of Partially Degenerate Electrons

$$E_2 = N_e kT \frac{F_{3/2}(\eta)}{F_{1/2}(\eta)} = 1.602 \times 10^{-12} N_e T(eV) \frac{F_{3/2}(\eta)}{F_{1/2}(\eta)} (erg/cm^3) \tag{4.37}$$

$$P_2 = \frac{2}{3} N_e kT \frac{F_{3/2}(\eta)}{F_{1/2}(\eta)} = 1.068 \times 10^{-12} N_e T(eV) \frac{F_{3/2}(\eta)}{F_{1/2}(\eta)} (dyn/cm^2) \tag{4.38}$$

where η is the degeneracy factor determined by

$$F_{1/2}(\eta) = \frac{\sqrt{\pi}}{4} \left(\frac{2\pi m_e k}{h^2}\right)^{-3/2} \frac{N_e}{T^{3/2}} = 1.468 \times 10^{-22} \frac{N_e}{T^{3/2}(eV)} \tag{4.39}$$

III. Debye-Hükel Correction Terms

$$\begin{aligned} E_3 &= -\left(\frac{2\sqrt{\pi}e^3}{3\sqrt{kT}}\right)\left(\sum_s N_s z_s^2 \theta_s\right)^{3/2} \tau(x) \\ &\times \left(1.5 - 1.5 \frac{TN_e\theta'_e}{\sum_s N_s z_s^2 \theta_s} \frac{\partial \eta}{\partial T} - \frac{\tau(x)'}{\tau(x)} T \frac{\partial x}{\partial T}\right) \\ &= -1.037 \times 10^{-22} \frac{1}{\sqrt{T(eV)}} \left(\sum_s N_s z_s^2 \theta_s\right)^{3/2} \tau(x) \\ &\times \left(1.5 - 1.5 \frac{TN_e\theta'_e}{\sum_s N_s z_s^2 \theta_s} \frac{\partial \eta}{\partial T} - \frac{\tau(x)'}{\tau(x)} T \frac{\partial x}{\partial T}\right) (erg/cm^3) \end{aligned} \tag{4.40}$$

$$\begin{aligned} P_3 &= -\left(\frac{2\sqrt{\pi}e^3}{3\sqrt{kT}}\right)\left(\sum_s N_s z_s^2 \theta_s\right)^{3/2} \tau(x) \\ &\times \left(0.5 - 1.5 \frac{TN_e\theta'_e}{\sum_s N_s z_s^2 \theta_s} \frac{\partial \eta}{\partial V} - \frac{\tau(x)'}{\tau(x)} T \frac{\partial x}{\partial V}\right) \end{aligned}$$

$$\begin{aligned} &= -1.037\times 10^{-22}\frac{1}{\sqrt{T(eV)}}(\sum_s N_s z_s^2\theta_s)^{3/2}\tau(x) \\ &\times (0.5-1.5\frac{TN_e\theta'_e}{\sum_s N_s z_s^2\theta_s}\frac{\partial\eta}{\partial V}-\frac{\tau(x)'}{\tau(x)}T\frac{\partial x}{\partial V})(dyn/cm^2) \end{aligned} \tag{4.41}$$

where

$$\begin{aligned} &\theta_e=\frac{F_{-1/2}(\eta)}{F_{1/2}(\eta)} \quad \theta'_e=\theta_e(\frac{F'_{1/2}(\eta)}{F_{-1/2}(\eta)}-\theta_e) \quad . \\ &\theta_s=1 \qquad\qquad \theta'_s=0 \qquad\qquad\qquad (s\neq e) \end{aligned} \tag{4.42}$$

$$\begin{aligned} \tau(x)=3x^{-3}[ln(1+x)-x+\frac{x^2}{2}] \simeq 1-0.75x(x\ll 1) \\ \tau'(x)=-\frac{3}{x}(\tau-\frac{1}{1+x}) \end{aligned} \tag{4.43}$$

$$\begin{aligned} x &= (\frac{2\sqrt{\pi}e^3}{k^{3/2}}\frac{1}{T^{3/2}})\frac{F_{1/2}(\eta)}{F_{3/2}(\eta)}(\frac{\sum_{s\neq e}N_s z_s}{\sum_{s\neq e}N_s})(\sum_s N_s z_s^2\theta_s)^{1/2} \\ &= 1.9377\times 10^{-10}\frac{1}{T^{3/2}(eV)}\frac{F_{1/2}(\eta)}{F_{3/2}(\eta)}(\frac{\sum_{s\neq e}N_s z_s}{\sum_{s\neq e}N_s})(\sum_s N_s z_s^2\theta_s)^{1/2} \end{aligned} \tag{4.44}$$

$$\frac{\partial\eta}{\partial T}=-\frac{3}{T}\frac{F_{1/2}(\eta)}{F_{-1/2}(\eta)}=-1.5\frac{1}{\theta_e T} \tag{4.45}$$

$$\frac{\partial\eta}{\partial V}=-2\frac{F_{1/2}(\eta)}{F_{-1/2}(\eta)}=-\frac{1}{\theta_e} \tag{4.46}$$

$$\frac{\partial x}{\partial T}=x\{-\frac{3}{2T}+[\theta_e-\frac{3F_{1/2}(\eta)}{F_{3/2}(\eta)}+\frac{N_e\theta'_e}{2\sum_s N_s z_s^2\theta_s}]\frac{\partial\eta}{\partial T}\} \tag{4.47}$$

$$\frac{\partial x}{\partial V}=x\{-\frac{1}{2V}+[\theta_e-\frac{3F_{1/2}(\eta)}{F_{3/2}(\eta)}+\frac{N_e\theta'_e}{2\sum_s N_s z_s^2\theta_s}]\frac{\partial\eta}{\partial V}\} \tag{4.48}$$

IV. Atomic Internal Structure Contribution

(Ionization and Excitation)

If we set $E_{o,1} = 0$ (neutral ground state) , then the internal contribution may be expressed as

$$E_4 = \sum_{s \neq e} N_s E_{s,1} + \sum_{s \neq 1} [\sum_i N_{s,i}(E_{s,i} - E_{s,1})] \tag{4.49}$$

If we set $E_{Z,1} = 0$ (fully ionized), then

$$E_4 = \sum_{s \neq e} N_s(E_{s,1} - E_{o,1}) + \sum_{s \neq 1} [\sum_i N_{s,i}(E_{s,i} - E_{s,1})] \tag{4.50}$$

4.4.2 Numerical Computations And Discussion

We have taken a carbon plasma as a sample calculation. The thermodynamic quantities P(pressure), E(internal energy) and C_p(heat capacity) are computed in the density and temperature region of our general interest.

In Figure 4.4 and Figure 4.5 we compare the internal energy and pressure calculated from different models. It can be seen that in the low density regime the LTE model significant overestimates the internal energy, while the Coronal model gives a constant internal energy in the density range of 10^{13} to 10^{22} cm^{-3}. Our calculation result converges to the Coronal equilibrium at low density and merges smoothly to the LTE at high density. Different models seems have little effect on the pressure. This is because the major contribution to the pressure comes from *free* electron translational motions in the plasma, while the electron density obtained from different models varies by only a factor of 1.5 to 2 for the plasma conditions we are dealing with.

Different contributions to the internal energy for several plasma conditions are plotted in Figure 4.6 and Figure 4.7. In most cases the major contributions are from atomic internal structure (*i.e.,ionizations and excitations*) and partial degenerate electrons. At high densities and low temperatures, however, the contribution of kinetic energy of the ion becomes important.

The isothermal internal energy and pressure curves are given in Figure 4.8 and Figure 4.9. As the plasma temperature increases, internal energy and pressure increase. In Figure 4.10 we plot the heat capacity as a function of plasma temperature. The heat capacity curve is a little bit more complicated, the variations of the heat capacity to the plasma temperature are closely related to the ionization stage distribution and atomic internal structure of the plasma. At very low temperature, the neutral atoms are the most abundant particle, a large amount of energy is needed to ionize the atoms and hence the heat capacity is high. As the temperature increases from 1 eV to about 2 eV, the abundance of neutral atoms decreases and the abundance of the first ionized ions increases. However, the temperature is not high enough to ionize the first ionized ions, so the major contributions to the heat capacity are the ionization energies of neutral atoms and the excitation energies of the first ionized ions. The decrease of the abundance of neutral atoms leads to the decrease of heat capacity in this temperature regime. As

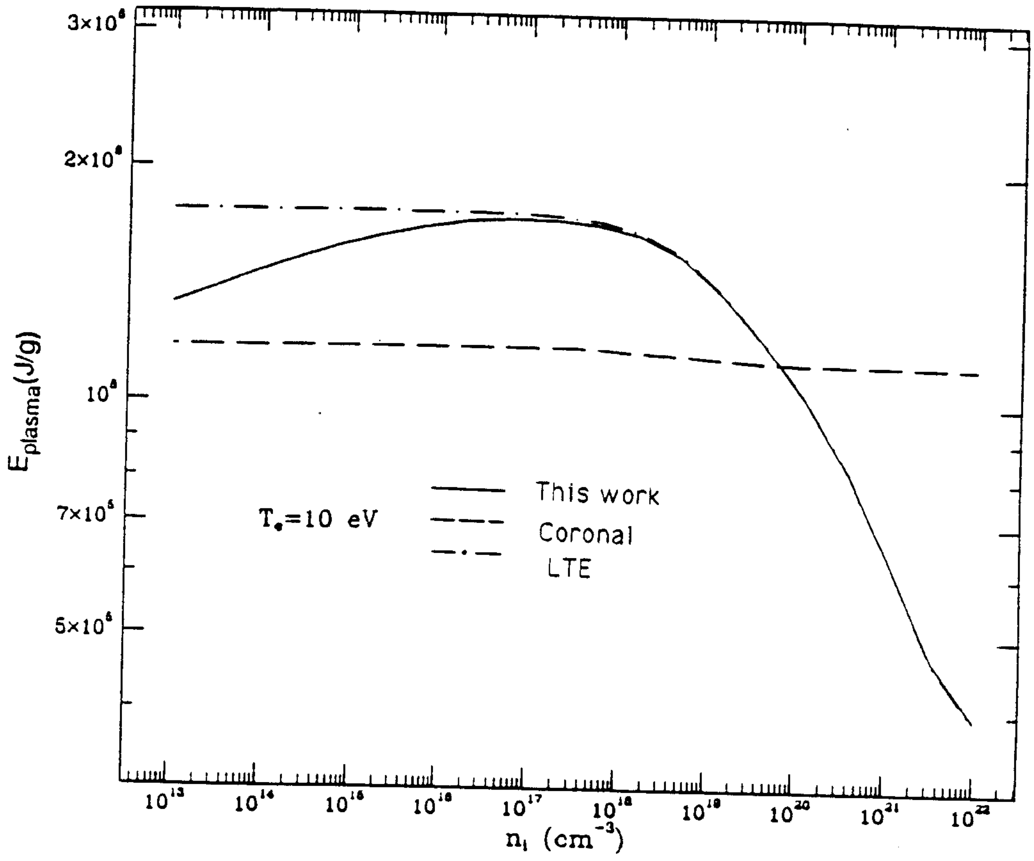

Figure 4.4: Comparison of different models in internal energy calculation

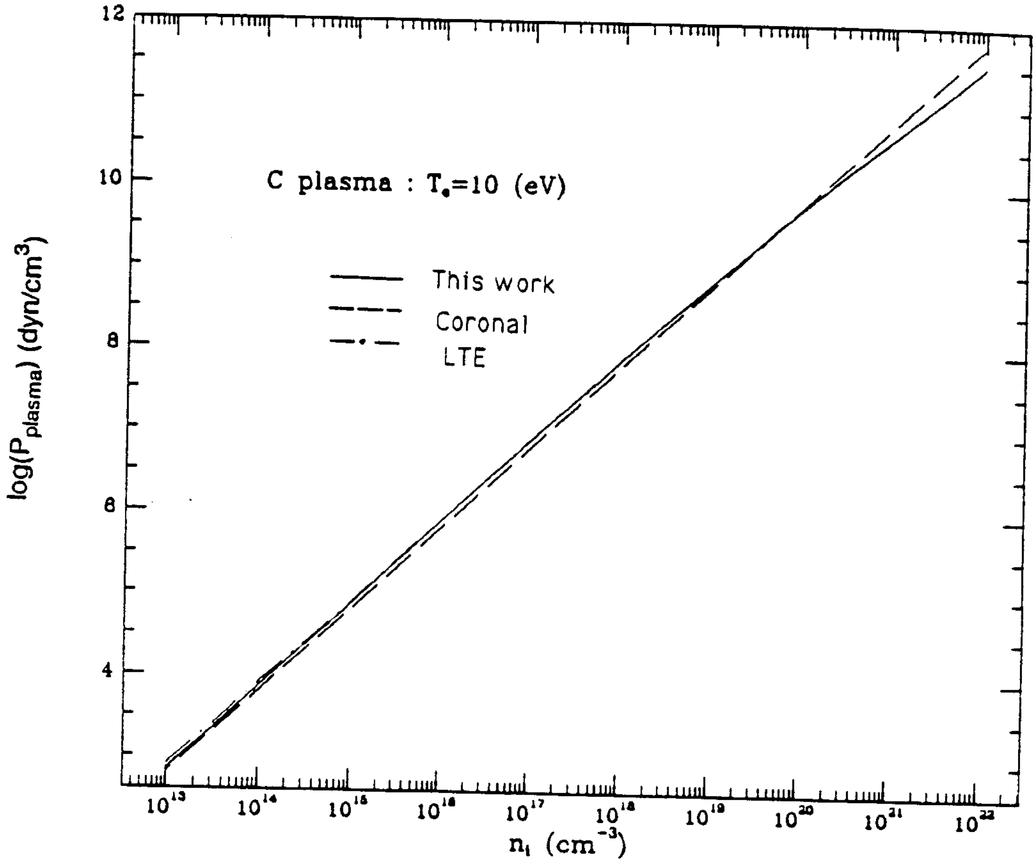

Figure 4.5: Comparison of different models in pressure calculation

temperature increases from 2 eV to 4 eV, the thermal ionization of the first ionized ion takes place and the increase of the abundance of the first ionized ions leads to the increase of the heat capacity.

The electron degeneracy parameter isothermal curves are shown in Figure 4.11. General speaking, for $\eta \leq -5$, the electrons are essentially nondegenerate. Our calculation shows that for $T \leq 100$ eV and $N_e \geq 10^{22}\ cm^{-3}$, electron degeneracy effects should be taken into account.

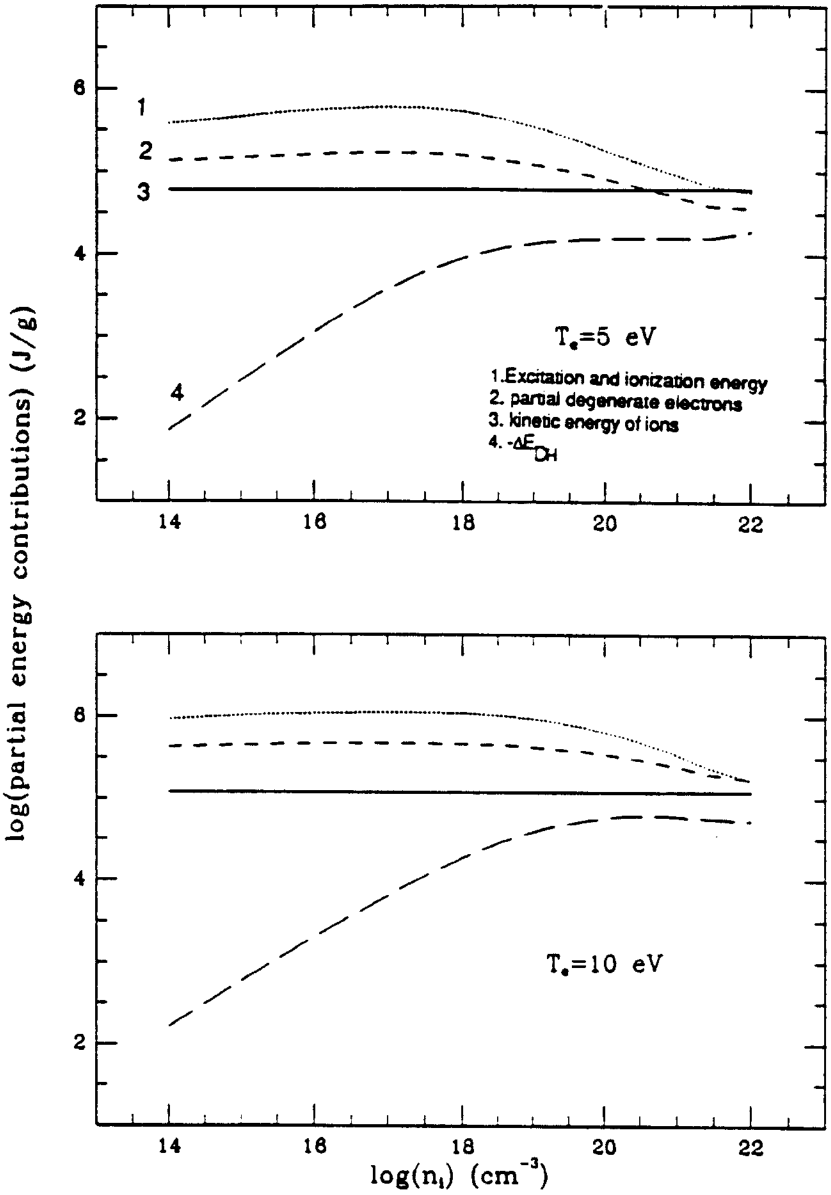

Figure 4.6: Comparison of different contributions to the internal energy for carbon plasmas at T=5eV and T=10eV

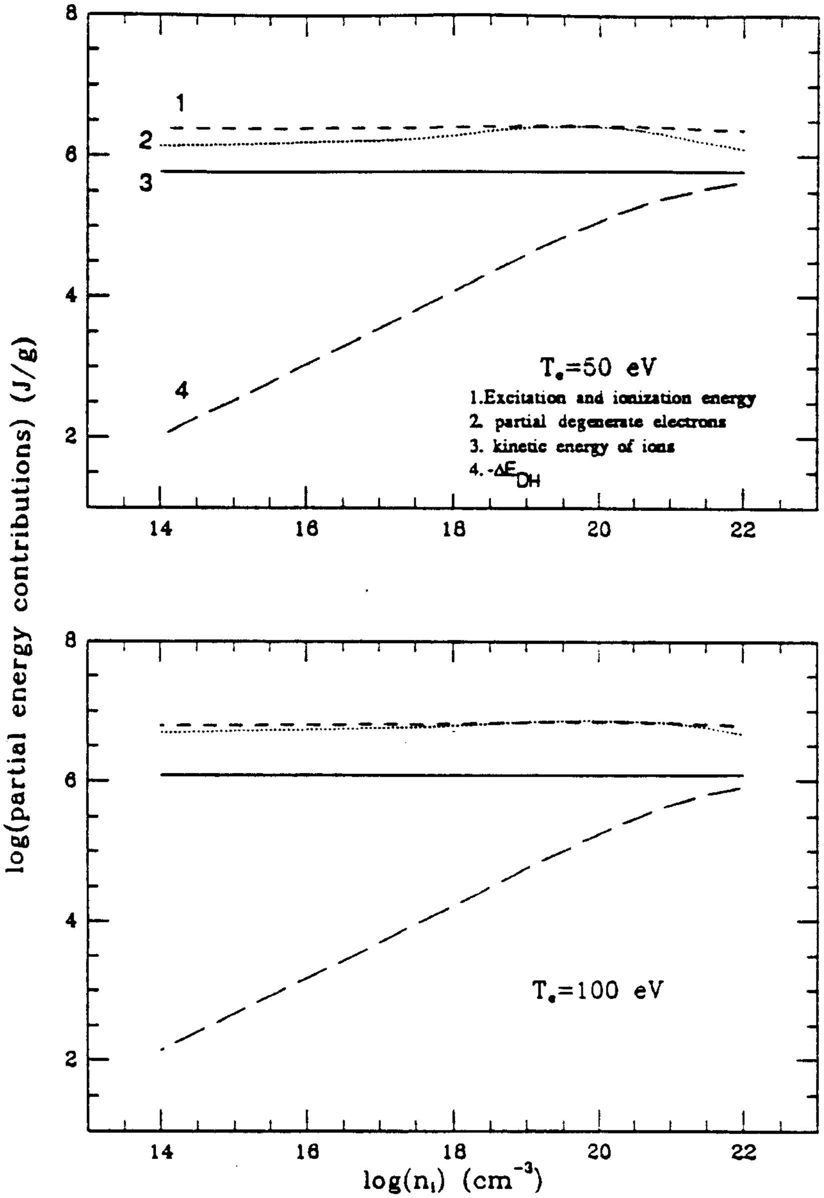

Figure 4.7: Comparison of different contributions to the internal energy for carbon plasmas at T=50eV and T=100eV

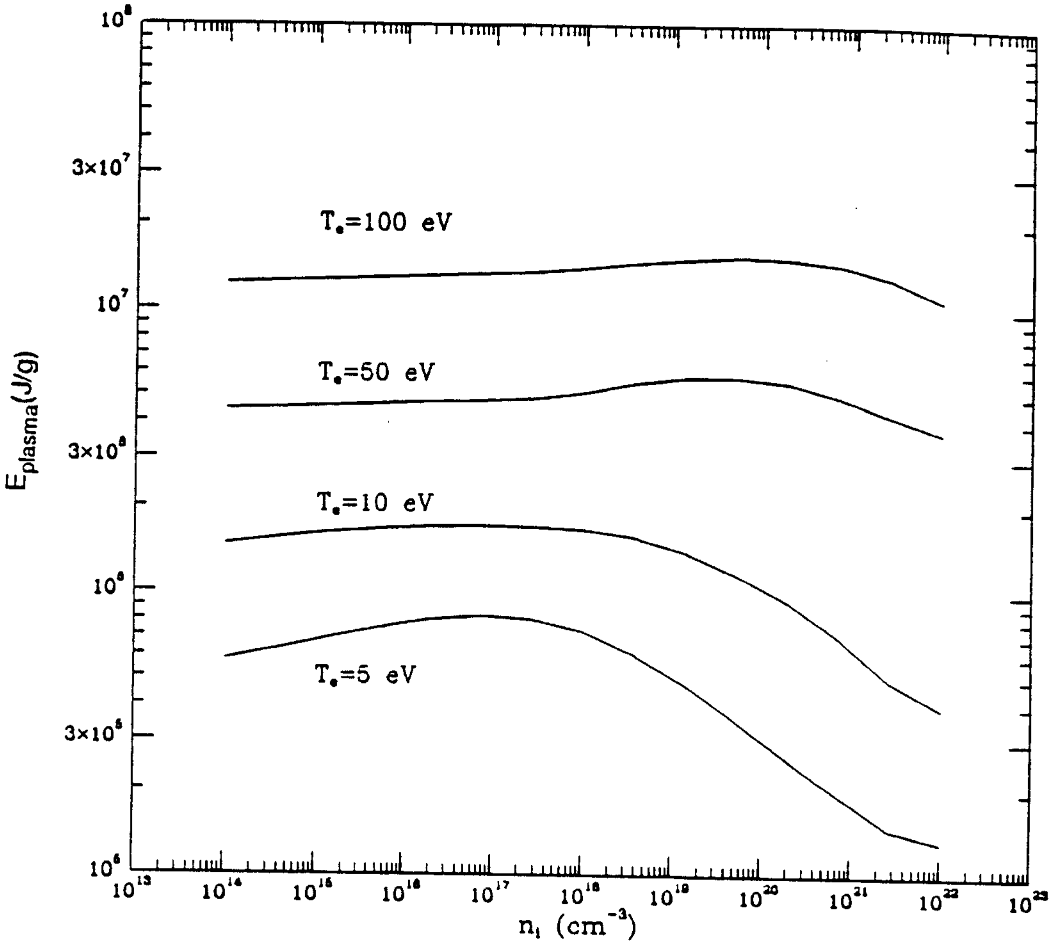

Figure 4.8: Isothermal curves for internal energy of carbon plasmas

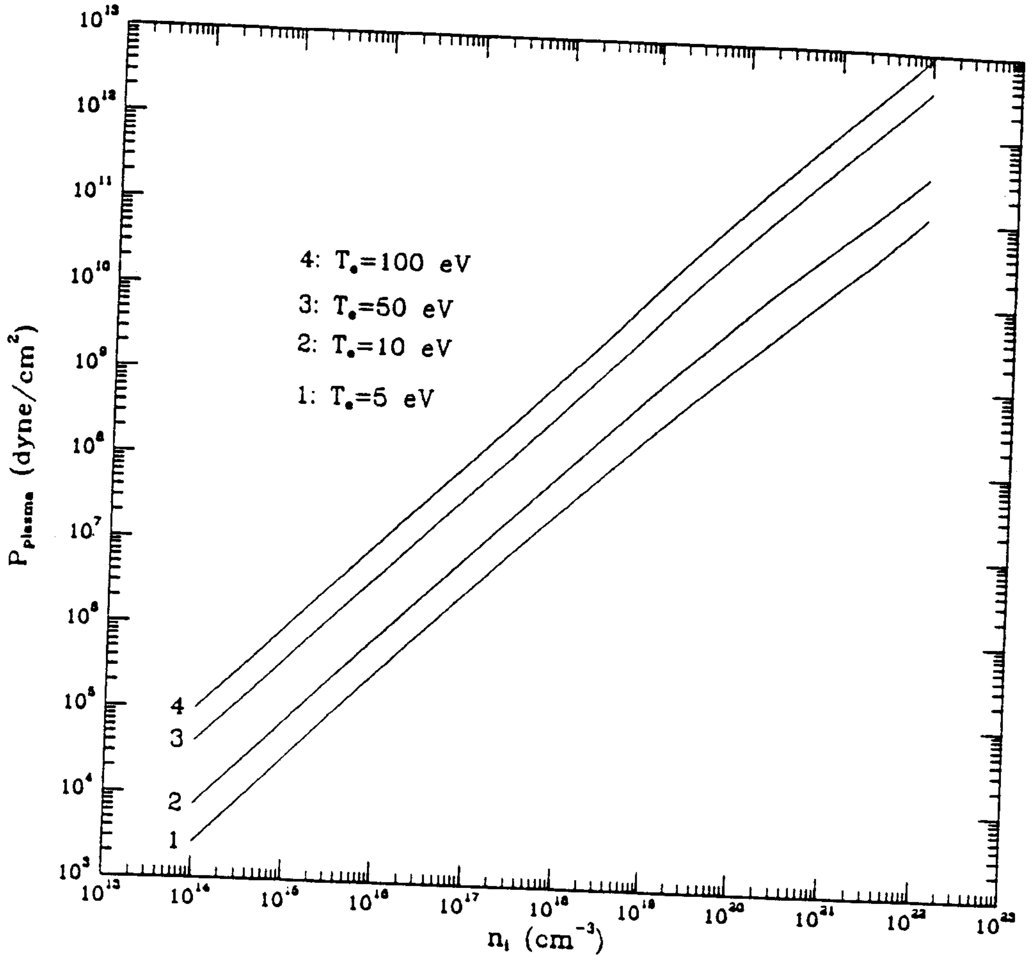

Figure 4.9: Isothermal curves for pressure of carbon plasmas

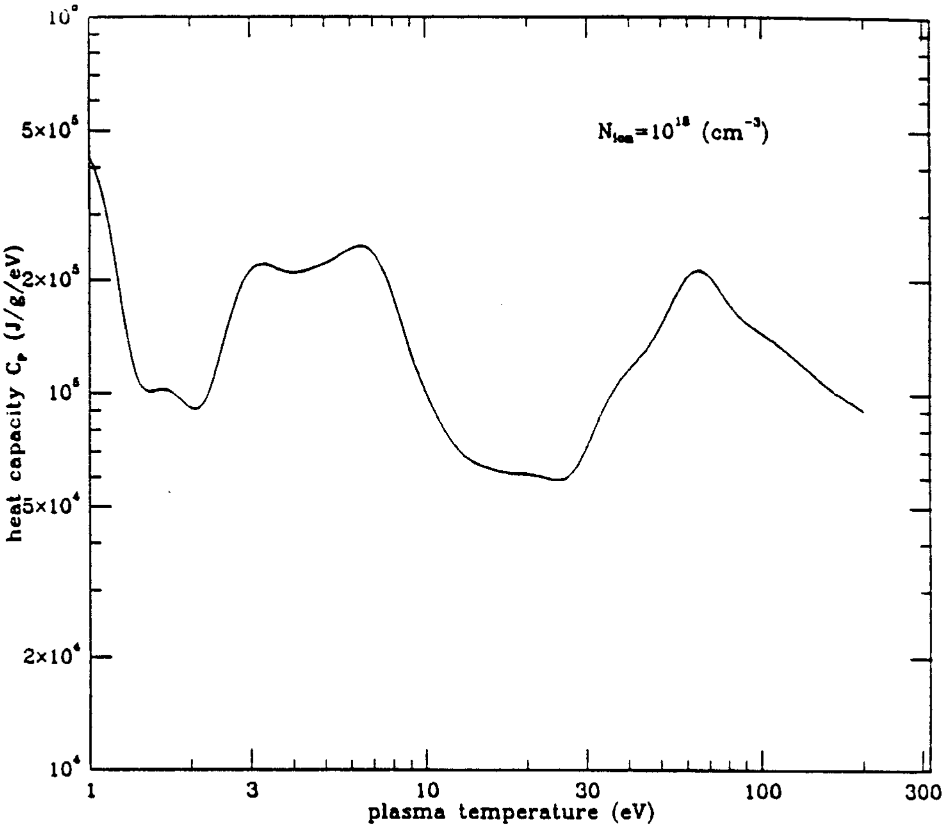

Figure 4.10: Heat capacity as a function of temperature for carbon plasma

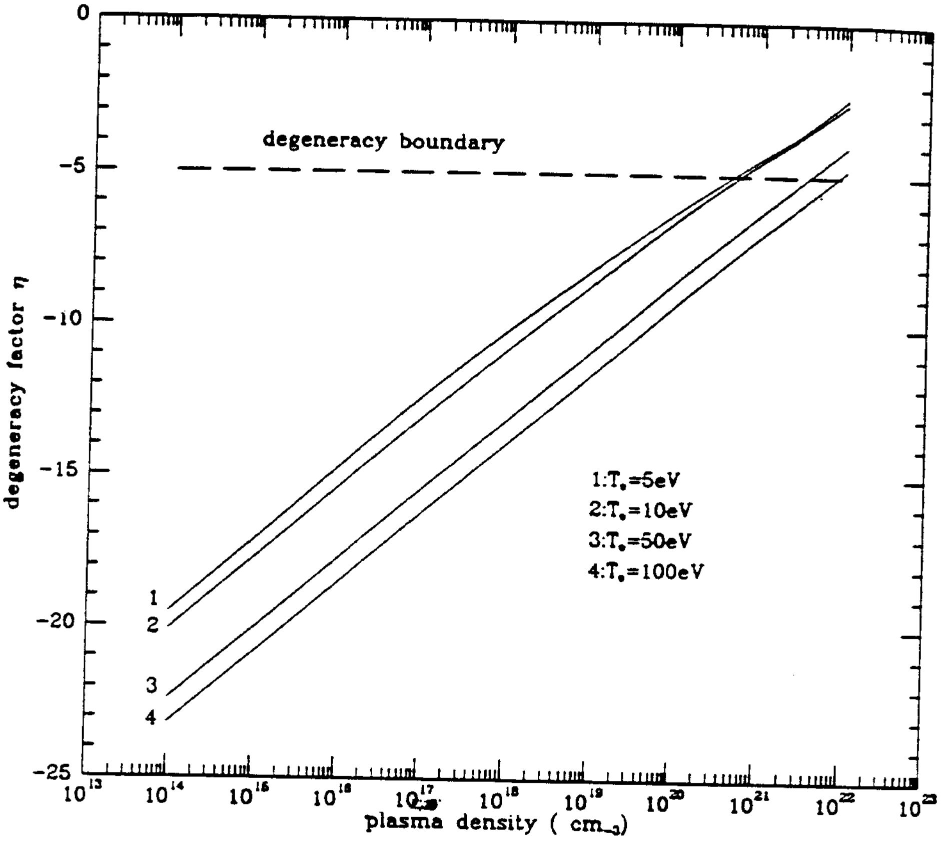

Figure 4.11: Isothermal curves for electron degeneracy parameter of carbon plasmas

4.5 Opacities of Non-LTE Plasmas

4.5.1 Computational Formulas

The opacity at any given frequency contains contributions from all possible transitions (*bound-bound, bound-free, free-free*) of all chemical species that can absorb photons at that frequency.

The contribution of a bound-bound spectral line to the monochromatic opacity is

$$\kappa_\nu(a;b) = \frac{\pi e^2}{mc} N_a f(a,b)\phi_\nu \tag{4.51}$$

where the profile factor is normalized to

$$\int \phi_\nu d\nu = 1 \tag{4.52}$$

The contribution due to photoionization is

$$\kappa_\nu = N_a \sigma_\nu^{bf}(a) \tag{4.53}$$

Here, N_a is the occupation number of the initial level.

The contribution of a free-free transition is

$$\kappa_\nu(N_z) = N_z N_e \sigma_\nu^{ff}(z) \tag{4.54}$$

where N_z is the number density of ions with charge z, N_e is the number density of electrons.

Other processes contributing to the opacity are coherent scattering and plasma oscillation scattering. Two forms of coherent scattering are Thomson (*radiation scattered by electrons*) and Rayleigh scattering (*radiation scattered by atoms or molecules*). Since Rayleigh scattering only becomes significant for cool plasmas, for ICF plasmas we only need to consider Thomson scattering:

$$\kappa_\nu = N'_e \sigma_T \tag{4.55}$$

where N'_e is the effective electron density which includes contributions from each bound electron for which the photon energy is greater than its binding energy, and

$$\sigma_T = \frac{8\pi e^4}{3m^2c^4} \tag{4.56}$$

is the Thomson scattering cross section. The scattering of photons by plasma oscillations can occur at low photon energies and high electron densities ($\geq 10^{19}\ cm^{-3}$). The plasma wave scattering coefficient can be written as

$$S^p_\nu = \begin{cases} (\omega_p^2 - \omega^2)^{1/2}/c & \text{if } h\nu \leq \hbar\omega_p \\ 0 & \text{if } h\nu > \hbar\omega_p \end{cases} \tag{4.57}$$

where

$$\omega_p = (\frac{4\pi e^2 N_e}{m_e})^{1/2} \tag{4.58}$$

is the plasma frequency.

Except for the scattering components, the monochromatic opacity must be corrected for stimulated emission. Summing over all levels and processes we have the general opacity expression[107]

$$\chi_\nu \ = \ \frac{\pi e^2}{mc}\sum_a \sum_{b>a} [N_a - (\frac{g_a}{g_b})N_b] f(a,b)\phi_\nu + \sum_a (N_a - N_a^* e^{-h\nu/kT})\sigma_\nu^{bf}(a)$$

$$+ \sum_{z>0} N_e N_z \sigma_\nu^{ff}(z,T)(1-e^{-h\nu/kT}) + N_e\sigma_T + S_\nu^p(1/cm) \tag{4.59}$$

The corresponding emissivity is[107]

$$\begin{aligned}\eta_\nu &= \frac{2h\nu^3}{c^2}[\frac{\pi e^2}{mc}\sum_a\sum_{b>a}(\frac{g_a}{g_b})N_b f(a,b)\phi_\nu + \sum_a(N_a^* e^{-h\nu/kT})\sigma_\nu^{bf}(a) \\ &+ \sum_{z>0} N_e N_z \sigma_\nu^{ff}(z,T)e^{-h\nu/kT}] \end{aligned} \tag{4.60}$$

Where η_ν is the emissivity in the units of $erg.cm^{-3}.sec^{-1}.Hz^{-1}.sr^{-1}$, N_a^* denotes the LTE occupation number of state a from the usual Saha-Boltzmann formula using the actual ion density $N_{z+1,0}$, namely,

$$N^*_{z,a} = N_{z+1,0}N_e \cdot 1.66 \times 10^{-22}(\frac{g_{z,a}}{g_{z+1,0}})T(eV)^{-3/2}e^{(I_{z,a}-\Delta E_{a0})/T} \tag{4.61}$$

In the LTE case, we have

$$\begin{aligned}\chi_\nu^* &= [\frac{\pi e^2}{mc}\sum_a\sum_{b>a} N_a^* f(a,b)\phi_\nu + \sum_a N_a^*\sigma_\nu^{bf}(a) \\ &+ \sum_{z>0} N_e N_z \sigma_\nu^{ff}(z,T)](1-e^{-h\nu/kT}) + N_e\sigma_T + S_{nu}^p(1/cm) \end{aligned} \tag{4.62}$$

and

$$\begin{aligned}\eta_\nu^* &= \frac{2h\nu^3}{c^2}e^{-h\nu/kT}[\frac{\pi e^2}{mc}\sum_a\sum_{b>a} N_a^* f(a,b)\phi_\nu \\ &+ \sum_a N_a^*\sigma_\nu^{bf}(a) + \sum_{z>0} N_e N_z \sigma_\nu^{ff}(z,T)] \end{aligned} \tag{4.63}$$

Writing $\kappa_\nu^* = \chi_\nu^* - S$, we see that $\eta_\nu^* = B_\nu\kappa_\nu^*$, as expected from the Kirchoff-Planck relation[107]. Hence one way to check whether the plasma is in LTE or not is to compare the spectra of κ_ν and η_ν/B_ν. If they are close, the plasma is close to LTE, otherwise the plasma is far from LTE.

The Roseland and Planck mean opacities are obtained by integrating the absorption, emission, and scattering coefficients over the photon energy. The Rosseland mean opacities are generally used in determining the transport characteristics of radiation through a medium, while the Planck mean opacities are used to calculate the rates of energy exchange between the plasma and radiation. In non-LTE cases, Planck mean opacities for absorption and emission need to be computed separately.

The Planck mean group opacities for absorption and emission in the photon energy range from $x_g = h\nu_g/kT$ to $x_{g+1} = h\nu_{g+1}/kT$ are defined by

$$\kappa_P^A(g) = \frac{1}{\rho}\frac{\int_{x_g}^{x_{g+1}} \kappa_\nu B_\nu(T_r)dx}{\int_{x_g}^{x_{g+1}} B_\nu(T_r)dx} \tag{4.64}$$

and

$$\kappa_P^E(g) = \frac{1}{\rho}\frac{\int_{x_g}^{x_{g+1}} \eta_\nu dx}{\int_{x_g}^{x_{g+1}} B_\nu(T_r)dx} \tag{4.65}$$

where ρ is the mass density, $B_\nu(T_r)$ is the Planck function characterized by the radiation temperature T_r.

The Rosseland mean group opacity is determined from a weighted average of the inverse of the total extinction coefficient, χ_ν. In this case, the radiative coefficients are weighted by the temperature derivative of the Planck function:

$$\kappa_R(g) = \frac{1}{\rho}\frac{\int_{x_g}^{x_{g+1}} (\frac{\partial B_\nu}{\partial T_r})dx}{\int_{x_g}^{x_{g+1}} (\frac{\partial B_\nu}{\partial T_r})\frac{1}{\chi_\nu}dx} \tag{4.66}$$

The mean opacities integrated over all photon energies can be computed from group opacities:

$$\kappa_{P,tot} = \frac{\sum_g \kappa_P(g) \int_{x_g}^{x_{g+1}} B_\nu(T_r)dx}{\int_0^\infty B_\nu(T_r)dx} \tag{4.67}$$

and

$$\kappa_{R,tot} = \frac{\int_0^\infty (\frac{\partial B_\nu}{\partial T_r})dx}{\sum_g \kappa_R^{-1}(g) \int_{x_g}^{x_{g+1}} (\frac{\partial B_\nu}{\partial T_r})dx} \tag{4.68}$$

4.5.2 Numerical Computations And Discussion

We have computed the monochromatic opacity and emissivity spectra for a pure carbon plasma at T=10 eV, $N_i = 10^{14} cm^{-3}$ and T=10 eV, $N_i = 10^{18} cm^{-3}$. In Figure 4.12 we show the spectra for the plasma at T=10 eV and $N_i = 10^{14} cm^{-3}$ calculated from a set of LTE occupation numbers. It is easy to see that the opacity spectrum and the emissivity spectrum are identical. This is the result of the Kirchoff-Planck relation[107]. However, when we used a new set of occupation numbers calculated from non-LTE CRE model, the resulting spectra are quite different. This is shown in Figure 4.13. Two points in the spectrum are of interest:

1. Inner shell contributions are very important. There are two *big jumps* in the continuum background, these are the photoionization edges of, respectively, the K-shell and L-shell.

2. The magnitude of emissivity is much smaller than that of opacity. This is because for a plasma at T=10 eV and $N_i = 10^{14} cm^{-3}$ the occupation

number of excited levels are much smaller than that estimated from LTE model, the plasma is far from the LTE.

Figure 4.14 shows the spectra for plasma at T=10 eV, $N_i = 10^{18} cm^{-3}$ with occupation numbers calculated from non-LTE CRE model. The opacity and emissivity spectra are close in this case. This is because as the density increases, the plasma is closer to LTE.

We have seen from Figure 4.12 to Figure 4.14 that the opacity and emissivity spectra are not smoothly varying functions of the photon energy. Thus, to evaluate the group opacity integrals with the desired accuracy, χ_ν and η_ν must be evaluated at a number of strategically placed points. Examples of this include points on either side of each photoionization edge, and several points in the vicinity of each *important* bound-bound transition energy. The integration scheme employed to evaluate the group opacities in our work is a trapezoidal method using logarithmic interpolation between adjacent points. By placing a reasonable number of mesh points near each *important* line transition energy (~ 11) and photoionization edge (3), the numerical accuracy of the integration is about a few percent.

The purpose of using group opacities rather than spectra themselves in the radiative hydrodynamic calculations is to reduce the computational time. However by doing so much of the detailed information is lost in the group opacities. When setting up a group structure (*e.g., number of groups and boundaries*), one must try to save as much information as possible. In Fig-

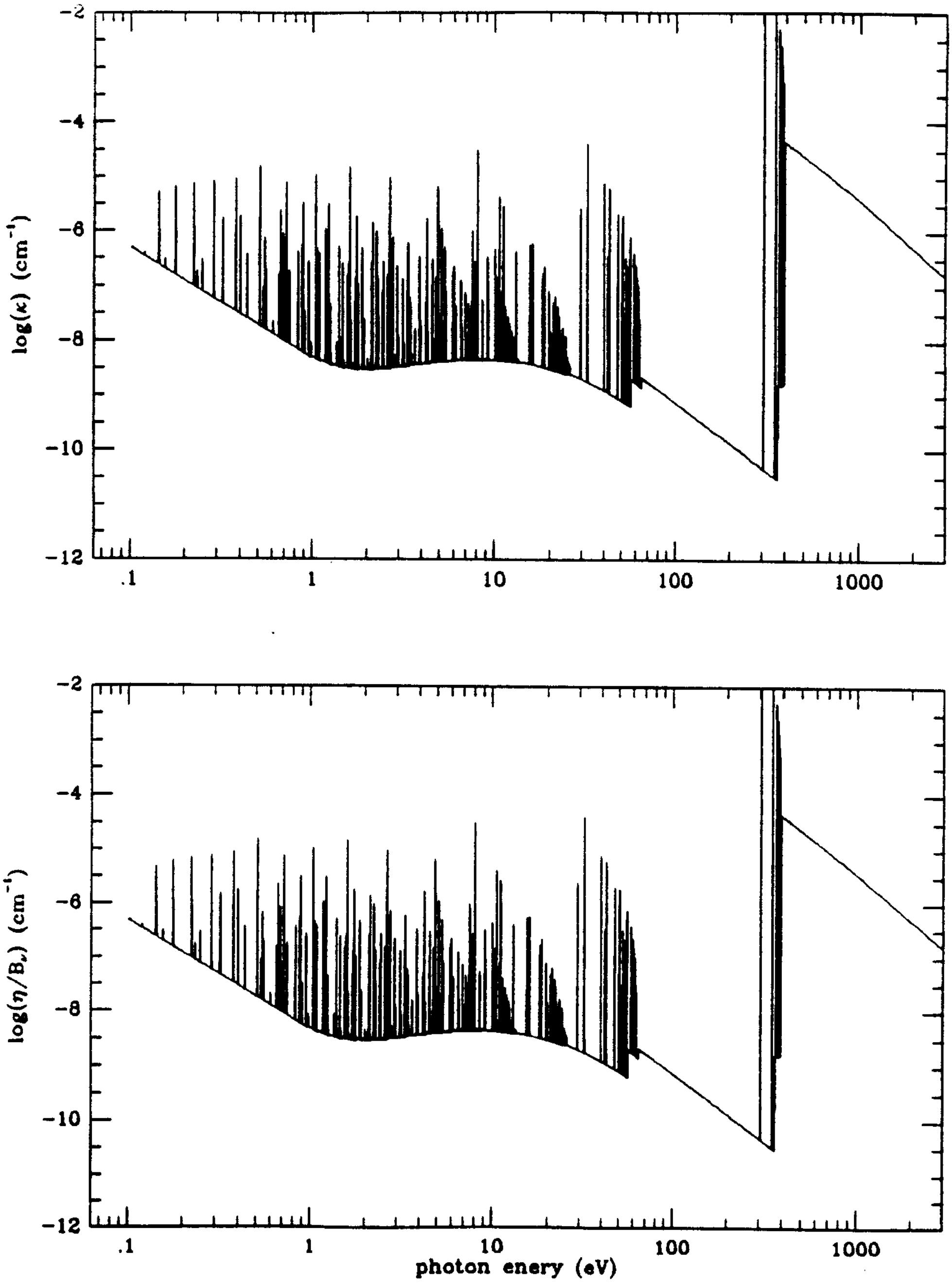

Figure 4.12: LTE result — Monochromatic opacity and emissivity spectra for C plasma at T=10 eV, $N_i = 10^{14} cm^{-3}$

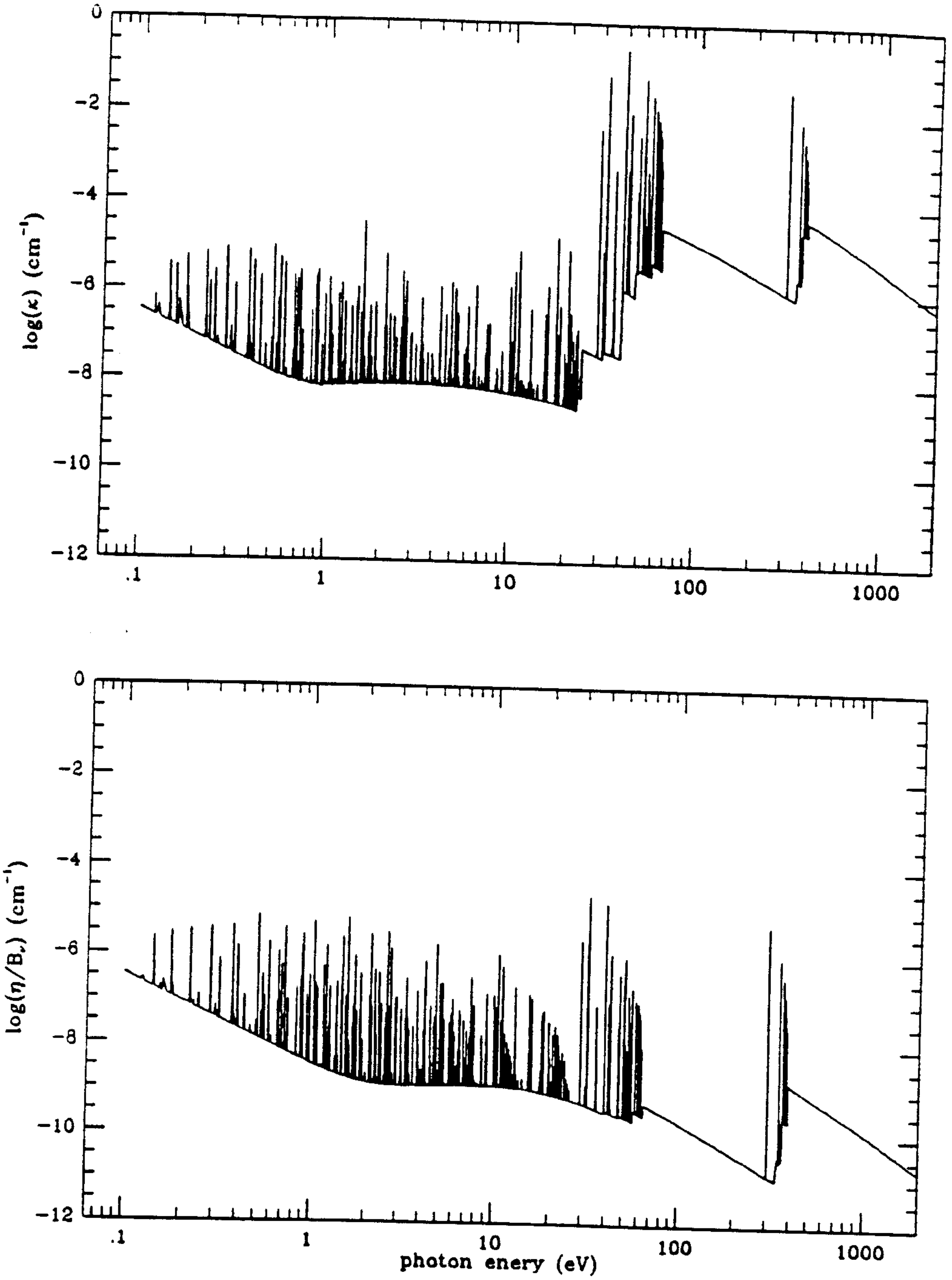

Figure 4.13: Non-LTE result — Monchromatic opacity and emissivity spectra for C plasma at T=10eV, $N_i = 10^{14} cm^{-3}$

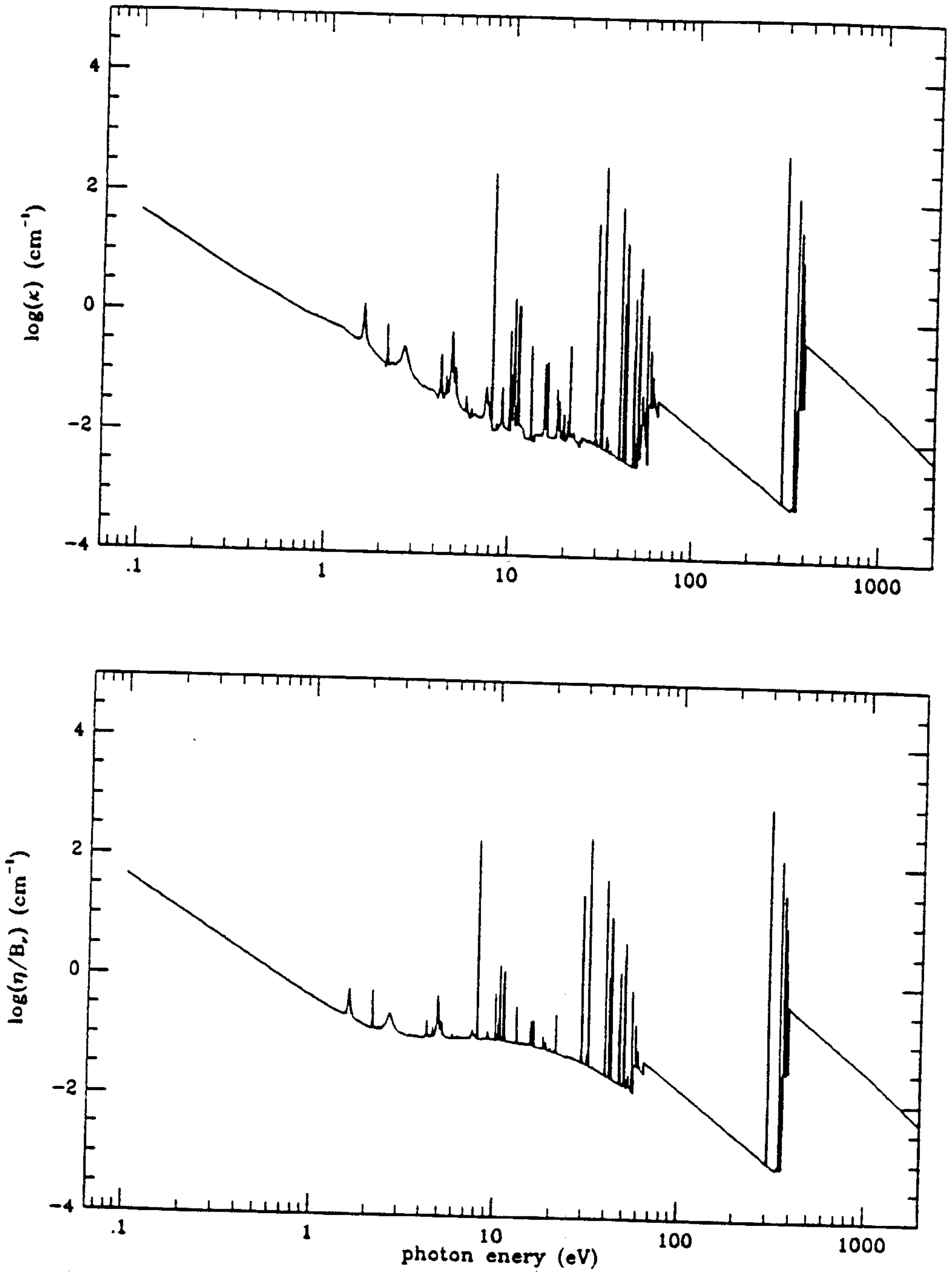

Figure 4.14: Non-LTE result — Monchromatic opacity and emissivity spectra for C plasma at T=10eV, $N_i = 10^{18} cm^{-3}$

ure 4.15 and Figure 4.16 we show the Planck and Rosseland group opacities calculated under different group structures and compare them with the corresponding spectra. In all cases, the group boundaries have been set in a " *prudent*" manner: we set narrow groups to bound those *important steep* regions, *i.e.*, important photoionization edges and lines. For the Planck mean opacity, 50 groups can give reasonably good representation to the spectrum, 20 groups can still give a roughly similar shape. Ten groups, however, misses almost all the important features except that K-shell jump. For the Rosseland mean opacity, the results are not very sensitive to the group structure. Even 10 groups can contain most of the important features of the spectrum. This is because the Rosseland mean is weighted with the inverse of the extinction coefficient and hence the "wings" of the lines and the continuum background are more important than the line center. The *steep jump* effect is less important in the Rosseland mean. Our calculations show that in radiative hydrodynamics computations, 50 group mean opacities are necessary in order to have the desired accuracy.

The effects of the accuracy of atomic data on opacity has always been questioned. In order to check this effect, we have computed the opacities with two sets of different atomic data but exactly the same plasma model. The 'accurate' atomic data are calculated using the Hartree-Fock method, while the 'approximated' atomic data are calculated from a hydrogenic model. The opacity results are shown in Figure 4.17 and Figure 4.18. It can be seen that

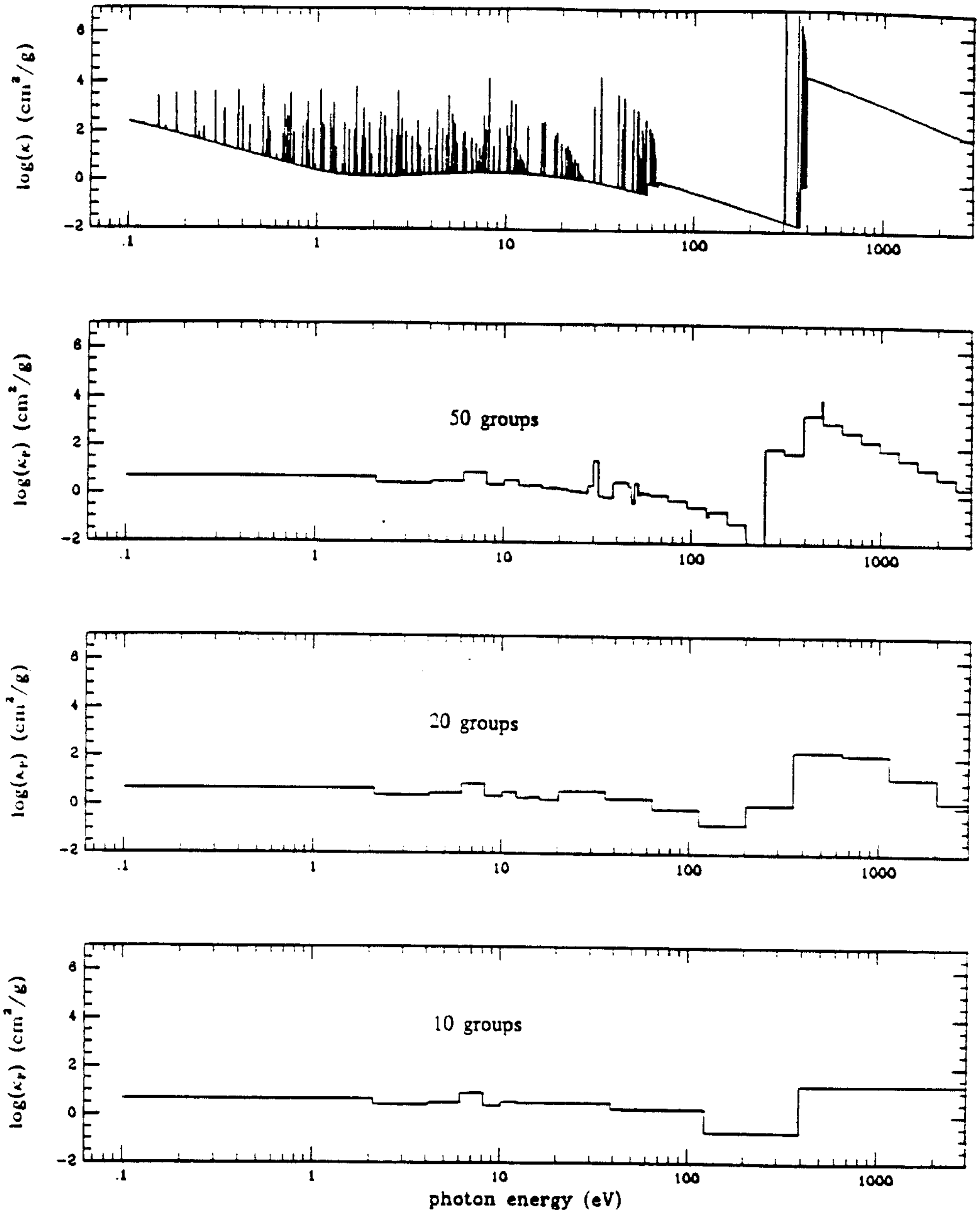

Figure 4.15: Comparison of Planck group opacity in three different group structure for C plasma at T=10eV, $N_i = 10^{14} cm^{-3}$

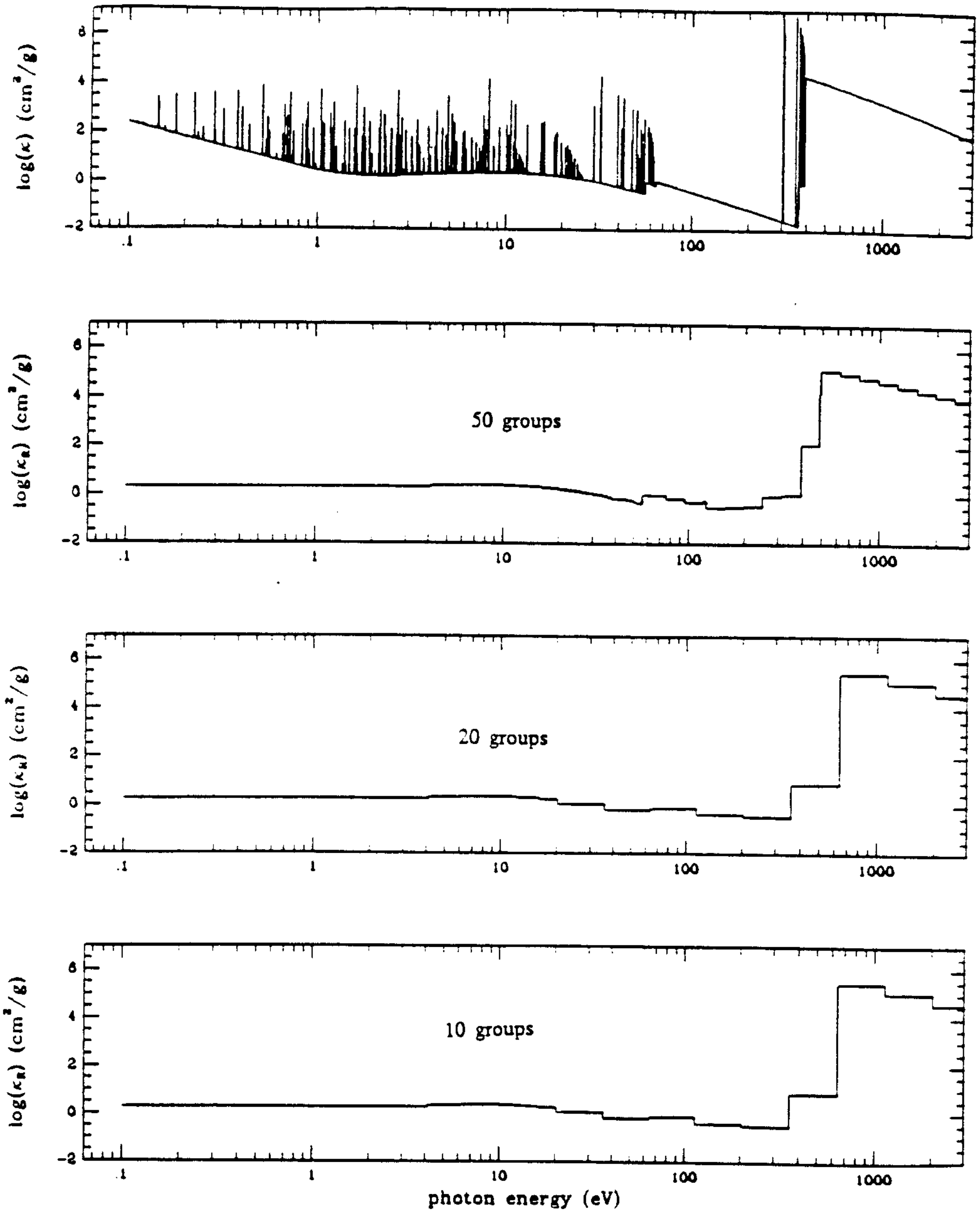

Figure 4.16: Comparison of Rosseland group opacity in three different group structure for C plasma at T=10eV, $N_i = 10^{14} cm^{-3}$

the opacities are quite sensitive to the atomic data. The differences of opacities from the two sets of atomic data can be as large as a factor of 5 in some groups. This shows that high quality atomic data are necessary for obtaining accurate opacities. On the other hand, however, the general features of the two sets of opacities are close. Hence, as a first order estimation, hydrogenic atomic data can still be a good choice.

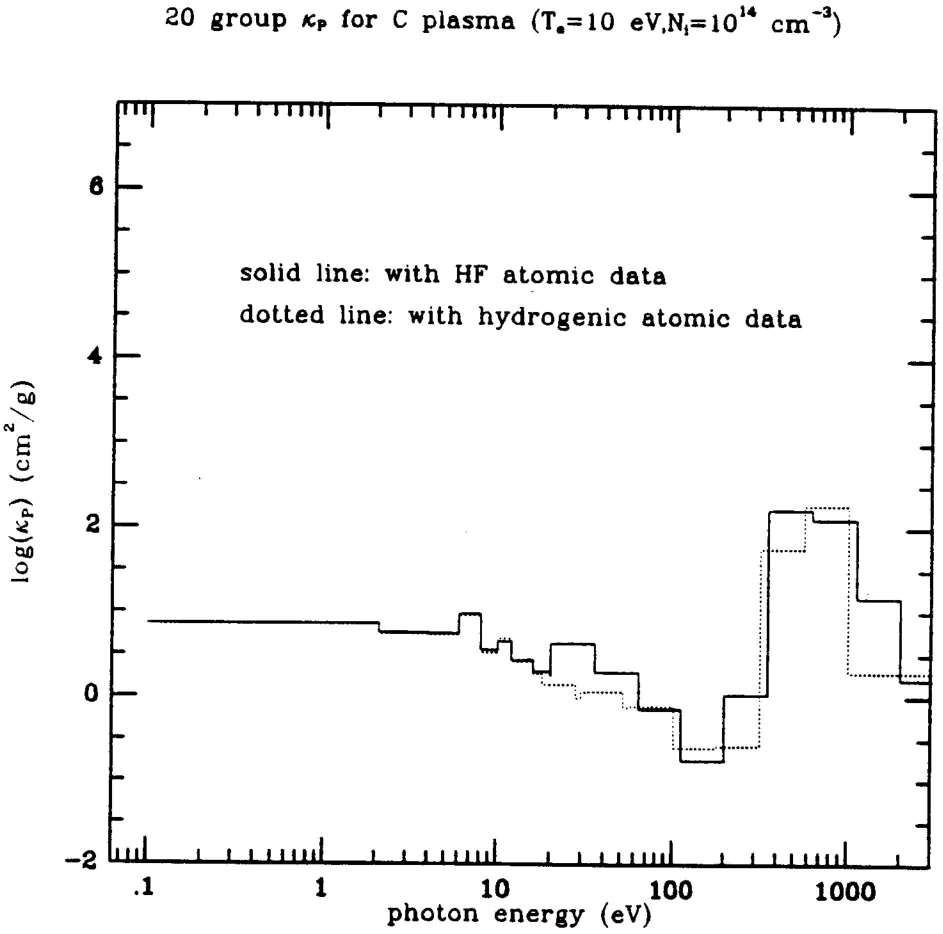

Figure 4.17: Affect of the accuracy of atomic data on Planck mean opacity

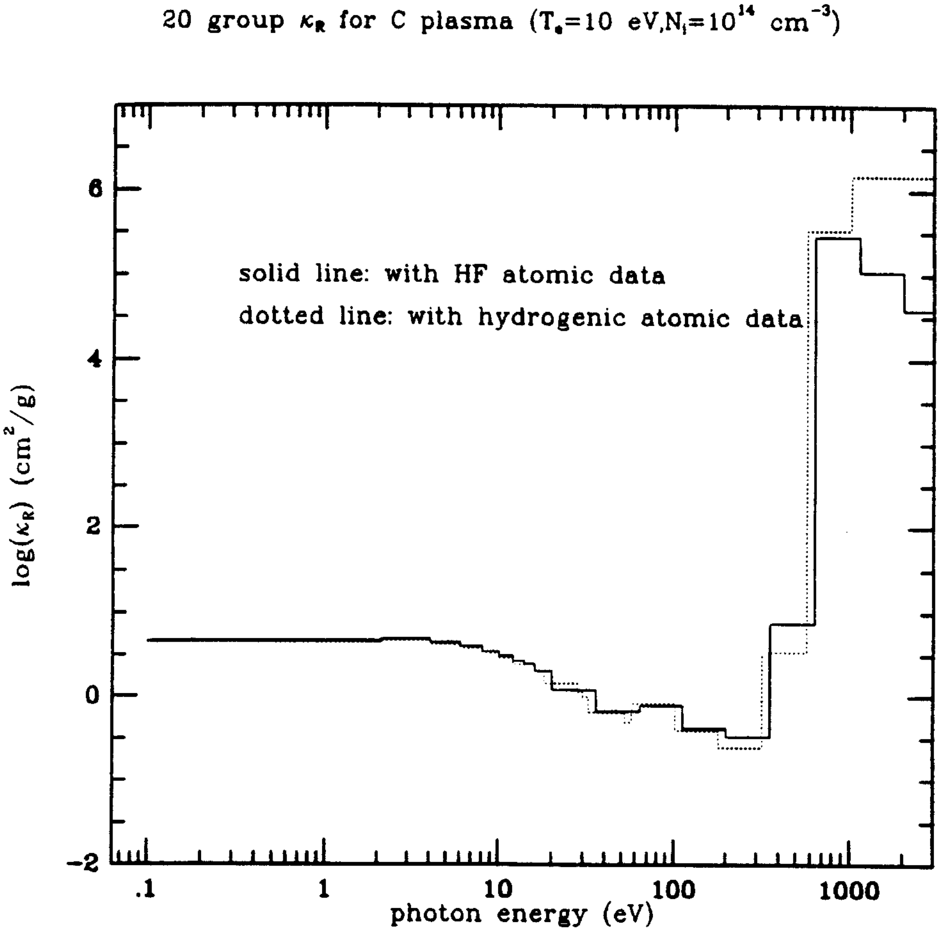

Figure 4.18: Effect of the accuracy of atomic data on Rosseland mean opacity

4.6 Computational Procedure And Data Management

We have developed a suite of computer programs for doing the computations of equations of state and opacities for non-LTE plasmas. This suite consists of three parts:

1. atomic data generator;
2. interface between atomic data and EOS and opacity calculations;
3. computations of EOS and opacities

There are five major programs included in the atomic data generator and they have been discussed in detailed in the second chapter. The rather huge amount of output of atomic data from the atomic data generator are stored in catalogue files. For example, the atomic data for neutral carbon are stored in five different files:

1. c6.lev — stores all the atomic structure data;
2. c6.osv — stores oscillator strengths and transition energies;
3. c6.pcs — stores photoionization cross sections;
4. c6.eac — stores electron collisional data;
5. c6.pac — stores proton collisional data.

The file names are designed for easy identification: c is the atomic symbol, 6 is the number of bound electrons, for the first ionized carbon ion, we have c5.lev, c5.osv, and so on. These raw atomic data need to be analyzed, processed and mapped to the formats suitable for input to the EOS and opacity computations. The "interface" stage involves selecting atomic data for specific levels, filling in the requested number of Rydberg energy levels based on a scaled hydrogenic approximation, and computing the rate coefficients from the raw atomic data. The analysis and interface of atomic data are carried out by the code ATABLE, which produces the atomic data files for the EOS and opacity computation code EOSOPC. Since the amount of atomic data required for the EOS and opacity calculations is rather large, especially for mixtures of elements, all the atomic data cannot be stored in the memory at the same time during the computation because of the limitation of computer memory. EOSOPC has been designed in such a way that the atomic data are stored in the memory ion by ion, *i.e.,* only one ion's data is stored in the memory. This reduces the memory requirement and enables the calculation to include more levels. A simplified flow chart of EOSOPC is shown in Figure 4.19.

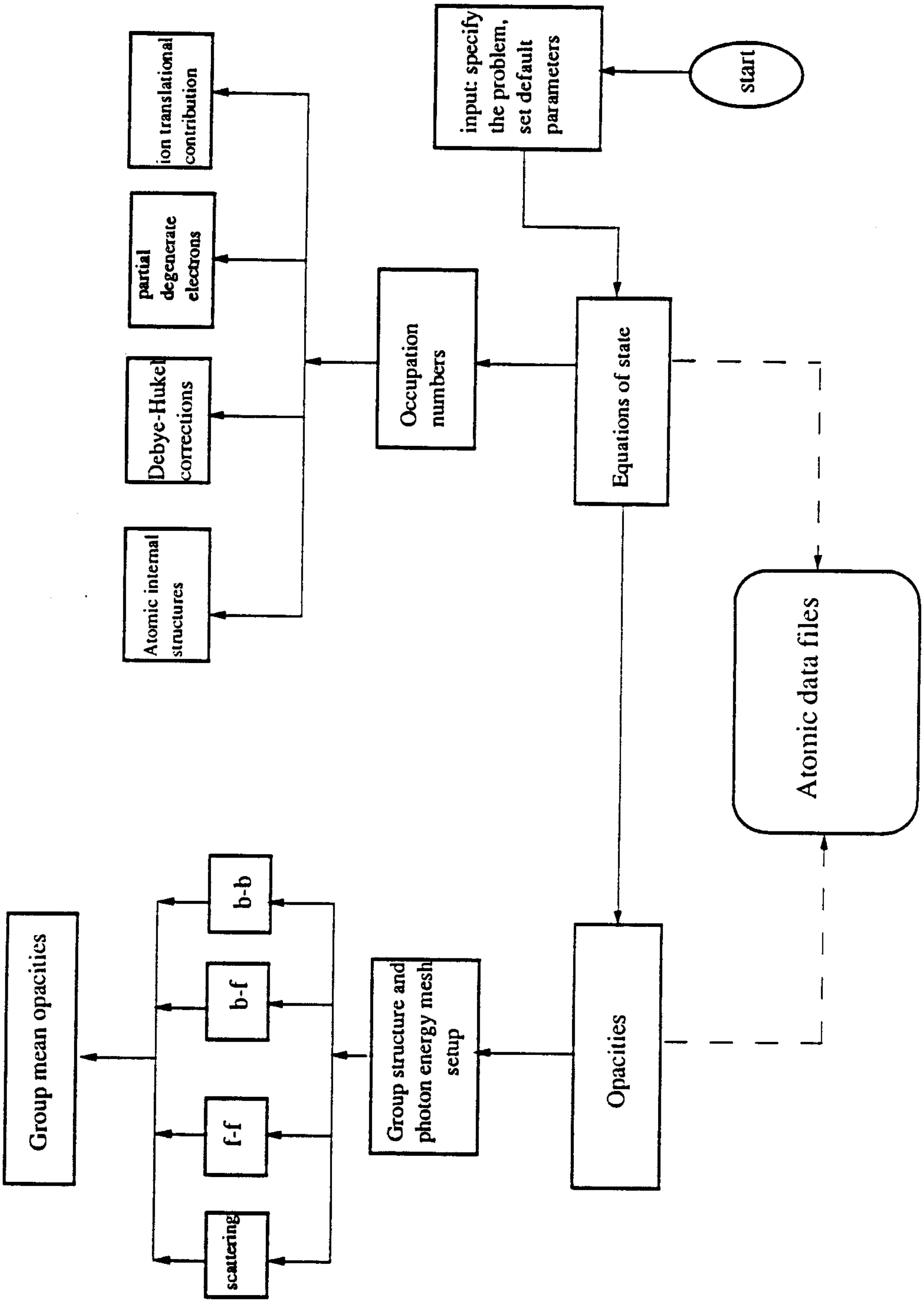

Figure 4.19: Simplified Flow Chart of EOSOPC

Chapter 5

Conclusions

I. Basic Atomic Data Calculation Suite

With the primary aim of generating large scale, high quality, atomic data for ICF/MCF research applications, a basic atomic data calculation suite has been created. The major features of this suite of programs are:

- **Atomic structure and radiative data:** Atomic energy levels, oscillator strengths and photoionization cross sections are calculated by using the Hartree-Fock method. The non-relativistic single configuration approximation is assumed for large scale calculations (*default setup*). The multiconfiguration calculation plus relativistic correction can be done to generate high accuracy data for specified levels. Generally, the accuracy of the data is better than fifteen percent for the single configuration HF calculations and a few percent for the multiconfiguration

HF calculations.

- **Atomic collisional data:** Electron impact excitation and ionization cross sections can be calculated using three different methods (*distorted wave approximation, first Born approximation and semiclassical impact parameter method*). A factor of 1.5 to 2 accuracy is expected for most calculations. Proton impact excitation and ionization cross sections are calculated using the plane-wave Born approximation. For high energy incident protons, the calculation can provide good estimation for the cross sections (within a factor of 2).

- **User friendly setup:** In large scale atomic calculations, one of the difficulties for users without much atomic calculation experience is the preparation of input files. We have developed a state generator which can generate a LS-coupling scheme table for most levels of each ion automatically with only a very simple interactive input. Also, the default setup of all programs has been checked carefully to insure the convergence of the calculations.

II. Al Kα X-Ray Spectrum Analysis

The applications of atomic data generated from our atomic calculation package to analyze the Al Kα x-ray spectrum obtained in recent PBFA II experiment has produced the following results:

- Each main peak and important high degree term-dependent structure in the spectrum has been identified. Our calculated wavelengths of Kα transitions agree well with the experimental data.

- Our collisional-radiative-equilibrium calculation with the inclusion of proton impact effects indicates that the peak electron temperature of the target plasma should be in the range of 40 eV to 60 eV.

- Our calculated spectrum for the thin plasma model qualitatively explains the experimental spectrum. By comparing our calculated spectrum with the experiment data and that of radiative transfer calculations we find that line opacity is very important to Kα x-ray interpretation.

III. Equations of State And Opacities

We have applied our atomic data to compute the equations of state and opacities of non-LTE plasmas. A non-LTE collisional-radiative equilibrium model which takes account of pressure ionization effects self-consistently has been developed. This model convergences to the Coronal equilibrium at low density and merges to LTE smoothly at high density. Non-ideal effects including pressure ionization, Debye-Hükel correction for charged particle interactions and electron degeneracy have been treated in the calculations of equations of state. Our calculations show that the contributions from partial degenerate free electrons and atomic internal structures to the equations of state are dominate except for low temperature and high density plasmas. Electron degeneracy effects are not obvious in the plasma conditions of our interest.

Our opacity computation code can setup the group structure automatically in a *prudent* manner. The calculation results show that the Planck mean opacities are very sensitive to the selection of the group structure. In order to have reasonable accuracy, 50 groups or more are recommended in practical multigroup radiative transfer calculations. The Rosseland mean opacities are less sensitive to the group structure, however, we still need to have at least 10 groups to insure the calculation accuracy. We have also checked the sensitivity of opacities to the accuracy of atomic data. Our results indicate that opacities are quite sensitive to the accuracy of atomic data. Accurate atomic data are necessary for obtaining high quality opacities.

IV. Further Considerations

- Our current atomic data calculations are basically limited to low-Z and intermediate-Z elements because we consider only the LS-coupling approximation and treat the relativistic effects as perturbations. High-Z elements are actually very important to ICF research. To properly treat these, we must extend our atomic data calculation package to including high-Z atomic data.

- The accuracy of collisional data is about a factor of 2 in our current calculations. This may be acceptable for preliminary investigation in practical plasma diagnostic applications. For doing detailed spectroscopy analysis, we may require better collisional data. It is important to have the capability to generate or/and access high quality atomic collisional data.

- It has been shown that ion beam-induced transitions offer many possibilities for deducing plasma conditions in ICF target experiments. Experimental Kα spectra in conjunction with a judicious mix of hydrodynamics simulations and non-LTE radiative transfer calculations can lead to an improved understanding of beam-plasma interaction physics. This issue is currently under study at UW-Madison.

Bibliography

[1] J.J. Watrous, G.A. Moses, R.R. Peterson,"*Z-PINCH - A Multifrequency Radiative Transfer Magnetohydynamics Computer Code,*" University of Wisconsin Fusion Engineering Program Report UWFDM-584, June 1984.

[2] O. Yasar, " *A Computational Model for Z-Pinch Plasma Channels,*" University of Wisconsin Fusion Technology Institute Report UWFDM-823, Feb. 1990.

[3] R.R. Peterson, G.A. Moses and G.W. Cooper, *Nucl. Tech./Fusion* **1.**, 377 (1981).

[4] J.J. MacFarlane, P. Wang and G.A. Moses,"*Implications of Non-LTE Buffer Gas Effects on ICF Target Chamber Design,*" Submitted to *Fusion Technology*, (1990).

[5] J. Bailey, et al.,"*Observation of $K\alpha$ X-Ray Satellites from a Target Heated by an Intense Ion Beam,*" *Lasers and Particle Beams*, (1990).

[6] G.C. Pomraning,"*The Equations of Radiation Hydrodynamics*," Prehaman Press, (New York, 1973).

[7] G.A. Moses, et al. *Fusion Technology* **15**, 756 (1989).

[8] W.J. Hogan, *Fusion Technology*, **15**, 541 (1989).

[9] J.J. Duderstadt, G.A. Moses, "*Inertial Confinement Fusion*", Wiley Interscience, (New York, 1982).

[10] D. Duston, et al. *Phys. Rev.* **A27**, 1441 (1983).

[11] J.J. MacFarlane. P. Wang, O. Yasar and G.A. Moses, *Bull. Am. Phys. Soc.* **34**, 2151, (1989).

[12] P. Wang, J.J. MacFarlane and G.A. Moses, *Bull.Am.Phys.Soc.* **35**, 2120 (1990).

[13] J.J. MacFarlane, P. Wang, *Bull.Am.Phys.Soc.* **35**,2022 (1990).

[14] A.K. Pradhan, *Physica Scripta* **35**, 840 (1987).

[15] M.J. Seaton, in "*Electronic And Atomic Collisions*", eds. H.B.Gilbody, et al., Elsevier Science Publishers B.V., 1988.

[16] J.J. MacFarlane,*Comput. Phys. Commun.* **56**, 259 (1989).

[17] L.D. Landau, E.M. Lifshitz, "*Statistical Physics,*" Addison-Wesley, (Reading, Mass., 1958).

[18] A.B. Cambel, et al. "*Real Gases*", Academic Press, (New York, 1963).

[19] J.P. Cox, R.T. Giuli,"*Principles of Stellar Structure*" **1**, Gordon and Breach, (New York, 1968).

[20] D.G. Hummer, D. Mihalas, *Ap.J.* **331**, 794 (1988).

[21] W. Ebeling, W.D. Kraeft, D. Kremp, "*Theory of Bound States and Ionization Equilibrium in Plasma and Solids*", Berlin: Akdemie, 1976.

[22] W. Ebeling, et al., *Ap.J.* **290**, 24 (1985).

[23] R.P. Feynman., et al., *Phys. Rev.* **75**, 1561 (1949).

[24] G. Fontaine, et al., *Ap.J.Supple.* **35**, 293 (1977).

[25] A.K. Pradhan, *Private Communication*, August 1990.

[26] C.F. Fischer,"*The Hartree-Fock Method for Atoms*", John Wiley and Sons, (New York, 1977).

[27] R.D. Cowan, "*The Theory of Atomic Structure and Spectra*", University of California Press, (Berkeley, California, 1981).

[28] D.R. Hartree, *Proc. Cambridge Phil. Soc.* **24**, 111 (1928).

[29] J.C. Slater, *Phys. Rev.* **81**, 385 (1951).

[30] P.A.M. Dirac, *Proc. Cambridge Phil. Soc.* **26**, 376 (1930).

[31] R.D. Cowan, *Phys. Rev.* **163**, 54 (1967).

[32] R.W.P. McWhirter, H.P. Summers, in "*Applied Atomic Collision Physics*" **2**, eds. H.S.W. Massey, et al., Academic Press, Inc., (New York, 1984).

[33] A. Chapman, T.G. Gowling, "*The Mathematical Theory of Non-uniform Gases*", 3rd ed., Cambridge Univ. Press, (New York, 1970).

[34] H. Griem,"*Plasma Spectroscopy*", McGraw-Hill, (New York, 1964).

[35] D. Salzmann, *Phys. Rev.* **A20**, 1704 (1979).

[36] D. Mosher, NRL Memorandum Report 2563 (March 1973).

[37] R.W.P. McWhirter, T.F. Stratton, in "*Plasma diagnostic Techniques*", eds. R.H. Huddlestone, et al., Academic Press, (New York, 1965).

[38] J.C. Slater, *Phys. Rev.* **34**, 1923 (1929).

[39] H.N. Russel, F.A. Saunders, *Ap. J.* **61**, 38 (1925).

[40] I.I. Sobelman, "*Atomic spectra and Radiative Transitions*", Springer-Verlag, (New York, 1979).

[41] U. Fano, *Phys.Rev.* **A140**, 67 (1965).

[42] E.U. Condon, H. Odabasi, "*Atomic Structure*", Cambridge, (New York, 1980).

[43] A. Hibbert, *Comput. Phys. Commun.* **9**, 141 (1975).

[44] A. Hibbert, *Comput. Phys. Commun.* **1**, 359 (1970); **2**, 180 (1971); **6**, 59 (1973).

[45] C.F. Fischer, *Phys. Rev.* **A34**, 1667 (1986).

[46] S. Farga, et al., *Comput. Phys. Commun.* **47**, 159 (1987).

[47] H.A. Bethe, E.E. Salpeter, "*Quantum Mechanics of One- and Two-Electron Atoms*", Springer-Verlag, (Berlin, 1972).

[48] J.C. Slater, "*Quantum Theory of Atomic Structure*" **2**, McGraw-Hill, (New York, 1960).

[49] L. Armstrong Jr., S. Feneuille,*Adv. At.Mol.Phys.* **10**, 1 (1974).

[50] R. Glass, A. Hibbert, *Comput. Phys. Commun.* **16**, 19 (1978).

[51] S. Fraga, et al., *Phys. Rev.* **A34**, 23 (1986).

[52] T. Koopmans, *Physica* **1**, 104 (1934).

[53] C.F. Fischer, *Comput. Phys. Rep.* **3**, 273 (1986).

[54] L. Brillouin, *J.Phys. Radium* **3**, 373 (1932).

[55] C.F.Fischer, *Comput. Phys. Commun.* **14**, 145 1978.

[56] N.S. Scott, A. Hibbert,*Comput. Phys. Commun.* **28**, 189 (1982).

[57] M.E. Riley, D.G. Truhlar, *J. Chem. Phys.* **63**, 2182 (1975).

[58] D.J. Kennedy, S.T. Manson, *Phys. Rev.* **A5**, 227 (1972).

[59] J.W. Cooper, *Phys.Rev.* **128**, 681 (1962).

[60] F. Herman, S. Skillman, "*Atomic Structure Calculations*", Prentic-Hall, (Eaylewood Cliffs, N.J., 1963).

[61] L.V. Chernysheva, et al., *Comput. Phys. Commun.* **11**, 57 (1976).

[62] C.F. Fischer, "*Beam-Foil Spectroscopy*" '**1**, eds. I.A.Sellin and D.Pegg, Plenum Press, (New York, 1976).

[63] H.R. Griem, "*Plasma Spectroscopy*", McGraw-Hill, (New York, 1964).

[64] C.R. Cowley, " *The Theory of Stellar Spectra*", Gordon and Breach, (New York, 1970).

[65] I.I. Sobelman, et al.," *Excitation of Atoms and Broadening of Spectral Lines*", Springer-Verlag, Berlin, Heidelery, (New York, 1981).

[66] H.R. Griem, "*Spectral Line Broadening by Plasmas*", Academic Press, (New York, 1974).

[67] H.R. Griem, *Phys. Rev.* **165**, 258 (1968).

[68] J.D. Hey, *J.Q.S.R.T.* **16**, 575 (1976).

[69] J.D. Hey, R.J. Bryan, *J.Q.S.R.T.* **17**, 221 (1977).

[70] A. Dalgarno, N. Lynn, *Proc. Phys. Soc.* **A70**, 802 (1957).

[71] E.U. Condon, G.H. Shortley, "*The Theory of Atomic Spectra*", Cambrideg Univ. Press, (New York, 1951).

[72] G.V. Marr, R.G. Houlgate, J.B. West, *J. Phys.* **B8**, 2638 (1975).

[73] J.W. Cooper, S.T. Manson, *Phys. Rev.* **177**, 157 (1969).

[74] C.D. Lin, *Phys.Rev.* **A9**, 181 (1974).

[75] P.G. Burke, K.T. Yaylor, *J.Phys.* **B8**, 2621 (1975).

[76] W.J. Karzas, R. Latter, *Ap.J.Suppl.* **56**, 213 (1961).

[77] D.R. Flower, M.J. Seaton, *Comput. Phys. Commun.* **1**, 31 (1969).

[78] H.A. Kramers, *Phil. Mag.* **46**, 836 (1923).

[79] I.I. Sobelman, et al.," *Excitation of Atoms and Broadening of Spectral Lines*", Springer-Verlag, Berlin, Heidelery, (New York, 1981).

[80] J.A. Belling, *J.Phys.*B. **1**, 136 1968.

[81] I.L. Beigman, L.A. Vainshtein, *Sov. Phys.* -JETP **18**, 503 (1964).

[82] A. Burgess, *AERE Report* **4818**, 63 (1964).; A. Burgess,H.P. Summer, *Mon.Not.R.Astr. Soc.* **174**, 345 (1976).

[83] A. Burgess, M.C. Chidicjimo, *Mon.Not.R.Astr.Soc.* **203**, 1269 (1983).

[84] M.J. Seaton, *Planet. Space Sci.* **12**, 55 (1964).

[85] W. Lotz, *Z.Phys.* **216**, 241 (1968).

[86] D.R. Bates, G. Griffing, *Proc. Phys. Soc.***A66**, 961 (1953).

[87] A.L. Merts, R.D. Cowan, N.H. Magee, LA-6220-MS (1976).

[88] U. Fano, *Phys.Rev.* **124**, 1866 (1961).

[89] A. Burgess, *Ap.J.* **141**, 1588 (1965).

[90] J. Chang, et al., in "*Proceeding of The First International Topical Conference on Electron Beam Research And Technology*", **1**, 82, eds. J.Yonas, (Albuquerque, New Mexico, 1975).

[91] D.J. Johnson, *Rev.Sci. Instrum.* **48**, 209 (1977).

[92] D.J. Johnson, S.A.Gddstein, *J. Appl. Phys.* **48**, 2280 (1977).

[93] D.J. Johnson, *Bull.Am.Phys.Soc.* **24**, 925 (1979).

[94] J. Bailey, et al., 1990, preprint

[95] E. Narli, Z. Zinamon, *J.Appl. Phys.* **52**, 7075 (1981).

[96] D. Duston, et al., *Phys.Rev.* **27**, 1441 1983.

[97] J.J. MacFarlane, P. Wang, *Laser and Particle Beam*, submitted, (1991).

[98] W. Smith, W. Weise, *Ap.J.Suppl.* **23**, 103 (1971).

[99] H.C. Grabske, G.J. Harwood, F.J. Rogers, *Phys.Rev.***186**, 210 (1969).

[100] G.M. Harris, *J.Chem.Phys.***31**, 1211 (1959).

[101] G.M. Harris, Phys. Rev. **A133**, 427 (1964).

[102] G.M. Harris, et al., *Phys. Rev.* **119**, 1832 (1960).

[103] W. Däppen, *Astr.Ap.* **91**, 212 (1980).

[104] A. Noels, R. Scuflaire, M. Gabriel, *Astr.Ap.* **130**, 389 (1984).

[105] W.J. Cody, H.C.Jr. Thacher, *Math.Comput.* **21**, 30 (1967).

[106] D. Mihalas, W. Däppen, D.G. Hummer, *Ap.J.* **331**, 815 (1988).

[107] D. Mihalas, "*Stellar Atmospheres*", W.H.Freeman and Company, (New York, 1978).

[108] J.A.R. Samson, R.B. Cairns, *J.Opt.Soc.Am.* **55**, 1035 (1965).

[109] G.V. Marr, J.B. West, *At.Data.Nucl.Data. Table* **18** 497 (1976).

[110] R.D. Hudson, V.L. Carter, *J.Opt.Soc.Am.* **57**, 651 (1966).

[111] R.F. Reilman, S.T. Manson, *Ap.J.Suppl.* **40**, 815 (1979).

[112] J.M. Khan, D.L. Potter, R.D.Worley, *Phys.Rev.* **A139**, 1735 (1965).

[113] A.K. Pradhan, in "*Atomic Processes in Plasmas*", eds. A. Hauer, A.L. Merts, American Institute of Physics, (New York, 1987).

[114] W.L.Van Wyngaarden, et al., *J.Phys.* **B9**, 1461 (1976).

[115] R.B. Christensen, et al., *JILA Data Center Report* **30**, Boulder (1985).